

THESE

Pour l'obtention du Grade de
**DOCTEUR DE L'ECOLE NATIONALE SUPERIEURE DE MECANIQUE ET
D'AEROTECHNIQUE**
(Diplôme National – Arrêté du 25 mai 2016)

Ecole Doctorale :
Sciences et Ingénierie en Matériaux, Mécanique, Énergétique

Secteur de Recherche : Énergétique, Thermique et Combustion

Présentée par : Flavio ACCORINTI

**TWO-PHASE POWER ELECTRONICS COOLING SOLUTION DESIGN IN AIR CONTEXT
ANSWERING TO THE OBJECTIVES OF THE HYBRID AIRCRAFT 2035**

Directeur de thèse : Yves BERTIN
Co-encadrants : Vincent AYEL, Sébastien DUTOIR

Soutenue le 05 Juin 2020

devant la Commission d'Examen

JURY

Président et rapporteur :

HARMAND Souad, Professeur, Université de Valenciennes

Rapporteur :

PLATEL Vincent, Maître de conférences, Université de Pau et des Pays de l'Adour

Membres du jury :

GATEAU Guillaume, Professeur, Institute LAPLACE, INP-ENSEEIH

DUTOIR Sébastien, Maître de conférences, Institute LAPLACE, Université Toulouse

AYEL Vincent, Maître de conférences, Institute Pprime, ISAE-ENSMA

BERTIN Yves, Professeur, Institute Pprime, ISAE-ENSMA

Á Marina

This project has received funding from the [European Union's Horizon 2020 (Cleansky 2 JTI) research and innovation program, 2014-2024] under grant agreement No 715483.



Remerciements

Je souhaite tout d'abord remercier Yves Bertin et Vincent Ayel, maîtres de science et de vie, pour m'avoir suivi pendant ces trois années, pour m'avoir conseillé et pour avoir participé à mon développement professionnel et personnel. Merci pour leur confiance ! Je veux remercier Vincent pour la deuxième fois de m'avoir dédié du temps même quand il n'avait pas de temps et de m'avoir donné envie d'aller plus loin quand je pensais : « ça sert à rien... ». Je souhaite remercier Sébastien Dutour pour m'avoir posé les bonnes questions aux bons moments. Je le remercie car ses questions, toujours appropriées, m'ont permis de prendre du recul pour améliorer mes travaux !

Mes remerciements vont à mes rapporteurs, Prof. Harmand et Prof. Platel qui ont pris le temps de lire ce manuscrit, malgré sa longueur et la langue anglaise. Je voudrais aussi les remercier pour leurs remarques et leurs conseils ainsi que pour les mots d'appréciation qu'ils ont voulu exprimer pour moi et mon travail. Je voudrais remercier tout le jury pour avoir assisté (en visio) à ma soutenance malgré les conditions « atypiques »...

Je tiens à remercier le consortium HASTECS. D'abord je veux remercier Najoua, toujours disponible à échanger par téléphone, même pendant des heures, et pour sa capacité d'alterner une blague à un calcul. C'était un plaisir de travailler avec elle, c'était une très belle collaboration ! Merci à toute l'équipe d'électroniciens (WP2). Merci à l'équipe WP6 : à Matthieu, avec qui j'ai eu le plaisir de partager des bières et des moments en dehors du boulot, pour son sourire, et à son chef, Xavier R., le « big boss » d'HASTECS, pour sa confiance. Merci à Sarah, Amal et Philippe. Merci à AIRBUS et plus en particulier à Jean-François pour sa contribution, son intérêt envers mon travail et sa confiance.

Je voudrais remercier Dominique Couton pour m'avoir mis à disposition le logiciel GRETh (EchTherm) sans lequel le chapitre sept de cette thèse n'existerait qu'en partie...

Merci à tous ceux qui m'ont accompagné pendant mon parcours. Bastien G. pour ses conseils et sa bonne humeur contagieuse, pour son amitié, pour les bons moments qu'on a partagé et pour ceux à venir ! Merci à Yann B. pour son soutien et... ses conseils ; à Florian M. pour son ouverture d'esprit et pour les longues discussions autour de la cuisine.

Merci à Filippo, avec qui j'ai partagé le bureau pendant deux années, pour tous les

échanges qu'on a eu ; merci à Maksime qui est toujours là, même quand il est à Paris ! Merci Arun. Merci à Tung et à tous les déjà docteurs et aux doctorants du labo. Merci à vous tous.

Merci aux italiens à Poitiers (d'hier et d'aujourd'hui) : Nathan (même si tu n'es pas italien ;), Antonio, Vincenzo, Barbara, Federico, Eleonora, Battista, Giuseppe, Marco, Carolina.

Merci à Jonathan Cormier, à Jean-Marie Petit, à Adel et Etienne pour leur bonheur.

Un remerciement spécial va à Gildas, avec qui j'ai partagé mon expérience sur BATH, avant cette aventure, et des cours. Il m'a donné les bons conseils aux bons moments. Peut-être que sans lui je ne serais pas là à tous vous remercier ! Merci à Eva pour sa bonne humeur et son sourire.

Je tiens à remercier toutes les gens qui font partie du labo, en particulier un grand merci va à Catherine L. sans laquelle tout serait à l'arrêt. Merci aux gens de l'équipe technique, qui m'ont « filé un coup de pouce » quand j'en ai eu besoin et pour les nombreux échanges en terrasse pendant la pause. Merci à Christophe qui a toujours répondu (positivement) à mes demandes d'installation de nouveaux logiciels. Merci à Catherine F., Nicolas P., Cyril, Jean-Christophe, Hervé, Sebastien...

Bien sûr, mes plus grands remerciements vont à Marina, ma femme et compagne de vie, à qui j'ai voulu dédicacer cette thèse. Merci de m'avoir toujours soutenu tout au long de mon parcours et surtout merci pour sa patience... Je veux enfin remercier mes parents et mon frère, Bitto, pour avoir toujours cru en moi !

Pendant cette expérience j'ai rencontré des gens inoubliables, et les journées passées avec vous tous je les apporterais pour toujours avec moi.

Merci à tous !

Contents

Remerciements	iii
List of Figures	xvi
List of Tables	xviii
Symbols and Abbreviations	xix
Résumé étendu (Français)	1
I HASTECS	
Hybrid Aircraft Academic reSearch on Thermal and Electrical Com- ponents and Systems	19
Introduction	21
1 Hybrid aircraft power electronics cooling issue	25
1.1 Why power electronics cooling?	25
1.2 The aircraft mission profile	28
1.3 A not constant cold source temperature	29
1.4 The cold source	32
1.4.1 Skin heat exchanger	33
1.4.2 RAM-air	35
II Hybrid aircraft power electronics cooling: from the state of the art to system selection	39
2 Overview of existing cooling solutions	41
2.1 Active cooling systems	44
2.1.1 Single phase cooling systems	45
2.1.1.1 Transport lines	45
2.1.1.2 The pump and the expansion tank	46

2.1.1.3	Heat sink heat transfer	48
2.1.1.4	The cold heat exchanger (HXG)	49
2.1.2	Two-phase active cooling systems	53
2.1.2.1	Pumped two-phase technologies	53
2.1.2.2	Vapour compression technologies	55
2.2	Passive cooling systems	58
2.2.1	Thermosyphons and Heat pipes	58
2.2.1.1	Thermosyphons	58
2.2.1.2	Heat pipes	60
2.2.1.3	Pulsating heat pipes (PHP)	64
2.2.2	Two-phase passive loops	65
2.2.2.1	Loop Heat Pipe (LHP)	65
2.2.2.2	Capillary Pumped Loop (CPL)	67
2.2.2.3	Capillary Pumped Loop for Integrated Power (CPLIP)	68
2.2.3	First comparison between two-phase passive cooling systems	70
2.3	Conclusion	70
3	Power electronics cooling: state of the art of heatsinks	73
3.1	Direct cooling systems: jet impingement and spray cooling	74
3.2	Indirect cooling systems	78
3.2.1	Cold plate	78
3.2.2	Mini and Microchannels	80
3.2.3	Porous media and metal foams	83
3.3	Conclusion	86
4	Technology choice	89
4.1	Comparison of high performance cooling systems	89
4.1.1	Technology screening	93
4.2	System selection	95
4.2.1	Cold source technology comparison	96
4.2.2	First approximation evaluation of mass and power coefficient	98
4.2.3	Cooling technology comparison	104
4.3	Conclusion	107

III CPLIP in HASTECS context	109
5 Capillary Pumped Loop for Integrated Power (CPLIP): working principle, experimental facility and numerical tool	111
5.1 CPLIP generalities and working principle	111
5.1.1 Evaporator	113
5.1.2 Condenser	115
5.1.3 Reservoir	117
5.1.4 Transport lines	118
5.2 Experimental facility	118
5.2.1 CPLIP 1.1: the experimental facility	119
5.3 Numerical models	122
5.4 CPLIP model	123
5.4.1 Navier-Stokes equations	124
5.4.1.1 General case (vapour and liquid lines, condenser)	125
5.4.1.2 Reservoir	126
5.4.1.3 Evaporator	133
5.4.2 Thermal/electrical analogy	134
5.5 Conclusion	137
6 CPLIP answer to HASTECS requirements: thermal characterisation	139
6.1 CPLIP experimental steady-state test campaigns	139
6.1.1 Operating conditions	139
6.1.2 CPLIP thermal response to different heat power levels	141
6.2 Post-processing tool and CPLIP real thermodynamic cycle	142
6.3 CPLIP thermal characterisation for HASTECS specifications	146
6.3.1 Steady-state experimental results and thermal conductance analysis	146
6.3.2 Evaporator-power module numerical analysis	151
6.3.2.1 Power electronics modules characteristics	151
6.3.2.2 Evaporator configuration	152
6.3.2.3 Finite volume analysis of power electronics module	153
6.3.3 Experimental thermal mission profile	157
6.4 Influence of vapour line pressure drop on the thermal response of the CPLIP	159
6.5 Conclusion	164
7 CPLIP optimisation for 2025 and 2035 requirements	167
7.1 Design point	167

7.2	CPLIP optimisation	169
7.2.1	Condenser optimisation	170
7.2.2	Condenser general characteristics	173
7.2.2.1	A condenser for 2025	174
7.2.2.2	A condenser for 2035	182
7.3	Back to design point	186
7.4	Overall power coefficient	188
7.5	Conclusion	189
IV	CPLIP behaviour under severe transient conditions	191
8	Severe transient phases: Start-up	193
8.1	Experimental operating conditions	193
8.2	Start-up behaviour	195
8.2.1	A severe start-up condition	195
8.2.2	Low intensity power load step: experimental analysis	198
8.3	Vapour front velocity evaluation	200
8.4	Discussion	202
8.5	Experimental and numerical results comparison	204
8.5.1	Effect of vapour line wall temperature	204
8.5.2	Effect of vapour line wall thermal inertia	206
8.6	Conclusion	208
9	CPLIP behaviour under sudden and violent acceleration stages	211
9.1	Accelerations in civil flight applications	212
9.2	Simulation conditions	213
9.3	CPLIP behaviour under perturbed transient acceleration field	214
9.4	Parametric study	221
9.5	Conclusion and perspectives	225
V	Conclusion and Perspectives	227
10	General conclusion	229
11	Perspectives	237
11.1	General perspectives	237
11.2	A newer technology: Capillary Jet Loop (CJL)	238

Bibliography	241
Appendix	257
A Working fluid discussion	259
B First approximation design	261
B.1 Active single phase (liquid cooling) first approximation design	261
B.1.1 The cold plate	261
B.1.2 Pump selection	262
B.1.3 Transport lines	262
B.1.4 Single phase cold heat exchanger	263
B.1.4.1 Skin heat exchanger first approximation design	263
B.1.4.2 Cold heat exchanger in a bank configuration	266
B.2 Two-phase solution first approximation design	268
B.2.1 The evaporator	268
B.2.2 Condenser design	268
B.2.2.1 Skin heat exchanger for a two-phase internal flow: con-	
denser first approximation design	268
B.2.2.2 Condenser design in tube bank configuration	273
C GRETh (EchTherm)	275
C.1 Continuous finned heat exchangers	275
C.1.1 Limits and hypothesis	275
C.1.2 Correlations	275
C.1.2.1 External side	275
C.1.2.2 Internal side	277
C.2 Louvered fins & microchannels heat exchanger	281
C.2.1 Limitations and hypothesis	281
C.2.1.1 External side	281
C.2.1.2 Internal side	282
D Heavy duty tests	285

List of Figures

0.1	Involved Labs	21
0.2	WPs and their interactions	22
1.1	Electric power losses scheme	26
1.2	Mass distribution of a 3-level PWM NPC electronic system (using 6th gen. 1700 V IGBT) equipped by a classical air forced convection cooling system [1].	27
1.3	Qualitative thermal mission profile and altitude variation as a function of time.	29
1.4	ISA diagram for pressure and temperature as a function of the altitude [2]	31
1.5	Cooling system loop as a broker	33
1.6	Skin heat exchanger 3D scheme [3]	34
1.7	Skin heat exchanger scheme [4]	34
1.8	Positioning scheme of skin heat exchanger [4]	35
1.9	RAM air.	36
2.1	Cooling systems classification.	41
2.2	General scheme of an active cooling system	44
2.3	Single phase cooling system concept scheme	45
2.4	Expansion vessels typologies	47
2.5	Heat transfer mechanism simplified scheme in the heat sink.	48
2.6	Co-current heat exchanger qualitative operating diagram	50
2.7	Cold side heat exchanger concept scheme	52
2.8	Air mass flow rate as a function of the external air temperature and altitude.	52
2.9	Pumped two-phase cooling system concept scheme.	54
2.10	Vapour compression concept diagram scheme.	56
2.11	Scheme of principle of an active two-phase thermal system equipped by a MMPS solution [5].	57
2.12	Thermosyphon [6]	59
2.13	Heat Pipe. [6]	61
2.14	Heat pipes application example	62

2.15 Pulsating heat pipes [6].	64
2.16 Loop Heat Pipe Scheme and thermodynamic cycle	66
2.17 Principle scheme and thermodynamic cycle of CPL and LHP loops	68
2.18 CPLIP scheme [7]	69
3.1 Spray cooling	75
3.2 Typical spray cooling curve [8]	76
3.3 Cold plate for electronic cooling [9]	79
3.4 Thermal and hydraulic performances of water, fuel and oil [9]	80
3.5 Microchannels	81
3.6 Metal foam example [10]	84
3.7 Micrographs of sintered porous medium (a), compressed metal foam (b) and metal foam (c)	84
4.1 Historical trend of heat flux density and thermal evacuation capability for active and passive technologies.	90
4.2 Maximal total thermal load and heat flux density histogram of active cooling techniques.	91
4.3 Maximal total thermal load and heat flux density histogram of passive cooling systems. [11].	91
4.4 Technology comparison [11]	92
4.5 Transport distance for different passive technologies	94
4.6 Unladen, fluid and total mass comparison for the considered technologies.	105
4.7 Mass composition of different cooling technologies	106
5.1 Scheme of principle of CPLIP	112
5.2 CPLIP thermodynamic cycle [12]	112
5.3 Evaporator assembly	113
5.4 Evaporator sections	114
5.5 Schematic of evaporation in a porous wick.	115
5.6 Condensation flow regimes [13]	116
5.7 Reservoir concept scheme	118
5.8 Schematic of the CPLIP 1.1 [12, 14, 15]	120
5.9 Evaporator concept scheme (sec. A-A)	120
5.10 Staggered grid	124
5.11 Reservoir schematic	127
5.12 Reservoir lower part discretisation	127

5.13	Reservoir higher part thermo-hydraulic model	131
5.14	Evaporator discretisation	133
5.15	Thermal/hydraulic-electrical analogy networks [16]	136
6.1	Example of NCG absence verification (methanol)	141
6.2	CPLIP temperature evolution as a function of the time, for different heat power applied to the evaporator (methanol, $T_{res} = 70^\circ\text{C}$ and $T_{sec} = 20^\circ\text{C}$) [12].	142
6.3	CPLIP thermodynamic cycle: comparison at $Q = 0.5\text{ kW}$ and $Q = 5\text{ kW}$ (methanol, $T_{res} = 70^\circ\text{C}$ and $T_{sec} = 20^\circ\text{C}$) [12].	144
6.4	CPLIP thermodynamic cycle: comparison at $T_{res} = 50; 60$ and 70°C (methanol, $Q = 1.5\text{ kW}$ and $T_{sec} = 20^\circ\text{C}$) [12].	145
6.5	CPLIP thermodynamic cycle: comparison at $T_{sec} = 5; 20$ and 40°C (methanol, $Q = 1.5\text{ kW}$ and $T_{res} = 70^\circ\text{C}$).	146
6.6	Evaporator thermal conductance, $G_{ev,res}$, based on the reservoir saturation temperature as a function of the thermal load (ethanol and methanol, $T_{res} = 50; 60; 70$ and 80°C , $T_{sec} = 20^\circ\text{C}$).	147
6.7	Mean diffuser wall temperature, \bar{T}_{diff} ; evaporator saturation temperature, T_V , as a function of the thermal load (methanol, $T_{sec} = 5; 20;$ and 40°C , $T_{res} = 70^\circ\text{C}$) [12].	149
6.8	$G_{ev,res}$ and $G_{ev,V}$ comparison as a function of the thermal power (meth- anol, $T_{sec} = 5; 20;$ and 40°C , $T_{res} = 70^\circ\text{C}$)	150
6.9	$HTC_{ev,V}$ and $HTC_{ev,res}$ comparison as a function of the thermal power (methanol, $T_{sec} = 20^\circ\text{C}$, $T_{res} = 70^\circ\text{C}$).	150
6.10	7th Generation Mitsubishi module	151
6.11	Evaporator configuration example [1].	152
6.12	Power module scheme and boundary conditions	153
6.13	Mesh example	154
6.14	Mesh independence temperature distribution (methanol, $T_{res} = 70^\circ\text{C}$)	155
6.15	Temperature map CASE 1 (junction view): $Q_{th,D} = 155\text{ W}$; $Q_{th,I} = 0\text{ W}$ (methanol, $T_{res} = 70^\circ\text{C}$).	156
6.16	Temperature map CASE 1 (evaporator-module interface view, according to Fig. 6.15): $Q_{th,D} = 155\text{ W}$; $Q_{th,I} = 0\text{ W}$ (methanol, $T_{res} = 70^\circ\text{C}$).	156
6.17	Temperature map CASE 2 (junction view): $Q_{th,D} = 12\text{ W}$; $Q_{th,I} = 133\text{ W}$ (methanol, $T_{res} = 70^\circ\text{C}$).	157
6.18	Temperature map CASE 2 (evaporator-module interface view, according to Fig. 6.17): $Q_{th,D} = 12\text{ W}$; $Q_{th,I} = 133\text{ W}$ (methanol, $T_{res} = 70^\circ\text{C}$).	157

6.19	Experimental thermal mission profile (methanol, $T_{sec} = 20^{\circ}\text{C}$, $T_{res} = 70^{\circ}\text{C}$).	158
6.20	Time dependent diagram of temperature evolution of the CPLIP for increasing vapour line pressure drop (methanol, $Q_{th} = 1\text{ kW}$, $T_{sec} = 20^{\circ}\text{C}$).	160
6.21	Thermodynamic cycle comparison between the highest and the lowest valve overture: $N/N_{max} = 0.25$ and $N/N_{max} = 1$ (methanol, $Q_{th} = 1\text{ kW}$, $T_{res} = 70^{\circ}\text{C}$ and $T_{sec} = 20^{\circ}\text{C}$).	161
6.22	\bar{T}_{diff} as a function of N/N_{max} and for different thermal loads (methanol, $T_{res} = 70^{\circ}\text{C}$; $T_{sec} = 20^{\circ}\text{C}$).	162
6.23	Temperature differences as a function of the valve overture (ethanol and methanol, $T_{res} = 70^{\circ}\text{C}$; $T_{sec} = 20^{\circ}\text{C}$).	162
6.24	Thermal conductance as a function of the pressure drop (ethanol and methanol, $T_{res} = 70^{\circ}\text{C}$; $T_{sec} = 20^{\circ}\text{C}$).	163
6.25	Overall pressure drop as a function of valve opening (N/N_{max}) and for different thermal loads (ethanol and methanol, $T_{res} = 70^{\circ}\text{C}$; $T_{sec} = 20^{\circ}\text{C}$).	164
7.1	Design point choice	168
7.2	Passive two-phase mass distribution (three parallel evaporators CPLIP: —CERBERE—)	169
7.3	Optimisation process of a heat exchanger.	171
7.4	Fin configurations used for 2025 solution [17]	173
7.5	Circular fins geometric characteristics	175
7.6	Condenser mass and thermal power coefficient as a function of fin thickness, δ .	176
7.7	Continuous fins geometric characteristics	177
7.8	Condenser mass distribution for optimised and not optimised solution	180
7.9	Cooling system overall mass and thermal power coefficient as a function of the thermal load	181
7.10	Components mass distribution for 16 kW CPLIP	181
7.11	Louvered fin condenser	183
7.12	Louvered fins and microchannels condenser mass distribution example	185
7.13	Louvered fin-microchannels equipped CPLIP mass distribution	186
7.14	Mass and thermal power coefficient as a function of the thermal load (2035)	186
7.15	Thermal load shape and temperature increase due to not treated thermal energy	187
7.16	Global power coefficient trends for 2025 and 2035 solutions	189

8.1	CPLIP: experimental facility	194
8.2	Heating process of the vapour line solid walls (methanol, $T_{res} = 70^\circ\text{C}$). . .	195
8.3	0 – 5 kW cold start-up (methanol, $T_{res} = 70^\circ\text{C}$, $T_{sec} = 20^\circ\text{C}$).	196
8.4	0 – 4 kW hot start-up failure (methanol, $T_{res} = 70^\circ\text{C}$, $T_{sec} = 20^\circ\text{C}$). . . .	197
8.5	Cold start-up (methanol, $T_{res} = 70^\circ\text{C}$, $T_{sec} = 20^\circ\text{C}$)	199
8.6	Hot start-up (methanol, $T_{res} = 70^\circ\text{C}$, $T_{sec} = 20^\circ\text{C}$)	199
8.7	Qualitative sigmoid profile as a function of the time	201
8.8	Temperature profiles as a function of the time, fitted curves for $Q_{th} = 2\text{ kW}$ (methanol, $T_{res} = 70^\circ\text{C}$, $T_{sec} = 20^\circ\text{C}$).	202
8.9	Experimental and numerical comparison for a cold start-up (methanol, $Q_{th} = 0.4\text{ kW}$, $T_{res} = 70^\circ\text{C}$, $T_{sec} = 20^\circ\text{C}$).	205
8.10	Vapour front qualitative shapes: real (up), numerical (piston shape, down)	205
8.11	Vapour line temperature profiles with (continuous lines) and without (dashed lines) solid wall thermal inertia (methanol, $Q_{th} = 0.4\text{ kW}$, $T_{res} = 70^\circ\text{C}$, $T_{sec} = 20^\circ\text{C}$)	206
8.12	Mass flow rate profiles with (continuous lines) and without (dashed lines) solid wall thermal inertia (methanol, $Q_{th} = 0.4\text{ kW}$, $T_{res} = 70^\circ\text{C}$, $T_{sec} =$ 20°C)	207
8.13	Vapour quality profiles with (continuous lines) and without (dashed lines) solid wall thermal inertia (methanol, $Q_{th} = 0.4\text{ kW}$, $T_{res} = 70^\circ\text{C}$, $T_{sec} =$ 20°C)	207
8.14	Real start-up condition $3 \times 0.8\text{ kW}$ (methanol, $T_{res} = 70^\circ\text{C}$, $T_{sec} = 20^\circ\text{C}$)	209
9.1	Qualitative diagram of acceleration impulse used for study	214
9.2	Total pressure variation diagram during acceleration impulse (methanol, $Q_{th} = 1\text{ kW}$, $T_{res} = 70^\circ\text{C}$, $T_{sec} = 20^\circ\text{C}$, $3g$, $H = 90\text{ cm}$)	215
9.3	Mass flow rate variation diagram during acceleration impulse ($Q_{th} = 1\text{ kW}$, $T_{res} = 70^\circ\text{C}$, $T_{sec} = 20^\circ\text{C}$, $3g$, $H = 90\text{ cm}$)	216
9.4	Condenser inlet to outlet pressure (top) and mass flow rate (bottom) dif- ference during acceleration impulse (methanol, $Q_{th} = 1\text{ kW}$, $T_{res} = 70^\circ\text{C}$, $T_{sec} = 20^\circ\text{C}$, $3g$, $H = 90\text{ cm}$)	217
9.5	Two-phase length variation during acceleration impulse (methanol, $Q_{th} =$ 1 kW , $T_{res} = 70^\circ\text{C}$, $T_{sec} = 20^\circ\text{C}$, $3g$, $H = 90\text{ cm}$)	219
9.6	Vapour quality variation during acceleration impulse (methanol, $Q_{th} =$ 1 kW , $T_{res} = 70^\circ\text{C}$, $T_{sec} = 20^\circ\text{C}$, $3g$, $H = 90\text{ cm}$)	219
9.7	Temperature variation during acceleration impulse (methanol, $Q_{th} = 1\text{ kW}$, $T_{res} = 70^\circ\text{C}$, $T_{sec} = 20^\circ\text{C}$, $3g$, $H = 90\text{ cm}$)	220

9.8	Acceleration impulsion time duration, Δt_{gp} , effect condenser outlet mass flow rate (methanol, $Q_{th} = 1 \text{ kW}$, $T_{res} = 70^\circ\text{C}$, $T_{sec} = 20^\circ\text{C}$, $H = 80 \text{ cm}$, 3g)	222
9.9	Qualitative diagram of accumulated liquid mass during perturbation perturbation (area Ξ) and returning mass during settling (area Γ)	223
9.10	Condenser-to-reservoir height difference effect on condenser outlet mass flow rate (methanol, $Q_{th} = 1 \text{ kW}$, $T_{res} = 70^\circ\text{C}$, $T_{sec} = 20^\circ\text{C}$, $\Delta t_{gp} = 0.25 \text{ sec}$, 3g)	224
9.11	Acceleration impulse intensity effect on the reversed mass flow rate and condensation length (methanol, $Q_{th} = 1 \text{ kW}$, $T_{res} = 70^\circ\text{C}$, $T_{sec} = 20^\circ\text{C}$, $\Delta t_{gp} = 0.25 \text{ sec}$, $H = 30 \text{ cm}$)	225
9.12	Pressure at condenser outlet for different acceleration intensity (methanol, $Q_{th} = 1 \text{ kW}$, $T_{res} = 70^\circ\text{C}$, $T_{sec} = 20^\circ\text{C}$, $\Delta t_{gp} = 0.25 \text{ sec}$, $H = 30 \text{ cm}$)	225
11.1	Capillary Jet Loop concept [18]	238
11.2	Injector principle scheme [19]	239
11.3	Scheme of principle of CJL adapted for HASTEC requirements	240
A.1	Comparison between different fluid using Mouromtseff number	259
A.2	Fluid to water comparison	260
B.1	Single phase cooling system scheme	261
B.2	Two different cold plate configurations	262
B.3	Skin heat exchanger	264
B.4	Hypothesis	265
B.5	Mesh configuration	266
B.6	Moody diagram	267
B.7	Tube bank configuration	268
B.8	Mesh configuration for two-phase flow	269
D.1	Heavy duty test (methanol, $T_{res} = 70^\circ\text{C}$, $T_{sec} = 20^\circ\text{C}$, $Q_{th} = 2 \text{ kW}$) . . .	285
D.2	Saturation conditions in the reservoir before and after the tests (methanol, $T_{res} = 70^\circ\text{C}$)	286

List of Tables

1.1	Temperature specifications [2]	31
2.1	Single phase cooling system synthesis	53
2.2	Synthesis of the main characteristics of CPL, LHP and CPLIP.	70
2.3	Pros and drawbacks comparison between passive cooling systems	71
3.1	Comparison of different porous media characteristics [20]	85
3.2	Active cooling systems pro & drawbacks	88
4.1	Main characteristics of the cooling systems	93
4.2	Technology generalities.	98
4.3	Cooling system main geometrical dimensions.	100
4.4	Single phase cooling system mass evaluation (first approximation design).	101
4.5	Pumped two-phase cooling system mass evaluation (first approximation design).	102
4.6	Two-phase passive cooling system mass evaluation (first approximation design of a three-evaporators-CPLIP).	103
4.7	Two-phase passive cooling system mass evaluation (first approximation design of three different one-evaporator-CPLIP).	103
4.8	Cooling systems geometrical characteristics.	104
6.1	Summary of experimental tests [12]	140
7.1	Thermal energy ratios during take-off and cruise stage	169
7.2	Individually finned condenser geometrical parameters for different fin pitches and thickness	175
7.3	Parametric study of continuous fins condenser.	177
7.4	Condenser configurations comparison.	177
7.5	Optimised solution geometry, 2025	179
7.6	Optimised solution thermo-hydraulic characteristics, 2025 (C: condensation zone; S: subcooling zone; G: global; F: fin)	179
7.7	Optimised results for the proposed electronic topologies (2025) [1, 21] . . .	182

7.8	Optimised solution geometry, 2035	183
7.9	Optimised solution thermo-hydraulic characteristics, 2035 (C: condensation zone; S: subcooling zone; G: global; F: fin)	184
8.1	Successful and unsuccessful start-up synthesis	198
8.2	Thermocouples distances	201
8.3	Velocity evaluation for hot and cold start up at 0.5 kW and a 2 kW power steps	202
9.1	Acceleration modules, wing zone up to O/B engine	213
9.2	Performed simulations	222

Symbols and Abbreviations

Abbreviations

CHF Critical Heat Flux

CHT Conjugated Heat Transfer

CLT Closed Loop Thermosyphon

CPL Capillary Pumped Loop

CPLIP Capillary Pumped Loop for Integrated Power

CPLTA Capillary Pumped Loop for Terrestrial Applications (see CPLIP)

FPHP Flat Plate Heat Pipe

GHP Grooved Heat Pipe

HP Heat Pipe

HT Heat Transfer

HTC Heat Transfer Coefficient

IGBT Insulated Gate Bipolar Transistor

ISA International Standard Atmosphere

LHP Loop Heat Pipe

MFR Mass Flow Rate

NCG Non condensable Gases

PHP Pulsating Heat Pipe

PPI Pore per Inch

Th Thermosyphon

VC Vapour Chamber

WHF Wall Heat Flux

Greek Symbols

α Fraction

α_g Vapour void fraction [—]

β Fluid Compressibility Factor

Ω Control Volume

ρ Density [kg · m⁻³]

σ Surface Tension [N · m⁻¹]

θ Wetting Angle [—]

Roman Symbols

ΔP Pressure Drop or Pressure Head [Pa]

\dot{Q} Heat [W]

\dot{W}_{comp} Work [J]

h Altitude [m]

A Heat transfer surface area [m⁻²]

C_v Valve Flow Coefficient [—]

D Diameter [m]

d_i Internal Diameter [m]

E Energy [J]

G Mass flow rate per unit area [kg · s⁻¹ · m⁻²]

g Gravity acceleration [m · s⁻²]

$G_{ev,res}$ Evaporator thermal conductance based on the reservoir saturation temperature [W/K]

$G_{ev,V}$	Evaporator's conductance based on the evaporator saturation temperature [W/K]	
H	Height	[m]
h	Enthalpy	[J · kg ⁻¹]
h	Heat Transfer Coefficient	[W · m ⁻² · K ⁻¹]
$h_{l,v}$	Latent Heat	[J · kg ⁻¹]
j_g^*	Dimensionless Vapour Mass Velocity	[—]
k	Thermal Conductivity	[W · m ⁻¹ · K ⁻¹]
K_V	Volumetric Heat Transfer Coefficient	[W · m ⁻³ · K ⁻¹]
L	Length	[m]
m	Mass	[kg]
N	Valve Number of Turns	
P_V	Evaporator's saturation pressure	[Pa]
Q	Thermal Power [Unless otherwise indicated]	[W]
R	Curvature Radius	[m]
R_p	Pore Radius	[m]
T_V	Evaporator's saturation temperature	[°C]
V	Volume	[m ³]
Fr	Froude number	[—]
We	Weber number	[—]

Subscripts

c	Condenser
cap	Capillary
ci	Cold fluid at the inlet of the heat exchanger
co	Cold fluid at the outlet of the heat exchanger

<i>D</i>	Diode
<i>diff</i>	Diffuser (wall)
<i>el</i>	Electrical
<i>ext</i>	External (side)
<i>f</i>	frictional
<i>g</i>	Gas (Phase)
<i>go</i>	Gas (vapour) only
<i>hi</i>	Hot fluid at the inlet of the heat exchanger
<i>ho</i>	Hot fluid at the outlet of the heat exchanger
<i>I</i>	IGBT
<i>I</i>	Inlet
<i>int</i>	Internal (side)
<i>l</i>	Liquid (Phase)
<i>lo</i>	Liquid only
<i>max</i>	Maximum
<i>O</i>	Outlet
<i>res</i>	Reservoir
<i>s</i>	Solid (Phase)
<i>sec</i>	Secondary side (cold source)
<i>sns</i>	Sensible (heat)
<i>th</i>	Thermal
<i>tot</i>	Total
<i>v</i>	Vapour (Phase)

Résumé étendu (Français)

Le projet HASTECS (Hybrid Aircraft academic reSearch on Thermal and Electrical Components and Systems) est un projet européen Clean Sky 2 financé par H2020-EU.3.4.5.1. L'objectif de ce projet est le développement d'outils pour la conception et le développement de l'avion du futur à propulsion hybride. En particulier le projet est concentré sur la recherche de la génération, distribution, conversion et management thermique de la chaîne de puissance électrique. Plusieurs instituts de recherche français participent au consortium HASTECS. Par exemple, les sujets liés à l'électronique de puissance et au moteur électrique concernent l'Institut LAPLACE à Toulouse, tandis que leur refroidissement est étudié à l'Institut Pprime à Poitiers. Le partenaire industriel du projet est AIRBUS. Six différentes équipes, associées aux différents WPs (Work Packages), travaillent sur le projet, chacune avec des tâches et objectifs différents. WP1 a pour but la recherche d'une technologie adaptée au moteur électrique (eMotor) ; WP2 travaille sur l'électronique de puissance. Ces engins sont utilisés pour convertir le courant électrique continu (DC) en courant alternatif (AC) pour l'alimentation du moteur électrique à la fréquence appropriée : l'équipe doit trouver une technologie de rupture et développer un modèle pour le design des modules de puissance. Le management thermique des eMoteurs et de l'électronique de puissance sont abordés respectivement par le WP3 et le WP4. Tous deux doivent trouver une solution de rupture pour le refroidissement des équipements associés. Au WP3 est demandé le développement d'un modèle à intégrer dans l'outil d'optimisation globale, tandis que le but du WP4, entre autres, est la recherche, la conception, l'optimisation, le développement et l'étude d'une solution d'avant-garde pour le refroidissement de l'électronique de puissance. Ce dernier work package devrait alimenter le WP2 avec des outils de conception simplifiés qui devront être intégrés dans le modèle de conception et d'optimisation globale de la chaîne de conversion hybride. Ainsi, WP2 et WP4 sont fortement couplés entre eux. Ensuite, le WP5 a pour but l'étude des décharges partielles, bus-bars et câbles et, pour finir, la tâche du WP6 est l'étude de l'intégration des sources auxiliaires : piles à combustible et batteries, pour une optimisation de la masse embarquée dans l'avion. Tous les WPs convergent vers le WP6. Le but de ce sujet présenté dans ce travail (WP4), principalement numérique, est de rechercher, concevoir, et optimiser une solution pour le refroidissement de l'électronique de puissance en

contexte aérien. Un tel système de refroidissement devrait être capable d'évacuer la chaleur tout en assurant le contrôle de température au niveau de la semelle des composants électroniques, et répondant aux contraintes de masse imposées par AIRBUS. À cet effet, des modèles ont été développés et certains, déjà existants, ont été modifiés et adaptés. Les principales problématiques stationnaires et transitoires ont été abordées et résolues et, quand cela a été possible, comparées avec des résultats issus de tests expérimentaux. La thèse est divisée en cinq parties. Ici, les problématiques scientifiques et technologiques d'ingénierie ont été abordées dans le but de proposer une solution robuste et fiable.

La problématique du refroidissement de l'électronique de puissance pour l'avion hybride

Le refroidissement de l'électronique de puissance est l'un des problèmes majeurs de la gestion des nouvelles motorisations électriques du futur. L'augmentation de la puissance électrique des composants a mené à l'augmentation de la puissance thermique à évacuer. Dans le passé, la problématique du refroidissement des composants électroniques a été sous-évaluée car les technologies classiques de refroidissement (convection forcée à air) étaient plus ou moins capables d'évacuer la puissance thermique tout en maintenant la température des composants électroniques à des niveaux raisonnables. Un grand effort a été fait pour augmenter l'efficacité des composants électroniques, mais comme cela était facilement prévisible, l'asymptote a été atteinte et les technologies de refroidissement n'ont pas évolué ! Dans le même temps, certaines technologies encore plus performantes n'étaient pas accessibles car les pertes thermiques étaient encore trop importantes. L'efficacité électrique ne devrait pas être vue comme un nombre à maximiser à tout prix : à n'importe quelle transformation d'énergie, des pertes thermiques y sont associées (qui peuvent être réduites mais pas annulées) et donc, quel que soit le système, le rendement sera toujours inférieure à 1. Si la puissance demandée par les moteurs électriques est $Q_{el} = 1.5 \text{ MW}$, en considérant une efficacité des modules de puissance $\eta_{el} = 99\%$, la puissance totale à fournir est de $Q_{el} = 1.515 \text{ MW}$, et les pertes associées de $Q_{th} = 15 \text{ kW}$. Cette valeur est bien loin d'être négligeable et un système de refroidissement capable d'évacuer cette puissance thermique est donc nécessaire. Dans le cas des applications à puissance électrique élevée, le problème est encore plus évident car les pertes doivent être évacuées en maximisant l'efficacité globale du système (électrique + thermique). L'optimisation n'est plus limitée à la simple optimisation de chaque composant du système, mais il est nécessaire de considérer le système dans sa globalité pour augmenter l'efficacité, calculée sur la base d'un indice. Dans le cas des applications aéronautiques, le système doit répondre aussi à des contraintes de masse et de volume occupé. Pour mesurer la légèreté d'un système, par rapport à son utilité, on introduit le concept

de coefficient de puissance, C_c [$\text{kW} \cdot \text{kg}^{-1}$]. Ce dernier représente la puissance électrique convertie pour chaque kg de masse du système, y compris du refroidissement. Deux objectifs ont été donnés pour résoudre le problème. Le premier objectif, à l'horizon 2025 est d'obtenir $C_{c,2025} = 15 \text{ kW} \cdot \text{kg}^{-1}$, tandis que celui à l'horizon 2035 est d'atteindre $C_{c,2035} = 25 \text{ kW} \cdot \text{kg}^{-1}$, a minima ! L'énergie demandée à la chaîne de propulsion d'un avion n'est pas constante dans le temps, mais varie en fonction des différentes phases de vol. Comme pour la puissance mécanique demandée aux moteurs électriques, la puissance que les modules de puissance doivent convertir et, par conséquent, la puissance thermique à évacuer, changent dans le temps. A partir d'un profil de mission type, cinq phases de vol peuvent être distinguées. Pendant la première phase, l'avion reste au sol et les pertes thermiques sont les plus faibles. La deuxième phase, de « take-off & climb » (décollage et ascension), peut être divisée en deux sous-phases : le take-off, qui représente le moment où l'avion accélère sur la piste et où la puissance maximale est demandée aux moteurs pour faire décoller l'avion, et l'ascension, où l'avion monte jusqu'à atteindre la hauteur h_{max} . La phase de croisière est presque stationnaire, la puissance thermique à évacuer est constante dans le temps et sa durée est d'environ 70 minutes. De façon identique à la deuxième phase, la phase de descente et atterrissage peut être divisée en deux sous-phases. Pendant la descente l'avion plane jusqu'à l'approche et c'est là qu'un pique de puissance est demandé. Enfin, pendant la phase de « taxi-in », la puissance thermique à évacuer est la même que pendant la phase de « taxi-out ». La variation dans le temps de la puissance thermique à évacuer est aussi accompagnée par une variation de température de l'air ambiant et donc de la source froide. Le lien entre l'altitude et la température de l'air est exprimée par le NASA's Earth Atmosphere Model [22], selon lequel, dans la troposphère ($h \leq 11\,000 \text{ m}$), le lien entre les deux grandeurs est linéaire. Les systèmes de communication radio, les systèmes embarqués et autres systèmes électroniques installés à bord sont aussi refroidis en utilisant directement ou indirectement l'air extérieur comme source froide. Comme la plupart de ces systèmes, l'idée développée au cours de cette thèse est d'utiliser l'air extérieur comme source froide, en utilisant une boucle de refroidissement pour transporter la chaleur de la source chaude à la source froide où la puissance thermique est définitivement évacuée. De plus, l'utilisation de « heatsinks » plus performantes, permettrait d'augmenter l'efficacité de l'échange thermique en atteignant des coefficients d'échange d'ordre de grandeur plus élevés que ceux liés à la simple convection forcée à air. Deux différentes technologies sont ici considérées comme sources froides : l'échangeur à peau (skin heat exchanger) qui introduit une résistance additionnelle à cause de la présence d'une paroi solide entre la tuyauterie de la boucle de refroidissement et l'air externe : la peau de l'avion ; et le système RAM-air qui permet un

contact direct entre l'air ambiant et les tubes de l'échangeur de chaleur. L'échangeur à peau peut être vu comme faisant déjà partie de l'avion, les tuyaux passent à l'extérieure de la couche isolante de l'avion. Pang et al. [4] ont analysé cette technologie pour un avion volant à Mach 0.9, et à 10 km d'altitude. En considérant deux emplacements différents pour l'échangeur à peau, ils ont trouvé une position défavorable, où le coefficient d'échange thermique était entre $45 - 51 \text{ W} \cdot \text{m}^{-2} \cdot \text{K}^{-1}$, tandis que pour la position la plus favorable le coefficient d'échange était entre $80 - 66 \text{ W} \cdot \text{m}^{-2} \cdot \text{K}^{-1}$. Le système RAM-air représente la technologie la plus ancienne permettant d'amener l'air extérieur à bord de l'avion pour être utilisé comme source froide pour le refroidissement des systèmes électroniques ou autres. Il est composé par une entrée d'air de type NACA, un diffuseur, le côté secondaire de l'échangeur de chaleur, une tuyère (simplement convergent) et la sortie d'air. Ce système est caractérisé, bien sûr, par un encombrement plus grand que celui de l'échangeur à peau, mais il est capable d'assurer des coefficients d'échange thermique bien plus élevés que ce dernier.

Solutions de refroidissement existantes

A cause de la complexité des systèmes de refroidissement, du nombre de composants, des différents principes physiques liés à leur fonctionnement, il n'existe pas de classification universelle. Les performances dépendent, bien sûr, du système de refroidissement et de son architecture, ainsi que de la typologie du « heatsink » (module de refroidissement situé au niveau de la source chaude) utilisé. En général, un système de refroidissement est utilisé pour maintenir la température du dispositif à refroidir contrôlée tout en évacuant la puissance thermique. Dans ce but, deux différentes méthodes sont utilisées :

- refroidir le dispositif en utilisant directement l'air externe (refroidissement à air ou, plus généralement, circuits de refroidissement ouverts)
- refroidir le dispositif en utilisant une boucle à circuit fermé (refroidissement liquide ou, plus en général, circuits de refroidissement fermés).

Dans le premier cas, à cause du fait que l'air extérieur est utilisé directement comme fluide caloporteur, en particulier dans le domaine aéronautique, il est nécessaire de considérer certaines contraintes comme la variabilité de la température, de la pression et de la masse volumique de l'air extérieur. Tous ces facteurs ont un impact pas tout à fait négligeable sur le coefficient d'échange thermique et donc sur les performances du système de refroidissement. La seconde méthode est plus pertinente. En effet, grâce à l'utilisation d'un circuit intermédiaire entre la source froide et le dispositif à refroidir, il y a un découplage entre le coefficient d'échange de l'échangeur secondaire et celui au niveau du « heatsink ». Tout ça est encore plus vrai lorsque l'on considère les systèmes de refroidisse-

ment diphasiques, actifs ou passifs. Dans ce cas, le coefficient d'échange du « heatsink » dépend de la technologie utilisée (microcanaux, mousse métalliques ou autres) et non pas des caractéristiques de l'air extérieur. Un circuit fermé est donc le choix le mieux adapté. Les systèmes à circuit fermé peuvent être divisés entre systèmes actifs et passifs. Dans les systèmes actifs l'utilisation d'une pompe ou d'un compresseur (selon la typologie) est nécessaire pour permettre le mouvement du fluide caloporteur dans la boucle. Les systèmes passifs, en revanche, utilisent la gravité ou la capillarité pour générer l'écoulement nécessaire au fluide de refroidissement. Dans les systèmes actifs, la pompe (ou compresseur dans le cas de systèmes à compression de vapeur), doit être conçue pour contrebalancer toutes les pertes de charge dans le circuit et assurer le bon débit pour l'évacuation de la chaleur. Un vase d'expansion est utilisé pour amortir des instabilités éventuelles (coup de bélier ou dilatation du fluide caloporteur due à l'augmentation de température). Les systèmes actifs peuvent être mono ou diphasique et, même si les principes de fonctionnement sont profondément différents, les composants sont peu ou prou identiques et jouent le même rôle. La technologie des systèmes actifs monophasiques est sans doute la plus ancienne, aussi connue comme "refroidissement à liquide", son utilisation est très étendue à cause de sa simplicité et de la bonne connaissance de phénomènes à la base de son fonctionnement. Le fluide est chauffé dans le "heatsink", puis s'écoule dans la ligne de transport et, finalement, il arrive dans l'échangeur froid où la chaleur est évacuée. Selon la disponibilité de la source froide, l'une des technologies présentées dans le premier chapitre peut être utilisée. L'une des principales limitations liées à l'utilisation de cette technologie est la forte dépendance entre la température de la source froide et la température de la source chaude et, par conséquence, de la température de jonction du composant. On démontre très facilement que la température de jonction a un lien direct avec la température d'entrée de l'air dans l'échangeur de chaleur, ce qui peut limiter l'application de cette technologie à notre cas. En effets, à cause des changements de température de l'air extérieur en fonction de l'altitude (ici on ne considère pas les changements de la masse volumique et de pression), la capacité de maintenir la température de jonction fixe, quelle que soit la condition opératoire, devient très difficile. Cependant, il est possible de garder cette caractéristique, mais au prix de pouvoir faire varier soit le débit du fluide caloporteur soit celui de l'air, en rajoutant un système de vannes et d'autres accessoires compliquant fortement le système de refroidissement et sa régulation. Dans les systèmes diphasiques, les chaleurs latente et sensible du fluide sont utilisées pour évacuer la chaleur : le "heatsink" est alors un évaporateur tandis que l'échangeur froid est un condenseur (avec sous-refroidissement). Le liquide sous-refroidi en provenance du condenseur/échangeur froid s'écoule vers l'évaporateur. Le fluide chaud

rejoint à nouveau le condenseur/échangeur froid où la chaleur est définitivement évacuée vers l'air extérieur et le cycle recommence. Les systèmes actifs diphasiques sont divisés en deux catégories : les systèmes pompés dont l'évaporateur opère forcément à une température plus élevée que le condenseur et où une pompe est installée sur la ligne liquide ; les systèmes à compression de vapeur dont l'évaporateur peut opérer à des températures plus basses que le condenseur (grâce à l'utilisation d'un cycle de Rankine) et où un compresseur est installé sur la ligne vapeur. Le liquide sous-refroidi provenant du condenseur, et traversant le réservoir, où les conditions de saturation sont imposées, rentre dans l'évaporateur où les chaleurs sensible (marginale) et latente sont évacuées. Dans cette technologie, le titre de vapeur en sortie de l'évaporateur est $x_{sortie} < 1$ tandis que la différence entre la température de saturation, T_{sat} , et la température d'entrée, T_{in} , est normalement négligeable ($T_{in} \leq T_{sat}$). De surcroît, si la surchauffe de la vapeur est absente on a $T_{out} = T_{sat}$. Le fluide ainsi complètement ou partiellement évaporé s'écoule dans la ligne vapeur jusqu'au condenseur. Ici la vapeur est condensée et sous-refroidie jusqu'à que sa température soit proche de celle d'entrée du fluide froid T_{ci} . Les systèmes à compression de vapeur permettent à l'évaporateur de travailler à une température plus faible que celle du condenseur. Dans ces systèmes, la vapeur en sortie de l'évaporateur doit être surchauffée pour ne pas avoir la dite « compression humide ». Si la surchauffe change à cause des changements des conditions opératoires, la valve de régulation agit pour conserver des conditions thermodynamiques constantes pour la vapeur. Ces technologies sont hautement performantes et avec des rendements très élevés, mais elles sont encore considérées comme prématurées pour la plupart des auteurs. Les systèmes passifs ne nécessitent quant à eux aucune forme d'énergie externe pour permettre l'écoulement du fluide dans la boucle. Dans les trente dernières années ces systèmes se sont imposés comme standards dans les applications spatiales, en particulier pour le refroidissement des systèmes radio et dissipatifs des satellites. Dans la suite, une très rapide explication des différentes technologies considérées dans ces travaux est reportée. Le thermosiphon est composé par un tube hermétiquement fermé à des deux extrémités et rempli d'une petite quantité de liquide. Quand la puissance thermique est appliquée au niveau de la partie inférieure (évaporateur), le fluide s'évapore et la vapeur s'écoule (à travers la section adiabatique) vers la partie supérieure : le condenseur. Ici, la vapeur se condense et le liquide s'écoule par gravité vers l'évaporateur où le cycle recommence. La condition nécessaire pour que ce système puisse fonctionner est que le condenseur se trouve au-dessus de l'évaporateur. Les caloducs capillaires sont, sous certains aspects, proches des thermosiphons. En effets, ils gardent la même structure que les thermosiphons, mais leur paroi interne est recouverte de tout son long d'une structure capillaire (rainures,

poreux frittés ou à mèche). Dans ce cas, le condensât est ramené par capillarité vers l'évaporateur. Ce mode de fonctionnement permet de dépasser la problématique liée à l'installation du condenseur au-dessus de l'évaporateur dans les thermosiphons. Les caloducs sont utilisés avec succès dans le cadre du refroidissement de la microélectronique, là où les distances de transport ne sont pas trop importantes (voir refroidissement puces d'ordinateurs ou de smartphones). Plusieurs typologies de caloducs sont décrites dans le manuscrit, le lecteur est invité à consulter la version intégrale du texte pour plus de détails. Parmi les systèmes passifs, citons les boucles passives à pompage capillaire. La Loop Heat Pipe (LHP) et la Capillary Pumped Loop (CPL) sont composées d'un évaporateur, d'un condenseur et d'un réservoir. La différence principale entre les deux systèmes est liée à la position de ce dernier : directement accolé à l'évaporateur pour les LHP. Cette configuration permet des échanges de masse et de chaleur entre les deux composants, ce qui permet la transmission d'une partie de la chaleur depuis l'évaporateur vers le réservoir. C'est le flux thermique qui modifie les conditions de saturation dans le réservoir même, en donnant lieu à la capacité d'autorégulation typique de cette boucle. Les CPL sont quant à elles caractérisées par un découplage entre l'évaporateur et le réservoir, qui est installé sur la ligne vapeur et relié à cette dernière à travers un petit tube dont le diamètre ne permet pas trop facilement des échanges de masse avec le reste de la boucle. Dans ce cas, les conditions de saturation y sont maintenues par un réchauffeur électrique. Ce principe de fonctionnement permet bien sûr de contrôler la température opératoire, mais le découplage entre le réservoir et l'évaporateur donne lieu à des instabilités et des oscillations, en particulier pendant les phases de démarrage. Ces deux technologies n'ont pas été retenues dans le cadre du projet HASTECS à cause de leurs limites. En revanche, un nouveau type de boucle, la Boucle Gravitaire à Pompage Capillaire ou CPLIP (Capillary Pumped Loop for Integrated Power) permet de dépasser toutes ces limitations et est parfaitement adaptée au refroidissement de l'électronique de puissance, ce pour quoi elle a été imaginée depuis 2006. Son principe de fonctionnement est décrit en détail dans le texte.

Refroidissement de l'électronique de puissance : état de l'art des "heatsinks"

Dans le chapitre 3 les différentes technologies disponibles pour les "heatsinks" sont présentées, telles que l'impact de jet, les microcanaux, les milieux poreux et mousses métalliques, pour donner une idée des technologies utilisables dans le cadre du projet HASTECS. Tous les systèmes caractérisés par un contact direct entre la surface à refroidir et le fluide de refroidissement appartiennent à la catégorie des systèmes à refroidissement direct. Ils sont donc caractérisés par l'absence d'une résistance thermique entre le fluide caloporteur et les composants électroniques. Ces sont des systèmes très

performants, dont le coefficient d'échange thermique est l'un des plus élevés. En général leur utilisation est justifiable quand la résistance convective du système direct est inférieure à la somme des résistances d'un système direct. Les systèmes à impact de jet et le refroidissement par spray ("spray cooling") ont des mécanismes d'échange thermique très complexes, et les phénomènes liés à leur fonctionnement ne sont pas complètement compris. Certains auteurs ne sont pas toujours d'accord pour ranger les deux systèmes dans la même catégorie, on peut tout de même affirmer que le concept de refroidissement par spray représente une extension du concept d'impact de jet. En général on peut dire que la différence tient du fluide caloporteur utilisé. Dans le "spray cooling" un mélange gaz/liquide est souvent utilisé pour permettre l'atomisation du fluide pendant son écoulement dans l'atomiseur, tandis que dans le cas de l'impact de jet l'échange thermique est strictement lié à la vitesse du fluide, souvent monophasique, canalisé vers la surface à refroidir. Au contraire des systèmes directs, dans les systèmes indirects il n'y a pas de contact entre le fluide de refroidissement et la semelle du composant électronique. A cette catégorie appartiennent les plaques à eau, les microcanaux, les mousses métalliques et les milieux poreux. Tous les systèmes ici nommés peuvent à la fois être utilisés dans des systèmes de refroidissement mono ou diphasiques. La plaque à eau est la configuration la plus basique, bien connue et beaucoup utilisée en raison de sa simplicité, en particulier dans sa configuration monophasique. Selon l'environnement, différents fluides peuvent être utilisés, et logiquement les performances et la masse finale du système de refroidissement en dépendent aussi. Par exemple, Sakanova et al. [9] ont étudié trois fluides caloporteurs monophasiques (eau, huile et fioul) dans un tel système, pour des applications aéronautiques, et ont conclu que l'utilisation du fioul était le meilleur compromis entre performances et masse du système. L'une des technologies les plus prometteuses pour l'évacuation de densités de flux de chaleur très élevées à partir des composants électroniques de petite taille : les « heatsinks » à microcanaux sont composés de matériaux à très faible résistance thermique traversés par une série de canaux parallèles dont le diamètre hydraulique est inférieur ou égal à 1 mm. Il est possible d'utiliser différents matériaux, mais le silicium est l'un des plus utilisés. Par exemple Colgan et al. [23] ont réussi à évacuer une densité de flux de $300 \text{ W} \cdot \text{cm}^{-2}$. Malgré la perte de charge élevée liée à cette technologie, ils ont démontré que son utilisation est valable en particulier pour sa capacité à maintenir une température plus ou moins uniforme au niveau de la puce à refroidir. En revanche, concernant la physique de ce système, actuellement il n'y a pas de modèle thermo-hydrodynamique universellement accepté et les résultats des différentes études de la littérature sont souvent contradictoires. Quoi qu'il en soit, les performances des microcanaux mono ou diphasiques sont indéniables, et les échangeurs de chaleur qui uti-

lisent cette technologie sont caractérisés par des coefficients d'échange volumétriques qui peuvent atteindre $10^8 \text{ W} \cdot \text{m}^3 \cdot \text{K}^{-1}$ contre des valeurs typiques des échangeurs classiques de $100 \text{ W} \cdot \text{m}^3 \cdot \text{K}^{-1}$ [24] ! Les milieux poreux et les mousses métalliques représentent une alternative valable aux microcanaux, en particulier si les densités de flux thermiques sont très élevées. Les mousses métalliques sont caractérisées par des surfaces d'échange thermique très élevées en raison de leur structure complexe et tortueuse constituée d'un matériau à très haute conductivité thermique. Le fluide s'écoule dans un « chemin » tortueux à travers la structure tridimensionnelle qui augmente ainsi la surface mouillée. La présence d'une mousse métallique n'augmente pas que la surface d'échange thermique, mais aussi la conductivité thermique effective des "heatsinks". Sa présence favorise l'homogénéisation du champ de température sur la surface du « heatsink » grâce à un effet diffusif propre à ce type de milieu. Ces effets de diffusion thermique sont différents selon que l'on considère des milieux poreux frittés ou non, étant donné que les contacts solide-solide et solide-liquide jouent un rôle fondamental dans les transferts de chaleur. En général, on peut dire que les milieux frittés sont caractérisés par des propriétés de diffusion thermique bien meilleures que les mousses ou les milieux non frittés. Ce phénomène les rend plus efficaces d'un point de vue de l'évacuation de la chaleur, mais le prix à payer est lié aux pertes de charges associées à ces systèmes. Même si on les considère dans une configuration diphasique, avec une réduction du débit nécessaire pour l'évacuation de la même quantité de chaleur, les pertes de charge associées à une telle configuration ne se réduisent pas par rapport à leur contrepartie monophasique.

Choix de la technologie

Il s'agit dans le chapitre 4 de choisir la solution la mieux adaptée aux besoins du refroidissement de l'électronique de puissance dans le cadre du projet HASTECS, tant du point de vue système que local au niveau de la source chaude. Tous les systèmes présentés précédemment sont capables d'évacuer la charge thermique requise tout en assurant des performances importantes, mais il est nécessaire que le système choisi soit capable de répondre aux contraintes de masse imposées dans le cadre du projet HASTECS pour permettre au système de voler. Pour bien choisir le système le plus adapté à répondre aux objectifs imposés, le choix va être basé sur une conception de première approximation et sur une comparaison des masses des systèmes : le plus léger sera celui qui sera choisi et optimisé par la suite. Deux systèmes actifs, mono et diphasique, équipés d'une plaque à eau, et un système passif à pompage capillaire, la CPLIP, seront donc comparés. Un certain nombre d'hypothèses, dont une explication détaillée est reportée dans le manuscrit, ont été faites. Bien évidemment toutes les conditions opératoires et conditions limites pour le dimensionnement sont maintenues constantes et identiques pour les trois

systèmes comparés. Le système monophasique est considéré dans sa forme la plus simple : les vannes et les autres accessoires de régulation ont été négligés dans cette première approximation. Les lignes de transport, chaude et froide, ont une longueur de 1 et 1,2 m et ont la même section transversale. Les trois « heatsinks » (six composants d'électronique de puissance à refroidir en parallèle) sont installés en parallèle et en position verticale, et sont traversés par neuf canaux parallèles, dont la section est de 0,8 cm, dans lesquels le fluide caloporteur s'écoule. L'échangeur froid air-liquide non-aileté à courants croisés a une longueur totale de 80 m. Il est composé de 5×20 tubes dont la section transversale est égale à celle des lignes de transports. La pompe est dimensionnée pour assurer un débit de $11,35 \text{ litres} \cdot \text{min}^{-1}$ et une pression de 590 kPa. Comme pour le système monophasique, le système diphasique actif a été conçu dans sa forme la plus simple. Il est aussi constitué de trois « heatsinks » installés en parallèle et verticalement. Comme déjà expliqué dans le chapitre 2, cette technologie ne nécessite pas la complète évaporation du fluide caloporteur, mais pour ne pas condamner a priori cette solution avec un débit plus élevé que nécessaire, il a été choisi un titre de vapeur $x = 1$ en sortie de l'évaporateur. Les lignes de transport ont la même longueur que celles du système monophasique, mais leur section transversale est différente. La ligne vapeur a un diamètre de 21,2 mm tandis que celui de la ligne liquide est de 3,5 mm. Le condenseur conserve la même configuration que l'échangeur de la technologie monophasique, 5×20 tubes dont la section transversale est celle de la ligne vapeur, mais sa longueur est de 50 m. Le débit qui s'écoule est d'un ordre de grandeur inférieure à celui demandé par le système monophasique. Pour des raisons de choix de pompe (consulter le manuscrit original pour plus d'infos), les « heatsinks » sont traversés par un seul canal à serpentin dont le diamètre hydraulique de la section transversale est de 12 mm. Pour la comparaison reportée dans ce chapitre, la CPLIP a été considérée selon deux configurations : une première utilisant une seule boucle équipée de trois évaporateurs installés en parallèle, et une deuxième utilisant trois boucles distinctes équipées d'un seul évaporateur, et dont la puissance thermique de chacune est un tiers de la puissance totale à évacuer. Dans tous les cas, les dimensions des évaporateurs sont proportionnelles à celles des modules de puissance installés. Ils sont équipés d'un milieu poreux en nickel dont la porosité est 73% et le diamètre moyen des pores est $6,2 \mu\text{m}$. Les lignes de transport, dans la configuration avec trois évaporateurs en parallèle, ont les mêmes dimensions que celles du système diphasique pompé. Les systèmes actifs monophasiques sont en général plus légers que les systèmes actifs diphasiques. Les deux technologies sont caractérisées par une même masse à vide, mais une quantité de fluide plus importante est contenue dans le système diphasique. Une telle quantité de fluide est justifiée par un volume du condenseur plus important et donc par un volume

du réservoir plus grand. Les systèmes actifs sont fortement impactés dans leur masse par la présence de la pompe, dont la masse est respectivement de 19% de la masse totale de la boucle monophasique et de 27% de la boucle diphasique. Ceci est la principale raison pour laquelle la CPLIP peut assurer une économie en masse d'au moins 20%. C'est la technologie dont la masse est assurément la plus faible et, même si elle n'a pas encore été optimisée, dont le coefficient de puissance ($\text{kW} \cdot \text{kg}^{-1}$) est le plus proche de celui imposé pour l'horizon 2025.

CPLIP : principe de fonctionnement, dispositif expérimental et modèle numérique

La boucle diphasique passive CPLIP est composée d'un évaporateur, d'un condenseur et d'un réservoir. En conditions stationnaires, la chaleur en provenance des modules de puissance installés sur l'évaporateur arrive aux niveaux des ménisques liquide/vapeur par conduction à travers le milieu poreux et déclenche la vaporisation au niveau de ces interfaces. La vapeur, en sortie de l'évaporateur, s'écoule à travers la ligne vapeur vers le condenseur où a lieu la désurchauffe, la condensation et le sous-refroidissement du liquide. Le liquide sous-refroidi s'écoule dans la ligne liquide vers le réservoir, divisé en deux parties séparées par une plaque. Même si, en conditions stationnaires, il n'y a pas d'échanges de masse entre les parties haute et basse du réservoir, le liquide en provenance du condenseur est chauffé par conduction à travers la plaque de séparation et par convection à travers le liquide contenu dans le réservoir. Le liquide s'écoule ainsi vers l'évaporateur, où il mouille à nouveau le milieu poreux et, chauffé par la chaleur dégagée par les chauffeurs électriques, vaporise en faisant recommencer le cycle. Le dispositif expérimental utilisé dans le cadre de cette thèse, aussi appelée CPLIP 1.1, a été à l'origine développé en 2006 pour des études liées au refroidissement de modules d'électronique de puissance pour des applications ferroviaires. Toute la boucle est en acier à l'exception de l'évaporateur, composé de différents matériaux pour assurer un transfert de chaleur adéquate entre les corps chauffants et le milieu poreux (ce dernier étant en nickel). Le réservoir est cylindrique, a un diamètre externe de 99,6 mm et une longueur de 308 mm. La hauteur de la plaque de séparation est de 6mm. La température et la pression de saturation du réservoir sont imposées par une cartouche chauffante installée dans la partie haute de ce dernier. Le bâti de l'évaporateur est en acier et nickel, et contient le milieu poreux en nickel dont la porosité est de 73%, le diamètre moyen des pores de $6,8 \mu\text{m}$ et la perméabilité de $6,53 \cdot 10^{-13} \text{ m}^2$. Trois artères liquides y assurent l'alimentation du liquide en provenance du réservoir. Le condenseur est un échangeur de type « tube-in-tube » dont la longueur est de 4,04 m, alimenté au secondaire par un mélange eau-glycol à 30%, refroidi par un cryostat d'une puissance nominale de 8 kW. Sur la ligne vapeur, en acier elle aussi, est installée une valve à travers laquelle il est possible d'augmenter les pertes

de charges afin d'étudier de quelle manière le comportement thermique de la boucle est influencé par un changement des caractéristiques hydrauliques. Le modèle, quant à lui, introduit au cœur de ce chapitre [25] est celui qui va être utilisé tout au long des chapitres suivants pour des études à la fois stationnaires et transitoires. Le modèle est du type monodimensionnel et homogène. Il résout les équations de conservation de la masse, de la quantité de mouvement et de l'énergie à travers l'analogie thermique-électrique en utilisant le solveur d'ESACAP®. Le fluide est considéré compressible tandis que la phase vapeur est considérée comme un gaz parfait. Les équations de conservation de la masse et de la quantité de mouvement sont résolues à travers deux maillages décalés pour permettre une stabilité numérique grâce au fait que les variables de pression et de vitesse ne se trouvent pas sur le même nœud et réduisant les erreurs dues aux propriétés thermophysiques basées sur les valeurs d'enthalpie et de pression. L'équation de l'énergie est résolue sous une forme enthalpique plutôt qu'en utilisant la température comme variable d'état. Ce choix permet d'aller au-delà des limitations liées à la définition de l'état physique du fluide à travers la température, qui autrement présenterait une discontinuité en correspondance à la température de saturation. Le modèle prend en charge la modélisation du réservoir, à la fois dans sa partie haute et sa partie basse. Les deux parties sont modélisées chacune à l'aide d'un seul nœud. En particulier, l'hypothèse d'homogénéité entre les deux phases fluides est respectée dans la partie basse, mais pas dans la partie haute, à cause de la coexistence des phases liquide et vapeur et de la présence d'une interface, mobile, qui les sépare. Les échanges de masse et d'énergie dans l'évaporateur sont très complexes et pas encore bien connus. Une approche de type « microscopique » serait trop complexe et onéreuse d'un point de vue du temps de calcul ; c'est pourquoi les auteurs [25] (et [26] avant lui) ont décidé d'utiliser des paramètres empiriques. Les valeurs des conductances expérimentalement obtenues seront donc utilisées dans ce but. La façon dont l'analogie thermique-électrique est utilisée pour la résolution du modèle est abordée à la fin du chapitre.

La réponse de la CPLIP aux contraintes d'HASTECS

L'analyse reportée dans ce chapitre est de type expérimental. Elle se base sur deux différentes campagnes de tests dont le but était de caractériser des points de vue thermique et hydraulique la CPLIP en régime stationnaire. L'étude paramétrique a pour but la connaissance de l'influence que la puissance thermique appliquée à l'évaporateur, \dot{Q} , la température de consigne au réservoir, T_{res} , et la température de la source froide, T_{sec} , ont sur le comportement de la boucle. En plus de ces trois paramètres thermiques, une étude hydraulique sur la réponse thermique de la boucle a été menée, dont le but était de connaître quelle influence ont les pertes de charge de la vapeur introduites à travers

la fermeture d'une vanne dont les caractéristiques hydrauliques sont connues. Dans le souci d'évaluer le coefficient d'échange à l'évaporateur, les valeurs des conductances thermiques ont été obtenues sur la base de la différence de température entre la paroi de l'évaporateur et la température de saturation du réservoir ($T_{diff} - T_{res}$) et entre la température de paroi de l'évaporateur et la température d'évaporation ($T_{diff} - T_V$). À cause de l'impossibilité de mesurer directement cette dernière, un outil de post-traitement basé sur la reconstruction du cycle thermodynamique a été utilisé se basant sur les valeurs de température mesurées. Les paramètres manquants ont été calculés en utilisant la relation entre pression et température sur la courbe de saturation. Les caractéristiques principales de la boucle ont été expliquées en utilisant ces cycles thermodynamiques simplifiés, qui montrent bien les raisons pour lesquelles la CPLIP s'est avérée particulièrement intéressante dans le cadre du projet HASTECS. Par exemple, la température de paroi de l'évaporateur ainsi que sa perte de charge sont fortement dépendantes de la puissance thermique appliquée, tandis qu'il n'y a pas de dépendance entre la température de la source froide et la température de l'évaporateur. Cette dernière caractéristique rend la CPLIP particulièrement efficace pour ce type d'applications où la température de la source froide varie, y compris de manière significative, mais nécessitant une température constante de la source chaude, telle que dans ce contexte aéronautique. Dans le même temps, il est possible de contrôler sa température en agissant sur la température de consigne imposée au réservoir. Bien évidemment, cela a un impact non négligeable sur les valeurs des conductances thermiques, qui varie aussi en fonction de la puissance appliquée à l'évaporateur et du fluide utilisé. Bien qu'il existe une différence entre les valeurs de conductances thermiques, selon si elles sont basées sur la différence ($T_{diff} - T_{res}$) : $G_{ev,res}$, ou sur ($T_{diff} - T_V$) : $G_{ev,V}$, il a été observé que pour des puissances élevées les différences entre ces dernières deviennent négligeables tandis que pour des basses puissances les valeurs divergent. Sur la base des valeurs de conductance mesurées il a été possible de mener une étude numérique aux volumes finis dans le but d'obtenir la carte des températures sur les modules de puissance dans les pires conditions opératoires. Le module choisi par l'équipe d'électroniciens a donc été précisément reproduit numériquement et des simulations 3D stationnaires ont été faites en résolvant l'équation de l'énergie. Bien évidemment, une étude de sensibilité sur la dimension du maillage a été également menée. Sur la base de la puissance appliquée sur les diodes et les IGBT, et rapportée aux dimensions des composants, il a été trouvé une densité de flux thermique atteignant respectivement $242 \text{ W} \cdot \text{cm}^{-2}$ et $92 \text{ W} \cdot \text{cm}^{-2}$. Malgré ces densités de flux les températures des composants les plus sollicités (les diodes) ne dépassent pas 130°C pour une température maximale de 150°C conseillée par les constructeur des modules.

La CPLIP est donc capable de maintenir la température contrôlée bien en-dessous du seuil indiqué. Pour ce qui concerne le régime transitoire, et dans le souci d'exploiter le comportement de la boucle pendant un profil de mission réel, la CPLIP 1.1 a été testée expérimentalement pour observer sa réponse en particulier pendant les phases les plus critiques : augmentation soudaine de la puissance thermique évacuée par les composants électroniques pendant la phase de décollage ; réduction violente de la puissance évacuée entre la fin de la phase de décollage et le début de la croisière. La boucle a démontré pendant ces tests être bien adaptée à de tels variations de puissance et les valeurs de température enregistrées collaient parfaitement avec les prévisions des modèles. L'étude du comportement de la boucle suivant des changements des caractéristiques hydrauliques a été abordée en utilisant la même méthodologie expérimentale et outil de post-traitement déjà décrits. La première impression est que l'augmentation des pertes de charge dans la ligne vapeur a le même impact que l'augmentation de la puissance thermique. Les températures ne dépendent pas que de la puissance appliquée à l'évaporateur, mais aussi des pertes de charges. La longueur de la ligne vapeur, la configuration de la boucle, la typologie et la configuration du condenseur, et le fluide caloporteur ont un impact sur la réponse de la boucle et en particulier les conductances thermiques sont particulièrement sensibles aux caractéristiques hydrauliques.

Optimisation de la CPLIP pour 2025 et 2035

Les résultats de l'optimisation d'une CPLIP aux l'horizons 2025 et 2035 sont présentés dans le chapitre sept. En se basant sur la distribution de masses de la CPLIP à trois évaporateurs en parallèle, il a été observé que le composant le plus critique était le condenseur. Sa masse à vide est le 40% du totale, et ses dimensions ont un impact sur la masse totale de fluide contenu dans la boucle (48% de la masse totale), et sur la masse à vide du réservoir (9%) dont le volume interne est égal aux volumes du condenseur et de la ligne vapeur cumulés. La réduction des dimensions du condenseur est donc la priorité si l'on veut obtenir les résultats demandés dans le cadre du projet HASTECS. Pour rappel, la solution retenue pour la source froide était une solution de type RAM-air, dont l'air s'écoule, dans la pire condition opératoire à une vitesse de $10\text{ m}\cdot\text{s}^{-1}$ et une température de $33\text{ }^{\circ}\text{C}$. Pour la solution 2025 deux différentes typologies de condenseur ont été étudiées et comparées afin de choisir la mieux adaptée. La solution la plus simple, celle qui prévoyait l'utilisation d'ailettes circulaires a été enfin écartée car elle ne permettait pas de parvenir à des masses « acceptables » selon les contraintes imposées par le projet HASTECS. En revanche, le condenseur à ailettes continues a permis de baisser la masse du condenseur même et de réduire sa longueur ainsi que le volume de fluide contenu. Dans la solution optimisée, la CPLIP est caractérisée par une masse d'environ 11 kg pour

l'évacuation d'environ $16 \text{ kW}_{\text{th}}$. Si l'on considère le système dans sa totalité (électronique de puissance + refroidissement) le coefficient de puissance totale obtenu est supérieur à $19 \text{ kW} \cdot \text{kg}^{-1}$ relativement à une cible imposée pour l'horizon 2025 de $15 \text{ kW} \cdot \text{kg}^{-1}$. Dans le but d'améliorer la solution de refroidissement à l'horizon 2035, une nouvelle technologie de condenseur à coupler avec la CPLIP a été proposée : le condenseur à microcanaux et ailettes à persienne permet une augmentation du coefficient d'échange externe de 3 à 5 fois celui d'un condenseur classique et une réduction du volume du fluide. Les résultats portant sur l'optimisation de la CPLIP équipée avec ce condenseur démontrent une augmentation des pertes de charge liées à cette technologie, mais malgré tout, elles restent en dessous de la capacité de pompage capillaire maximale $\Delta P_{\text{cap,max}}$. Si cette augmentation est par ailleurs comparée à l'augmentation de performances (dans ces travaux considérés comme la réduction en masse), on peut observer une réduction significative de la masse du système de refroidissement, qui est autour de 5 kg pour l'évacuation d'environ $16 \text{ kW}_{\text{th}}$. Dans ce cas, le coefficient de puissance imposé à l'horizon 2035 a été plus que doublé !

Conditions transitoires sévères : démarrage

Dans le but de mieux comprendre les limitations de la CPLIP, dans le chapitre 8 une étude sur son démarrage est proposée. En particulier, il est très intéressant d'exploiter comment les conditions environnementales, telles que la température initiale de la ligne vapeur, en plus des paramètres classiques (puissance appliquée à l'évaporateur) peuvent influencer le comportement de la boucle pendant ses phases de démarrage. L'analyse présentée ici est basée sur des résultats expérimentaux et numériques effectués sur le modèle et le dispositif expérimental présentés dans le cinquième chapitre. Comme dit précédemment, l'attention est portée sur la température initiale de la ligne vapeur, tandis que tous les autres paramètres, tels que la température de consigne au réservoir et la température de la source froide, sont fixés (70°C et 20°C respectivement). Par mesure de simplicité, les définitions de démarrage à froid et à chaud ont été utilisées pour indiquer un démarrage dont la température initiale de la ligne vapeur est respectivement égale ou supérieure à la température ambiante (20°C). À partir des résultats expérimentaux, on a observé que la boucle a pu démarrer à froid sans problèmes particuliers jusqu'à des échelons de puissance de 0-5 kW, tandis qu'à chaud, même pour une puissance de démarrage plus faible, la CPLIP a échoué dans son démarrage. L'analyse expérimentale effectuée sur un démarrage à froid et à chaud à faible puissance a démontré, dans le cas chaud, une augmentation importante de la vitesse du front de vapeur dans la ligne vapeur, qui peut être un ordre de grandeur plus élevée pendant le démarrage à chaud qu'à froid. La plus faible vitesse du front de vapeur, pendant le démarrage à froid, est

due à l'énergie échangée entre le fluide et les parois solides de la ligne vapeur, entraînant une recondensation de la vapeur issue de l'évaporateur. Pendant le démarrage à chaud, une plus faible différence de température entre la vapeur et les parois solides atténuent ce phénomène et rendent les démarrages plus violents. Si cette quantité d'énergie est calculée pour un démarrage à chaud et à froid, on peut observer que l'énergie relâchée par la vapeur dans le attein environ 5 kJ dans le premier cas et 9 kJ dans le deuxième. Ces valeurs d'énergie ne sont pas négligeables, car elles correspondent à une puissance de 0,5 kW appliquée à l'évaporateur pendant un temps de quasiment 20 s et 10 s respectivement. La plus petite quantité de vapeur re-condensée pendant le démarrage à chaud amène à des vitesses du front de vapeur plus élevées, ce qui peut entraîner un décrochage de la boucle. Pour mieux comprendre les enjeux, les résultats expérimentaux ont été comparés avec des résultats numériques où l'énergie thermique des parois solides a été modifiée en agissant sur l'inertie thermique des parois solides qui a été supprimée pour vérifier et valider l'observation du comportement hydraulique expliqué expérimentalement.

Comportement de la CPLIP sous conditions d'accéléérations sévères

La vérification sous condition de vibrations sévères est plus que naturelle dans le secteur de l'aéronautique, c'est pourquoi une étude sur l'influence d'accéléérations sévères sur le comportement de la CPLIP est abordée dans le dernier chapitre. En absence d'un banc expérimentale permettant l'étude de ce comportement, une étude numérique a été réalisée, dont les limitations sont bien expliquées dans le texte. L'étude est divisée en deux parties, une première liée à la compréhension des phénomènes, et une deuxième étude paramétrique. Dans tous les cas, pour des raisons de stabilité numérique, une impulsion d'accélération dont l'intensité et la durée dans le temps sont variables a été appliquée à la CPLIP pendant ses opérations en régime stationnaire. L'influence la plus remarquable de la présence d'un champ d'accélération sévère qui perturbe le comportement de la CPLIP est bien sur liée aux caractéristiques hydrauliques de la boucle. Il a été observé une forte variation du champ de pression tout au long de la CPLIP qui amène à un débit négatif de liquide qui s'écoule du réservoir vers l'évaporateur. Ce comportement, anormal, est responsable d'une réduction de longueur de condensation car le liquide en provenance du réservoir repousse le front de vapeur en arrière, en modifiant aussi les conditions de saturations dans le condenseur même. Malgré ces modifications très importantes dans le comportement hydraulique de la boucle, sa réponse thermique ne semble pas être affectée de manière significative : la vapeur continue à être produite dans l'évaporateur et poussée vers le condenseur. Les paramètres qui ont une influence au premier ordre sur le comportement hydraulique de la boucle sont la durée dans le temps de la perturbation, la différence de hauteur entre le condenseur et le réservoir, et bien sûr l'intensité de la

perturbation. Si, d'une part, il n'est pas possible de contrôler ni la durée ni l'intensité des perturbations, de l'autre part il est nécessaire de garder, en phase de conception la moindre distance entre le condenseur et le réservoir. En effets ce dernier a un impact relevant sur le terme $\rho(k \cdot g) H$ ainsi que sur le temps de stabilisation de la boucle en conditions stationnaires.

Part I

HASTECS

Hybrid Aircraft Academic reSearch on Thermal and Electrical Components and Systems

The first part of this work is an introduction to the issues which HASTECS project faces with. After a general introduction to the project and the teams that are giving their contribution for the development of future hybrid aircraft, the attention is focused on high density power electronics cooling issue. The data and the challenges to successfully solve the problem are here introduced.

Introduction: HASTECS project

HASTECS (Hybrid Aircraft academic reSearch on Thermal and Electrical Components and Systems) is a Clean-Sky 2 European Project financed by H2020-EU.3.4.5.1. It has the purpose to develop innovative tools and models to be used by European aircraft constructors for the design and the development of future hybrid propulsion aircrafts. HASTECS project is especially focused on research of generation, distribution, conversion and thermal management of electric power.

HASTECS consortium involves different French Research Institutes. It is at LAPLACE institute, in Toulouse, where power electronics and electrical motors are studied while at Pprime Institute in Poitiers, their adjoined cooling systems are researched. AIRBUS is the main industrial partner of the project.



Figure 0.1: Involved Labs

Six different teams, so called WPs (Work Packages), work on the project and each of them has different tasks and objectives. WP1 has the purpose to find a technology to be used for electrical motor (eMotor). It has the purpose to develop a complete model to

be used for its design. WP2 team works on power electronics. Such devices are used to convert electrical direct current (DC) to alternating current (AC) to supply eMotors with the required electrical frequency. The purpose of WP2 is to find a disrupting technology and to develop a model for converters design. Thermal management of eMotor and power electronics converters is handled by WP3 and WP4, respectively. Both teams have the purpose to propose cutting-edge technologies for thermal management. To WP3, in particular, is required the development of a model to be integrated in the optimisation tool. WP4's aim, rather, is to find, design, optimise, develop and study an *avant-gard* solution for power electronics cooling. It should supply WP2 with simplified tools for the development of a unique model for electronic converters and their cooling system. Such model will be finally integrated into the overall one for the optimisation of the conversion chain. WP2 and WP4 are strongly coupled between them. WP5 has the purpose to analyse partial discharges, bus-bars and cables. Finally, WP6's task is to study system integration and auxiliary sources: fuel cells and batteries. All work packages converge to WP6 system integration.

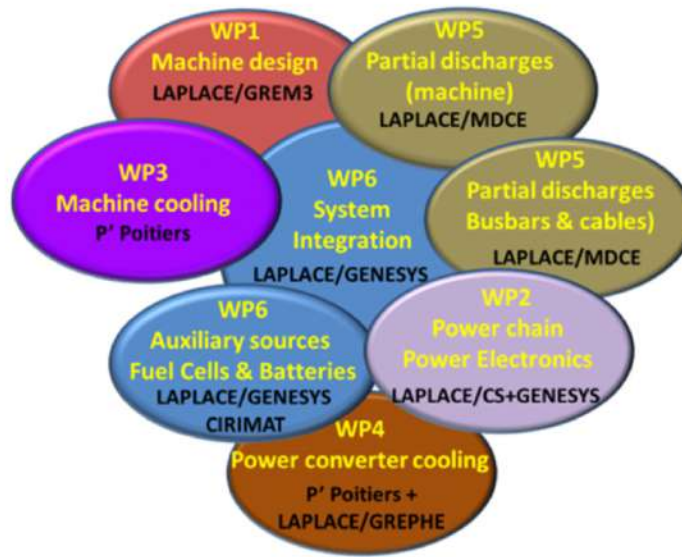


Figure 0.2: WPs and their interactions

“[...] The electric motors and power converters are designed by LAPLACE Laboratory in Toulouse while innovative solutions for cooling of these devices are proposed by the Pprime institute in Poitiers. Some prospective study on future high energy density auxiliary sources (batteries, Lithium Ion) are currently being developed in LAPLACE with the expertise of the CIRIMAT Centre. [...] Finally, the overall system will be analyzed and even optimised thanks to an integrated design model which is currently built which

involves the whole power system. This system level design tool couples the devices models (efficiency and weights) with the whole weight of the aircraft and subsequently with power and thrust needs to fly the mission“ [cit.] [27].

The aim of the research presented in this thesis (WP4), mainly numerical, is to find, design and optimise a technology for high power density electronics cooling. Such cooling solution should be able to evacuate the required thermal power from power electronics converters, ensuring temperature control at level of chips and responding to the requirements imposed by AIRBUS to let the entire system fly. Such constraints are especially related to the mass of the whole system: power electronics converters and adjoined cooling system. For the purpose, models have been developed, and existing ones adapted and modified to fit the requirements of the project. Steady-state and transient issues have been numerically addressed and, when possible, compared to experimental results. Design and optimisation softwares have been used to finally solve the problem and to propose the best possible performing solution.

This thesis is divided in five parts where technological, engineering and scientific issues are addressed to solve the problem and to propose a robust and reliable solution.

The first part is an introduction to explain why do we need a high performing cooling system in the context of this project.

The second part, composed by three chapters, reports a wide extent state of the art of electronics cooling technologies. In particular, due to the complexity of the existing cooling systems, such state of art has been divided in two. The first part, reported in the second chapter, is an overview of cooling systems using a system approach. Closed loop cooling systems and their components are here introduced, and pros and drawbacks, related to their use, highlighted. Active single and two-phase, and passive two-phase, cooling systems are here outlined, reporting the actual limits of each technology as well. The third chapter, instead, addresses the issue related to local heat evacuation from electronic components. Here, the attention is focused on the hot side of the cooling systems. Different technologies are introduced and analysed on the basis of current literature results. Finally, the fourth chapter represents a technology screening. The most adapted technologies will be compared on the basis of a first approximation design, and the choice will be done using the mass of the overall cooling system as index.

In the third part, the retained technology will be analysed. Working principle, experimental facility and numerical model of CPLIP will be introduced in the fifth chapter. A thermal characterisation of the CPLIP, based on experimental data, will be presented in the sixth chapter to show how it is able to answer to HASTECS requirements. Finally, optimisation of CPLIP is proposed in the seventh chapter to achieve the best

configuration for 2025 and 2035.

In the fourth part, the attention is focused on CPLIP behaviour during severe and harsh start-up phases — chapter eight — and during severe and sudden acceleration stages — chapter nine —.

Finally, general conclusions and perspectives are addressed in the fifth part.

Hybrid aircraft power electronics cooling issue

1.1 Why power electronics cooling?

Power electronics cooling problem is one of the main technological issues by which modern society is facing with. The increasing electrical power to be processed by power electronics components, inevitably bring to increasing thermal load to be evacuated. In the past, power electronics cooling issue has been underestimated because of the capability (more or less) of classic air forced convection heatsinks to evacuate the thermal power by maintaining controlled the temperature at level of chips. Great efforts have been done, from an electronic point of view, to optimise electronic components and architectures, and to increase their efficiency. As it was easily foreseeable, the efficiency asymptote has been reached and the electric power to be processed continued to increase. At the same time, some high-efficiency power electronics configurations were not accessible because of still high thermal losses related with.

Electric efficiency¹ should be not seen just as a number to be reached and maximised. In any case the efficiency is lower than one, and one must be aware *because any kind of energy transformation is related to inevitable thermal losses and so, whatever the system, the efficiency cannot never be equal to unity!*

To give the reader an idea on how important losses are, even in the case of high electrical efficiency, lets make a simple example based on the issue we are going to discuss in this work.

On the basis of the scheme reported in Fig. 1.1, starting by the hypothesis that power electronics efficiency is $\eta_{el} = 99\%$, the adjoined thermal losses linked to this particular system are $(1 - \eta_{el}) = 1\%$.

From the knowledge of the electrical power to be supplied to electrical motors Q_{el} ²,

¹The electric efficiency is defined as the ratio between the power to be converted and the total power necessary to converters: electronics components outlet to inlet power ratio.

²The discussion in this work is “only” limited to power electronics and its adjoined cooling system. Here we do not face with electrical motors issues.

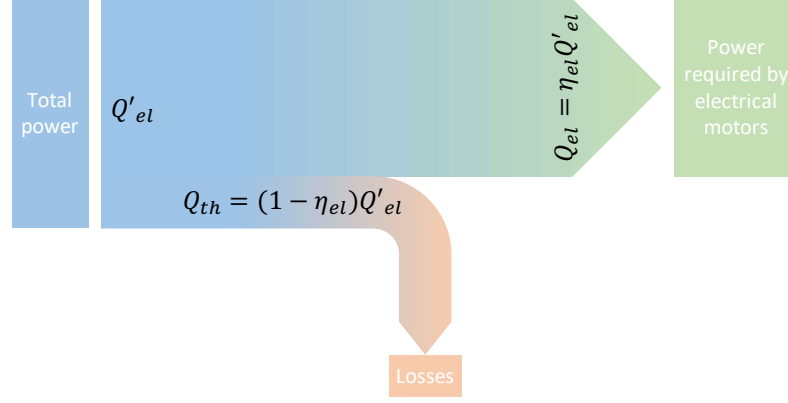


Figure 1.1: Electric power losses scheme

power electronics converters need to be supplied with an electrical power, Q'_{el} , calculated as:

$$Q'_{el} = \frac{Q_{el}}{\eta_{el}} \quad (1.1)$$

so, the related thermal losses are:

$$Q_{th} = (1 - \eta_{el}) Q'_{el} \quad (1.2)$$

Now, if the power required by electrical motors is $Q_{el} = 1.5 \text{ MW}$ [27], considering the above cited electric efficiency ($\eta_{el} = 99\%$), the total power to be supplied to electronics converters is 1.515 MW (from eq. 1.1), and the adjoined thermal power losses are $Q_{th} = 15 \text{ kW}$ (from eq. 1.2). This value is obviously far to be negligible and a cooling system, able to evacuate this quantity of energy, is required!

Thermal and electronics issues nowadays go hand in hand and researchers of both subjects need to converge after some iterations to let modern technologies work well.

In the case of high-power applications the problem is more evident and, even if electric efficiency is pretty high, thermal losses are not negligible: they need to be treated in the best way to increase the overall system efficiency. Optimisation process is not limited to get the highest electric efficiency possible but, on the base of an index, the best overall performances for the whole system should be found, by also considering the cooling technology that inevitably is related with. At the same time, the system should be designed to be fully integrated in the aircraft system and to maximise the total vehicle's performance and efficiency. A system must be so considered into the architecture where it should be placed [28].

The problem is not only related to the “simple” heat evacuation, but some constraints

are applied in the case of aeronautics field. In fact, to let power electronics and the adjoined cooling system fly, they should be as lightweight and compact as possible.

To have a measure on how lightweight the system is, let's now introduce the concept of *power coefficient*, C_c . The latter, measured in $[\text{kW} \cdot \text{kg}^{-1}]$, indicates the total power that power electronics modules are able to convert per each kilogram of system mass, including the whole cooling system. Obviously, the higher the power coefficient, the better the performance of the system. Two different targets have been imposed for minimum power coefficient value. The first objective, referred to the year 2025, is to design and optimise power electronics and their associated cooling system with the purpose to obtain an overall power coefficient, $C_{c,2025} = 15 \text{ kW} \cdot \text{kg}^{-1}$, while a power coefficient, $C_{c,2035} = 25 \text{ kW} \cdot \text{kg}^{-1}$ has to be reached for 2035! To show how far from the targets a classical solution is, let's now consider as an example a classical power electronics configuration (3-level PWM NPC), optimised at the best, and its adjoined cooling system, but using a classical forced air convection technology. The perceptual mass distribution of each component in the system is reported in Fig. 1.2 [1].

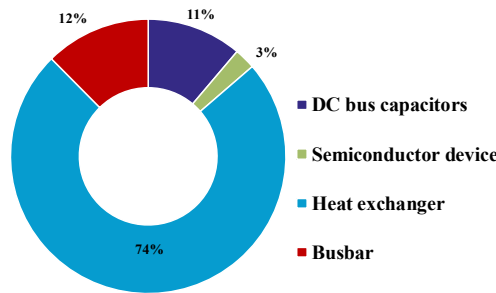


Figure 1.2: Mass distribution of a 3-level PWM NPC electronic system (using 6th gen. 1700 V IGBT) equipped by a classical air forced convection cooling system [1].

As one can notice from the pie chart, almost three-quarters of the entire system mass is due to the cooling system (heat exchanger in the diagram). Because of the low heat transfer coefficient (HTC) related to air forced convection technology, the high mass is due to extended heat transfer surface area related to the use of finned surfaces. In this case the adjoined power coefficient, less than $9 \text{ kW} \cdot \text{kg}^{-1}$, is too low if compared with the minimum admissible value (2025) and no warranties are given on the capability to limit the temperature of electronic components. The latter are in fact characterised by different maximal temperature requirements following chips constituting material. For example, pure Si components maximal temperature is limited to about 150°C , SiC components may in general withstand up to 175°C , but GaN components maximal temperature

is much lower than 150°C ³. To overcome such limitations, great efforts have to be done to ensure the evacuation of thermal load, to control the temperature of electronics components, and to reduce the mass of the cooling system!

1.2 The aircraft mission profile

The energy required to propulsion chain of the aircraft is not constant with time due to variation of mechanical power required by motors and following the different flying stages. Due to linear relation between supplied electrical power and thermal losses in power electronics converters system, the same shape of mission profile can be identified in both cases. Referring to thermal losses, five different stages can be identified in the mission profile, qualitatively reported in Fig. 1.3:

- I. Taxi-out
- II. Take-off and climb
- III. Cruise
- IV. Descent and landing
- V. Taxi-in

During the first stage, between the time t_0 and t_I , very limited in time, thermal power losses are the lowest ones (Q_{min}) and the aircraft remains on the ground (see the corresponding altitude profile reported above the mission profile in Fig. 1.3). The second stage (take-off and climb) can be divided in two different sub-stages: the take-off sub-stage, corresponding to the aircraft acceleration on the runway until detachment, and the climb sub-stage. In the first sub-stage, the maximal power is required during acceleration, so a high amplitude power step is applied (from Q_{min} to Q_{max}). During the climb sub-stage the power required slightly decreases until Q_{II} at the end of this phase. From t_I to t_{II} (almost 20 min) the altitude continues to increase. Once the maximal altitude, h_{max} , is reached, thermal power suddenly decreases from Q_{II} to Q_{III} : cruise begins. The latter, from t_{II} to t_{III} , is characterised, in theory, by steady-state operation. Its duration is, in this case, in the order of 70 min; the thermal power evacuated by power modules is almost one half of that evacuated during the very beginning of take-off stage and the altitude does not change. Like take-off and climb stage, descent and landing stage can be divided in two sub-stages: the descent is characterised by a decrease of the

³In the following of this work only SiC components will be considered.

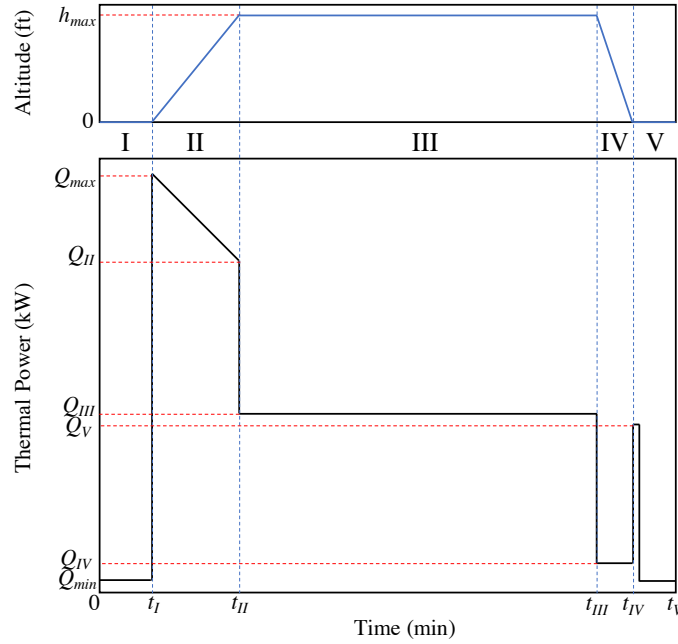


Figure 1.3: Qualitative thermal mission profile and altitude variation as a function of time.

thermal power (from Q_{III} to Q_{IV}) and the airplane planes until approaching. When the aircraft approaches, a power peak, characterised by a maximal intensity (Q_V) almost equal to that of cruise stage, is produced. Finally, during the taxi-in, the thermal power to be evacuated is the same as taxi-out.

As shown in Fig. 1.3, during the mission, the altitude changes as a function of time, and so air temperature, density and pressure change as well. This inevitably impacts the cooling system choice and temperature operating range. In the following sections, a discussion on temperature variation as a function of altitude is reported and two different methods to use external air as cold source are proposed. Also, in the following chapters, the mission profile will be quantitatively shown and analysed, for different power electronics configurations. A method based on an energetic analysis is reported to calculate the cooling system design point.

1.3 A not constant cold source temperature

As already mentioned in the previous section, when talking about aircraft, the air temperature is not constant as a function of time and different conditions are encountered during the mission: the air thermodynamic conditions (temperature, T ; pressure, p and air density, ρ) change as a function of altitude. By considering the NASA's Earth At-

mosphere Model [22], temperature, pressure and density, in Celsius degrees, kPa and $\text{kg}\cdot\text{cm}^{-3}$, respectively, are related to the altitude, h [m], by the following relations⁴:

Temperature

$$T = 15.04 - 0.00649 h \quad (1.3)$$

Pressure

$$p = 101.29 \left[\frac{(T + 273.15)}{288.08} \right]^{5.256} \quad (1.4)$$

Density

$$\rho = \frac{p}{0.2869 (T + 273.15)} \quad (1.5)$$

Referring to the altitude diagram, reported above the mission profile in Fig. 1.3, during stage I, the operating condition corresponds to the ground one. In this case, temperature of air (before and during the taxi-out and during and after the taxi-in stages) is obviously dependent on the geographical location, the season and the time of the day. From the beginning to the end of stage II and from the beginning to the end of stage IV, temperature varies as a function of altitude and so as a function of the time, as shown in Fig. 1.3. During the cruise, temperature is considered stationary: the flight altitude does not change.

The ISA (International Standard Atmosphere) diagram (see fig. 1.4) graphically relates temperature and altitude. Temperatures are reported on the abscissa, while altitude, in feet (ft), on the ordinates. The red line is the definition of ISA temperature as a function of altitude for standard ground temperature condition ($h = 0$ m, $P = 1$ atm, $T = 20^\circ\text{C}$), while each parallel line defines the value $\text{ISA}(\pm T)$ following the changes due to the place, the season and the time of the day.

In the following of this document, a value of $\text{ISA}(+18)^\circ\text{C}$ is assumed as input for cold source calculations. This value, in fact, well agrees with thermodynamic conditions realised on the ground for 60-65% of the airports in the world [2].

⁴Here, are reported only the laws relating the thermodynamic condition to the altitude, h , in the troposphere ($h \leq 11\,000$ m).

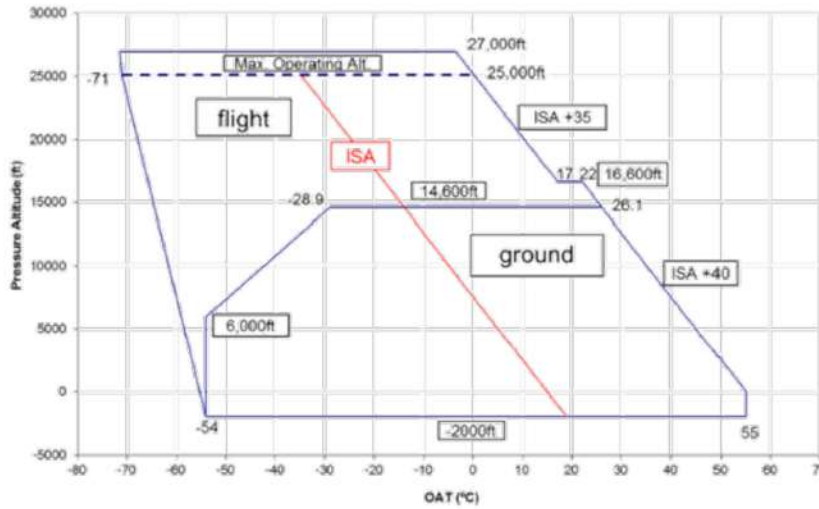


Figure 1.4: ISA diagram for pressure and temperature as a function of the altitude [2]

This choice is not related to a showstopper or to an infeasibility of the HXG design for a higher ISA value, covering a larger number of the airports in the world, but to specification requirement [2]. Such ISA value, in fact, allows to cover 100% of the airports in the Northern Europe, such as the Norwegian market, for which the hybrid aircraft is at first previewed. In particular, from specification data sheet [2], in table 1.1, the temperature boundary conditions for ground and high altitude flight phase are reported.

<i>Flight phase</i>	Normal ground operating conditions	Normal flight operating conditions	Severe operating conditions (low temperature condition)
Temperature (°C)	+33	+28	-15
<i>Flight phase</i>	Severe operating conditions (High temperature condition)	Operating during start-up after soak at low temperature	Operating during start-up after soak at high temperature
Temperature (°C)	+53	-40	+53

Table 1.1: Temperature specifications [2]

Table 1.1 details: normal operating conditions, related to external environment; severe

operating conditions, related to temperature values that may be realised in some unpresurised and non-temperature controlled position of the aircraft. To impose the boundary conditions to solve the problem — especially for the determination of real heat transfer coefficient values on the external side of the cold-heat-exchanger/condenser —, the following hypothesis have been assumed⁵:

1. The temperature of cold air at the inlet of the nacelle or the temperature of the air flowing upon the fuselage, in the worst operating condition, is equal to ambient temperature (33 °C, as indicated in table 1.1)
2. The velocity of the air at the inlet of the nacelle⁶ or upon the fuselage, corresponds to the aircraft velocity during taxi-out stage (I): $10 \text{ m} \cdot \text{s}^{-1}$.

1.4 The cold source

Radio communication, avionics system and other electronics equipments installed on board are cooled by using directly or indirectly external air as cold source (it depends if a closed loop circuit is inserted between the cold source and the components to be cooled). Like these systems, the idea developed in this work is to use the same cold source to cool the power electronics modules, but in a smarter way. It is so necessary to find a link between power electronics modules and cold source where heat will be definitively evacuated to the external ambient.

The general idea, as shown in fig. 1.5, is to use a closed loop cooling system to transport heat from the hot source⁷ (heatsink), where power modules are installed on, to the cold source. The use of a vector loop allows to evacuate in a more efficient and smart way the thermal power generated by chips. Moreover, the use of an intermediate cooling loop allows to use higher efficiency heatsinks, such as microchannels, porous media or metal foams. In fact, the higher the quality of the heatsink, the higher the efficiency of the system itself, as observed by Dolley *et al.* [28, 29].

A cooling system is, in most cases, a way to transport heat from the source to another location where its evacuation is in general simpler, while the use of external air as a secondary fluid in a heat exchanger is the easiest way to definitively evacuate the thermal

⁵Considering that the power electronics and its adjoined cooling system can be placed in the fuselage (PIF) or in the nacelle (PIN), the cold source nature changes as a function of the position in the aircraft.

⁶Only in the case where the nacelle is considered, the value of air intake equivalent diameter is calculated to respect the desired dynamic conditions (point 2), on the first heat-exchanger tube-rank.

⁷A definition for heatsink is given in chap. 2 page 42.

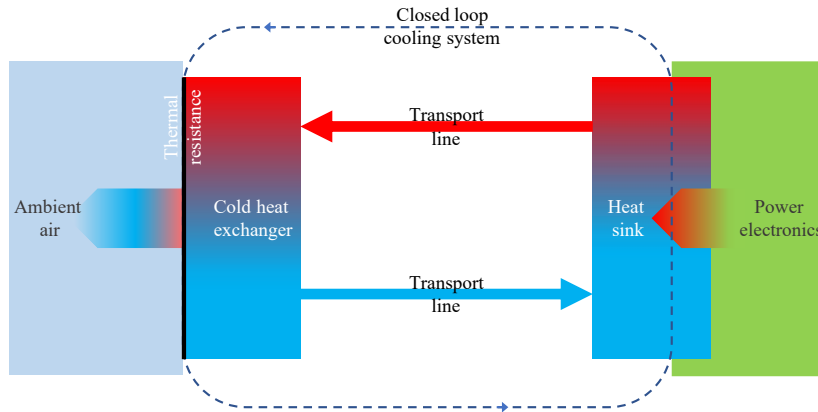


Figure 1.5: Cooling system loop as a broker

load transported by the coolant fluid. However, the use of the latter is related to air temperature and thermal resistance on the secondary side (see Fig. 1.5).

Two different technologies are introduced here: skin heat exchanger (see sec. 1.4.1), which introduces an additional resistance, due to the presence of a solid wall, between external air and cold heat exchanger’s tubes; and RAM air (see sec. 1.4.2), which allows a direct contact between the external air and the tubes of the cold heat exchanger.

In the past, both technologies have been used, as they are, to cool embedded systems (“air cooling”) and rarely an intermediate closed loop circuit was added between them and the chips to be cooled [30]. In particular, in the case of RAM air, the problem is strongly related to air temperature and velocity, so to heat transfer coefficient, variation.

1.4.1 Skin heat exchanger

The skin heat exchanger is an “already-integrated-system”, today used on aircrafts, such as the CL-600 Challenger [31], to cool avionics equipment⁸.

In 1989, Howard (McDonnell Douglas Corporation) deposited a patent on skin heat exchanger [3]. The system was described as able to provide cooling and ensuring required heat evacuation for avionics systems. In fig. 1.6 a simplified scheme taken from the Howard’s patent of his skin heat exchanger is reported.

A skin heat exchanger, as shown in Fig. 1.6 and Fig. 1.7, is a part of the aircraft itself and is installed outside of the aircraft insulation layer. It is composed by the low thermal resistance aircraft skin, fin and base panel (23 and 27, respectively, in Fig. 1.6). Hot

⁸For “already integrated system” the inventor means a system that does not need extremely weight-expensive radiator systems, metal fasteners, rivets and so on, on the outer side of the skin of the vehicle [3]

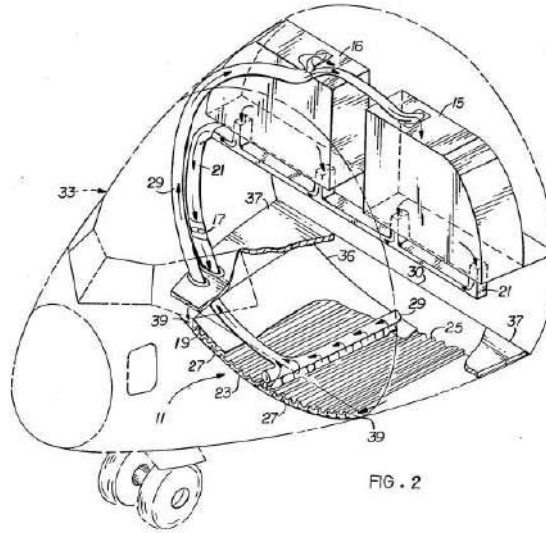


Figure 1.6: Skin heat exchanger 3D scheme [3]

cabin air flows into the hot side, while the “cold source” is the cold air available outside of the aircraft [4]. On the hot side, the air is forced, by using some fans, for example, to enter the cabin where electronic systems are installed. Hot air, flowing in the tube, reaches the heat exchanger.

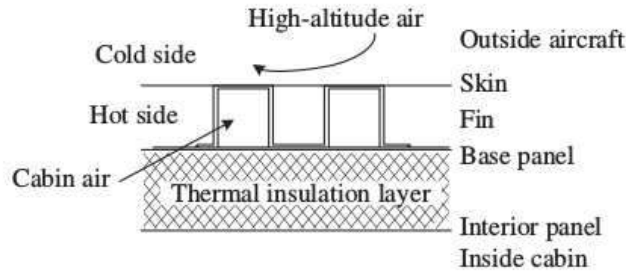


Figure 1.7: Skin heat exchanger scheme [4]

Pang *et al.* [4] have analysed, assuming an aircraft cruising at Mach 0.9, at 10 km of altitude, the behaviour of a skin heat exchanger positioned in two different positions, as reported in Fig. 1.8.

Position 1, defined as unfavourable, is relative to a parallel flow of external air with the skin heat exchanger, while position 2, defined as favourable, is relative to a windward angle. They obtained an overall heat transfer coefficient (HTC), in the less favourable position of skin heat exchanger, of $45 - 51 \text{ W} \cdot \text{m}^{-2} \cdot \text{K}^{-1}$, while in the most favourable position the HTC ranges between 66 and $80 \text{ W} \cdot \text{m}^{-2} \cdot \text{K}^{-1}$. This kind of technology,

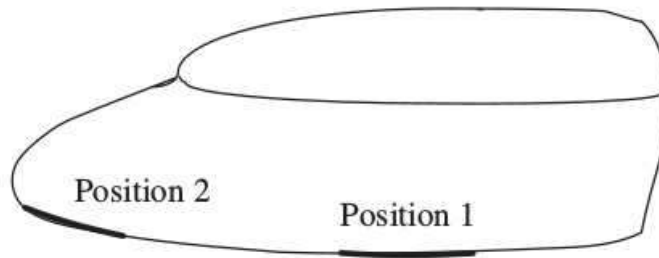


Figure 1.8: Positioning scheme of skin heat exchanger [4]

already used for electronics cooling, has been already considered, as secondary side of a LHP condenser for the same purpose [32]. A reduction of the heat transfer coefficient as a function of the altitude, principally due to a reduction of air density, was also observed by Fleming *et al.* [32]. As reported by them, even if the HTC increases as a function of the Mach number, over 40 000 ft ($\simeq 12\,200$ m) the dependence of HTC on the velocity is negligible. However, the results of Fleming *et al.* [32] show the capability to maintain temperature controlled and to evacuate the heat power because of positive heat flux (from the aircraft skin to the external air). Otherwise, for high Mach numbers and low altitudes, one assists to an inversion of the heat flux direction principally due to a higher adiabatic wall temperature than the skin temperature. This phenomenon is mainly due to aerodynamic heating effects [32]. Using this technology, Ashemi *et al.* [33] numerically studied electronics equipment cooling. A heat transfer rate higher than 15 kW had to be evacuated in their case, by maintaining the temperature controlled at 105°F (40.56 °C).

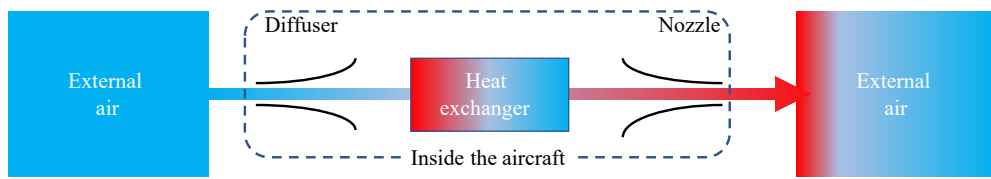
1.4.2 RAM-air

“When air is taken aboard an aircraft in flight, it undergoes an increase of pressure which is called the —ram effect—, and a cooling system which uses such air is called a RAM-air cooling system.” [34]. RAM-air is maybe the oldest technology, used in aircraft applications, to bring external air on board⁹. Its working principle is simple and the number of components limited. In Fig. 1.9b a principle scheme of this technology is reported. It is composed by an air intake, obtained on the aircraft structure, which shape can be NACA type to reduce the influence on the lift to drag ratio; an heat exchanger, where air coming from the intake is heated by the devices to be cooled and, finally, an air outlet, where air is released to external environment. The air, entering from intake diffuser, is subject to a pressure and temperature increase: the air temperature at the exit of the intake diffuser is almost equal to the total temperature of ambient air; while

⁹It was mostly used with air cooling heatsinks.



(a) RAM air intake example [35]



(b) RAM-air general scheme

Figure 1.9: RAM air.

the static pressure is lower than the total pressure of atmospheric air. The diffuser has the purpose to reduce and stabilise the air flow velocity. In the heat exchanger, heat is evacuated by the coolant fluid and air, flowing within a nozzle, is rejected to the ambient through the outlet duct. The outlet duct conveys the air to the outlet of the system where the exit nozzle is used to expand air and so to generate thrust to partially damp lift losses due to the presence of air intake [30]. RAM-air cooling system is the simplest way to use external air as a secondary side heat exchanger (see Fig. 1.9b). However, its influence on the aerodynamics characteristics of the aircraft could be not negligible and so, it should not be used on such aircrafts which mission is limited in time (less than thirty minutes) [34]. The additional mass related to the use of this kind of system is mostly due to the presence of the inlet diffuser, ducts and outlet nozzle. RAM air may be characterised by a quite large volume encumber: other than diffuser and nozzle, the duct has to be designed to avoid any high flow resistance, due to supersonic flows that may be realised in some flight conditions, during the entire mission [30]. Grabow and Kazan [36] designed, in 1996, a high performing cooling system, using this technology as cold source for the secondary side of a liquid-to-air and a air-to-air heat exchanger. They were able to evacuate up to 5 kW of thermal load by requiring a maximum electrical power of 2 kW to let the whole cooling system work. Because of the dimensions and the complexity of the equipment to cool (fighter aircraft pod), their system was equipped by a series of

“accessories” such as valves and by-passes, and different fans to drive the airflow to the different heat exchangers. Finally a ACM (Air Cycle Machine¹⁰) was positioned between the air inlet and the outlet, where compressor and blower were respectively installed. The highest advantage of a ACM driven RAM-air cooling system is the capacity to decrease the temperature of air at the inlet of the heat exchanger on the secondary side. It has to be noted that, in the case analysed in ref. [36], more extreme conditions, typical of military applications, were encountered in the air intake because of extreme aircraft velocity (up to Mach 1.2)¹¹. The compressor is used to increase the air pressure, after heat exchanges, before the expansion in the nozzle to minimise the effects on the lift losses. Before Grabow and Kazan, Grabow *et al.* [37] have done a similar study for fighter avionic’s pods cooling. Instead of using a unique technique based on the ACM-driven RAM-air, they used a coupling of a direct RAM-air system and a driven-RAM air intake. To avoid problems linked to high Mach numbers flights ($Ma > 1$), especially related to the lowering of the mass flow rate into the RAM-air intake, they programmed to use the direct RAM-air for low Mach numbers/low altitude flights and the RAM-driven technique for high Mach numbers/high altitude flights. This solution allowed them to provide the adequate avionics cooling in a huge range of operating conditions.

RAM-air seems to be the most performing solution, ensuring the lowest temperature available at any time of the mission profile. However, problems are mostly related to heat exchangers, that should be as compact as possible, and to the ducts which impose a not neglecting penalty to volume encumber. Some solutions are thought to embed RAM air heat exchanger within the engine inlet [28]. However this solution is more adapted in conventional propulsion aircraft in which bleed air can be extracted from fan.

Both skin heat exchanger and RAM-air seem to be suitable technologies to evacuate the thermal load generated by electronics components. They have to be coupled with a “liquid cooling system” to have a better control of the cooling rate. Skin heat exchanger is characterised by lower overall performances. It is mainly due to presence of an additional thermal resistance, and to difficulties in use of fins to increase the heat exchanger surface area. Higher heat exchanger dimensions are surely related to this technology if compared with RAM-air one. On the other side, RAM-air is a more flexible solution to be used on the cold source side. It allows the use of a finned, and so compact, heat exchanger. Moreover, the duct dimensions can be controlled, during design process, to control and optimise the air velocity to maximise the HTC.

In the following chapters, a research of high performing and efficient cooling loops is

¹⁰ A turbo-compressor system.

¹¹ At such velocities the air entering from the ram air is subject to a temperature increase due to the isentropic transformations.

reported to finally select the best solution adapted to solve the problem. Its thermal and hydraulic characteristics in steady and transient conditions will be exploited.

Part II

Hybrid aircraft power electronics cooling: from the state of the art to system selection

The part two of this work is focused on the analysis of different solutions that potentially could help to solve the problem related to high power density electronics cooling. Composed by three chapters, in this part, active single and two-phase and passive two-phase cooling systems will be analysed at first using a system approach, by considering all the main components of such system. So, the attention will be focused on the hot side, introducing and analysing different high performing heatsink technologies. Finally, on the basis of a first approximation design, a comparison is introduced to choose the most adapted cooling system for the application discussed in this work.

Overview of existing cooling solutions

Due to the high complexity of cooling systems, the number and typology of components and the physical phenomena at the base of their working principle, it does not exist a universal way to classify them. In fact, different point of views are considered when talking about. Actually, with the word cooling system one can either indicate the hot heat exchanger (HXG), where the thermal load is transferred to the coolant, or the whole system, by considering transport lines, pumps or compressor if any, accessories and so on. Different performances characterise cooling systems following their typology. However, they may be classified on the base of their general working principle and main physical characteristics of heatsinks.

To try to give a classification, by considering either installation and heat transfer mechanism occurring in the hot side, or heatsink as it will be called in this work for simplicity, in Fig. 2.1 a diagram based on the main heat transfer mechanisms, thermodynamic principles, and hydraulic characteristics is reported.

In general, a cooling system is used to maintain the temperature controlled on the device to be cooled by evacuating the required thermal load. To accomplish this job two different methods can be used:

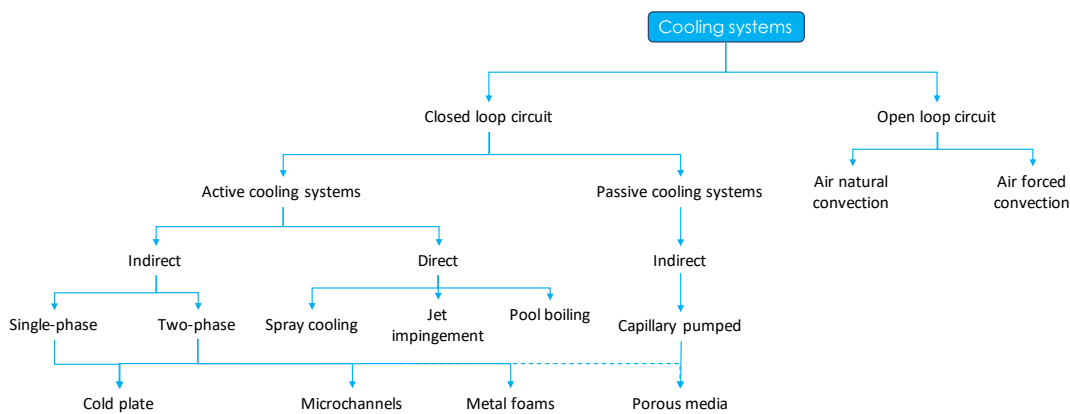


Figure 2.1: Cooling systems classification.

- Cool the device by directly using external air (air cooling, or in general called open loop circuits).
- Cool the device by using an intermediate circuit (liquid cooling, or in general called closed loop circuits).

In the first case, due to the fact that external air is directly used as coolant, in particular in aeronautics fields, one has to face with some issues, such as the variability of ambient air temperature, velocity and density on which the heat transfer coefficient (HTC) depends. The second method, which is also usually called “liquid cooling”, uses a closed loop circuit to transfer the heat to another point where its extraction is simpler. In this case, it is possible to overcome the limitations of air cooling by, for example, using some kind of regulating valves. This allows to maintain the temperature controlled on the device to be cooled, even when cold source condition changes are significative during the mission of the aircraft. As it will be observed later in this chapter, some kind of technologies do not need any kind of controlling system because of their “auto-regulating” ability. It is the case of some passive two-phase systems. Other cooling technologies, instead, need regulating accessories which could be, in some cases, detrimental in this application field (it is the case of active single-phase systems).

However, a closed loop circuit behaves as a “smart broker” between the heatsink, where heat is evacuated from the device to be cooled to the working fluid, and the cold source (heat exchanger), where heat is definitively evacuated to the external ambient air. In order to have smarter and more efficient solutions, only closed loop circuits will be considered here and the following definitions will be used:

- **Heat sink** the device through which the thermal power is evacuated from the base plate of power electronics modules to the coolant (hot source).
- **Coolant** or working fluid, is the fluid used to transport the thermal load from the hot to the cold source.
- **Cold source** is the heat exchanger used to evacuate the thermal load from the coolant to the ambient air.

According to Fig. 2.1, closed loop circuits cooling systems can be divided in two categories: active and passive. Active cooling systems are characterised by the presence of a pump or a compressor, following the technology, to move the fluid into the circuit. Passive cooling systems use gravity or capillary forces to make the fluid flow into the loop. The difference is obviously in the amount of energy required by the cooling system to operate.

With reference to the heatsink, active cooling systems can be classified in different ways. A first classification is about direct and indirect. Direct cooling systems are characterised by a direct contact between coolant and electronic components. The heat exchange mechanism depends on temperature and heat flux ranges. Forced or natural convection, or evaporation/boiling, are the main heat exchange mechanisms. In general, in this kind of systems, particular attention has to be paid to the choice of the coolant, in contact with the electronic devices: dielectric fluids must be used. In the case of indirect cooling systems, the coolant is confined into a case (usually made of a high conductivity material) in which the fluid can flow. So, because of the presence of an interface between the electronics components and the working fluid, an additional thermal resistance is added. The heat transfer mechanism is conduction between the base plate and the heatsink and forced or natural convection, or boiling/evaporation, between the heatsink and the working fluid. Either direct and indirect cooling systems can be single or two-phase and, following the efficiency and thermo-hydraulic requirements of the problem to be solved, different heat sink technologies may be used¹. Otherwise, due to the use of gravity or capillary phenomena to move the fluid into the loop, all passive solutions are liquid/vapour two-phase systems. Capillarity only occurs in presence of a porous medium. So, a confinement is necessary in two-phase passive cooling systems which may thus only be indirect.

All active cooling systems can be divided in single and two-phase according to the heat transfer mechanism. In single phase case, sensible heat is used to transfer the thermal load from the heat sink to the working fluid, which is subject to a temperature increase from the inlet to the outlet. In two-phase case, sensible heat-rate is usually negligible and latent heat is used to allow a phase change of the working fluid (generally evaporation). In this case, a difference in vapour quality occurs between the inlet and the outlet of the heatsink.

In this work, two different approaches are used to show the state of the art of the actual cooling technologies. In this chapter, a discussion about active single and two-phase cooling loops and capillary pumped (passive two-phase) technologies is presented. Working principles and concept schemes of such technologies are introduced to explain how they work and to analyse pros and drawbacks of each one.

In chapter 3, instead, the attention will be focused on the heatsink. Different heat extraction mechanisms and technologies will be compared, the working principle explained and actual performance level introduced.

¹An overview of different heatsink technologies is presented in chapter 3.

2.1 Active cooling systems

Systems requiring an external source of energy to move the fluid into the loop are defined as active cooling systems. The general operating scheme is reported in figure 2.2 where the main components of the loop may be distinguished.

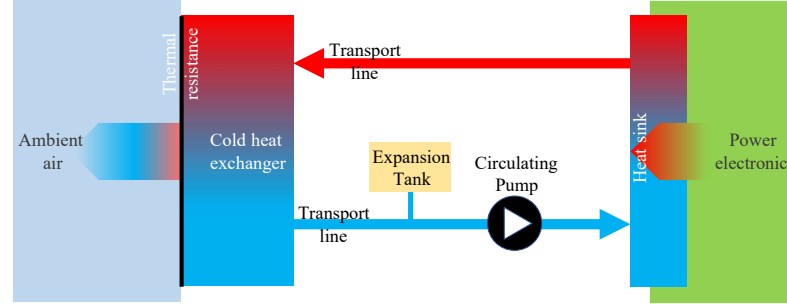


Figure 2.2: General scheme of an active cooling system

The circulating pump, or the compressor in the case of vapour compression technologies, has to be designed to counterbalance all the pressure drops in the loop and to maintain the necessary mass flow rate to evacuate the thermal load from the heatsink, where thermal load is transferred to the coolant. In the cold heat exchanger, heat is definitively evacuated to the external ambient. An expansion tank is used to prevent fluid expansion, eventual water-hammers and other instabilities to mechanically damage loop's components.

Active cooling systems can be single or two-phase. Even if heat transfer mechanisms are quite different between them, the constituting components play the same role. In two-phase systems either latent and sensible heats are used: the heatsink is an evaporator and the cold source becomes the condenser (with sub-cooling). Referring to the scheme reported in fig. 2.2, and for standard two-phase pumped circuits, in steady state conditions, the sub-cooled fluid coming from the cold heat exchanger/condenser, flows to the heatsink. Hot fluid or vapour reaches the cold heat exchanger or condenser where heat is definitively evacuated to the external ambient. Through the return transport/liquid line, sub-cooled liquid return to the evaporator where the loop starts again. The expansion tank is also used to impose and regulate saturation conditions, but this point will be better approached in the following. In other cases, the pump is replaced by a compressor, the tank suppressed and an expansion valve mounted on the liquid line, obtaining a Rankine vapour compression cycle.

In the case where a direct contact technology is used, such as jet-impingement/spray-cooling, the scheme reported in figure 2.2 is also valid, but a collecting tank must be

provided to ensure that fluid is in liquid state before its return to the evaporator.

2.1.1 Single phase cooling systems

Single phase cooling systems, also called “liquid cooling”, are maybe the simplest and most used configuration. The physical principle of this technology is relatively simple and, in its “classical configuration”, is the best-known technology.

The working fluid, heated in the heatsink, flows within the transport lines, ideally adiabatic, to the cold heat exchanger. A pump is used to move the fluid into the loop and it has to be designed to ensure the adequate mass flow rate and the necessary pressure head to counterbalance for all the pressure drops in the circuit. Some accessories, such as expansion vessel and valves have to be provided to ensure the smooth functioning. In fig. 2.3 a concept scheme is reported.

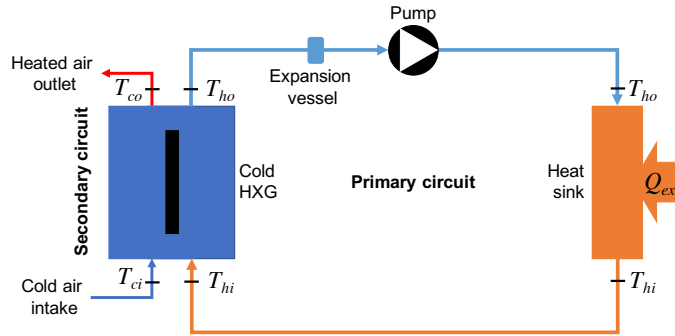


Figure 2.3: Single phase cooling system concept scheme

Starting from the heat sink, the sensible heat, evacuated by the devices to be cooled, let the working fluid temperature to increase from T_{ho} to T_{hi} . The working fluid joins the cold heat exchanger (Cold HXG) where, in steady-state condition, it transfers sensible heat to the secondary fluid. The primary circuit working fluid temperature decreases from T_{hi} to T_{ho} while the secondary circuit working fluid temperature increases from T_{ci} to T_{co} .

Depending on the availability of the cold source and the performance requirements, one of the technologies introduced in sec. 1.4 may be used.

2.1.1.1 Transport lines

Transport lines are simply tubes. They should allow the fluid to flow with the lowest distributed pressure drop possible and minimising heat losses.

For single-phase flows, transport line design is based on the assumption that liquid velocity should be limited to $u_{max} = 2 \text{ m}\cdot\text{s}^{-1}$. This assumption is in general used in industrial and building application for two main reasons. The first one, purely mechanical, is to avoid erosion of tubes that may occur for pretty high liquid velocities. The second one, fluid-dynamics in nature, is to avoid high pressure drops and instabilities, such as water hammers and subsequent mechanical danger and noise due the exaggerate liquid velocity in the ducts.

Starting from the required mass flow rate, tube internal diameter is calculated as:

$$D_i = \sqrt{\frac{4\dot{m}_l}{\rho_l \pi u}} \quad (2.1)$$

where u is the fluid mean velocity through the tube having cross-sectional diameter D_i .

In literature, two methods are used to calculate the maximum velocity as a function of the flow typology. In the case of laminar flow, because of the parabolic velocity profile along the cross section of tube, the liquid maximum velocity is calculated in correspondence of the tube axis: $u_{max} = 2u$. In the case of turbulent flow, because of high velocity gradients in the boundary layer, the maximum velocity is related to the mean one as $1.3u \leq u_{max} \leq 1.5u$.

In general, if no phase change occurs, the tube inner diameter is the same for both hot and cold lines and thermophysical properties change is usually neglected. Any eventual volume variation, as it occurs during operations and due to the working fluid temperature difference, is dumped by the expansion tank.

2.1.1.2 The pump and the expansion tank

The pump is the component that allows the liquid flow within the primary circuit. It has to be designed to ensure the required mass flow rate to evacuate the thermal power and the necessary pressure head to cross over all the pressure drops in the loop.

The electric power to drive the pump is calculated as:

$$P_{elec} = \frac{\rho_l \dot{V}_l \Delta P_{tot}}{\eta_{pump}} \quad (2.2)$$

where \dot{V}_l is the working fluid volumetric mass, ΔP_{tot} the total pressure drops in the loop (considering both distributed and localised one) and η_{pump} the pump efficiency which rarely is higher than 40%. The higher the pumping power, the higher the pump's mass. They are used in either single and two-phase active cooling systems and are chosen in

the same way.

The expansion tank is used in all closed loop circuits to reduce any kind of instability related to pressure oscillations or fluid expansions due to temperature variations. In this last case, in fact, the fluid expands or reduces its volume. If volume variations are not considered and contained during design stage, they can lead to serious mechanical damages all over the circuit. Two of the most used kinds of expansion vessels are diaphragm expansion vessels, showed in Fig. 2.4a, and free surface expansion vessels, shown in Fig. 2.4b. Even if the purpose is the same, different operating principles characterise these two typologies.

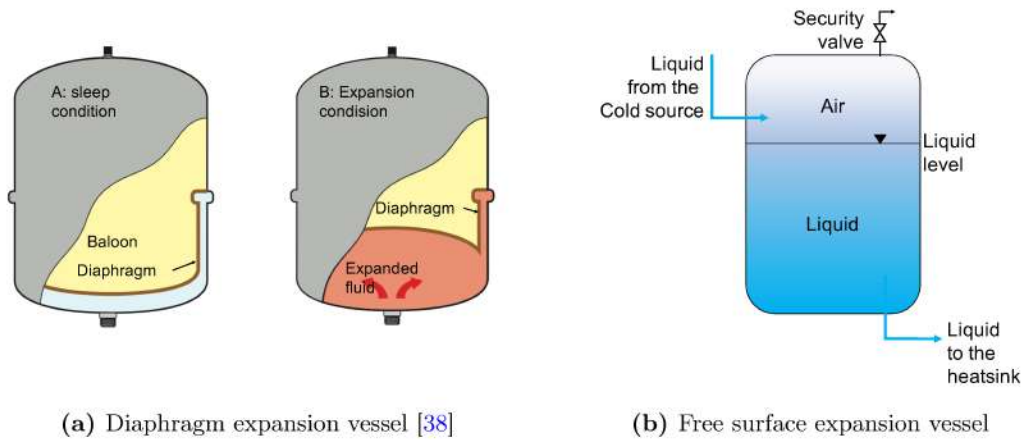


Figure 2.4: Expansion vessels typologies

Diaphragm expansion vessel is only “activated” when a pressure change of the fluid occurs consequently to a volume variation. It is composed by a gas charged, usually nitrogen (N), balloon; a diaphragm, separating the nitrogen and the working fluid, and a metallic case. When liquid expansion occurs, the latter enters in the vessel and deforms the elastic membrane until pressure equilibrium between nitrogen contained in the balloon and liquid into the circuit is reached.

Free surface expansion vessel (Fig. 2.4b) is characterised by the presence of air in the upper-side of the vessel and liquid in the bottom-side. In this case, a direct contact between liquid and air occurs. The liquid, coming from the cold source, always enters in the vessel and, in the case where a pressure variation in the circuit takes place, it is dumped by air. In this case, the free surface of liquid changes its position until pressure equilibrium. This kind of expansion tank is the one used in cars’ engines cooling systems and, as it will be better explained later, it is also used in two-phase cooling systems. In the latter, air is mixed with vapour of the working fluid and saturation condition are

imposed.

However, a security valve, usually a spring-loaded pressure relief valve, is used to protect the circuit from exaggerate pressure increases that can occur in some cases (usually due to design error). If pressure in the expansion vessel is higher than the setting value of the valve, the latter opens and pressure is released to the ambient.

2.1.1.3 Heat sink heat transfer

Following the efficiency requirements, the heatsink (discussed in chap. 3) has to be able to ensure the adequate cooling of electronics devices allowing control of their surface temperature.

Due to sensible heat exchange, a strong dependency between mass flow rate and heat-sink temperature exists in single-phase case.

From the knowledge of thermal power evacuated by the electronic components, Q_{th} , the mass flow rate, \dot{m}_l , can be evaluated by eq. (2.3):

$$Q_{th} = \dot{m}_l c_{p,l} (T_{hi} - T_{ho}) \quad (2.3)$$

Under the hypothesis of adiabatic transport lines and in absence of any kind of regulation system, the temperature of the liquid at the inlet of the heat sink, T_{ho} , is imposed by the cold heat exchanger primary side outlet².

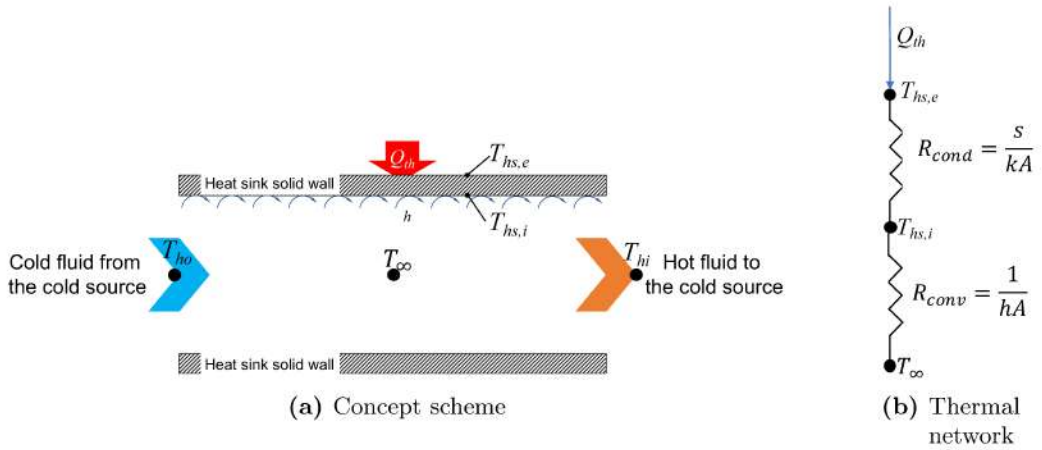


Figure 2.5: Heat transfer mechanism simplified scheme in the heat sink.

²All the variables are referred to the cold heat exchanger, with respect of the convention reported in fig. 2.3

According to schemes reported in Fig. 2.5 (where a schematic of transversal section of the heatsink is reported with the related heat transfer mechanism and the associated thermo-electrical network, respectively Fig. 2.5a and Fig. 2.5b), the coolant side heat sink wall temperature $T_{hs,i}$, can be simply obtained by the Newton's law:

$$Q_{th} = h A (T_{hs,i} - T_{\infty}) \quad (2.4)$$

where, h is the fluid equivalent heat transfer coefficient (calculated on the base of the electronic baseplate), A is the heat transfer surface area and T_{∞} the working fluid bulk temperature (calculated as the arithmetic mean between the plate's inlet and outlet temperature, T_{ho} and T_{hi} , respectively).

By combining equation 2.3 and 2.4, the bulk to wall temperature difference can be written as:

$$(T_{hs,i} - T_{\infty}) = \frac{\dot{m} c_{p,l} (T_{hi} - T_{ho})}{h A} \quad (2.5)$$

The heatsink external wall temperature, related by relation $(T_{hs,e} - T_{hs,i}) = \frac{Q_{th}}{\frac{kA}{s}}$, is calculated as:

$$T_{hs,e} = [\dot{m}_l c_{p,l} (T_{hi} - T_{ho})] \left[\frac{1}{\frac{kA}{s}} + \frac{1}{hA} \right] + T_{\infty} \quad (2.6)$$

From eq. (2.6) one may notice that to maintain a constant heatsink wall temperature, $T_{hs,e}$, at constant T_{hi} and T_{ho} , the mass flow rate, \dot{m}_l , and the heat transfer coefficient, h , need to change contemporarily. As it will be shown in sec. 2.1.1.4, for the cold source temperature differences realised in this application, up to $\simeq 80$ K, MFR (mass flow rate) adjustment is not a practical way.

2.1.1.4 The cold heat exchanger (HXG)

The cold heat exchanger allows evacuation of thermal load from the working fluid, flowing in the primary side circuit, to the secondary side one. Even in this case, the heat transfer mechanism is based on sensible heat exchange between hot and cold fluid. The hot fluid, flowing in the primary side, releases the thermal power to the cold source (secondary side) which nature, in this particular study case, is limited to one of the technologies presented in section 1.4. The logarithmic mean temperature difference method is used to obtain the heat exchanger geometrical dimensions and, a posteriori, the NTU method is used to calculate the heat exchanger efficiency ε .

Considering a co-current heat exchanger, its operating diagram is qualitatively reported in fig. 2.6. There, heatsink inlet to outlet temperature difference, ΔT_{hs} , under the hypothesis of adiabatic transport lines, and the secondary fluid inlet to outlet temperat-

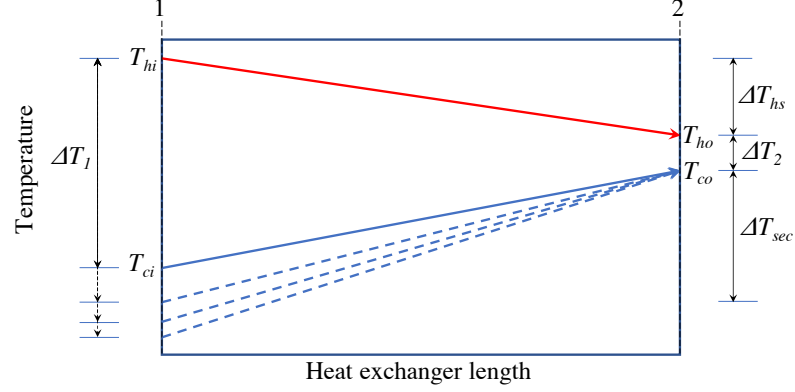


Figure 2.6: Co-current heat exchanger qualitative operating diagram

ure difference, ΔT_{sec} , on which the following discussion is based are also reported.

The primary circuit working fluid enters in the heat exchanger at temperature T_{hi} . It evacuates the thermal load, Q_{th} , to the cold fluid which temperature increases from T_{ci} (corresponding to the RAM-air inlet temperature, for example) to T_{co} . Hot fluid leaves the heat exchanger at temperature T_{ho} . — The heatsink inlet temperature, T_{ho} , depends on T_{ci} —.

In classical applications, where the cold source temperature is fixed and does not change as a function of time, unless minor temperature change occurs (for example a night/day temperature oscillation in the case of an air-cooler HXG), the heat exchanger works at constant T_{ci} , so no T_{ho} change occurs. In this case, thermal transformations are only verified following the continuous lines in Fig. 2.6. In aeronautics field, on the contrary, according to the mission profile, the cold source inlet temperature, T_{ci} , is not constant, but it cyclically changes as a function of the altitude (see section 1.3). Temperature differences up to about 80 K may occur and such temperature change may impact the mean logarithmic temperature difference (LMTD) unless a regulating system is used on the primary or secondary side to control heatsink inlet condition.

Considering the design equation of a heat exchanger, the heat power to be evacuated is calculated as:

$$Q_{th} = U A \Delta T_{lm} \quad (2.7)$$

where: A is the heat transfer surface area; U the global heat transfer coefficient and ΔT_{lm} the logarithmic mean temperature difference, calculated as:

$$\Delta T_{lm} = \frac{\Delta T_1 - \Delta T_2}{\ln \frac{\Delta T_1}{\Delta T_2}} \quad (2.8)$$

When a change in T_{ci} occurs, two different scenarios are realised.

In the first case, mass flow rate rules. No regulating equipments are available on the circuit, neither on the primary or the secondary side. For given Q_{th} , ΔT_{hs} is fixed by the primary fluid mass flow rate (eq. 2.3) and ΔT_{lm} is fixed: in eq. (2.7), heat exchanger heat transfer area and overall heat transfer coefficient are fixed by design conditions. The whole heat exchanger diagram, in this case, will readapt its working point to maintain constant temperature differences, but changing heatsink working temperatures range. For constant inlet to outlet heatsink temperature difference, ΔT_{hs} , heatsink wall temperature, $T_{hs,e}$, and consequently junction temperature, change as a function of altitude/time. This solution is the simplest one, but not acceptable. In fact, the junction temperature is limited to an operating range, that, in most cases, is not compatible with external high-altitude ambient air temperature. Often, the junction temperature should be maintained as constant as possible, independently from the cold source temperature, to ensure power modules reliability and lifetime. To avoid such problems, a mass flow rate control system may be used to maintain the junction temperature regulated and fixed. On the basis of heat exchange on the secondary side, the air mass flow rate is calculated by eq. (2.9):

$$Q_{th} = \dot{m}_{air} c_{p,air} (T_{co} - T_{ci}) \quad (2.9)$$

Combining eq. (2.3) and eq. (2.9), it is:

$$\dot{m}_l c_{p,l} (T_{ho} - T_{hi}) = \dot{m}_{air} c_{p,air} (T_{co} - T_{ci}) \quad (2.10)$$

From relation (2.10), according to Fig. 2.7, one can observe that for fixed T_{hi} and ΔT_{hs} , to maintain the heatsink temperature as constant as possible, the air mass flow rate, \dot{m}_{air} , needs to be adjusted for any variation of T_{ci} . So, during climb and descent stages, a continuous regulation of external mass flow rate, \dot{m}_{air} , is required. Moreover, external air velocity variations occurring during taxi-out and take-off and climb stages transitions should be considered as well: they impact the air mass flow rate at the inlet of the heat exchanger.

To show required air mass flow rate variation as a function of altitude (to evacuate a thermal load of 15 kW and to maintain a fixed temperature difference on the heatsink, $\Delta T_{hs} = 12$ K), it has been calculated for three different working fluids (methanol, ethanol and water) as reported in Fig. 2.8. There, only temperature variations are considered.

The higher the altitude and the lower the external air temperature, the lower the required mass flow rate. A regulation of this type is not ease-to-implement. It might be strongly problematic and it could imply the use of valves and other regulation systems,

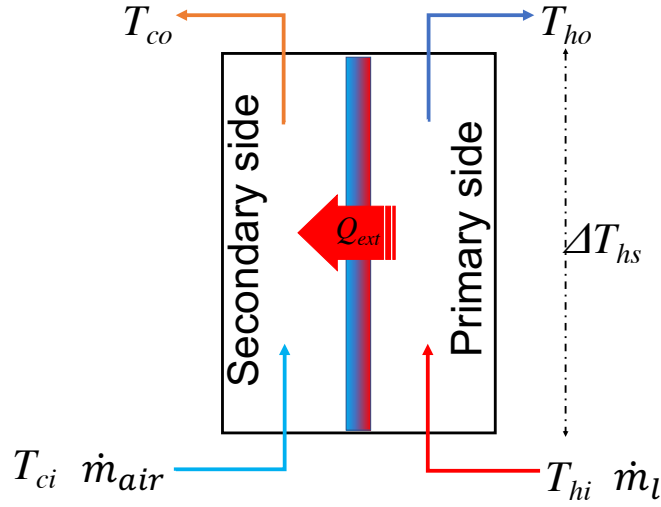


Figure 2.7: Cold side heat exchanger concept scheme

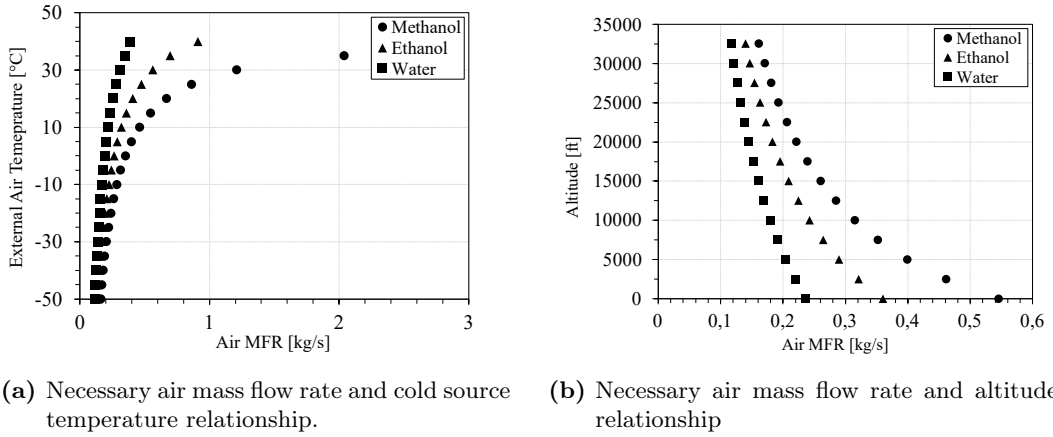


Figure 2.8: Air mass flow rate as a function of the external air temperature and altitude.

such as variable section nozzles. In order to respect the efficiency requirements in the context of HASTECS project, this is an option that cannot be retained. However, considering that the most part of radio communication and embedded systems are today cooled using this kind of technology, it will be considered for comparison purposes. In alternative to secondary air mass flow rate regulation, primary liquid mass flow rate regulation should be considered to maintain a constant heatsink temperature. In this case, a regulation valve such as a three-way-valve or a variable-speed-pump should be considered, but reducing the efficiency of the whole cooling system and increasing the overall mass.

Pros	Drawbacks
Very well known physics phenomena	Heatsink inlet temperature dependent on the cold source temperature
Easy to design	Strongly dependence on the operating point
-	Heatsink temperature dependent on the mass flow rate
-	Not flexible
-	Necessity of regulation accessories

Table 2.1: Single phase cooling system synthesis

2.1.2 Two-phase active cooling systems

Pumped two phase cooling systems are divided in two categories with different physical working principles and thermodynamic characteristics. In *pumped two-phase* technology the evaporator operates at higher temperature than condenser and a pump is installed on the liquid line. In *vapour compression* technology, because of the use of Rankine cycle, the evaporator can operate at lower temperature than condenser and a compressor is used on the vapour line.

2.1.2.1 Pumped two-phase technologies

Two-phase pumped cooling systems are the most effective way to evacuate the thermal load by increasing the overall efficiency of the cooling system itself.

Most of the authors that analysed this kind of technology focused their attention on performances, heat transfer efficiency and heat recovery requirements. When talking about electronics cooling, in fact, the attention is in particular paid to chips and data server cooling, which are characterised by quite high heat flux densities, but pretty small heat transfer surfaces. In this case, despite the really high heat flux densities, the heat rate to be evacuated is limited if compared with application analysed in this work.

The effectiveness of this kind of technologies has been demonstrated by Thome and Brunch [39]. By comparing two-phase pumped systems with single-phase ones, they showed that, to maintain constant chip temperature, the use of two-phase technology allows sensitive pumping power saving and using a lower coolant mass flow rate. If, instead, the same pumping power than active single-phase technology is used, a temperature difference of 13 K is realised in favour of two-phase one.

Such solutions are currently designed to fit the thermal evacuation requirements of military aircrafts. In those cases, very high thermal power, up to hundreds of kilowatts, with peaks in the order of thousands of kilowatts, must be evacuated [40]. The American society ACT develops two-phase technologies to be used for civil and military applications. They ensure a lowering of overall system mass due, in particular, to the reduction of the mass flow rate and pumping power [41].

Even if the concept scheme for this kind of technology is similar to the one related to single-phase cooling systems, the operating principle is completely different. Here, latent heat is used to extract heat by hot source.

In Fig. 2.9 the concept scheme of a pumped two-phase cooling system is reported.

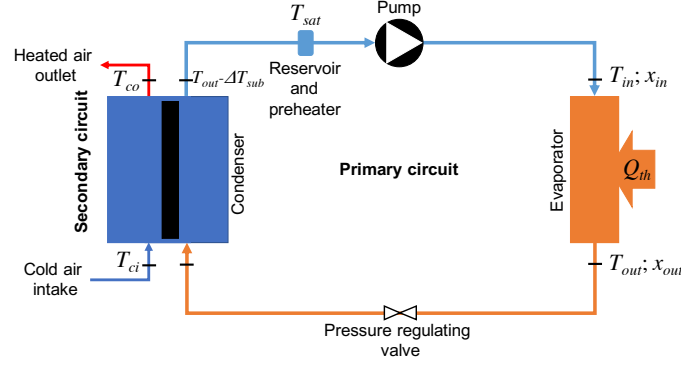


Figure 2.9: Pumped two-phase cooling system concept scheme.

In the case where a free surface tank is used as a reservoir, where saturation conditions are imposed, subcooled liquid coming from the condenser enters in it. The liquid flows within the liquid line to the evaporator, where heat is exchanged according to eq. (2.11).

$$Q_{th} = \dot{m} h_{l,v} (x_{out} - x_{in}) + \dot{m}_l c_{p,l} (T_{sat} - T_{in}) \quad (2.11)$$

Usually the vapour quality at the exit of the evaporator, x_{out} , is lower than unity and the temperature difference between the saturation temperature, T_{sat} , and the liquid entering in the evaporator, T_{in} , is usually negligible ($T_{in} \leq T_{sat}$). Sensible heat exchange in eq. (2.11) is negligible and, if no superheating occurs, vapour leaves the evaporator at saturation temperature, $T_{out} = T_{sat}$. The partially or completely evaporated fluid flows within the vapour line to the condenser, where heat is rejected and liquid subcooled before returning to the pump. Liquid temperature depends on the undercooling level imposed to the heat exchanger and so on the cold source temperature, T_{ci} . Subcooled liquid flows within the reservoir where it is heated until saturation condition and the cycle

starts again [41]. More generally, the reservoir, used to impose the saturation conditions, is separated from the circuit and is linked to it by a tube. No subcooled liquid flows within it, and in this case liquid temperature is $T_{in} < T_{sat}$.

If superheating occurs in the evaporator, the scheme of principle needs to be modified according to the fluid temperature change occurring into the evaporator. In this case no pressure regulating valve is needed on the vapour line. The superheated vapour directly flows to the condenser which has to be designed to ensure the necessary length, either for condensing and sub-cooling.

However, the position and the configuration of the circuit are imposed by system requirements. For example, in the case of Marcini *et al.* [42], a variable speed pump was used to regulate the fluid mass circulating into the circuit and a stepper motor valve, installed just before the evaporator, was used to control vapour quality through MFR regulation. In other cases, the sub-cooler may be separated from the condenser, usually valid for heat exchangers operating at fixed temperatures, this configuration avoids to use an electric heater in the reservoir and saturation conditions are imposed in heat exchanger as a function of T_{ci} . This kind of configuration requires to the evaporator to operate at higher temperature than in the condenser.

2.1.2.2 Vapour compression technologies

Vapour compression technology allows to evaporator to works at lower temperature than condenser. A concept scheme of this particular technology is presented in Fig. 2.10. Superheated gas, at the exit of the evaporator, is compressed up to the pressure corresponding to condenser's operating temperature. Once subcooled liquid condition is reached at the condenser outlet, the liquid flows through an expansion valve decreasing the fluid static pressure and bringing it to saturated vapour condition. So, the fluid flows to the evaporator and the cycle re-starts.

Because of the thermodynamics characteristics of these kind of systems, the vapour compression technology is able to lower the evaporator temperature below the condensing one. If in two-phase pumped systems, the liquid must be subcooled before entering the pump, installed on the liquid line, in this case, to avoid "wet compression", the vapour has to be superheated before its entering in the compressor [40, 43]. If the superheating required by the evaporator changes, due to a change of operating characteristics, the expansion valve regulates the superheating level to maintain fixed operating conditions. Even if some authors describe this technology as premature, especially for problems related to micro-compressors reliability and efficiency [44], when applied to electronics, it is successfully used in aeronautics fields for military applications.

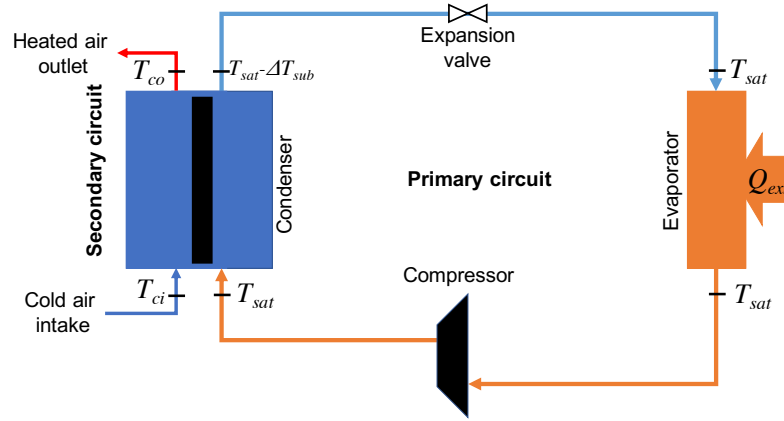


Figure 2.10: Vapour compression concept diagram scheme.

Mancin *et al.* [45] studied a vapour cycle system used to cool high heat flux density electronic components in avionic packages: a cold plate was used as evaporator and a tube-in-tube heat exchanger, supplied by two independent water flow rates controlled in temperature, was used as condenser. They obtained a coefficient of performance, COP, between 1.05 and 5.80. Trutassanawin's [46] refrigeration system was able to evacuate a $40 - 75 \text{ W} \cdot \text{cm}^{-2}$ on a 1.9 cm^2 chip and maintaining its temperature lower than 85°C . Comparing vapour compression technologies to the most promising cooling techniques, this is the only technology³ able to lower the junction temperature below the cold source temperature. However, they are affected by some integration difficulties. Today, the challenge is the compressor miniaturisation and efficiency increasing, especially at small scales, to make them more flexible and to reduce vibration and noise [44].

This technology is described as reliable enough in steady state applications, but during sudden and violent transient phases it demonstrates its biggest limitations. The latter are in particular related to instabilities concerning the entering of liquid phase into vapour compressor. This is true during severe transient phases related to sudden and violent variable-gravity stages. As reported by Chen *et al.* [5], the major issue is mostly related to multi-evaporator configuration. To solve the problem, they introduced a system, reported in Fig. 2.11, able to suppress flow instabilities, separating liquid and vapour phase in a two-phase flow, by using a Microchannel Membrane Phase Separator (MMPS). A first MMPS is installed after the evaporators. It separates liquid and vapour phase of an eventual two-phase flow at the exit of the evaporators. The liquid is sent back to the evaporators inlet, where an ejector⁴ is installed, driving the liquid in the recirculation

³Unless Peltier cells are considered.

⁴Ejectors are passive devices able to generate a pressure difference. They require a sufficient momentum to the fluid to raise the suction flow pressure.

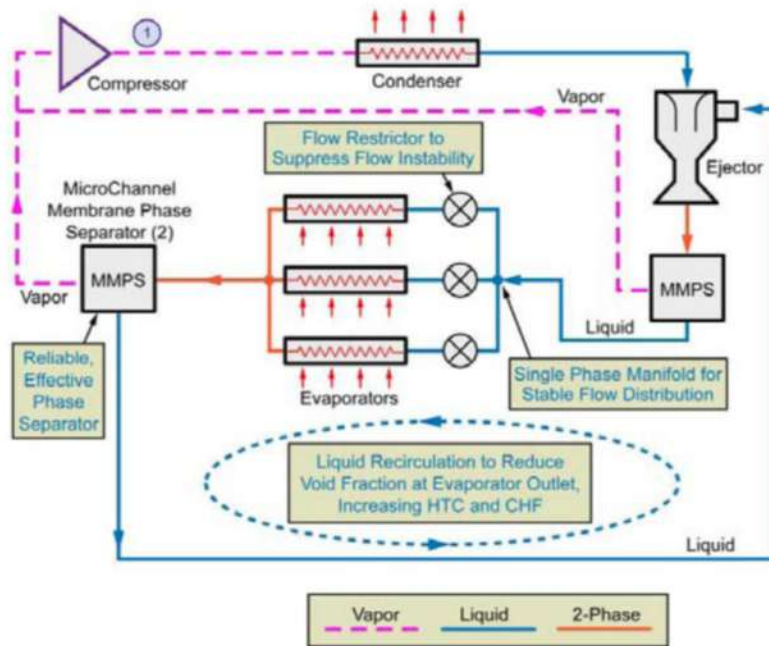


Figure 2.11: Scheme of principle of an active two-phase thermal system equipped by a MMPS solution [5].

loop. An other MMPS is installed before evaporators and separates eventual liquid and vapour phases at the exit of the ejector. In this case, vapour phase is sent to the compressor inlet, while the liquid phase to the evaporators inlet. A great complexity characterises this kind of system, in which it is not possible to control each phase of the flow without using a by-pass control loop.

Even if vapour compression technology is able to lower the evaporator temperature below the condenser's one, it has to be underlined that, because of the higher specific volume of vapour, compared with liquid one, the work required to vapour compression technology is higher than that required to *pumped* two-phase cooling systems to provide the same differential pressure between compressor/pump inlet and outlet. Marcinichen *et al.* [42] proposed three different kind of "two-phase cooling cycle". They compared the performance of a liquid pumped two-phase technology, a vapour compression cycle and a hybrid one. They used a variable speed pump to control MFR in the circuit, while a stepper motor valve was used to control vapour quality at the outlet of the evaporator.

The scheme of principle of this kind of technology is not so different than that of single-phase one.

Even if this technology is one of the most promising, flexible and potentially efficient, its use in aeronautical field could be a gamble, even due to its instabilities during some

transient stages. On the other hand, pumped two-phase cooling systems will be retained to be compared with other promising technologies introduced in the following.

2.2 Passive cooling systems

In contrast to active cooling systems, passive cooling systems do not require any external source of energy to move the coolant. Neglecting systems using natural convection because of its low heat transfer coefficient, here we will only refer to two-phase passive technologies.

During the latest thirty years passive cooling systems, such as *heat pipes*, *thermosyphons*, CPLs (*Capillary Pumped Loops*) and LHPs (*Loop Heat Pipes*), began to be used in aeronautical and aerospace fields [47]. The main advantages of these systems are their simplicity, adaptability and efficiency. Some of them, such as thermosyphons, have been used since a long time in terrestrial applications, such as railway field, for IGBTs cooling, while other ones have begun to be used since the latest ten years [48, 49, 50].

2.2.1 Thermosyphons and Heat pipes

Heat pipes (HP) and thermosyphons are successfully used in applications do not requiring high transport distances. Generally, they are able to transport heat powers from a few dozens of Watt up to 1 kW for distances ranging between 10 cm and few meters. They are today used for thermal control, temperature homogenisation or as thermal diodes [51]. They are particularly useful when the heat sink and the cold source are located up to a few meters. Today, capillary heat pipes are effective to evacuate heat flux up to $100 \text{ W} \cdot \text{m}^{-2}$ and reducing hot-spot influence by flattening the temperature field on the surface to be cooled. Vapour chamber has been successfully used as heat spreader, to reduce temperature gradients on electronic components and evacuating heat flux densities up to $220 \text{ W} \cdot \text{cm}^{-2}$ as Reyes *et al.* reported [52].

2.2.1.1 Thermosyphons

A thermosyphon is a finite closed tube filled with a small quantity of fluid at saturated state. Its higher and lower ends are closed and sealed, while air is sucked-out. When thermal load is applied to the lower end (evaporator), the working fluid evaporates and vapour flows within the adiabatic length to the condenser. Here, heat is evacuated and condensed fluid flows back to the evaporator, thanks to gravity forces, sliding on the lateral walls of the device. The essential condition that allows a thermosyphon to operate is obviously the ability for the condensate to flow back to the evaporator.

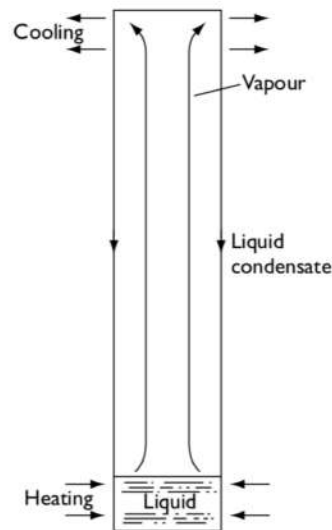


Figure 2.12: Thermosyphon [6]

A vertical installation or any other kind of favourable direction is so necessary to allow the condenser to be positioned over the evaporator.

At the evaporator, three different heat transfer mechanisms occur following the intensity of the heat flux and the liquid/vapour phase distribution. The working fluid stratifies in the evaporator, it is so affected by three different behaviours: liquid pool, liquid film and vapour. For small heat fluxes, natural convection occurs in the liquid pool; for medium and high heat fluxes, mixed convection and nucleate boiling may take place. Different factors, such as filling ratio (FR, the liquid over the evaporator volume ratio), inclination angle, heat power load, and aspect ratio influence the performance of the thermosyphon. Among them, the most important is the filling ratio. A small amount of liquid contained in the thermosyphon easily brings the device to dry-out. This is a detrimental condition that leads to failure of the device. A pretty high amount of liquid may cause flooding in the evaporator. In this case the liquid remains in the condenser or in adiabatic section and is no more able to return back to the evaporator. However, this is not the only condition that prevents the liquid to flow back to the evaporator. In fact, if thermal load to the evaporator is too high, violent boiling can prevent the liquid to flow back to the evaporator and choking occurs if vapour velocity is higher than the sonic limit. In this case, vapour, flowing in the centre of the thermosyphon, experiences a shockwave and the device stops to work. When vapour expansion is violent, instabilities may occur due to reduction of hydraulic head (geyser boiling). This phenomenon does not limit thermal and hydraulic operations of the device, but, due to vibrations related to, this phenomenon can be detrimental from a mechanical point of view [53, 54]. For

example, using water as working fluid, Ong and Lim [53] experimentally observed that the best performing condition for the thermosyphon is vertical condition with a filling ratio equal to unity. Abou-Ziyan *et al.* [55] investigated the performances of a vibrated and a stationary thermosyphon with water and R134a as working fluids. The heat flux densities were measured from 4 to 28 W·cm⁻² with water and from 1.6 to 3.8 W·cm⁻² with R134a. They found that the adiabatic length, like the filling ratio, deeply influences the behaviour of the device. The maximum heat transport capability is influenced by the working fluid: a difference of one order of magnitude was found between water, characterised by the best performances, and R134a. Filippeschi and Franco [56] experimentally investigated, using water and ethanol as working fluids, the influence of the main parameters on a thermosyphon. They did not observe an important influence of the filling ratio if water was used as working fluid while, using ethanol, a higher sensitivity to the FR was tracked down other than higher instabilities.

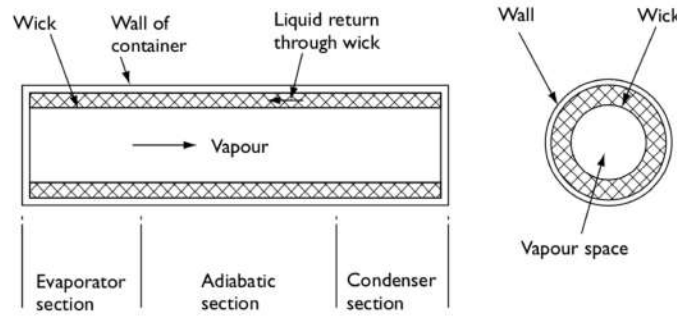
As well as instabilities, thermosyphons are strongly limited by their inability to work whatever the position. For this reason, capillary driven technology, such as HP, LHP and CPL are worth of attention, more than thermosyphon, here introduced just for completeness.

2.2.1.2 Heat pipes

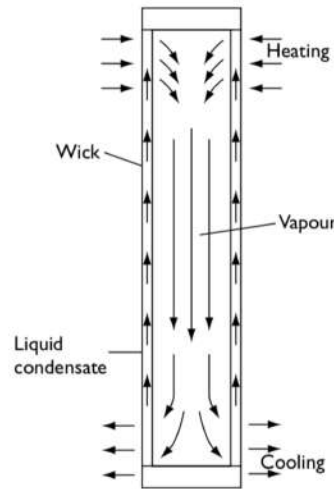
Capillary Heat Pipes (HP) are under certain aspects close to thermosyphons, but thanks to capillary pumping liquid is sucked back from condenser to evaporator. This, obviously, allows HPs to potentially well operate whatever their orientation.

According to Fig. 2.13a, heat pipes are composed by a tube internally coated with a thin layer of porous material (wick) and closed at the higher and lower ends. A small quantity of liquid is inserted and air is sucked out.

As thermosyphons, HP can be divided in three different thermal sections: evaporator, where the thermal load is applied, adiabatic zone and condenser. In the evaporator, vapour is formed and naturally flows within the adiabatic zone (into vapour space, see Fig. 2.13b) to the condenser section. Here, vapour condensates and liquid come back to the evaporator thanks to capillary forces caused by the menisci curvature in the porous wick. Heat pipes are characterised by high thermal performances, and can be used in several applications. Beyond the classical use, for cooling purposes, they are successfully used as thermal diodes and thermal switches (for variable conductance HPs) [6] as soon as heat spreaders. According to their design, they can operate over a wide range of temperatures (from 4 K to 2300 K) and for pretty high heat flux densities, up to 20 kW·cm⁻² with lithium used as working fluid [6]. However, HPs began to be widely used in electronics



(a) Concept scheme.



(b) Working principle.

Figure 2.13: Heat Pipe. [6]

cooling because of their adaptability to the geometry to be cooled, easy integration, as well as their capability to maintain a uniform temperature field on the surface to be cooled and their property to transport heat to another point where the evacuation is simpler. In particular, according to geometry, different kind of heat pipes exist, from flat heat pipe (FHP) to micro heat pipes. The latter are used in array configuration allowing a direct concurrence to microchannels (see sec. 3.2.2). A typical application concerns chips cooling of “smart devices” we every day use and everybody has in his pocket (see Fig. 2.14a). Sometimes they are used by devices constructors for advertising purposes (Fig. 2.14a and 2.14a) [57, 58].

Ray and Kew [6] classify HP in five categories. Including Loop Heat Pipes (LHP), the other categories are tubular, flat plate, micro heat pipes and direct contact systems. Tubular HPs represent the “basic” category of heat pipes and different design features may be used in particular in electronics application field. For example, for power electronics

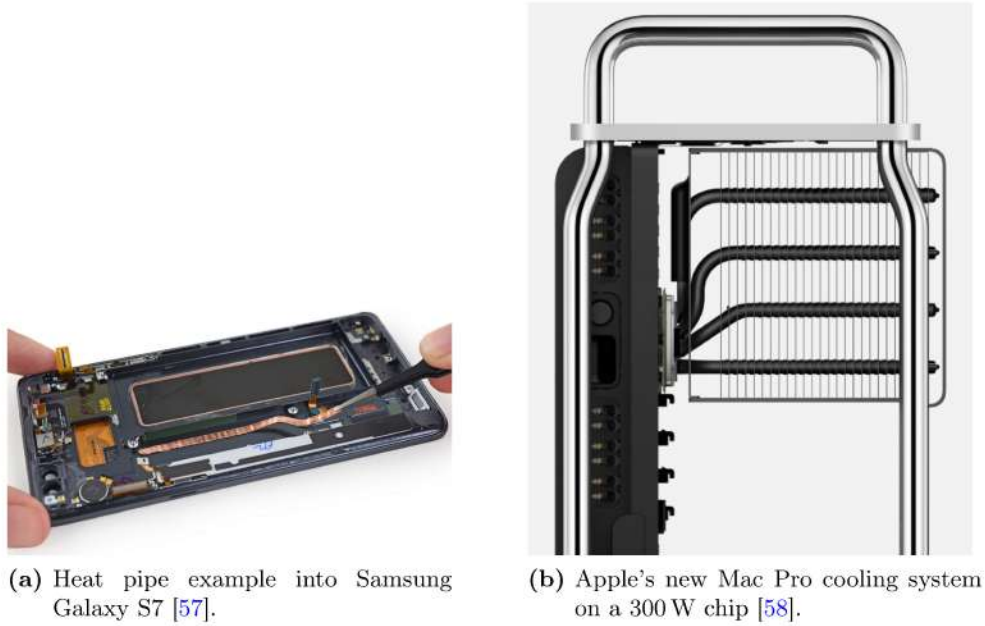


Figure 2.14: Heat pipes application example

cooling on high speed trains, their adiabatic section is electrically insulated. The ceramic insulation insert is able to hold-off very high electric voltage, in the order of kilovolts [6].

Flat plate heat pipes (Fig. 2.14a) are the mostly used, in particular for micro-electronics cooling purposes for their particular ability to flatten the temperature field and so, to obtain a nearly isothermal surface on the device to be cooled [6]. The electronics chips can be directly mounted on HP. In this case, a heat conducting electric insulation layer is used between chips and HP evaporator. In other cases, electronic components are mounted on heat pipes using such heat spreader or any other kind of structural component [59]. Flat plate heat pipes FPHP may be bended as they can fit into small devices, as is the example of laptop computers. However, bending angle of FPHP should be optimised, as well as HP length because of decreasing thermal performances. Chen and Chou [60] experimentally observed a bell shape thermal conductivity behaviour as a function of thermal power. By exploiting different bending angles of adiabatic length, they observed an increase in thermal conductivity of almost 3 times: from $2 \text{ kW} \cdot \text{m}^{-1} \cdot \text{K}^{-1}$ at a bending angle $\alpha = 0^\circ$ to over $6 \text{ kW} \cdot \text{m}^{-1} \cdot \text{K}^{-1}$ at a bending angle $\alpha = 90^\circ$.

Micro and miniature HPs are widely used in electronics components cooling and are worthy of attention because of their efficiency, lightweight and passivity. They are characterised by diameter in the range $0.3 - 6 \text{ mm}$. They can work in thermosyphon mode,

without a wick coating, or in HP mode when a sintered powder, a metal-fibre or a grooved wick are being used. Different working fluids can be used, from pure water to ethanol, methanol or dielectric fluids [6, 59]. They are successfully used to evacuate thermal power up to 250 W on distances up to 200 mm. Low thermal resistances characterise this particular technology, from $1.5 \text{ K}\cdot\text{W}^{-1}$ for lower outer diameter HPs to $0.6 \text{ K}\cdot\text{W}^{-1}$ for higher diameters HP [59]. As reported by Chen *et al.* [61], the smaller the channel transversal section of HPs, the higher the heat transfer coefficient (HTC) and the higher the heat transfer surface area per unit flow volume. For this reason, micro heat pipes (MHP) were worth of attention other than for their ability to evacuate thermal heat flux densities up to $1 \text{ kW}\cdot\text{cm}^{-2}$ (for small heat sources). However, they are no longer used for small transport distances, in the order of centimetres, because of their low thermal performances. In fact, at such little transport lengths, at which MHPs were used, conduction heat transfer mechanism gets the upper hand on two-phase heat transfer one, undermining HPs themselves. If a temperature flattening is required and so the thermal heat flux needs to be reduced, by increasing the heat dissipating surface, from the dissipating device, the heatsink can also be equipped by a vapour chamber which can be characterised by very high thermal conductivities, up to $800 \text{ W}\cdot\text{m}^{-1}\cdot\text{K}^{-1}$ [59].

However, strong limitations may affect HPs. If, for example, the temperature at evaporator is quite low, no vapour menisci are formed and so no fluid circulation occurs in the device: the pressure difference between the evaporator and the condenser is not sufficient (vapour viscous limit) for the liquid to come back to the evaporator by capillary effect. As the temperature increases, the vapour velocity increases as well, but it is limited to sonic limit to avoid chocking. Capillary limit occurs when the capillary pressure is too low to counterbalance the overall pressure losses due to the fluid flow: $\Delta P_{cap} < \Delta P_{tot}$. The capillary pressure head ΔP_{cap} , reported in eq. (2.12), is a function of the surface tension of the working fluid, σ , and of the curvature radius, R , of the liquid-vapour interface in pores of the wick.

$$\Delta P_{cap} = \frac{2\sigma \cos \theta}{R} \quad (2.12)$$

The total pressure drop, ΔP_{tot} , is the sum of the frictional pressure drop in the porous wick, viscous pressure drop of vapour during its path from the evaporator to the condenser, internal and gravity pressure drops .

However, it exists a maximum value of capillary pressure head, $\Delta P_{cap,max}$: as well as the thermal load increases, the curvature radius R tends to decrease until it reaches its

minimum value, $R = R_p$. The maximal capillary pressure head is so defined as:

$$\Delta P_{cap,max} = \frac{2\sigma}{R_p} \quad (2.13)$$

When the minimal value of R_p is reached, any eventual augmentation of thermal load at evaporator will lead to a regression of the liquid/vapour front in the primary wick, with the consequent system failing [62]: dry-out occurs and HP stops to work.

2.2.1.3 Pulsating heat pipes (PHP)

Pulsating Heat pipes (PHP) belong to the category of wickless heat pipes. In this particular devices, heat is transferred under the form of latent heat through the vapour and sensible heat through the liquid slugs. The working principle is different than that of classic HP. In this case, the fluid flow is not imposed by a capillary structure in which capillary forces take place to push the liquid from the condenser to the evaporator. Its pattern is imposed by surface tension effects in a smooth tube causing phase separation resulting in the formation of slugs of liquid dispersed into vapour bubbles. As one can observe in Fig. 2.15, the device is formed by a serpentine, partially filled of liquid, which cross section dimension is in the order of capillary dimension.

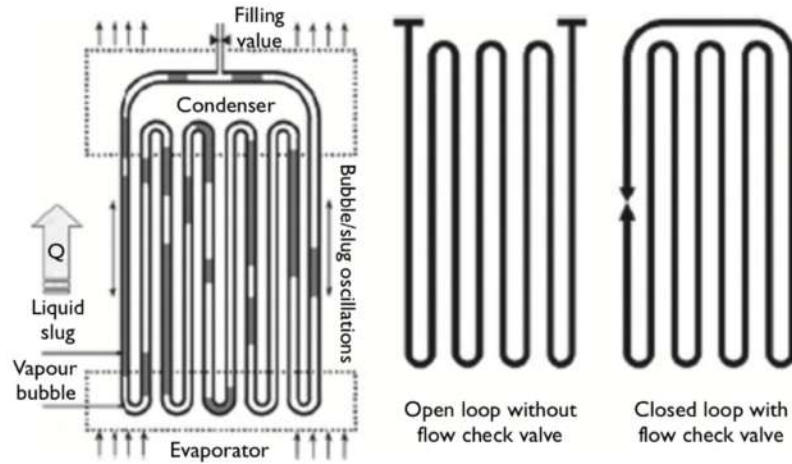


Figure 2.15: Pulsating heat pipes [6].

When thermal load is applied to evaporator, the working fluid evaporates and vapour pressure increases bringing to vapour bubbles growing in the evaporation zone. The liquid slugs and vapour bubbles are so pushed to the condenser where lowering of the vapour pressure occurs and condensation takes place. Bubbles growing and collapsing bring to the typical oscillating motion of liquid into the adiabatic section of the PHP.

Despite the simplicity of this technology, the working principle is not completely known, but its potentialities, in particular for electronics device cooling are undeniable. Fundamental and applied studies are currently in progress to increase the knowledge about this particular technology such as in refs. [63, 64, 65, 66, 67, 68, 69, 70].

2.2.2 Two-phase passive loops

LHP and CPL belong to the category of two-phase passive loops and are characterised by a decoupling between liquid and vapour lines. The same components constitute LHP and CPL: evaporator, composed by a porous wick confined in a metallic housing; reservoir, condenser and transport lines. The difference between the two loops is the position of two-phase reservoir. LHPs are characterised by a *hydraulic* and a *thermal* coupling between the evaporator and the reservoir. It is due to a direct contact between the two components, that are connected together, to allow heat and mass exchanges between them. The two-phase reservoir is installed immediately before the evaporator and receives a part of the heat flux. A buffer volume is directly linked with the porous wick in the evaporator. So, an eventual surplus of vapour can return into the reservoir.

CPLs are characterised by a *hydraulic decoupling* between the reservoir and the evaporator, as explained by Nikitkin [47], Lossouarn [50] and Blet [71]. The reservoir is installed on the liquid line, and linked to it by a little tube [47]. This particular configuration does not facilitate hydraulic exchanges between the two components [50]. Because of such decoupling between the two entities, CPL is characterised by a slower time constant (so called “thermal” time constant) during transient operations. There are strong operating differences between the two systems. LHPs are characterised by robustness and auto-regulation ability, while the direct coupling between reservoir and evaporator does not easily allow regulation of saturation point [71] that is one of CPL characteristics.

Nikitkin and Cullimore [47] described the difference between the two loops, and said that between them many technologies could be imagined and developed.

2.2.2.1 Loop Heat Pipe (LHP)

Loop Heat Pipes (LHP) can be seen as an extension of the concept of classic heat pipes. LHP are characterised, as HPs, by the presence of an evaporator and a condenser, but a decoupling between vapour and liquid line exists. Beyond the separated transport line feature, LHP is characterised by the presence of a reservoir where saturation conditions (temperature and pressure) are “automatically” established [6]. Despite the fact that the LHPs represent an “evolution” of HPs, they are characterised by higher capillary

pumping head if compared to HPs, allowing transport of heat for several meters (up to 21 meters) [72].

Loop heat pipes are characterised by a direct coupling between the evaporator and the reservoir. The direct link between the two components makes possible the transmission of a part of the heat flux from the one to the other. The heat flux modifies the saturation conditions in the reservoir. The equilibrium between the saturation conditions in the reservoir and the flow of cold fluid at the inlet makes possible its typical auto-regulation capacity. Moreover, the contact between the porous mesh and the reservoir walls increases the robustness of the system: the liquid at the inlet of the porous wick is directly provided by the reservoir.

To explain the loop operating principle, we will refer to the scheme and the thermodynamic diagram reported in Fig. 2.16.

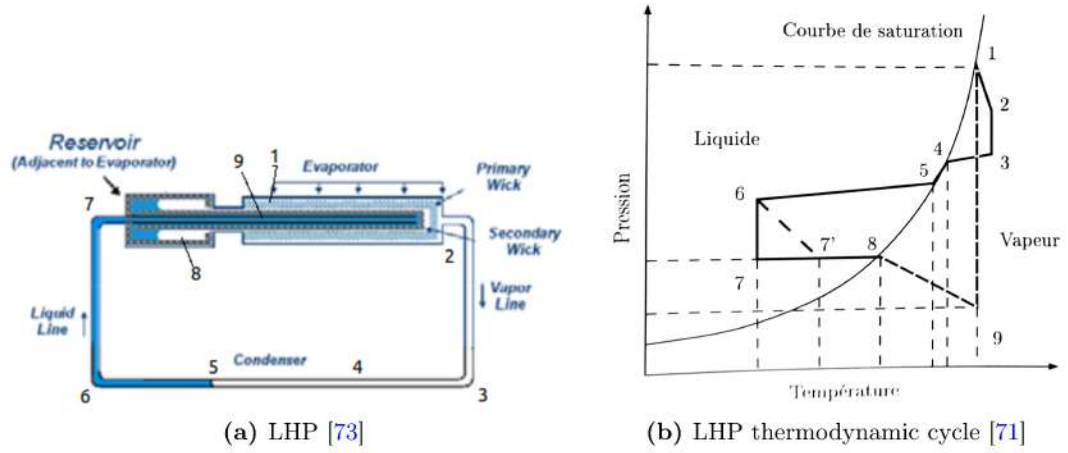


Figure 2.16: Loop Heat Pipe Scheme and thermodynamic cycle

When the thermal load is applied to the evaporator wall, it reaches the liquid menisci in the porous wick and triggers the evaporation (point 1). Vapour pressure increases and vapour leaves the evaporator slightly superheated by evaporator walls (point 2). Vapour flows through the vapour line into the condenser (point 3) where it is initially cooled until saturation condition is reached (point 4 on the saturation curve), so condensed (4-5) and undercooled (5-6). Subcooled liquid flows through the liquid line to reservoir inlet (point 7). Here, it is heated by a fraction of the heat flux received by the thermal load until saturation conditions are reached (point 8, corresponding to the reservoir thermodynamic conditions at equilibrium). Then, liquid flows through the porous wick until the liquid/vapour menisci (point 9), where capillary forces take place and the cycle starts again. Saturation conditions in the reservoir are not imposed, but depends on

heat balance. A change of the thermal load leads to a change of saturation conditions in the reservoir, displacing the point 8 on the saturation curve and modifying the whole thermodynamic cycle. The loop adapts the operating point to respect the global balance of the loop [26].

Gravitational effects influence the loop behaviour and must be taken into account. In fact, the presence of a gravity field modifies the fluid distribution, in particular between the compensation chamber and the evaporator core [62]. Two important parameters have to be considered when a LHP operates in gravity fields. The *elevation*, which is the relative position between the evaporator and the condenser, and the *tilt*, which represents the relative position between the evaporator and the compensation chamber. A modification of tilt can modify the liquid distribution between the evaporation core and the compensation chamber. In adverse tilt conditions, the evaporation core is filled with vapour, so, it could lead to an increase of the operating temperatures of the loop [62]. At positive tilt, the evaporation core is completely flooded with liquid.

2.2.2.2 Capillary Pumped Loop (CPL)

Capillary pumped loops (CPL) use the same mechanisms than LHP to let the fluid flow into the loop, so equations (2.12) and (2.13) are still valid in this case. As said above, the differences between the two loops is the position of the reservoir which modifies the operating characteristics and the behaviour of the whole system. In CPLs, the saturation point in the reservoir is generally fixed by using an electric heater. So, in this case, the reservoir is used as a compensation chamber where the reference point for the thermodynamics cycle is constant and has to be controlled during operations.

To explain CPL working principle, even in this case, the concept scheme and the thermodynamic cycle will be used (see Fig. 2.17).

Comparing thermodynamic cycles of LHP and CPL reported in Fig. 2.16b and 2.17b, no difference exists between the thermodynamic states (1 to 7). On CPLs, a change of thermal load applied to the evaporator will lead to a temperature change of evaporator itself. On the other hand, a shift of the whole cycle on the saturation curve takes place: thermodynamic states will change respecting the saturation conditions constraint imposed to the reservoir (point 8). It is worth of attention that a change of heat load at the evaporator leads to a change of condensation length in the condenser. So, its conductance adapts itself maintaining a constant temperature in the loop [25]. This is one of the most important CPLs characteristics: the temperature level control capacity, that makes of CPLs one of the most flexible system. On the other hand, due to the decoupling between reservoir and evaporator, they are characterised by high instabilities

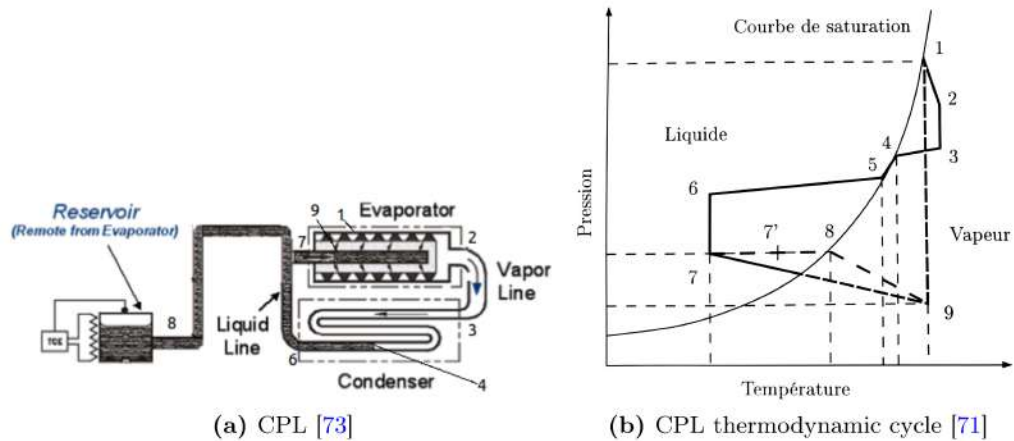


Figure 2.17: Principle scheme and thermodynamic cycle of CPL and LHP loops

and oscillations [50], in particular during start-up stages [74].

The described systems are characterised by a great robustness and auto-adaptability, in the case of LHPs, and by an undeniable temperature levels regulation ability in the case of CPLs.

2.2.2.3 Capillary Pumped Loop for Integrated Power (CPLIP)

During the last years, a new loop typology has been developed to solve the problems related to the use of CPLs and having the reliability and robustness of LHPs. The Capillary Pumped Loop for Terrestrial Applications (CPLTA), or Capillary Pumped Loop for Integrated Power (CPLIP), is not really a CPL-LHP operating conditions mixing, but it is another kind of loop. It is more similar to a CPL, but with a higher energetic and mass coupling between reservoir and evaporator thanks to gravity forces. It was designed for the first time by the Belgian society EHP (Euro Heat Pipe) for power electronics thermal control for the railway field purposes [50].

The CPLIP, which a concept scheme is reported in Fig. 2.18, is characterised by a particular architecture that makes possible hydraulic and thermal couplings between reservoir and evaporator. The reservoir (R) is installed above the evaporator (E) and the two components are linked by a liquid line, continuously supplying⁵ the evaporator with liquid. If eventual vapour bubbles are formed in the wick, they are evacuated flowing up to reservoir while the liquid is forced by gravity to enter the evaporator. In this case, especially during the start-up stages, compared to classical CPLs, loop crisis are absent [50] and system reliability is high.

⁵During normal operating conditions.

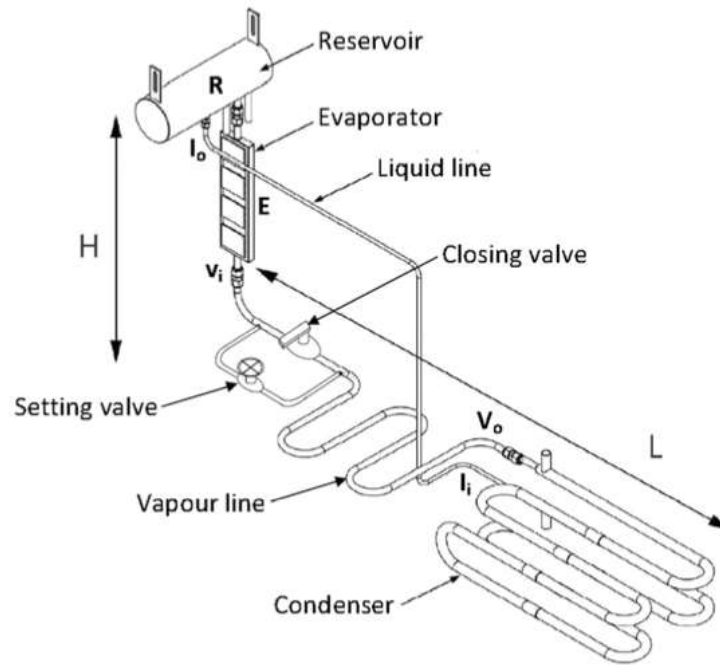


Figure 2.18: CPLIP scheme [7]

The reservoir is physically divided in two parts. The higher part, having the higher volume, contains the liquid-vapour interface. The height of the interface changes as a function of loop operating regimes: “variable conductance mode”. Like in classical CPLs, it is possible to control the saturation conditions in the reservoir and so, the evaporation temperature [49]. The lower part, directly linked to the liquid line and characterised by a smaller volume than the higher part, contains the under-cooled liquid coming from the condenser. The two parts of reservoir communicate through a small opening which makes possible mass transfer between both volumes and so pressure and energy balances. The controllability of reservoir temperature, by using an electric heater, makes possible a great stability of the loop especially during transient regimes such as start-ups [74].

Like CPLs and LHPs, the evaporator contains a porous wick, which, using capillarity effect, described in sec. 2.2.1.2, is able to pump the liquid into the whole loop. Different materials may be used for this component. In such cases the use of a Nickel porous wick determines the reduction of the particles size, leading to an increase of ΔP_{cap} and so to an increase of the performances of the whole loop.

Like CPLs, the condenser must be designed to allow complete condensation and the adequate subcooling of working fluid to avoid two-phase flow in the liquid line and so vapour bubbles at the inlet of reservoir. A too small condenser has not a sufficient length

to ensure liquid under-cooling, while a too long one could lead to quite large pressure drop, determining in some cases the failure of the loop. It has been demonstrated that the condenser has the ability to adapt its conductance to maintain a constant evaporating temperature [14, 12] by adapting the condensing length to the thermal load that has to be evacuated. This point will be better and deeply explained in chapter 6.

It has to be noted that the loop is successfully used today to cool the power electronics components on a train operating on the RATP line in Paris [48] since 2012, by evacuating heat flux densities from $20 \text{ W}\cdot\text{cm}^{-2}$ up to $40 \text{ W}\cdot\text{cm}^{-2}$.

2.2.3 First comparison between two-phase passive cooling systems

In tables 2.2 and 2.3 the main pros and drawbacks of most important passive technologies are reported.

A first comparison between CPL and LHP has been made by Delalandre [26] and his table has been completed by adding the CPLIP characteristics (table 2.2). In table 2.3 a comparison between the passive cooling technologies is reported, considering their pros and drawbacks.

Properties	CPL	LHP	CPLIP
Regulation	+	−	+
Robustness	−	+	+
Integration	+	+	(\sim)+
Maturity	+	+	\pm

Table 2.2: Synthesis of the main characteristics of CPL, LHP and CPLIP.

2.3 Conclusion

Due to complexity, intrinsic characteristics and possible configurations, it is difficult to classify cooling systems. However, in this chapter, a possible classification was proposed by splitting them in different categories and by grouping them on the basis of their basic physics and working principles. Starting from general point of view, on the basis of the thermodynamics operating principles beyond each cooling loop, they were divided in active and passive cooling systems.

Active and passive loop circuits were introduced, considering the whole system and their basic physics. So, the main components of such cooling circuit were analysed under a thermo-hydraulic point of view. Pros and drawbacks were introduced to easily

Technology	Pro	Drawback
<i>LHP</i>	Auto-regulation capacity	Incapability to control temperatures
	Robustness	
<i>CPL</i>	Temperature regulation possibility	Instabilities
		Slow start-up
<i>CPLIP</i>	High stability [75]	External source of energy required
	Independence between cold source and junction temperature	
	Heat flux densities up to $40 \text{ W} \cdot \text{cm}^{-2}$	
	Heat transport capacity up to 10 m [75]	
<i>HP</i>	Highly performing up to $100 \text{ W} \cdot \text{cm}^{-2}$ (HP)	Low transport distance on the ground
	High performances as heat spreaders [51] (Vapour chamber case)	
	High versatility	
<i>Thermosyphons</i>	Simplicity in construction	Instabilities (geyser effect)
		Favourable position mounting (condenser above the evaporator)
		Highly influenced by accelerations

Table 2.3: Pros and drawbacks comparison between passive cooling systems

understand, even in the following of this work, why a system can be retained and why another is not adapted for this particular application case.

Active single phase cooling systems are not, in general, able to maintain a constant temperature level during operation if the secondary side temperature changes as a function of time, unless such a kind of control system is added on the circuit. However, this kind of technology is today widely used, because of its simplicity, for electronics cooling purposes, so it is worthy of attention for comparison purposes. Two-phase active cooling systems are a rising technology, and in particular vapour compression cycle is an interesting solution that begins to be used in aeronautics field. Despite its performances, and its ability to lower the evaporator temperature below the cold source one, this technology is unfortunately at its early stages, and some problems, in particular related

to compressor's hydraulics, have to be solved. Moreover, to damp instabilities naturally related to this application field, the use of complex regulating systems is necessary.

The attention was also focused on passive two-phase cooling systems. In particular working principle of thermosyphons, heat pipes, loop heat pipes and capillary pumped loop (with particular attention to a new kind of gravity CPL) were introduced. Literature results were considered in terms of thermal resistance, transport distance, heat evacuation capability to understand which system is the most adapted for this particular application field.

Passive two-phase technologies began to be used for electronics cooling purpose since the thermal heat flux densities became too high and the air forced convection showed its limitations. Heat pipes are able to evacuate high heat fluxes densities, but heat transport capability is limited. They are not an interesting technology for this application case. Loop heat pipes (LHP) and capillary pumped loop (CPL) are worthy of attention, and in particular the CPLIP (Capillary Pumped Loop for Integrated Power) because of its ability to maintain a constant operating temperature to the evaporator whatever the cold source temperature.

With reference to active cooling systems, and considering only the heatsink, in the following chapter different "brand new" heat evacuation technologies, considering the heat transfer characteristics at the level of the hot source base plate, will be introduced and compared with the purpose to understand if one of them is worthy of attention to compete with passive two-phase technologies in terms of evaporator/hot source thermal and hydraulic performances.

Classic cold plates, micro and mini channels, porous media and metal foams, as well as jet impingement and spray cooling, will be analysed, independently from their systems and in their single and two-phase version.

Power electronics cooling: state of the art of heatsinks

In the previous chapter the attention was focused on the whole cooling system, to introduce the working principle of different kinds of cooling loops. Here, a different point of view is used, in fact, performances of a cooling loop change following the typology of the heatsink used. Over the last thirty years, many research teams have worked on the issue and different technologies have been continuously compared and studied. In general, it is not possible to argue that it exists a better solution than another, but the choice depends on necessity and performance requirements. A trade-off has to be found in most cases. Cooling system performances strongly depend on the ability to evacuate the required thermal load with the lower mass flow rate possible: in other words the HTC needs to be maximised. In fact, the higher the HTC, the lower the mass flow rate required and the higher the cooling system efficiency: the cooling system performances and its ability to maintain the temperature of the electronics components controlled depends on the performances of the heat sink itself. The latter is, in fact, the first stage where the thermal load is evacuated by electronics components to the coolant. Single-phase and some active two-phase cooling systems can be studied by decoupling the heatsink performances from the rest of the system. In this case, it is possible to analyse the behaviour of the heat sink, its performances and characteristics, independently from the nature and performances of the cold source or any other component in the loop. In the following, efforts have been made to classify heatsinks in two categories: direct cooling systems, for which the cooling fluid is directly in contact with the electronic baseplate; and indirect cooling systems where the coolant is confined in a separated circuit (no contact occurs between the working fluid and the electronic components in this case). In this chapter the most suitable heatsink configurations are analysed, the basic physics of the different technologies explained, and pros and drawbacks of each one underlined.

3.1 Direct cooling systems: jet impingement and spray cooling

As already explained in the previous chapter, direct cooling systems are characterised by the absence of a thermal resistance (material layer) between the device to be cooled and the coolant. However, the use of direct cooling technology is affordable only when the direct cooling convective thermal resistance is lower than the sum of all resistances related to an indirect cooling system [76]. In this work only jet impingement and spray cooling technologies will be analysed and no other direct cooling technologies, such as pool boiling¹, will be considered.

The line separating the spray cooling from the jet cooling technology is thin. However, both are characterised by a great complexity in heat transfer mechanisms and the governing phenomena are not fully known today. Some authors put spray cooling and jet impingement into different categories, while others (put them) in the same one [20]. However, it can be said that spray cooling represents an extension of impingement cooling concept [77]. The difference between the two systems essentially comes from the nature of the working fluid. In general, spray cooling systems use a gas/liquid mixture to assist the atomisation of the fluid when flowing within the atomiser (nozzle). In the case of jet impingement, only one-phase fluid (liquid or gas) is used and the heat transfer rate is strongly related to fluid velocity.

Spray cooling The mechanism of spray cooling is based on the principle of shattering the cooling fluid when passing into a very small orifice. A dispersion of fine droplets that impact the heated surface is so created. Depending on the surface temperature, droplets evaporate or form a liquid thin film able to remove, thanks to latent heat of evaporation in addition to conventional single phase heat removal mechanisms, a large amount of energy. In general, it has been observed that this technology is very attractive because of its capability of high heat flux removing (up to $10^3 \text{ W}\cdot\text{cm}^{-2}$), with extremely high overall convective Heat Transfer Coefficients (HTC), higher than $5 \times 10^5 \text{ W}\cdot\text{m}^{-2}\cdot\text{K}^{-1}$. It is so able to maintain a uniform temperature field on the cooled surface (if an array is used) with pressure drop values up to 250 kPa, but requiring high MFR (up to $44.2 \text{ Liters}\cdot\text{min}^{-1}$) [20]. This technology is characterised by the absence of any kind of thermal resistance, such as a solid wall, and the suppression of the thermal grease layer between the components and the cooling fluid on the base of IGBTs [78].

The operating circuit, in a closed loop, is the same presented in figure 2.2, with the

¹Pool boiling will be not considered in the context of the present study because of the difficulties related to the integration of such technology in the aircraft environment.

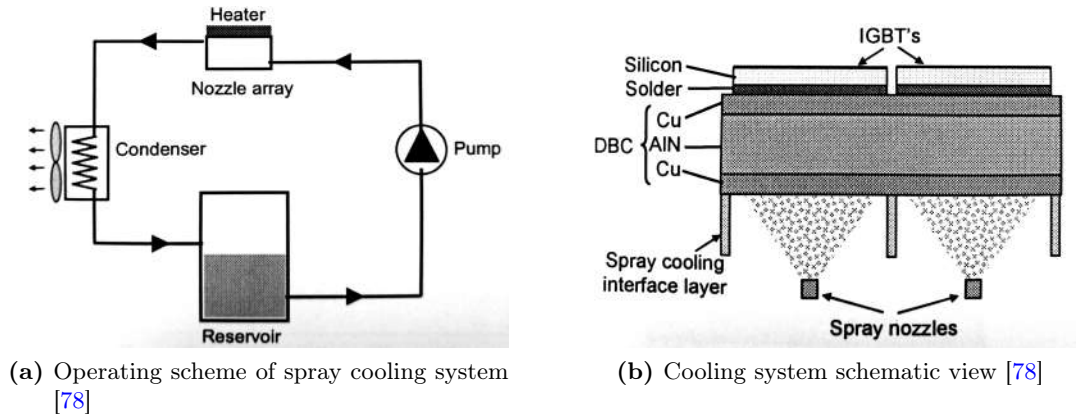


Figure 3.1: Spray cooling

addition (of a series) of filters to avoid fouling, and consequently, obstruction of the very small orifices. In figure 3.1a and in Fig. 3.1b a simplified operating scheme of the loop and a schematic operating principle of a spray cooling heatsink are respectively reported.

The pump has to be powerful enough to ensure the necessary pressure at the inlet of the nozzles. In fact, the cooling efficiency of the system strongly depends on droplet dimensions: the lower the droplet diameter, the higher the system performances. Lower droplets diameter requires higher pressure difference between the nozzle inlet and outlet. Pressure is not the only parameter on which droplet size depends. In fact, it also depends on the mass flow rate and nozzle geometry. In general, there is a unique relation between the required inlet to outlet nozzle pressure difference, and the necessary mass flow rate to reach the desired droplet dimensions. As well as droplet diameter, other parameters influencing the cooling efficiency are droplet distribution and velocity, impact angle and roughness of impacting surface.

Wang *et al.* [79] carried out a study on the influence of different surface characteristics and different additives in the cooling fluid, using different heating powers. By comparing drilled, finned and a combination of both surface geometries, they concluded that combined surface is the best trade-off to obtain a good heat transfer efficiency. To avoid formation of stagnation regions that can occur under the hollow cone spray nozzle, and so to increase the heat transfer rate, it is possible to increase the inclination angle. Kim *et al.* [8] reported that it exists an optimal angle between the impinging surface and the spray direction that should not exceed the value of 40° . Lin *et al.* [80] performed experiments to study the behaviour of a spray cooling pattern on an up to $490 \text{ W} \cdot \text{cm}^{-2}$ heated source equipped by lateral walls. They observed that the droplets impinge the hot surface and “splash” on the lateral sides. The splashed liquid is restricted by the

walls and forced to rebound the space surrounding the sprays. They concluded that the interaction between the spray and the surrounding fluid is stronger in the case of multiple nozzles, making a more uniform HTC.

Single and two-phase heat transfer mechanisms may take place depending on temperature of the wall to be cooled and wall heat flux [8]. In figure 3.2 an example of a typical spray cooling curve is reported. As reported by Kim [8], it is possible to divide the curve in two parts: the first one is characterised by a linear dependency between the wall temperature and the heat flux. As the latter increases, phase change occurs and becomes more important until dry-out outside of the impact area.

Because of the contact between the coolant fluid and the electronic component, this particular technology needs the use dielectric fluids. One assists to a deterioration of cooling system performances [20] due to the lower thermal conductivity, specific heat and latent heat of vaporisation of this kind of fluids.

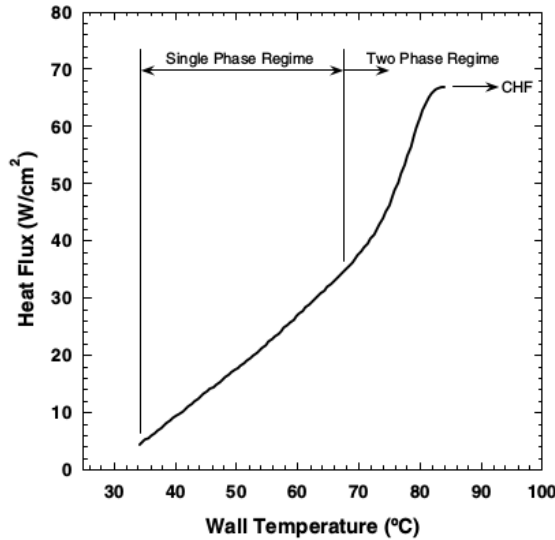


Figure 3.2: Typical spray cooling curve [8]

Jet impingement Jet impingement generally uses air or liquid as working fluids, so forced convection is the main heat transfer mechanism. Even if thermal properties make of air a less performing fluid, if compared to liquids, its high velocity in the impinging zone determines very high HTCs, that tend to quickly decrease out of this zone [20]. Molana and Banooni [81] divide the jet dynamics in three zones. The first one, called “free jet zone”, is situated from the outlet of the nozzle until the target. The second one is where a deceleration of the impinging fluid occurs due to the interaction between

the fluid and the heated solid zone. The third zone is where the fluid wets the target and flows on it. The dynamics of jet impingement do not change so much if a gas or a liquid are used as working fluids. The main difference is due to the amount of fluid that does not participate to the heat transfer process because of the “loss” of liquid after the impingement. In this case, in fact, droplets splat and do not participate to the heat transfer process, lowering the heat transfer performances [81]. Comparing spray cooling, with no phase change, and jet impingement, thermal performances of both technologies are quite different. Oliphant *et al.* [77] performed a comparison between the two technologies in single phase configuration concluding that, for the same heat transfer rate than jet impingement, the liquid mass flow rate of “non-boiling” spray impingement is one order of magnitude lower. According to them, very different heat transfer mechanisms occur between single-phase spray cooling and jet impingement. Different boundary layer thicknesses were recorded. In fact, if liquid jet impingement forms a “well defined” boundary layer that rapidly moves outwards the heated surface, the spray-impingement boundary layer thickness is definitely lower (0.1 – 0.5 mm for liquid jet impingement and 10 – 30 μm for single-phase spray cooling) [77]. However, it has been found that jet impingement is characterised by the highest heat transfer coefficient for single-phase heat exchange, as reported by Whelan and Robinson [82]. They found HTC values up to almost $50 \text{ kW} \cdot \text{m}^{-2} \cdot \text{K}^{-1}$ using high mass flow rate (over than $20 \text{ Liters} \cdot \text{s}^{-1}$) and with pressure drop up to 70 kPa (for the highest mass flow rate). Despite the high pressure drop registered, they concluded that the performance benefits, in terms of HTC, are higher than the penalty introduced by high pressure losses. Even if air is used as working fluid, this technology is able to reach high performances due to high Nusselt numbers deriving by high Reynolds numbers (one more time the velocity is the main factor for HTC increasing) [83]. Guo *et al.* [83] numerically and experimentally studied the transient behaviour of a 120 mm-diameter circular stainless steel plate, cooled by an air-jet, to find the influence of the Reynolds number on the heat transfer. They obviously found that the higher the Re, the higher the Nu number and that the latter increases as a function of time (starting from zero at time 0 s) until the assessment that occurred after almost 50 s.

Both for jet impingement and spray cooling, the use of an array of nozzles [84] or a coupling with other solutions, such as the combination with a transversal air flow [85], is suitable to have a more uniform heat transfer coefficient and so to obtain better performances. Ionic wind, for example, is used in addition to jet impingement for this purpose. This technology uses an interaction between ions and neutral molecules to perturb the hydrodynamic boundary layer and to enhance the heat transfer coefficient of

an existing flow. The interaction between ions and neutral molecules is called ion-drag, and is defined using a body force equation consisting of Coulombic force (force due to permittivity gradient and electrostriction force). In other words, a corona discharge is used to generate ions and to perturb the higher boundary layer [86].

Worth of attention is the work of Oliveira and Barbosa [76]. They have successfully inserted this kind of technology into a vapour compression cycle. By using R-134a as working fluid they were able to evacuate up to 160 W from a 6.36 cm² heated surface ($\phi \simeq 25 \text{ W} \cdot \text{cm}^{-2}$), maintaining the temperature controlled up to 35 °C and reaching HTC values up to 14 kW·m⁻²·K⁻¹. Oliveira and Barbosa moreover exploited the influence of the reservoir (saturation temperature) on the overall performances of their system. They concluded that the increase of saturation temperature lowers the overall performances of the system. This is due to an increase of the compressor electrical consumption and to lower condenser performances due to a reduction of the subcooling rate; while, it almost not impacts the temperature of the cooled surface.

Despite their performances, the drawbacks related to their physics and working principle represent a limiting factor to the use of such cooling technologies. In particular, in the case of jet impingement, high liquid or air velocities are necessary to evacuate the heat, so corrosion is one of the main limiting factor. Integration problems affect these technologies in this application field. For example, the use of a collector tank, necessary to fetch the liquid after the impinging on the surface to be cooled, could not be a practical way for HASTECS application case.

3.2 Indirect cooling systems

Indirect cooling systems are characterised by the presence of a “solid wall” between the working fluid and the electronic baseplate. This leads to the presence of a supplementary thermal resistance between them. In the following, three different technologies are introduced. Starting from the most classical one, the cold plate, for which only single-phase heat transfer is here considered, microchannels and forced convection into porous media are introduced considering both single and two-phase heat transfer mechanisms for the latter.

3.2.1 Cold plate

Cold plate is one of the most simple existing technologies. It is composed of a simple tube or channel, directly mounted under the plate to be cooled, in which the coolant flows. Its simplicity and low cost makes of it one of the most used technologies in liquid



Figure 3.3: Cold plate for electronic cooling [9]

cooling of electronic equipments. In fig. 3.3 an example of cold plate is reported.

Sensible heat is used to evacuate the thermal load from the plate. So, the fluid enters into the tube below the base plate (at temperature T_{ho}) and it leaves the heat sink at higher temperature (T_{hi})²:

$$Q_{th} = \dot{m}_l c_{pl} (T_{ho} - T_{hi}) \quad (3.1)$$

Different fluids can be used depending on environment, thermal performance and mass requirements. In order to achieve a good trade-off between performances, compatibility (between fluid and tube material) and system mass, Sakanova *et al.* [9] experimentally and numerically investigated thermal performances of different fluids, according to mass requirement, of a cold plate to be used for high power density electronics converters in “future” aircrafts (see Fig. 3.4). They studied thermal and hydraulic performances of oil, fuel and water, by changing the number of fluid passages in the plate, and to evacuate an amount of thermal losses between 0.5 and 2% of the 50 kW_e-power converters ($0.25 \leq Q_{th} \leq 1 \text{ kW}_{th}$). On one hand, they concluded that water is the best choice because of its thermal performances, but, on the other hand, this fluid is not used anywhere else for this purpose on board, so the additional required weight determines a mass penalty for the overall system. Pressure drops related to the use of oil are too high, “unless a less viscous oil is used” and the thermal resistance due to the use of this fluid does not allow its application: it was not able to meet the specifications regarding the maximum junction temperature requirements of power modules. They concluded that fuel could be the best trade-off between thermal and hydraulic performances in such applications [9].

The major problem of cold plate heatsinks is the strong dependency among the amount of heat to be extracted, the mass flow rate and the cold plate-inlet-temperature, as also

²The same notation of Fig. 2.3 is used.

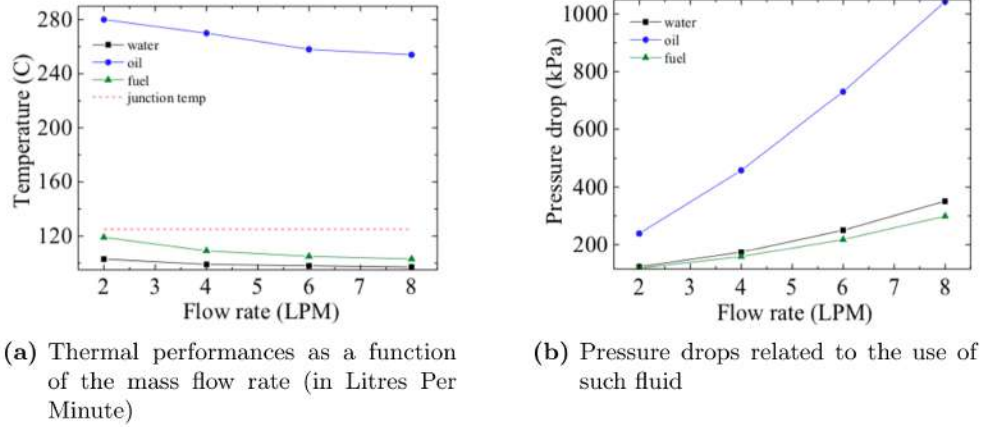


Figure 3.4: Thermal and hydraulic performances of water, fuel and oil [9]

underlined by Douchet *et al.* [87]. Obviously, because of upper and lower limits of working fluid temperature, to avoid icing or evaporation, the higher is the heat flux to be extracted, the higher is the required mass flow rate (eq. 3.1). Moreover, heat sink temperature is also dependent on the mass flow rate, so a some kind of regulation system, such as regulating valves are necessary to maintain a constant temperature if the cold source temperature changes during operations (see sec. 1.3).

3.2.2 Mini and Microchannels

Single-phase microchannels This is one of the most promising technology, and it is the direct concurrent of micro heat pipes arrays, for high heat flux density evacuation. Microchannels heat sinks are formed by a very low thermal-resistance-material traversed by a series of parallel channels which hydraulic diameter is lower or equal than 1 mm. In figure 3.5a, and 3.5b, are respectively shown a typical microchannel heatsink and a typical example of microchannels micrography.

Different materials may be used for microchannels, but silicon is from far one of the most used one. Colgan *et al.* [23], for example, used a silicon heat sink with water as working fluid applying a heat flux density of $300 \text{ W} \cdot \text{cm}^{-2}$. They demonstrated that, despite the high pressure drop induced by microchannels, it is possible to cool a chip with very high performances and maintaining a more or less constant temperature on the baseplate of the electronic components!

Concerning the physics of such system, actually there are not generally and accepted heat transfer models and physics laws to be applied in this field of thermo-fluid-dynamics, and the results between different authors are sometimes strongly contradictory [88]!

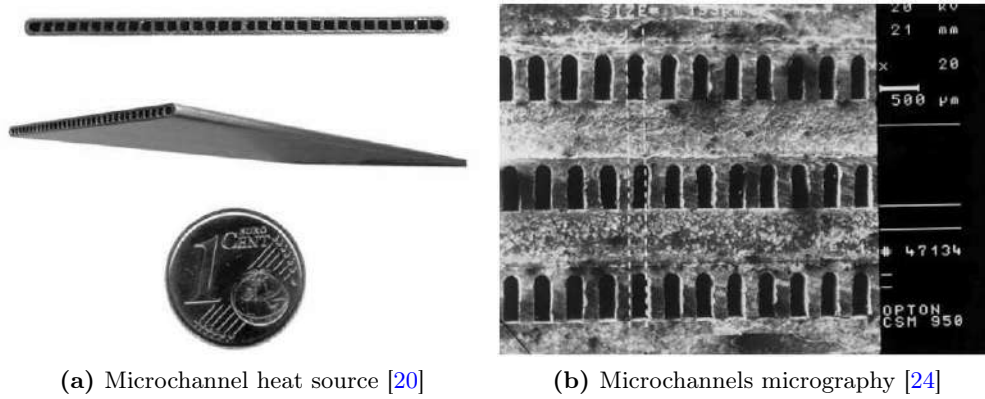


Figure 3.5: Microchannels

For example, according to Avramenko [89], in the case of very small hydraulic diameters of the channels, the behaviour of the fluid cannot be modelled by using the classical laws of the fluid *contuum*. This is essentially due to the reduced length scale of the flow. Fluid flow in microchannel is regulated by “sophisticated” fluid mechanisms and thermal processes that take part on the fluid-solid walls interface. Nevertheless, researches made in this field demonstrate that classical relations for Nusselt number calculations remain appropriate and may give accurate results [24]. Grohamann [88] made an experimental and theoretical research, validated by the application of different correlations, on single and two-phase flows in microchannels. He observed that, regarding single-phase heat exchange, there are no differences between the heat transfer mechanisms between micro and macro scale tubes. The increase of the heat transfer coefficient is given by a greater influence of rugosity on the channel surface. The smaller the dimension of the channel, the higher the influence of rugosity, because of the greater perturbation in the fluid-dynamics length scales. On the contrary, Alm *et al.* [90], by comparing results of classical heat exchanger theory with experimental ones, obtained that, on a ceramic microchannels heat exchanger, classical correlations underestimate the heat transfer coefficient value. At the same manner, while applying the *LMTD* method to predict the heat transfer rate, Koyama and Asako [91] found a good agreement between experimental and theoretical results. Experimental pressure drop measurements were almost 10 times higher than those obtained by applying classical correlations.

However, thermal performances of microchannels are undeniable. In fact, they are characterised by very high exchange-surface per volume ratio, and very high volumetric heat transfer coefficients, up to $10^8 \text{ W} \cdot \text{m}^{-3} \cdot \text{K}^{-1}$, when compared to classical-heat exchangers-values (around $100 \text{ W} \cdot \text{m}^{-3} \cdot \text{K}^{-1}$) [24]. The volumetric heat transfer coefficient, K_V , is

based on the volume of the heat exchanger, V , the heat exchanger correction factor, ψ , the heat power and logarithmic mean temperature difference respectively, Q and ΔT_{lm} . It is calculated as reported in eq. (3.2) [24]:

$$K_V = \frac{Q}{V \psi \Delta T_{\text{lm}}} \quad (3.2)$$

The high volumetric heat transfer coefficient value is not only due to the particular flow characteristics, but also to the high aspect ratio in the transversal section. This allows the solid walls to behave as fins. Heat transfer coefficient up to $22 \text{ kW} \cdot \text{m}^{-2} \cdot \text{K}^{-1}$ can be reached, even if pressure drops may reach values up to 7 bar for a 12-millimeters-long heat exchanger [90] (it has to be noted that pressure drop is strongly related to channels transversal section dimensions, material and construction process as reported by some authors, [90, 91]). This technology is being used in electronic chips cooling, because of its compactness and ease-to-integrate property. Zhang *et al.* [92] used microchannels to study the cooling of a $12 \times 12 \text{ mm}^2$ chip footprint. By applying a heat flux up to $136 \text{ W} \cdot \text{cm}^{-2}$, they obtained a very low value of thermal resistance ($0.44 \text{ K} \cdot \text{W}^{-1}$). They also found very high pressure drop: increase of mass flow rate of about 50% leads to increase of pressure drop value of about 120%, while decrease of thermal resistance is not significative (about 6%). Agostini *et al.* [20] reported Genert *et al.*'s. system, developed to cool desktop computers, able to operate below 0°C evacuating a thermal heat flux up to $250 \text{ W} \cdot \text{cm}^{-2}$. By using this technology, Ljubisa *et al.* [93] were able to maintain a constant IGBT junction temperature at 52°C and a diode junction temperature at 75°C .

Despite thermal performances, extremely high pumping powers are required [20], limiting the use of this technology for the application field considered in this study.

Two-phase microchannels In the latest few years, two-phase flows studies for microchannels evolved, and then heat extraction capability has exceeded $100 \text{ W} \cdot \text{cm}^{-2}$ and actually is going to achieve $300 - 500 \text{ W} \cdot \text{cm}^{-2}$. This technology, unfortunately, and more than single-phase case, is particularly affected by contradictory models describing the physical phenomena. Many authors [20, 94, 95] agree on the fact that the flow boiling models, related to macro-scale, are not adequate to extrapolate the phenomenon in micro-scales. So, this kind of micro-heat exchangers technology is affected by a lack of prediction, design and optimisation methods. For example, according to Agostini *et al.* [20], the heat transfer coefficient is strongly dependent on heat flux and vapour quality, while Yen *et al.* [94] and Grohamann [88] agree on the fact that it is weakly dependent on vapour quality. However, heat flux is the most influential parameter for heat transfer coefficient: a too low value of the latter could cause instabilities during the transition

from single to two-phase flow [88]. Instabilities have been also observed by Agostini and Bontemps [96] when vapour quality x becomes higher than 0.4. In this case, a decreasing value of heat transfer coefficient has been observed due to intermittent dry-out. During this phenomenon the wall is periodically dried and re-wetted because of the passage of liquid slugs: the liquid layer in correspondence of the tube wall is thinned down by vapour bubble passage. This high frequency phenomenon occurs before reaching the CHF. The heat transfer coefficient decreases as the vapour quality increases, then remains constant towards vapour quality $x = 1$. They also suggest that, for high mass flow rates (MFR), the probability for dry-out to occur is higher because of the higher liquid film that is dragged out from the walls. This behaviour is obviously the opposite than the one observed in traditional/small-size tubes where HTC increases while wall heat flux (WHF) and MFR increase.

Beyond all the problems related to the flow boiling in microchannels, their use in electronic devices cooling is very performing. Actually, a maximum heat flux of $350 \text{ W}\cdot\text{cm}^{-2}$ has been achieved with a more than one order of magnitude decreasing pressure drop value if compared with single phase microchannels technology.

3.2.3 Porous media and metal foams

Porous media and metal foams are an alternative to microchannels, especially for high thermal heat flux evacuations. Both are characterised by porosity ε (empty to total volume ratio) and mean particle size diameter.

Metal foams are characterised by a very high heat transfer surface due to the presence of the “mesh”, generally made of high conductivity material. The fluid is subject to a tortuous path, in the foam structure, that increases the wetted surface and so the “interstitial” heat transfer. An example of foam is reported in Fig. 3.6, while in Fig. 3.7, micrographs of sintered porous medium, metal foam and compressed metal foam are reported.

The presence of the mesh in porous media not only increases the heat transfer surface, if compared to that of “only fluid”, but also the effective thermal conductivity of the medium itself.

This phenomenon leads to the homogenisation of temperature field on the heated surface [98]. Different thermal behaviours have been observed between sintered and non-sintered porous media. First of all, spreading and heat diffusion in sintered and non-sintered materials are quite different. It is mainly dependent on the solid-to-solid and solid-to-liquid interfaces between heatsink walls and porous medium, and among porous medium/heatsink walls and working fluid. In general sintered meshes are characterised

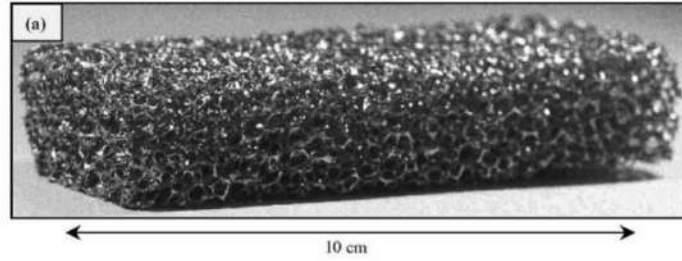
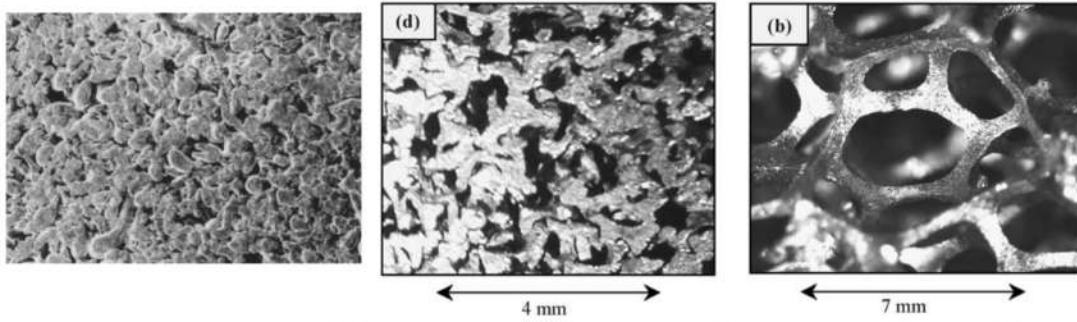


Figure 3.6: Metal foam example [10]



(a) Sintered porous medium [97] (b) Compressed metal foam [10] (c) Metal foam [10]

Figure 3.7: Micrographs of sintered porous medium (a), compressed metal foam (b) and metal foam (c)

by a higher spreading property. It is mainly due to a “densified network” of solid particles, due to sintering process, and to a higher contact surface with the heatsink walls: lower void fraction. In general, the greater the contact surface between the porous structure and the heat source wall, the smaller the contact thermal resistance. So, heat exchange becomes more efficient [99]. Hetsroni *et al.* [97] studied a porous heat sink characterised by a 32% porosity and a pores average diameter of $20\ \mu\text{m}$. Using water as working fluid, they evacuated a heat flux density up to $600\ \text{W}\cdot\text{cm}^{-2}$ with a bulk-to-wall temperature difference of $55\ \text{K}$ ³. By making a comparison between their *Aluminium* foam and a sintered porous material, they found that sintered material is more performing than the foam, because of a “better” contact between particles in the media. Zhang *et al.* [100] made an experimental study on the influence of porosity on heat exchanges in copper foam materials. They studied copper foams with porosities from 60% to 90% and pore densities ranging from 60 PPI (pores per inch) to 100 PPI. All the foams with porosity

³Even though the very high thermal heat flux densities, all the experiments here reported have been done by using reduced heating surfaces, in the millimetre magnitude order. In this case a $5 \times 2\ \text{mm}^2$ heating surface was used.

between 80 and 90% and pore density in the range 60 – 100 PPI, were not sintered. They concluded that thermal resistance reduction is due to the particular structure and composition of the porous medium. In table 3.1 a comparison between two porous media characteristics and their heat transfer capabilities is reported⁴.

Porous medium typology	Porosity	Heat sink material	Thermal resistance [K·cm ² ·W ⁻¹]	$\Delta P/\Delta L$ [MPa·m ⁻¹]	Q_{max} [W·cm ⁻²]
Sintered particle [24]	47%	Copper	0.166 ÷ 0.752	32	-
Sintered particle [99]	46%	Bronze	0.667	0.74	-
Sintered particle [97]	32%	Stainless Steel	0.092	232	600
Foam [100]	80%	Copper	0.134	2	41.7
Compressed Foam [10]	67%	Aluminium alloy	0.463	7.2	68.8

Table 3.1: Comparison of different porous media characteristics [20]

On one hand, very high heat flux densities have been evacuated with this cooling technology, but, on the other hand, awfully high pressure drops characterise it. Boomsma *et al.* [10] performed an experimental research on metal foam heat exchanger performances. Despite the high heat flux density evacuation capability, $\simeq 69 \text{ W}\cdot\text{cm}^{-2}$ (1100 W on a $4 \times 4 \text{ cm}^2$ surface), they obtained high pressure drop values: over $70 \text{ bar}\cdot\text{m}^{-1}$ in some cases. Many authors took into account pressure drop and made some researches about this specific topic. Jiang *et al.* [24] compared the performances of microchannel heat exchangers with sintered porous media ones. By taking into account both thermal and hydraulic performances, they concluded that, despite the higher thermal performances of porous media heat exchangers, pressure drops of microchannels heat exchanger are lower. Using the same mass flow rate in both technologies, they observed that, for a ratio of 2.25 between the volumetric heat transfer coefficients of porous media and microchannels, respectively, the corresponding porous-media-to-microchannel pressure drop ratio was 5. They concluded that, despite the strong gap existing between the two technologies in terms heat exchange performances, it should be better to use microchannels because of their lower pressure drop.

By considering two-phase heat exchange mechanism applied to this particular technology, it was observed that despite the lower mass flow rates necessary to evacuate the

⁴It has to be underlined that the pressure drop is a function of the working fluid, the mass flow rate, the porous typology and so on.

thermal load, pressure drops do not decrease. Peterson *et al.* [101] conducted a study on two-phase porous channels. They found, at constant liquid velocity, increasing pressure drop consequent to increasing heat flux. This was essentially due to the increase of vapour quality. The highest pressure drop was obviously related to the lowest particle diameter in the wick. They observed the pressure drop difference between an empty channel and a wick equipped one (supplied at constant inlet liquid velocity and constant heat flux) to be up to two orders of magnitude. According to Peterson *et al.*, Chen *et al.* [102] found, at constant liquid velocity, an increase in pressure drop consequent to a reduction of mean particle diameter and to an increase of thermal heat flux (at constant flow rate and heat flux).

3.3 Conclusion

In this chapter, the problem related to the extraction of heat load from the heatsink has been dealt. Only technologies related to active cooling systems have been here introduced. In fact, for these particular cooling techniques it is possible to split the hot from the cold side of the cooling system and to analyse the behaviour of the heat sink independently from the rest of the circuit. Here, only technologies adapted for HASTECS specifications were introduced and analysed. Particular attention was paid to micro and minichannels, porous media and metal foams. Even if for the sake of completeness jet impingement and spray cooling have been here introduced, this particular technologies, despite the very high thermal and hydraulic performances have not been retained. The main reason of the exclusion of jet impingement technology, whatever its form, is mainly related to integration difficulties and a such kind of corrosion. In fact, in this case, it necessary to use a collection tank to collect the fluid. This is not a practical choice for the problem we are facing in this work.

Cold plate heatsink is up to now the most used technology, even in active two-phase/vapour compression technology configurations, but its limitations in heat transfer coefficient and strong dependence of thermal performances on mass flow rate, do not make of it a suitable technology in its single-phase configuration.

Microchannels and metal foams represent the best solution to be used in active cooling system configuration. In fact, they allow high heat transfer coefficients and almost independence of thermal performance on mass flow rate. Unlike, the high pressure drops can represent a strong limitation. It has to be also considered that the higher pressure drops, in particular for microchannels technology, are strongly related to the material and production processes. These technologies give the best in active-two-phase config-

uration, where pressure drop are up to two orders of magnitude lower than single-phase configuration. In such case heat transfer coefficient is higher.

Sintered porous media are not suitable neither in single and in two-phase configuration. Pressure drop are quite high and, despite heatsink thermal performances, the required pumping power should be extremely high. However, their use is necessary in the case of two-phase passive cooling system, because of capillarity effect related to the use of sintered porous media in two-phase systems.

In the following chapter, a comparison of just introduced heat sink technologies will be done, in terms of heat evacuation capability and heat transfer coefficient, also observing the evolution of such technology during the years. Passive two-phase cooling systems will be compared to show the current state of the art.

To finally choose the most adapted solution in context of HASTECS project, the mass of a single-phase and of an active two-phase cooling systems, both equipped with a cold plate, calculated on the basis of a first approximation design, will be compared with a Capillary Pumped Loop for Integrated Power, CPLIP.

Technology	Pro	Drawback
<i>Single-phase Microchannel</i>	High cooling performance	Pressure drops up to $22 \text{ Mpa} \cdot \text{m}^{-1}$
		High temperature gradients along the plate (if compared with two-phase MC) [20]
<i>Two-phase Microchannel</i>	Low required Mass Flow Rate [20]	Back-flow and instabilities
	High HTC and increasing with temperature	Lacking in thermal exchange mechanisms
	Low pressure drop if compared with single-phase MC [20]	
<i>Cold Plate</i>	High simplicity	Junction temperature strongly dependent on cold source temperature
		High dependency on MFR
		Weight and size strongly dependent on working fluid properties
<i>Porous media</i>	High cooling performance	Pressure drops up to up to $227 \text{ MPa} \cdot \text{m}^{-1}$ [97]. Required very high pump power! [24]
	Very good temperature distribution	
	Heat transfer surface extremely extended	
	Very low thermal resistance especially in sintered materials	Performances highly dependent on CHF [103]
	Heat transfer enhancement	
	Smaller wall super-heats than microchannels	
<i>Jet impingement/Spray cooling</i>	Very high heat transfer coefficient	Lower performances of dielectric fluids [20]
	Very high heat removal capacity	Necessity of a compatibility study between the fluid and the electronic components
	Very low temperature gradients in on heat source	Non-uniform HTC if one jet is used
	No thermal interfaces required	Erosion
		Lack of physical model for Heat Transfer prediction

Table 3.2: Active cooling systems pro & drawbacks

Technology choice

4.1 Comparison of high performance cooling systems

In the previous chapters the most promising cooling technologies have been studied to understand their operating principles and to analyse their main pros and drawbacks. The purpose is not only to research the best lightweight available solution to evacuate the thermal load, but also the one able to ensure the temperature requirements at junction level.

Thermal performances All analysed systems are able to evacuate high heat flux densities, ensuring good thermal performances and high HTC. Some of them are today successfully used¹.

The number of studies has incredibly increased during the latest thirty years, pushed by a continuous increase of the electrical power and the miniaturisation of electronic components. Observing this evolution as a function of time, according to figures 4.1a and 4.1b, it may be noticed that either active and passive technologies are characterised by the same trend and the performances increase during the time.

By analysing literature data, in some cases great importance is given to heat flux density (Fig. 4.1a) and low thermal powers are often applied to small heat transfer surface areas (in the order of 1 mm^2). In other cases, the attention is focused on the total heat power to be evacuated (Fig. 4.1b), but not considering the thermal power per surface unit. The way of presenting results is after all due to the purpose of the single study: — the end justifies the means —. For example, the majority of the studies related to active techniques (jet impingement/spray cooling, microchannels and porous media/ metal foams) are focused on heat flux density. This is maybe related to small dimensions of the chips mounted on the heatsinks, or even to limit the pressure drop on the hot side and consequently the required pumping power. No pumps are required in the case of passive cooling systems. Performances of a given capillary driven technology

¹Let's mention heat pipes used in smart devices and computer/server chips cooling because of their compactness and adaptability (see bendable FPHP), for example.

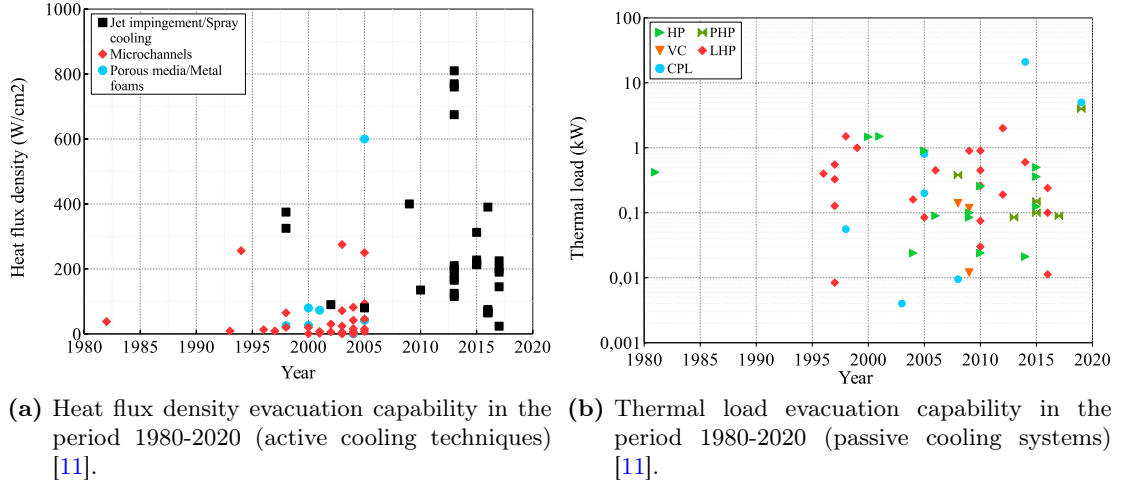


Figure 4.1: Historical trend of heat flux density and thermal evacuation capability for active and passive technologies.

are strictly related to capillary pressure head of the porous wick and so to the heat transferred and the transport distance. Larger evaporators may be used, sometimes in the order of tens centimetres. In those cases, even if pretty high thermal powers are applied to the evaporator, the thermal-power to surface ratio decreases.

Therefore, comparing the results related to a given technology, significative variations may be noticed depending on the points of view. In Fig. 4.2, the highest heat flux density and the highest thermal load related to each active cooling technique are reported for comparison purposes. Considering for example the porous heatsink, if the heat flux density is used to evaluate its performances, Hetsroni *et al.* [97] reached the best results (evacuating about $600 \text{ W} \cdot \text{cm}^{-2}$, but using a quite small thermal load). If the thermal load is considered instead, the best results are related to the work of Chen *et al.* [102] who evacuated 0.4 kW , but obtaining a heat flux density one order of magnitude lower ($80 \text{ W} \cdot \text{cm}^{-2}$) than Hetsroni *et al.* Faulkner *et al.* [104] evacuated $275 \text{ W} \cdot \text{cm}^{-2}$ using microchannels, but the highest thermal load, evacuated by Lazarek and Black [105], was 11.5 kW . The latter corresponds to a heat flux density of $38 \text{ W} \cdot \text{cm}^{-2}$. At the same way, considering jet impingement, the highest heat flux density evacuated by Zhang *et al.* [106] was $810 \text{ W} \cdot \text{cm}^{-2}$, corresponding to a total thermal load of 1045 W , using water as working fluid. This result does not match with the most performing technology, measured using the thermal load. In fact, Ortiz and Gonzalez [107] evacuated a total thermal power of almost 60 kW , obtaining less than one-half of Zhang's heat flux density ($375 \text{ W} \cdot \text{cm}^{-2}$) and using the same working fluid.

In fig. 4.3, heat transfer evacuation capability of most researched passive technologies

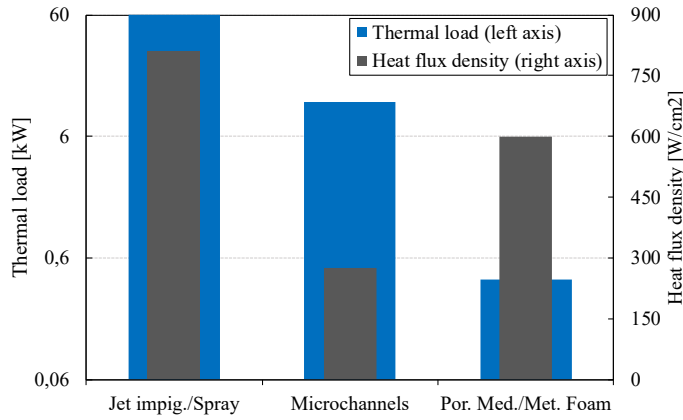


Figure 4.2: Maximal total thermal load and heat flux density histogram of active cooling techniques.

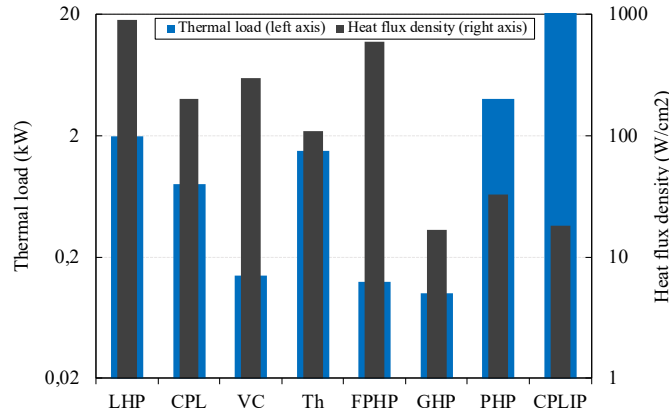


Figure 4.3: Maximal total thermal load and heat flux density histogram of passive cooling systems. [11].

is reported. The solution presented by Maydanik *et al.* [108] is worth of attention. He presented an experimental research on a flat plate evaporator LHP heated with two different heaters (one of 9 cm^2 and another of 1 cm^2) on which the heat load has been varied from 5 to 900 W. He reached a maximal evaporator temperature of 275°C applying the highest thermal load on the smallest heater surface. Because of the spreading effect related to the use of the same evaporator, whatever the heater dimension, he registered a maximal heat flux density of $900 \text{ W}\cdot\text{cm}^{-2}$. This result does not match on the thermal load side. In this case, the highest thermal load evacuated was that of Kang in 2012 [109]: about 2 kW. The same differences have been found analysing CPL's literature data. Meyer *et al.* [110] evacuated a heat flux density of $200 \text{ W}\cdot\text{cm}^{-2}$ using a heat power of just

4 W, but the highest power evacuation observed is related to a CPL for Integrated Power (CPLIP), characterised by a theoretical thermal load of 21 kW in railway application field [48]. In figure 4.4 equivalent HTC against heat power evacuation capability for such technologies is reported. The same results together with other system characteristics (thermal load, thermal power, transport distance etc.), resulting from literature data, are reported in table 4.1.

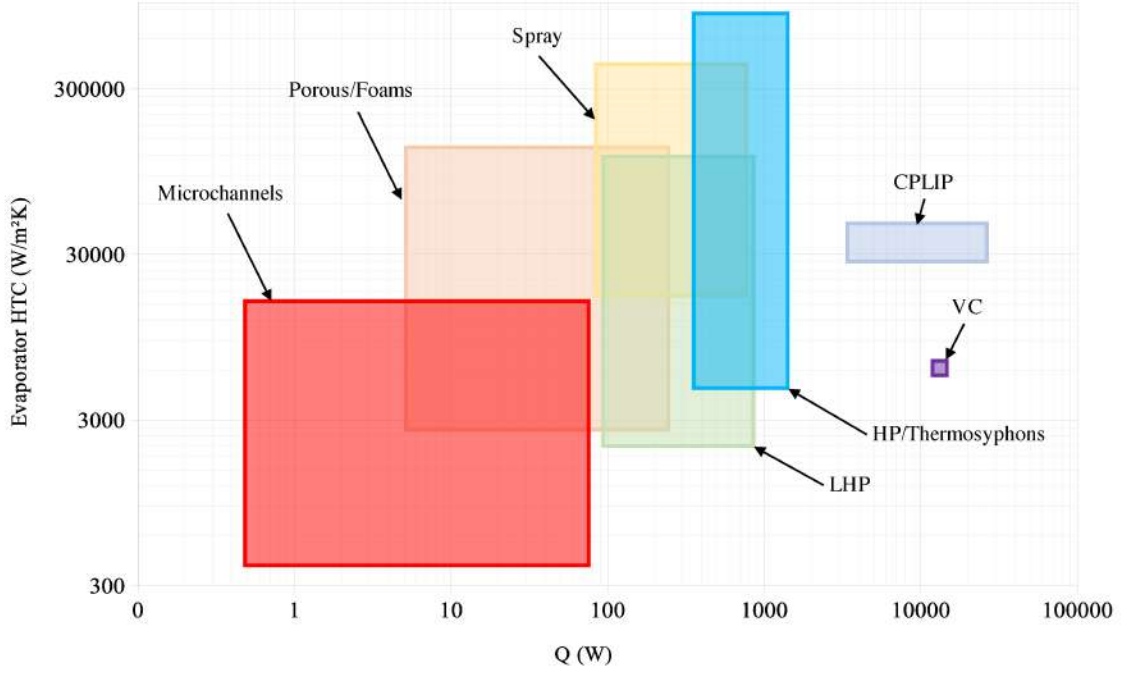


Figure 4.4: Technology comparison [11]

Transport distance Observing table 4.1 it may be noticed that active cooling systems are related to pressure drops, while passive ones are related to transport distance L [m]. Either in active and passive cooling systems, pressure drops are obviously dependent, *inter alia*, on the circuit length. On one hand, for active ones, pumping power can be increased according to overall pressure drop in the circuit, and without changing the thermal characteristics of the heatsink. On the other hand, for passive cooling systems, the loop length is limited by capillary pressure head or gravity pressure drop. In Fig. 4.5 the heat power as a function of transport length is reported for such passive technologies. From there one can notice in a more clear way that some technologies, like CPL or LHP, due to higher heat transport length, are more adapted than others for power electronics cooling in aeronautics field: the higher transport distance, the higher the flexibility of such solution.

Technology	\dot{Q}_{max} [W · cm ⁻²]	HTC_{eq} [W · m ⁻² K ⁻¹]	Pressure drop [MPa · m ⁻¹]	L [m]
<i>Single-phase HT in microchannels</i> [23]	up to 300	10 000 - 100 000	1.8	-
<i>Single-phase HT in porous media</i> [97]	up to 600	25 000 - 100 000	232	-
<i>Two-phase HT in microchannels</i> [Kosar et al.][20]	up to 250	60 000 - 150 000	0.309	-
<i>Two-phase HT in porous media</i> [102]	up to 80	40 000 - 10 000	2.2	-
<i>Jet impingement</i> [20]	up to 1820	300 000	0.241	-
<i>Mini vapour cycle</i> [45]	76	25	-	-
<i>Ionic wind enhancement</i> [86]	30	400	-	-
<i>Cold-plate</i> [9]	7.46	2750	-	-
<i>LHP</i> [72, 108]	130 - 900	30 000	-	30
<i>CPL</i> [75]	100	-	-	2 - 5
<i>CPLIP</i> [48, 75]	20 ÷ 40	27 000	-	up to 10
<i>HP</i>	100	30 000	-	up to 0.5

Table 4.1: Main characteristics of the cooling systems

4.1.1 Technology screening

The best performing technology does not exist, but the choice of a system depends on the particular requirements of the issue to be solved. For the specifications assigned to this work package in the frame of HASTECS project, a good candidate solution should:

1. be as lightweight as possible;
2. ensure the lowest energy consumption for its operations;
3. ensure the highest cooling performances;
4. be easily integrable;
5. ensure the highest transport length possible (in the case of passive cooling systems)

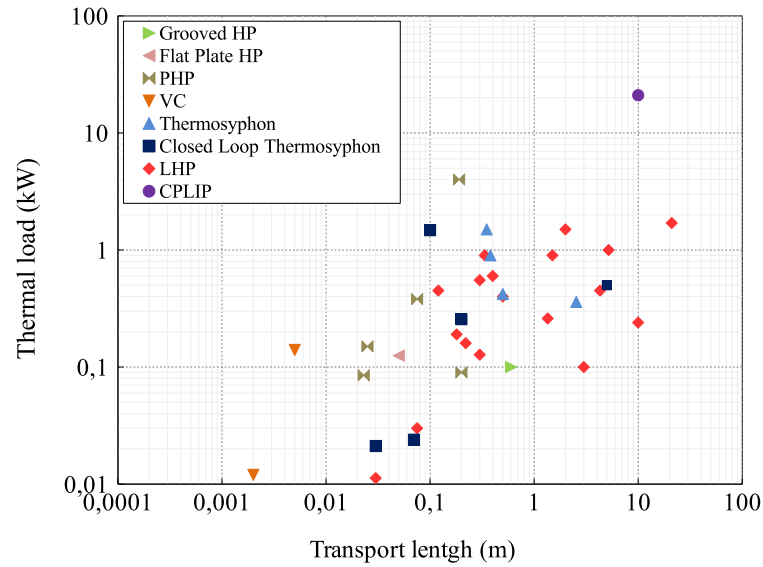


Figure 4.5: Transport distance for different passive technologies

or, in the case of an active technique, a good trade-off between pressure drops and pump-power-consumption;

6. ensure temperature controllability to the heat sink;
7. ensure high reliability.

All the enumerated points need to be respected to obtain a full working power electronics cooling system for hybrid propulsion aircraft in the context of HASTECS project (operating conditions are described in chap. 1).

By considering the length that the heatsink should have in the direction of the fluid flow, in the order of 10 cm, due to the high pressure drops related to, neither microchannels and porous media can be retained for active single-phase configuration. The high pressure drops related to such heatsink could heavily impact the overall system performances: the mass of the pump is proportional to the overall pressure drops in the circuit. At the same way, considering these technologies as part of a two-phase pumped cooling system, pressure drops are still high, even if lower than their liquid-cooling counterparts. This kind of cooling technique cannot be retained at the moment. Despite their high thermo-hydraulic overall performances, jet impingement and spray cooling cannot be retained, a priori, for integration issues. Moreover, the HTC is strongly dependent on the droplet dimension and so, on the pressure difference between the inlet and the outlet of the nozzles. Even in this case, high pumping powers are required. Vapour compression

is promising and it is the only technology (except for Peltier cells) able to lower the heat-sink temperature below the cold source one. Unfortunately it is moving its first steps in this application field, so it will be not considered at this stage. Phase Change Materials (liquid/solid), PCMs, have not been considered for the purposes of this work. They are in general used to stock thermal energy to be re-used after. After an analysis² based on an energy criterion to approach the design of an undersized, “conventional”, cooling system installed in parallel to a PCM able to damp the amount of not treated energy, it was concluded that the mass penalty introduced by the PCM is higher than the mass saving deriving from the undersizing of the cooling system itself.

Despite its low overall thermal and hydraulic performances, cold plates (in single phase configuration) are nowadays used in most applications, even in aeronautics field. This technology is worth to be considered at the first stage of the present research to demonstrate how a “brand-new” technology overcomes the limitations of a “classical” one.

None of the wicked or wickless HPs (classic HP, FPHP, GHP, micro-HP, PHP, thermosyphons and CLT) ensure the requirements, because of their limited transport distance (lower than one meter). However, passive cooling systems are promising and some of them respond to all requirements! Loop heat pipes and capillary pumped loops seem to be the best candidates for such purpose. Despite the very high thermal and hydraulic performances, LHPs are not able to ensure the required temperature controllability. CPLs suffer of instabilities, in particular during their long start-up stages, but CPLIP has a very good behaviour, even during severe transient phases [1, 111]. The latter satisfies most of the enumerate conditions: it is efficient, passive, stable and robust. It allows temperature controllability, thanks to the fixed saturation point in the reservoir. It appears to be the best candidate to solve the problem.

In the following, a deep comparison between three technologies (CPLIP, single-phase and active two-phase cooling systems, both equipped by a cold plate) is reported to analyse, under an engineering stand point, pros, drawbacks and limitations related to such technologies.

4.2 System selection

The mass of the cooling system is the index used to select the most appropriate solution for hybrid propulsion aircraft power electronics cooling issue. —*The purpose of the work is after all to find a cut-off technology, able to work in the most critical cases, with the lowest energy requirement and the lowest mass possible*—. Single phase cooling solution

²Different PCMs characterised by different melting temperatures have been exploited

is considered to compare the results of two-phase active and passive technologies, and to have an evaluation of the mass saving related to the use of the latter. Moreover, with the purpose of choosing the best cold source technology, between those presented in sec. 1.4, a heat exchanger is in the following designed, independently from the rest of the system, to evaluate its performances³.

4.2.1 Cold source technology comparison

To choose the best adapted cold source technology, a design of a heat exchanger is here proposed to quantitatively compare skin heat exchanger and a tube bank HXG inserted in a RAM-air circuit (see also section 1.4).

To remind, a skin heat exchanger uses the external skin of the aircraft to cool the primary side fluid. No contact obviously occurs between the external air and the tubes, because of the presence of a low thermal resistance layer (the aircraft skin) between them. *A priori*, this solution is the best candidate to be used if power electronics and the adjoined cooling system emplacement is the fuselage (PIF - Power electronics In the Fuselage).

On the other hand, RAM-air allows the use of a crossed-flow air-liquid HXG. The latter is composed by staggered and equispaced tubes. Air velocity in correspondence of the first tube rank can be better controlled (during the design process), allowing higher heat transfer coefficient than skin HXG.

In accordance to models presented in Appendix B.1.4.1 and B.1.4.2 a design based comparison is here reported for both technologies. The heat exchanger will be designed to evacuate a thermal load of 15 kW and to ensure a temperature difference of 40 K (from 80 °C at the inlet to 40 °C at the outlet). Even if, at this stage, only the heat exchanger is considered, the same conclusion are also valid for condenser.

Skin heat exchanger During the mission of the aircraft, pretty high differences occur in air density (see sec. 1.3) and velocity between the ground stage and the high altitude flight. The design of a heat exchanger needs to be considered in steady state [17], so the worst operating conditions are used for the purpose. The latter are obviously realised for the lowest air velocity flowing on the external side of the fuselage, during taxi-out and taxi-in stages, and for the highest external air temperature, T_∞ , and the lowest air density.

Considering all these parameters, the external side HTC, h_{ext} , may be obtained in a quite similar way of an airflow flowing on a flat-plate which curvature radius is pretty

³All calculation details are reported in Appendix B

large. So, according to Pang *et al.* [4], correlation (4.1) may be used to calculate the external Nu number:

$$\text{Nu}_{\text{ext}} = 0.2948 \text{Re}_L^{0.5} \quad (4.1)$$

In this case, a very small value of HTC was found, about $5 \text{ W} \cdot \text{m}^{-2} \cdot \text{K}^{-1}$, corresponding to an airflow flowing on a 1.5-meter-long flat-plate at $10 \text{ m} \cdot \text{s}^{-1}$. The resulting heat exchanger length is in the order of $2 \cdot 10^3 \text{ m}$ and, consequently, pressure drops related to such dimension are fairly high. The total heat transfer surface area, corresponding to the $2.2 \cdot 10^3$ -meter-long heat exchanger tube having a diameter of 10.5 mm, to ensure a maximum liquid velocity of $2 \text{ m} \cdot \text{s}^{-1}$, is about 73 m^2 , while the aircraft skin surface area is just below 62 m^2 . This is a nonsense! To check the just obtained values, let's simply apply the Newton's law to evaluate the necessary heat transfer surface area to evacuate $Q_{th} = 15 \text{ kW}$ for a wall to air temperature difference $(T_w - T_\infty) \simeq 40 \text{ K}$. If the previously obtained heat transfer coefficient value is used ($5 \text{ W} \cdot \text{m}^{-2} \cdot \text{K}^{-1}$), the resulting heat transfer surface area is 75 m^2 , according with calculation from the model. A whole aircraft is not enough to evacuate such thermal load.

The skin heat exchanger, the potentially most adapted solution to be used in an eventual PIF configuration, is absolutely not adapted for the purpose!

Tube rank configuration (RAM-air) The same boundary conditions expressed before were used even in this case. The heat exchanger configuration (assigned *a priori*) is a staggered not finned tube bank composed by 5×20 tubes, spaced of 1.5 times the condenser-tube-diameter and with a single-tube-length of 0.8 m. Because of the heat exchanger configuration, the external side heat transfer coefficient is $144 \text{ W} \cdot \text{m}^{-2} \cdot \text{K}^{-1}$, so the corresponding tube total length is⁴ 80 m!

Comparisons are not necessary in this case. A staggered tube bank is the best configuration for the heat exchanger/condenser. RAM-air configuration answers to requirements. RAM-air intakes are usually installed in the centre of the aircraft, and so it could be also used when power electronics and its cooling systems need to be installed in the fuselage. However, it has to be underlined that an installation in the nacelle (Power electronics in the Nacelle - PIN) is suggested to take advantage of an eventual and maybe larger air intake.

More studies are required, in particular related to aerodynamics, to weigh up pros and drawbacks related to the use of a RAM-air system or a nacelle air intake.

⁴For more details about the relations used in this case, the interested reader can find more informations in sec. B.1.4.2.

4.2.2 First approximation evaluation of mass and power coefficient

To remind, the overall power coefficient is:

$$C_{c,tot} = \frac{Q_{el}}{m_{el} + m_{th}} \quad (4.2)$$

Being the mass of the whole electronic system equal to 60 kg (as described by WP2 [21]), the cooling system should have a maximum mass, $m_{th} = 40$ kg, to satisfy the power coefficient requirement for 2025 ($C_{c,2025} = 15 \text{ kW} \cdot \text{kg}^{-1}$).

In table 4.2 the main characteristics of the below analysed cooling techniques are reported.

Technology	Evaporator	Condenser	Cold source
Liquid cooling	Cold plate (parallel channels)	Not finned tube bank	RAM-air
Pumped two-phase	Cold plate (serpentine)		
Capillary pumped (CPLIP)	Sintered porous medium		

Table 4.2: Technology generalities.

For comparison purpose, the same constituting materials, working fluid⁵ and boundary conditions will be used for all considered technologies.

To simplify the first approximation design, either for active and passive two-phase technologies, the condenser will be designed by neglecting subcooling section. However, the sensible heat rate necessary to lower the primary fluid temperature close to the external air one is 5-10% of the total thermal power. The related subcooling length does not exceeds 5 m and all the obtained HXG/condenser dimensions are rounded-up to the closest higher round value, sometimes exceeding such length.

The comparison is based on the following assumptions:

- The heat power to be evacuated is 15 kW;
- RAM-air is considered as cold source.
- Either two-phase, active and passive, and single phase solutions are considered using the same heat exchanger configuration (not finned tube bank⁶).

⁵A discussion and a comparison between the working fluids is reported in Appendix A

⁶see Appendix. B.1.4.2 for more details.

- The air frontal velocity on the first HXG tube rank is equal to the aircraft velocity during taxi-out-and-in stages ($10 \text{ m}\cdot\text{s}^{-1}$).
- The cold fluid temperature at the inlet of the cold side corresponds to the worst operating condition: 33°C , realised on the ground during the taxi-out and in stages.
- Three parallel heatsinks are used to evacuate the thermal load;
- Stainless steel is used as solid material;
- Methanol is used as working fluid for all compared technologies⁷;
- All tubes: transport lines and heat exchanger/condenser have the same thickness ($t = 0.6 \text{ mm}$);
- Liquid velocity is limited to $2 \text{ m}\cdot\text{s}^{-1}$ in the liquid lines (both for single and two-phase systems) and vapour velocity is limited to $20 \text{ m}\cdot\text{s}^{-1}$ into vapour line of two-phase systems;
- The evaporator to condenser distance is supposed to be 1 m and the reservoir to condenser height difference is 20 cm. Vapour and liquid line lengths⁸ are respectively 1 and 1.2 m.
- Eq. (2.3) and eq. (2.11) are respectively used for single and two-phase fluid mass flow rate estimation, and in the last case assuming a vapour quality $x = 1$ at the exit of the evaporator;
- Fluid thermophysical properties are assumed to be constant for a given fluid-phase;
- Fouling is not considered.

In table 4.3 the main geometrical dimensions of the considered cooling systems are reported.

Single phase cooling system Single phase cooling system is considered in its simplest form. No regulating valves or other accessories are taken into account. The 1-meter and the 1.2-meter-long transport lines (hot and cold respectively), are characterised by the same transversal section, imposed by fixed coolant velocity and mass flow rate. The

⁷Except water, that is the most performing fluid, but limited by its high freeze point and for compatibility issues, methanol is a good candidate for single-phase cooling solution as well. In Appendix A is reported a detailed comparison between different working fluids.

⁸In absence of information about dimensions, integration and environmental constraints the transport line length has been, arbitrary, chosen to simplify the calculations.

	Liquid cooling	Two-phase active	Two-phase passive
Hot/vapour line length (m)	1	1	1
Hot/vapour line diameter (mm)	10.5	21.2	21.2
Cold/liquid line length (m)	1.2	1.2	1.2
Cold/liquid line diameter (mm)	See hot/vapour line	3.5	3.5
Condenser diameter (cm)	Same than hot/vapour line diameter		
Heatsink dimensions (cm ²)	12.4 × 12.2	12.4 × 12.2	12.4 × 12.2
Reservoir/condenser height difference (m)	0.2	0.2	0.2

Table 4.3: Cooling system main geometrical dimensions.

three parallel vertically mounted heatsinks have dimensions of $12.4 \times 12.2 \text{ cm}^2$ and are equipped by four power electronics modules installed face-to-face (in couple of two). They are traversed by nine 0.8 cm-side-squared parallel channels in which the coolant flows (allowing a theoretical temperature difference between the inlet and the outlet of 40 K). The 80-meters-long air-liquid crossed-flow cold HXG is not finned on its external side. The staggered tube bank is composed by 5 rows of 20 tubes (the tube distance is imposed to be 1.5 times the condenser-tube-diameter) and a single-tube-length of 0.8 m. The pump is designed to ensure the required pressure head (590 kPa) and mass flow rate ($11.35 \text{ Liters} \cdot \text{min}^{-1}$). It has been selected from a wide range of pumps used for aeronautics field. The loop is completely fulfilled of liquid and should be pressurised to avoid boiling issues in heatsink channels.

In table 4.4, results, in terms of mass for each component constituting the single phase cooling system, are reported. The unladen mass is more than three times the mass of the fluid contained in the system, and about 35% of the unladen mass is due to the pump. Considering the obtained system mass, the thermal power coefficient, $C_{c,th}$, is just above $0.3 \text{ kW} \cdot \text{kg}^{-1}$. Considering electronics components total mass equal to 60 kg, the total power coefficient C_c is $13.8 \text{ kW} \cdot \text{kg}^{-1}$. The latter is close to HASTECS' target for 2025 ($15 \text{ kW} \cdot \text{kg}^{-1}$)⁹, but all previously explained issues related to low efficiency and temperature control inability cannot be neglected!

⁹If water was used as working fluid, mass saving related to its use is lower than 5% and its impact on the power coefficient negligible.

	Fluid Volume (m ³)	Fluid Mass (kg)	Solid Volume (m ³)	Unladen mass (kg)	Total mass: solid+fluid (kg)
Hot line	9.15E-05	0.07	2.15E-05	0.17	0.23
Cold HXG	7.32E-03	5.35	1.72E-03	13.40	18.75
Cold line	9.15E-05	0.07	2.15E-05	0.17	0.23
Expansion tank	7.41E-03	5.42	3.59E-04	2.80	8.22
Heatsink	2.11E-04	0.15	3.34E-04	7.81	7.96
Pump	-	-	-	13.00	13.00
<i>Total</i>	1.51E-02	11.06	2.45E-03	37.35	48.41

Table 4.4: Single phase cooling system mass evaluation (first approximation design).

Active two-phase cooling system Like single-phase, active two-phase solution has been designed in its simplest form (reported in Fig. 2.9). Even in this case a three parallel-heatsink-evaporator was considered. The latter is vertically mounted and its external dimensions are related, as always, to power electronics modules ones. This technology generally does not require the complete evaporation of the working fluid at the outlet of the heatsink, so a vapour quality x lower than 1 should be imposed for mass flow rate calculation ($\dot{m} = Q/h_{lv}\Delta x$). If a vapour quality $x < 1$ is chosen, the corresponding mass flow rate is higher than that required for the complete evaporation of the working fluid, negatively impacting pump mass, tube cross sections and so the overall loop mass. For comparison purposes a vapour quality $x = 1$ has been adopted at the outlet of the heatsink to not *a priori* “condemn” this technology. The mass flow rate value is one order of magnitude lower than single phase solution. A serpentine configuration has been chosen for the cold plate to avoid too low liquid velocities. The 12-millimetre-side squared-section serpentine traverses ten times the heat sink. The 1-meter-long vapour line and the 1.2-meter-long liquid line are characterised by a hydraulic diameter of 21.2 mm (twice than single phase solution) and 3.5 mm-hydraulic-diameter, respectively. The fifty-meter-long condenser has the same hydraulic diameter than the vapour line. It is considered using the same configuration described before: 5 tube rows of 20 tubes each, but with single tube length of 0.5 m. Due to the one order of magnitude lower mass flow rate than single phase solution, no pumps in aeronautics family were available. A general purpose pump has been used in this case. Like single-phase solution, a height difference of 20 cm between the condenser outlet and the reservoir inlet is considered. The results of the mass evaluation for this kind of cooling technology are reported in table 4.5.

Two phase cooling systems are characterised by a reservoir total volume equal to the cumulated volumes of fluid contained in the condenser and in the vapour line. This

	Fluid Volume (m ³)	Fluid Mass (kg)	Solid Volume (m ³)	Unladen mass (kg)	Total mass: solid+fluid (kg)
Vapour line	4.62E-04	0.34	4.69E-05	0.37	0.70
Condenser	2.17E-02	15.89	2.20E-03	17.18	33.06
Liquid line	9.41E-06	0.01	7.65E-06	0.06	0.07
Reservoir	2.22E-02	4.06	5.18E-04	4.04	8.09
Evaporator	5.27E-04	0.00	1.99E-04	1.55	1.55
Pump	-	-	-	10.43	10.43
<i>Total</i>	0.04	20.29	0.00	33.62	53.91

Table 4.5: Pumped two-phase cooling system mass evaluation (first approximation design).

explains the high fluid mass characterising this kind of technology (double than single phase system). However, due to a reduction of the pump mass and to a lower unladen mass, the higher amount of fluid has a small impact on the global power coefficient, C_c , that, in this case, is about $13.6 \text{ kW} \cdot \text{kg}^{-1}$.

Passive two-phase cooling system: CPLIP Two different configurations are here considered for comparison purposes: three parallel evaporators CPLIP, also called CERBERE [71], and three parallel CPLIPs: each one designed to evacuate a single-electrical-phase thermal losses.

Three parallel evaporators configuration: CERBERE

At first, the three parallel evaporators configuration is considered. Neglecting the sensible heat rate and because of the complete evaporation of the fluid, the same mass flow rate than two-phase active solution has been obviously obtained. The two-millimetres-thick nickel evaporator casing has the same external dimensions than other technologies (depending on the power electronics modules installed on). The nickel porous wick is characterised by a porosity of 73% and a mean pore-diameter of $6.3 \mu\text{m}$. Vapour and liquid line dimensions are the same than active-two-phase solution. In table 4.6 the mass evaluation for this configuration is reported. Due to the same mass flow rate value than two-phase active technology, the same tube vapour line and so condenser transversal section is used.

By using the just obtained cooling system mass to calculate the global power coefficient, it results $C_c = 14.3 \text{ kW} \cdot \text{kg}^{-1}$! This value is the closest one to the 2025 target ($C_{c,2025} = 15 \text{ kW} \cdot \text{kg}^{-1}$). Anyway, this solution needs to be optimised: an increase of the power coefficient is thus expected.

	Fluid Volume (m³)	Fluid Mass (kg)	Solid Volume (m³)	Unladen mass (kg)	Total mass: solid+fluid (kg)
Vapour line	4.62E-04	0.34	4.69E-05	0.37	0.70
Condenser	2.17E-02	15.89	2.20E-03	17.18	33.06
Liquid line	9.41E-06	0.01	7.65E-06	0.06	0.07
Reservoir	2.22E-02	4.06	5.18E-04	4.04	8.09
Evaporator	1.07E-04	0.08	2.12E-04	0.86	2.82
<i>Total</i>	4.45E-02	20.37	2.99E-03	22.50	44.75

Table 4.6: Two-phase passive cooling system mass evaluation (first approximation design of a three-evaporators-CPLIP).

Three parallel loops

Assuming the case where three parallel loops work independently, each one cooling one electrical-phase, each CPLIP should be designed to evacuate one-third of the total thermal losses. In this case, the total mass of the cooling system is obviously given by the sum of the masses of all CPLIPs. Smaller components dimension than CERBERE characterises this solution. Vapour and liquid lines have the same lengths (defined in table 4.3) than its three-heads counterpart, but smaller hydraulic diameters: respectively 14 and 2 mm. The 23-meter-long condenser has the same configuration than before, but due to the smaller hydraulic diameter the heat transfer surface area is obviously lower. In this case, the condenser staggered tube bank has 5-rows of 6 tubes each, a single-tube-length of 0.8 m and a tube distance 1.5 times the condenser hydraulic diameter. The mass evaluation of three-parallel CPLIPs configuration is reported in table 4.7. Actually, if this last result is used to calculate the power coefficient, a value of $C_c = 16 \text{ kW} \cdot \text{kg}^{-1}$ is obtained: higher than the target 2025!

	Fluid Volume (m³)	Fluid Mass (kg)	Solid Volume (m³)	Unladen mass (kg)	Total mass: solid+fluid (kg)
Vapour line	1.54E-04	0.11	2.75E-05	0.21	0.33
Condenser	3.54E-03	2.59	6.33E-04	4.94	7.53
Liquid line	3.14E-06	0.00	4.90E-06	0.04	0.04
Reservoir	3.70E-03	0.68	2.14E-04	1.67	2.35
Evaporator	1.07E-04	0.08	2.12E-04	0.86	0.94
<i>Total</i>	7.50E-03	3.46	1.09E-03	7.72	11.18/CPLIP

Table 4.7: Two-phase passive cooling system mass evaluation (first approximation design of three different one-evaporator-CPLIP).

4.2.3 Cooling technology comparison

A comparison of the characteristics resulting from the first approximation design are reported in table 4.8. Despite the already expressed low efficiency and strong dependency between operating temperature range and mass flow rate, single phase cooling system is in general lighter than two-phase active technology (see Fig. 4.6). Both technologies are characterised by almost the same unladen mass, but a two times higher quantity of fluid is contained in two-phase active solution.

Higher condenser and vapour line internal tube diameters (two times than those of single phase solution), and a greater reservoir volume justify the higher amount of fluid in two-phase solution. Both technologies are, as expected, strongly impacted by the pump that, in active single and two-phase technologies are, respectively, 27% and 19% of the total mass (see Fig. 4.7). So the use of a CPLIP can ensure a mean mass saving of about 23%.

	Liquid cooling	Two-phase active	CERBERE	3×CPLIP
Thermal load [kW]	15	15	15	3×5
Total MFR [kg·s ⁻¹]	0.14	0.014	0.014	3×0.0046
Heatsink configuration	9 parallel squared channels; $D_h = 8$ mm	Single-channel serpentine; 10 passages; $D_h = 12$ mm	Porous wick	Porous wick
Condenser length [m]	80	50	50	3×23
Condenser diameter [mm]	11	24	24	14
Cold HXG/condenser configuration	Staggered tube bank; 5×20 tubes of 0.8 m; equispaced 1.5 diameters	Staggered tube bank; 5×20 tubes of 0.5 m; equispaced 1.5 diameters	Staggered tube bank; 5×20 tubes of 0.5 m; equispaced 1.5 diameters	Staggered tube bank; 5×6 tubes of 0.8 m; equispaced 1.5 diameters
Reservoir volume [m ³]	7.13E-03	2.22E-02	2.22E-02	3×3.70 E-03
Total mass (kg)	48.4	53.9	44.7	33.6
First approximation global power coefficient, C_c (kW·kg⁻¹)	13.8	13.2	14.3	16

Table 4.8: Cooling systems geometrical characteristics.

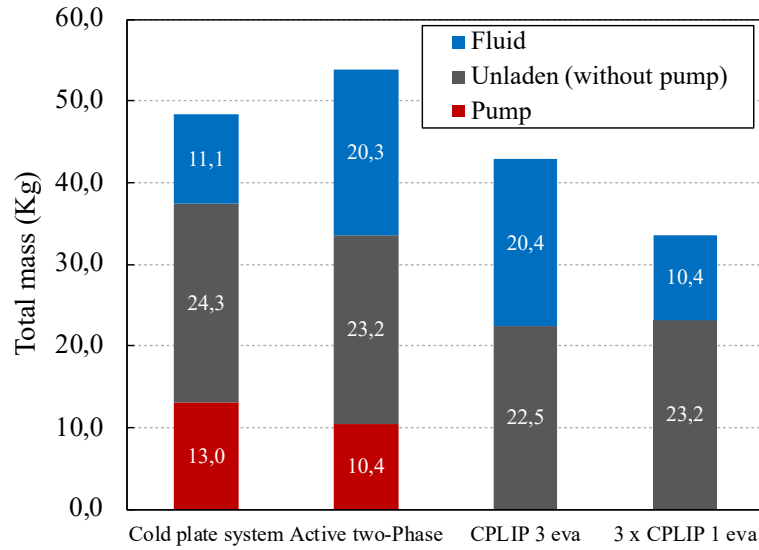


Figure 4.6: Unladen, fluid and total mass comparison for the considered technologies.

Cold-heat-exchanger/condenser and fluid are the second and the third heaviest components in active technologies.

Despite the great difference in terms of unladen mass, the quantity of fluid filling the pumped two-phase technology and the CPLIP is almost the same. Pumped two-phase cooling system and CPLIP, with three parallel evaporators, share the same components dimensions, but their working principle is quite different in nature. They share condenser configuration and dimensions as well as vapour line, liquid line and reservoir dimensions. Evaporator of pumped two phase technology (cold plate) is lighter than CPLIP's one (wicked). The difference is mainly due to the presence of the nickel porous wick in the capillary pumped solution, while empty channels compose the evaporator of active two-phase technology. If in pumped two phase cooling system, no fluid fills the evaporator in stand-by condition, in the case of the CPLIP, the evaporator is filled with liquid.

The use of three different CPLIPs allows a significative mass saving (about 26%) than CERBERE, but some integration issues may be solved. In this case, in fact, three independent loops need to be installed side by side and electronic components, positioned on the evaporators, have to be linked between them. Even if the mass of CERBERE configuration is higher than the maximum mass requirement, it has to be considered that this solution is not optimised yet.

CPLIP is mostly impacted by condenser and fluid mass. In this last case the fluid mass is almost 50% of the total mass and the 40% is due to the condenser. Obviously,

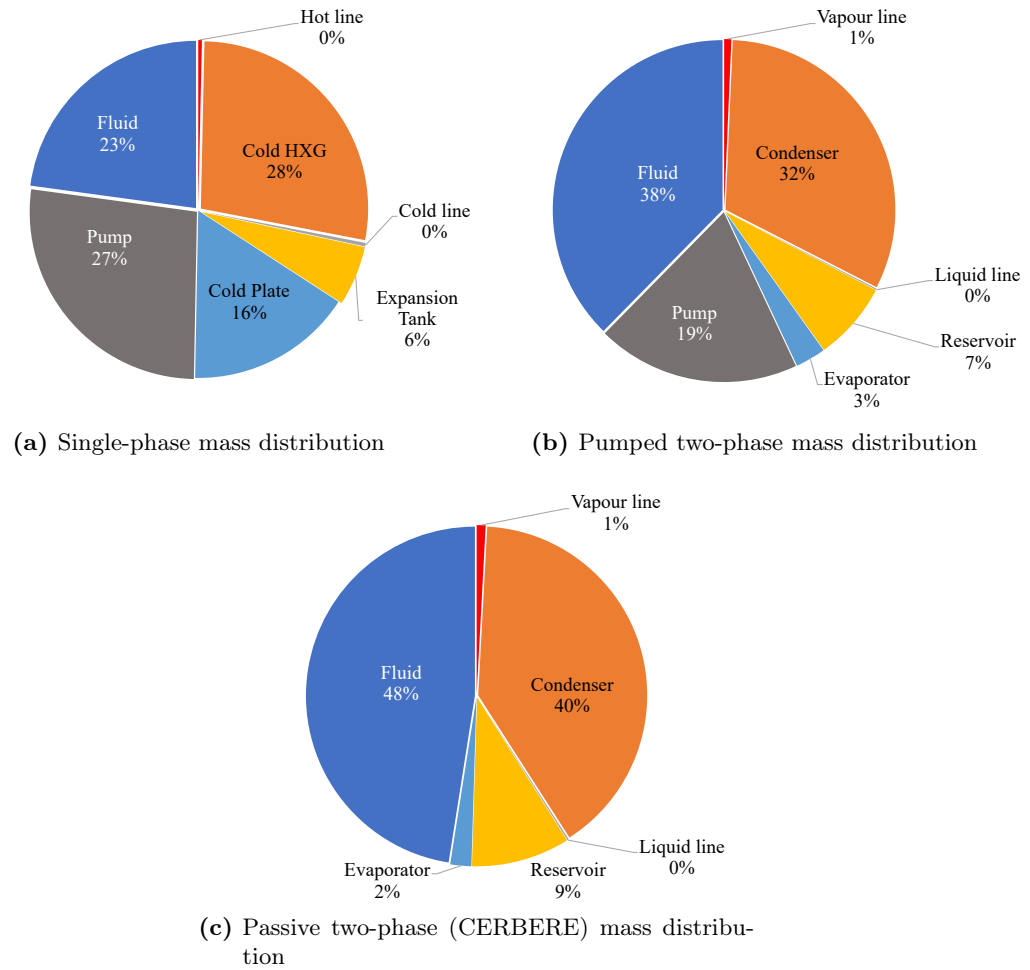


Figure 4.7: Mass composition of different cooling technologies

the lower the unladen mass, the higher the perceptual weight of fluid in the cooling system. However, the fluid is mostly present in the condenser, the longest component for all analysed technologies. So, the smaller the condenser, the lower the quantity of fluid filling the loop and also the lower the reservoir volume. The condenser is the main component on which the optimisation process should be focused. Note that liquid and vapour line masses are negligible for all systems.

Actually, between the compared technologies only the CPLIP is the one able to ensure the closest value of the power to mass ratio [$\text{kW} \cdot \text{kg}^{-1}$] to the minimal requirements.

4.3 Conclusion

In this chapter a comparison between different cooling devices was introduced, considering the heat evacuation capability, the maximal HTC and the evolution of each technology.

Jet impingement and spray cooling, microchannels and, porous media and metal foams were compared to have a broad knowledge of the actual state of the art concerning electronics cooling. Considering either single and two-phase exchange mechanisms, the latter is the best choice to ensure higher HTC as well as lower pressure drop on the hot side. The main problems related to the use of these particular cooling techniques is, in fact, related to their pressure drops. The higher the pressure drop, the higher the energy required by the cooling system to work and so the lower the power coefficient that should be proportionally reduced to consider the pump efficiency.

Passive two phase cooling systems are nowadays widely used for the same purposes and their performances increase time by time. These technologies are today able to ensure the adequate cooling with relatively high transport distances, as is the case for two-phase passive loops (see LHP/CPL/CPLIP).

A first approximation design and a comparison was also introduced in this chapter to finally choose the most adapted cooling solution for the purpose of this work. Actually, neither classic liquid cooling systems and active two-phase technologies are able to ensure, following the first approximation design, the mass requirement. On the other hand, CPLIP, is able to ensure the mass requirement, and, even if optimisation is needed this technology crosses over, in a particular configuration, the minimal power to mass ratio, C_c . Three separate parallel CPLIPs configuration represents the more lightweight solution, ensuring a power coefficient higher than $15 \text{ kW} \cdot \text{kg}^{-1}$ (2025 target). Its volume encumber could be higher than a CERBERE and some integration issues could affect such arrangement. For CERBERE, the power coefficient is slightly lower than that required for 2025, but an optimisation must be performed.

CPLIP seems to well responds to power electronics requirements either for the targets of 2025.

CPLIP's working principles, characteristics, numerical models and experimental facility will be introduced. Experimental tests and numerical simulations will be used to show how this loop is able to ensure the temperature and mass requirements. A particularly fine CPLIP optimisation will be so presented to check if this technology, coupled to the electronic components, is able to answer to requirements of 2035.

Part III

CPLIP in HASTECS context

After an introduction on the state of the art of the Capillary Loop for Integrated Power (CPLIP), its working principle, the experimental facility and the numerical model used in this study, are here introduced. CPLIP will be experimentally characterised from a thermal and hydraulic point of view to analyse its behaviour in presence of high heat flux densities, to know if it meets HASTECS requirements and to evaluate evaporator thermal conductances. An experimental stress test, based on the response of the loop in a real aircraft mission profile cycle is introduced to show its capabilities. Finally, it will be designed and optimised, according to power electronics requirements, to evaluate its performances in terms of power coefficient, C_c , either for targets 2025 and 2035.

Capillary Pumped Loop for Integrated Power (CPLIP): working principle, experimental facility and numerical tool

The Capillary Pumped Loop for Integrated Power (CPLIP), or CPLTA (Capillary Pumped Loop for Terrestrial Applications) as it is also called, is a two-phase passive loop which design has been enhanced from classical CPLs. In the latter, no mass exchanges are possible because of the small diameter of the tube linking the liquid line and the reservoir [47]. Low stability during harsh transient stages and long response time during loop start-up [74] characterise CPLs. Thanks to gravity and a higher thermo-hydraulic coupling between the compensation chamber and the evaporator, linked by a vertical tube, problems affecting CPLs were solved in CPLIP. Mass exchanges are so possible: the liquid contained in the reservoir is forced by gravity to come down to the evaporator, and if vapour bubbles are formed in the latter, they can return-up to reservoir.

In this chapter, an introduction on the CPLIP is presented and its working principle discussed. The physical phenomena governing its components are explained and the experimental facility introduced. Finally, the numerical model used in this study is presented.

5.1 CPLIP generalities and working principle

Like other capillary pumped systems, CPLIP is constituted by evaporator, condenser, compensation chamber (or reservoir) and transport lines (vapour and liquid). The thermodynamic working principle is explained using the scheme reported in Fig. 5.1 according to the qualitative thermodynamic cycle of Fig. 5.2.

In steady state conditions, the heat coming from the evaporator walls, point E_i , (where the hot source is installed) reaches the liquid menisci by conduction through the porous wick particles and the vapour contained in it. Vaporisation occurs at the liquid/vapour interface (point V) following the pressure difference between reservoir (res) and the

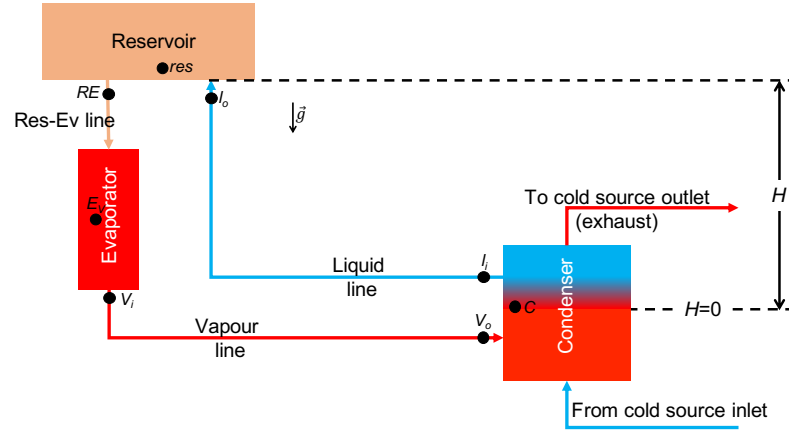


Figure 5.1: Scheme of principle of CPLIP

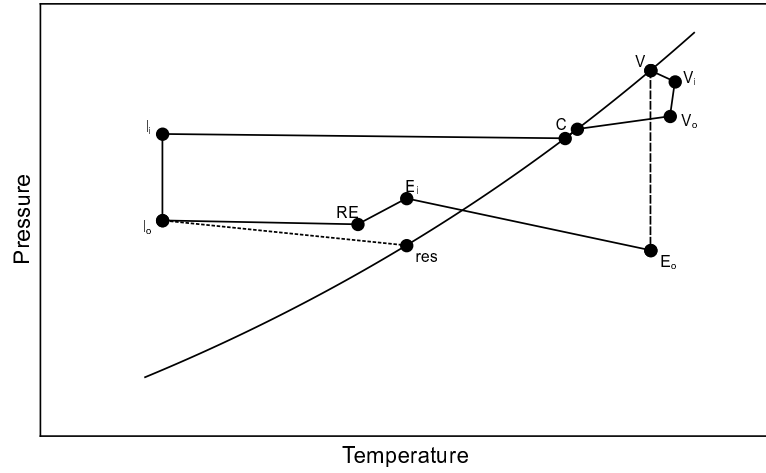


Figure 5.2: CPLIP thermodynamic cycle [12]

evaporator itself. Vapour, subject to a small pressure drop in the evaporator, reaches the inlet of the vapour line slightly superheated by evaporator walls (point V_i) and, subject to viscous pressure drop, flows to the condenser within the vapour line (point V_o). In the condenser, vapour temperature decreases, from superheated to saturated condition (on the saturation curve), until condensation occurs (point C). Oversizing of this last component is necessary to allow the required sub-cooling: the liquid should quit the condenser as close as possible to the cold source inlet temperature. Subcooled liquid enters the liquid line in the condition l_i , it flows within it and enters in the reservoir in condition l_o . In CPLIP, pressure drops in the liquid line are mostly due to gravity, $\rho_l g H$ (given the difference of height, H , between the condenser outlet and the reservoir inlet),

and marginally to viscous effect. In reservoir, saturation conditions are imposed using an electric cartridge heater and controlled using a PID regulator and a thermocouple, so that the point res is fixed on the diagram. Liquid, entering in the reservoir in condition l_o , flows within its lower part. Due to convective and conductive heat exchanges between the higher and the lower part of the reservoir, liquid quits it in condition RE (hotter than l_o point). It enters into the evaporator by gravity, where it wets the porous wick. Here, liquid is heated from the temperature corresponding to condition RE until the evaporator's saturation one. Finally, evaporation, and so mass transfer from liquid to vapour phase, takes place. Pressure head, due to capillary effect, allows the fluid to flow into the loop making the cycle to start again.

Even if a system approach is here used to describe the behaviour of the CPLIP, a description of each component is reported to give the reader an overview of the different phenomena occurring in this kind of loop.

5.1.1 Evaporator

The evaporator, the component where the most complex physical phenomena take place, is the “engine” of the CPLIP. Energy exchanges and mass transfer, from liquid to vapour phase, occur here to evacuate the thermal load, while capillarity generates the fluid motion in the loop.

The evaporator is constituted by a low thermal resistance enclosure which contains a sintered porous wick. Even if different materials can be used for the purpose, high thermal conductivity wick materials are preferred to obtain a heat spreading from the enclosure walls to the centre of the wick itself. Evaporator assembly and transversal sections are respectively reported in Fig. 5.3 and Fig. 5.4.

The liquid, forced by gravity, enters in the arteries (see Fig. 5.4a and Fig. 5.4c) and

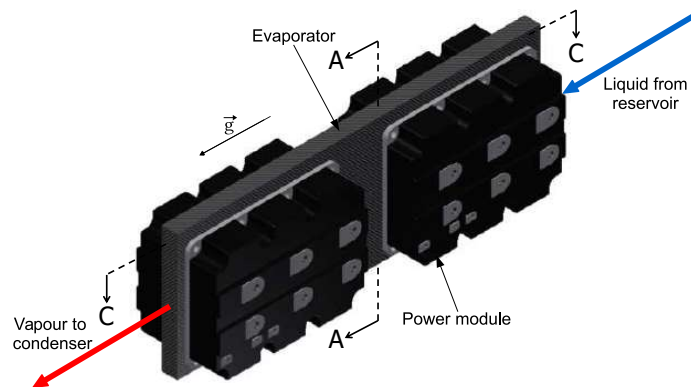


Figure 5.3: Evaporator assembly

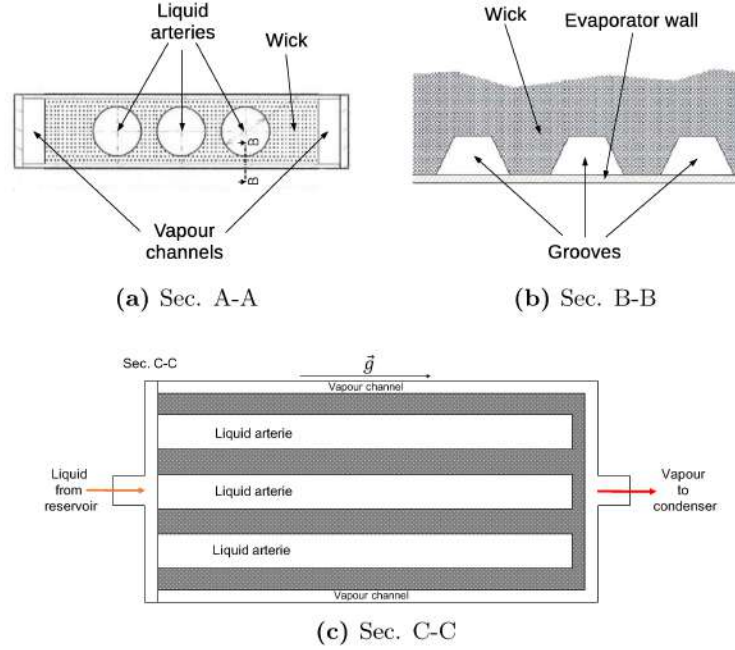


Figure 5.4: Evaporator sections

penetrates the porous wick. The evaporator, vertically mounted, is uniformly heated from two opposite sides. When the heat flux is applied to the (vertical) bounding surfaces, the wick temperature increases. By conduction, the heat is transferred to the wick particles and the wetting liquid. When the latter reaches and crosses-over the saturation temperature, according to reservoir conditions, evaporation occurs in the wick (see Fig. 5.5). The interface between the liquid and the vapour phases is constituted by menisci supported by the porous structure. In correspondence of the point where solid, liquid and gaseous phases are in contact (triple line), a force field is created and the system evolves towards a new equilibrium generating a curvature in the meniscus profile. The liquid below the meniscus is depressurised (P_l) relatively to the vapour phase (P_v) above the interface. Such differential pressure, also called capillary pressure head, created between the two phases of the fluid is due to the presence of superficial tension forces (σ) able to counterbalance the overall pressure drop in the loop. Considering the meniscus curvature radius r_m , the capillary pressure ($P_v - P_l$) is defined by the Young-Laplace law:

$$P_v - P_l = \Delta P_{cap} = \frac{2\sigma}{r_m}$$

Due to the geometrical relations between the meniscus-curvature-radius, r_m , and the pore capillary radius, r_c , through the contact angle, θ_m : $2/r_m = 2 \cos \theta_m / r_c$, the maximum

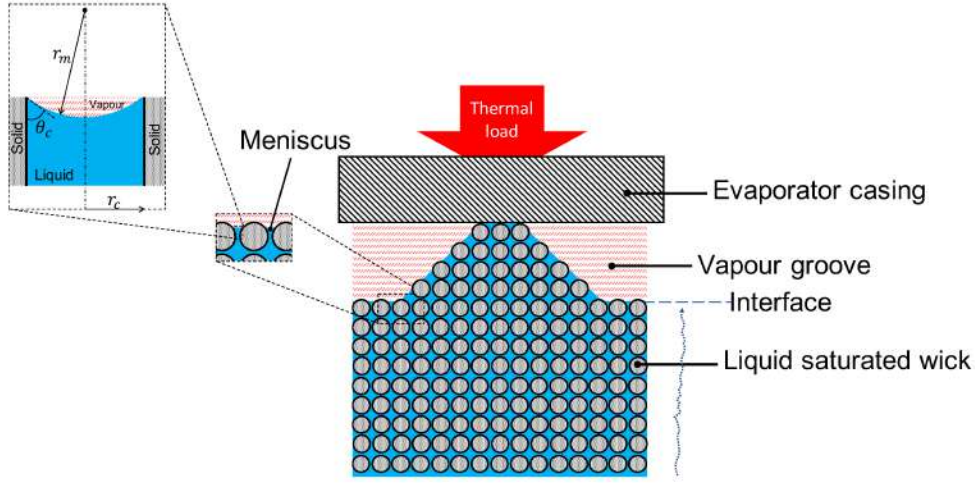


Figure 5.5: Schematic of evaporation in a porous wick.

capillary pressure head, $\Delta P_{cap,max}$, is defined by a meniscus curvature radius, r_m , tending to the capillary pore radius, r_c . The contact angle θ_m , characteristic of the couple solid-liquid, is an important indicator of the wettability of the porous wick: the way on which the liquid phase spreads onto the solid surface. $\theta_m \leq \pi/2$ indicates a wetting liquid, while $\theta_m > \pi/2$ characterises a non-wetting liquid.

Factors, in general, influencing the behaviour of the porous wick [112] are the geometrical characteristics of the wick, such as matrix structure, pore number and dimensions, and matrix topology. Beyond the geometrical ones, other influencing factors are the fluid-solid interactions (see also θ_c).

In general, the complexity of evaporation process into the porous media do not allow a simple modelling of this component of the loop. To simplify the task, a 2D flow has been assumed for the resolution of the fluid flow, but great differences exist between 2D and 3D results. In some cases 2D results are related to “false phenomena” that in reality do not occur, as in particular underlined by Mottet *et al.* [113, 114].

5.1.2 Condenser

The condenser is the component where heat is definitively evacuated to the external environment. In general, it is a classic heat exchanger where latent and sensible heats are exchanged between external and internal fluids to evacuate the thermal load. Classically, in the first part of the condenser only latent heat is exchanged between the primary and the secondary fluid and, if sub-cooling is required, sensible heat is exchanged in the

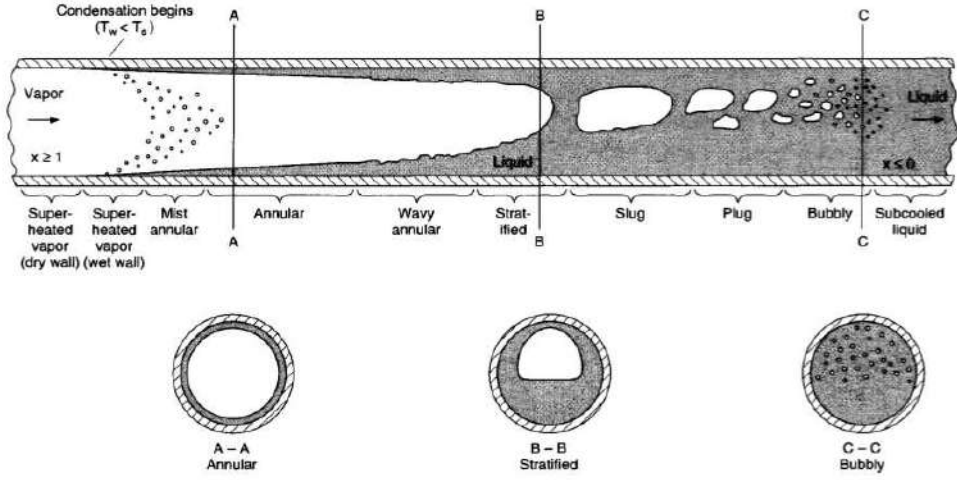


Figure 5.6: Condensation flow regimes [13]

remaining part to lower the temperature of the condensed fluid.

Condensation is, together with evaporation in the porous structure, one of the most complex phenomena occurring in the loop. A qualitative scheme of condensation occurring in a tube is reported in Fig. 5.6. When the wall temperature is lower than the local saturation one, condensation starts on the tube walls, but the fluid bulk remains in superheated conditions. Due to mass exchanges from vapour to liquid phases, a thin film of liquid begins to be formed on the tube walls: annular flow. The velocity of the fluid decreases because of the higher density of the liquid compared to the vapour one. Depending on the orientation of the condenser and the shear to gravity force ratio, one can assist or not to a stratification of the liquid in the lower part of the tube. Waves can be formed on the liquid film and they could become big enough to form slugs (slug flow). Slugs of liquid will intermittently push the plugs of vapour towards the exit of the condenser. So, after a bubbly flow, depending on the condenser length, sub-cooled liquid leaves the condenser. In this last section of the condenser only single phase heat transfer occurs, and, as a function of the heat flux density, the fluid temperature can be easily calculated from sensible heat transfer and single phase (liquid) correlations. Due to the complexity of the flow pattern, different models exist to predict the fluid behaviour. On the basis of the dimensionless vapour mass velocity, j_g^* (see eq. (5.1), where apart from the already known parameters, G [kg·s⁻¹·m⁻²] is the mass flow rate per unit area), the flow pattern can be identified as [13]:

$$j_g^* = \frac{xG}{[g\rho_g(\rho_l - \rho_g)d_i]^{1/2}} \quad (5.1)$$

If $j_g^* < 0.5$, stratified condensation occurs. Because of the presence of gravity, vapour, condensed in top part of the tube, drop-off around the tube walls. The liquid is collected in the lower part (see sec. B-B of fig. 5.6) where, due to the presence of shear forces, it axially flows forward. In this case, the calculation of the heat transfer coefficient is not dependent on the stratified part which contribution may be in general neglected [13]. It is the case of Chato correlation, for example.

If the vapour velocity becomes high enough, the influence on the heat transfer coefficient of the stratified liquid in the lower part of the tube cannot be neglected anymore, and the interfacial vapour shear stress can influence the heat transfer coefficient of the fluid film in the higher part of the tube wall. In this case, either the liquid accumulated in the lower part of the tube and the vapour need to be considered for HTC calculation.

Finally, when the vapour velocity is pretty high, *i.e.* $j_g^* > 1.5$, laminar flow model is no more adapted and turbulence models have to be used for HTC prediction: gravitational effects become almost negligible and no more stratification occurs. In this case the fluid regime is more similar to the annular one (showed in sec. A-A reported in fig. 5.6).

Condenser design is not easy and, because of the presence of all these complex phenomena, numerical methods should be used to predict condenser behaviour and its internal HTC.

5.1.3 Reservoir

Reservoir position and internal structure distinguish the CPLIP from a classical CPL. This component deeply influences the operation of the loop and its behaviour. In Fig. 5.7 a schematic of the reservoir is reported. A separation plate divides the reservoir in two parts. Lower and higher parts communicate through an orifice allowing mass and energy exchanges between them. An electric cartridge heater is used to control saturation temperature, and so saturation pressure, by controlling the electrical power supplied.

In steady-state conditions, sub-cooled liquid, coming from the condenser, flows within the reservoir lower part and no mass exchanges occur with the higher part. There, it is pre-heated until the outlet temperature, T_{RE} , before flowing towards the evaporator (see Fig. 5.1). If loop operating conditions change, mass and energy exchanges between the two sections of the reservoir occur adapting its thermo-hydraulic conditions to the new working point. During transient phases, liquid mass exchanges through the orifice lead to a change of the height of liquid-vapour interface and so to variation of the saturation conditions in the reservoir higher part. Generally, transient phenomena of evaporation and condensation are fast enough to consider the thermodynamic state of the reservoir at nearly constant saturation conditions [25].

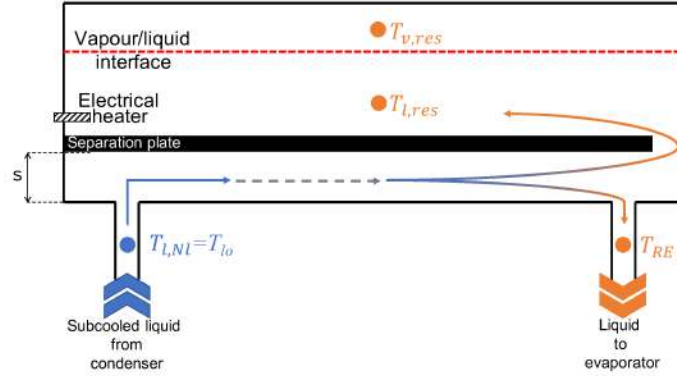


Figure 5.7: Reservoir concept scheme

5.1.4 Transport lines

Except quite smooth internal tube walls requirements, to ensure the lowest pressure drop possible, and particular constraints related to weight-saving or transport distance, transport lines do not require particular characteristics.

Vapour, generated in the evaporator, flows within the vapour line. Due to higher vapour velocity than that related to the liquid flow in the liquid line¹, viscous pressure losses are generally higher. It is so necessary to verify that distributed pressure drops (cumulated with all other ones in the loop), for a given tube diameter and length, are lower than the maximal capillary pressure head in the porous wick. In general, the vapour line diameter should be dimensioned to ensure the lower vapour velocity possible: the one that minimise the pressure drops according to the highest MFR realisable, corresponding to the highest thermal load.

In the liquid line, the undercooled liquid flows from the outlet of the condenser to the reservoir inlet (point represented with the subscript l, Nl in Fig. 5.7 and corresponding to the point lo in Fig. 5.2). Some instabilities could occur if liquid velocity is too high. In general, like all industrial applications, the liquid line diameter is calculated to limit the maximal velocity to $2 \text{ m}\cdot\text{s}^{-1}$, in the case where the maximal mass flow rate occurs (maximal thermal power applied to the evaporator).

5.2 Experimental facility

Over the last decade, Capillary Pumped Loop for Terrestrial Applications have been studied by different authors and for many research purposes [1, 14, 48, 71, 26, 74, 115].

¹In steady state condition $\dot{m} = \rho_v A_v u_v = \rho_l A_l u_l$ in the vapour line (v), and the liquid line (l), respectively.

Prior to the experimental facility used in this study, CPLIP was developed for terrestrial applications. Its purpose was to solve problems related to the use of classical CPLs: low robustness, slow start-up and instabilities during this transient phase. CPLIP was developed for the first time in 2006 for thermal control of power electronics in railways field, whence the name Capillary Pumped Loop for Integrated Power. The first prototype, called “CPLIP 1.0” was built by Euro Heat Pipes (EHPTM) to perform feasibility studies related to power electronics cooling. Power electronics modules were installed on the evaporator and, because of its ability to ensure the temperature requirements on the electronic components, a second prototype (with the same characteristics than the first one) has been built for the same purposes. The latter, like the first one, was equipped by an air-to-liquid condenser to ensure as realistic as possible operating conditions. A maximal air mass flow rate of $1251 \cdot \text{s}^{-1}$ was supplied by a blower to the secondary side of the condenser, which tubes were equipped by 4 mm-spaced-fins generating a maximal external pressure drop of 400 Pa [15].

5.2.1 CPLIP 1.1: the experimental facility

In 2008 a new prototype has been built by EHPTM and Pprime Institute at the ISAE-ENSMA. The CPLIP 1.1, studied for the first time by D. Lossouarn during his Ph.D thesis [15], has been modified (suppressing some measurement equipments) for educational purposes and is still wondrously operating (as it will be shown later) —despite, sometimes, “mistreatments” from students—.

Referring to fig. 5.8, a detailed description of the experimental facility used in this work (CPLIP 1.1) is reported in the following.

The whole loop is made of stainless steel, with the exception of the evaporator where different materials are used to ensure the adequate heat transfer from the heating bodies to the porous wick (see Fig. 5.9).

Reservoir is cylindrical with an external diameter $D_{res} = 99.6 \text{ mm}$ and a length $L_{res} = 308 \text{ mm}$. Its total volume is $V_{res} = 2398.5 \text{ cm}^3$. The height of the separating plate from the reservoir lower wall (s in Fig. 5.7) is 6 mm, so, its volume is $V_{res,low} = 58.7 \text{ cm}^3$. The saturation conditions are imposed using a heating cartridge in the higher part of the reservoir in the liquid phase. Here, on the base of the temperature measurement, it is possible to set the operating point and to control the saturation temperature to the desired value using a PID controller. A temperature platinum sensor has an accuracy of $\pm 0.1^\circ\text{C}$, while the pressure sensor, used to measure the absolute pressure in the reservoir (GE druck PDCR3500), has an accuracy of $\pm 0.1\%$ in the operating range, 0 – 5 bar. The coupling of both sensors allows to measure and control the saturation conditions and, as

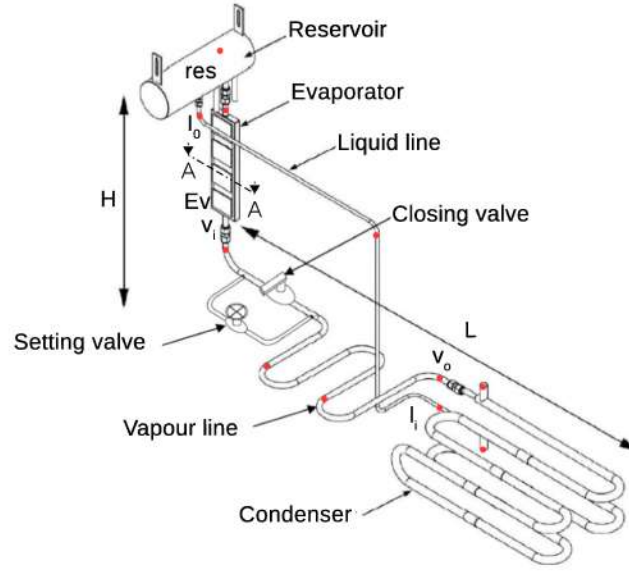


Figure 5.8: Schematic of the CPLIP 1.1 [12, 14, 15]

it will be better explained later, to verify the absence of non condensable gases.

The evaporator is constituted by a stainless steel enclosure, overall dimensions of $296 \times 83 \times 18 \text{ mm}^3$, which contains the nickel porous wick (dimensions $283 \times 68 \times 16 \text{ mm}^3$). The latter (transversal sections reported in Fig. 5.4a and Fig. 5.4b) is characterised by a porosity of 73%, an average pore diameter of $6.8 \mu\text{m}$, a permeability of $6.53 \cdot 10^{-13} \text{ m}^2$ and an effective thermal conductivity of $5 \text{ W} \cdot \text{m}^{-1} \cdot \text{K}^{-1}$. As shown in fig. 5.4a and 5.4c, three liquid arteries allow to supply the liquid coming from the reservoir. The trapezoidal vapour grooves (see fig. 5.4b), which dimensions are 1.2 mm-major, 0.6 mm-minor base and 0.6 mm-height, allow the evacuation of the vapour. The stainless-steel enclosure (see Fig. 5.9) is equipped by eight thermal diffusers (four on each side) positioned face-

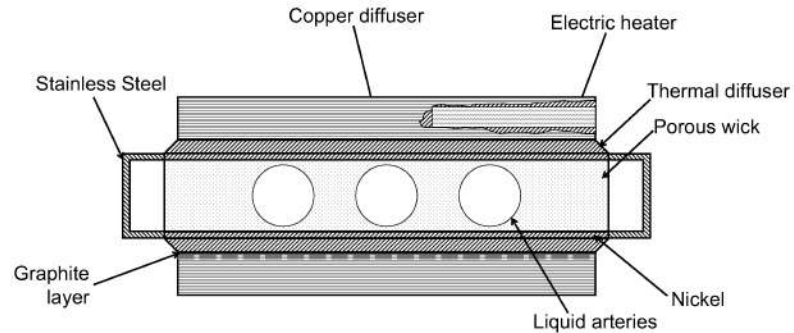


Figure 5.9: Evaporator concept scheme (sec. A-A)

to-face (height 4 mm). Each diffuser is equipped by four thermocouples inserted into external grooves. A copper diffuser is installed on each of them allowing the insertion of the cylindrical heating resistances (two per each one) to simulate the heat sources. A thermal graphite layer (TIM) is used between the first and the second diffuser [50]. The thirty-two evaporator's wall type-T thermocouples have an accuracy of $\pm 0.5^\circ\text{C}$. The evaporator heating resistances are linked to the electrical power supplier (Xantrex, up to 300 V and 30 A) that allows a regulation of the thermal power up to about 8 kW.

The condenser is installed in a favourable position, under the evaporator at a height of 50 cm. It is a 4.04-meter-long, tube-in-tube, heat exchanger supplied on the secondary side by a mass flow rate, up to $20 \text{ kg}\cdot\text{s}^{-1}$ [50], of 30%-ethylene-glycol-water solution cooled by an up to 8 kW thermo-cryostat. The primary fluid side tube has an external diameter of 14 mm and the secondary one has an external diameter of 21.3 mm. Tube thicknesses are 1 and 1.5 mm, respectively.

Vapour and liquid lines are made of stainless-steel like the rest of the loop. The 2.05-meter-long vapour line has the same condenser primary side tube diameters (12 and 14 mm-internal and external-side-diameter, respectively). The liquid line (1.5 m long) has an internal diameter of 6 mm and a thickness of 1 mm. Transport lines are insulated, with a stainless-steel to insulating layer thermal resistance ratio of $2\cdot 10^{-4}$. Bends are included in the vapour line to make it longer.

As one can observe on the scheme reported in fig. 5.8, the vapour line is equipped by a settling valve that allows to regulate vapour pressure drop, by reducing the fluid flow section. The valve flow coefficient, C_v , depends on the number of turns, N , following the polynomial law:

$$C_v = F_c[0.0103N^4 + 0.0909N^3 + 0.178N^2 + 0.3766N + 0.0016] \quad (5.2)$$

with the conversion factor $F_c = 0.116$.

The vapour mass flow rate is related to the flow coefficient as reported in eq. (5.3):

$$\dot{m}_v = 22.4 C_v \sqrt{\Delta P \cdot p_{sat}} \quad (5.3)$$

Red points in fig. 5.8 indicate the position of the 0.1-millimeter-diameter T-type thermocouples installed all over the CPLIP. In particular, in addition to the saturation temperature platinum sensor (T_{res}), the reservoir is equipped by other two thermocouples in its lower and higher parts (named T_{RL} and T_{RV} , respectively). The vapour line is equipped by four thermocouples (named T_{v1} to T_{v4} from the evaporator to the condenser, respectively). The first one is installed at 8 cm from the evaporator outlet and

the others distanced of 49, 69 and 79 cm. The liquid line is equipped by three thermocouples, named T_{l1} to T_{l3} , respectively positioned at the outlet of the condenser, in the middle of the line and at the end. The condenser secondary fluid side thermocouples are installed at the inlet and outlet of the condenser itself [111].

5.3 Numerical models

The complexity of the phenomena regulating the working principle of capillary pumped systems makes of modelling one of the most complex tasks. Other than the classical Navier-Stokes equations (continuity, momentum and energy equations), phase change phenomena have to be considered during this job. In the case of the porous wick, the task is more arduous because of the not well known thermo-fluid dynamic laws.

Many studies have been conducted to model the thermo-fluid dynamic behaviour of a porous wick in which phase change phenomena occur. Mottet *et al.* [113] modelled the behaviour of a LHP's capillary wick in which evaporation occurs. Using the finite volume method, with ammonia as working fluid, they got more realistic results with 3D simulations and obtained the classical bell-shape thermal conductance curve. Beyhaghi *et al.* [116] developed a novel analytical model, using different working fluids (a series of alkaline) and a polycarbonate wick to study the variation of the characteristics of the porous wick (porosity and mean bead radius) to obtain the optimal design.

However, none of the models cited above is adapted for its use in a system approach, that should consider all the phenomena occurring in a capillary pumped loop in a “reasonable” calculation time. Even if numerical results well agree with experimental ones, CFD is a too expensive method to be used during design and optimisation of the overall loop — especially for industrial applications —.

Actually, for a CPILP, it does not exist a standard commercial tool for its design and to estimate its performances. Although many efforts have been done to model this loop to find a good way to design it and predict its behaviour in many configurations and operating conditions [16, 49, 26, 25, 117]. Modelling results well agree with experimental ones, and some models, such as the Blet's one [25], are able to predict with a good agreement the real behaviour of the loop. Unfortunately, this model needs some empirical entries (evaporator and reservoir thermal conductances) to evaluate the thermal behaviour of the loop.

Thanks to the completeness and some peculiarities of the Blet's model, it was used for the purposes related to the present work after adaptation and modification. In particular, as it will be better explained in the following, both steady and transient simulations were

performed to analyse and understand some experimentally observed phenomena. In the following a simplified explanation of the Blet's model is reported.

5.4 CPLIP model

Blet's model [25] is an evolution of Delalandre's model [26]. While the second one [26] was created to study the CPLIP in a single evaporator configuration, the first one [25] represents an adaptation and an improvement of the previous one with the purpose to study a three parallel evaporators configuration of the CPLIP. Thanks to the use of a more advanced reservoir model, and the ability to predict any kind of negative mass flow rate (reversed flow) into the loop², the Blet's model is an important upgrade of the previous one, able to overcome all the limitations and instabilities of Delalandre's model.

The fluid is considered compressible and the vapour phase is considered as a perfect gas. Enthalpy is used instead of temperature as variable in the energy equation. This choice allows to overcome the limitations related to the use of the temperature to define the physical state of the fluid. In fact, if temperature is used, the fluid thermophysical properties present a discontinuity in correspondence of the saturation temperature. Thanks to the hypothesis of homogeneous fluid, the different fluid properties can be defined as a function of the vapour mass fraction, x , and considering the enthalpy. No more discontinuities are related to the physic state of the fluid in correspondence of the saturation temperature. According to McAdams formulation, in fact, the phase change is managed as follows:

$$\begin{cases} h < h_{l,sat}(P) & x = 0 & \text{(liquid phase)} \\ h_{l,sat}(P) \leq h \leq h_{v,sat}(P) & x = \frac{h - h_{l,sat}(P)}{h_{v,sat}(P) - h_{l,sat}(P)} & \text{(two - phase)} \\ h > h_{v,sat}(P) & x = 1 & \text{(vapour phase)} \end{cases}$$

All fluid's thermophysical properties, in single or two-phase state, are so evaluated from pressure, P , and enthalpy, h , as well as the fluid temperatures.

Beyond the just cited assumptions, other strong hypothesis on which the model is based are [25]:

- conduction thermal resistance is neglected in the radial direction in the transport lines;

²This particular characteristic will be particularly useful during the study of the CPLIP in a cycle of sudden and violent accelerations.

- the higher part of the reservoir is always in two-phase state and the vapour phase is always considered in saturation condition: the reservoir higher part is the only “place” where the hypothesis of homogeneity of the fluid is not respected, so vapour and liquid phases always co-exist here;
- the porous wick is always filled of liquid, so the liquid/vapour interface is always positioned in correspondence of the mesh. The fluid-flow in the latter is considered fully developed and one dimensional in the direction of the wick thickness.

A staggered grid (see fig. 5.10) is used to model mass, momentum and energy exchanges in the loop.

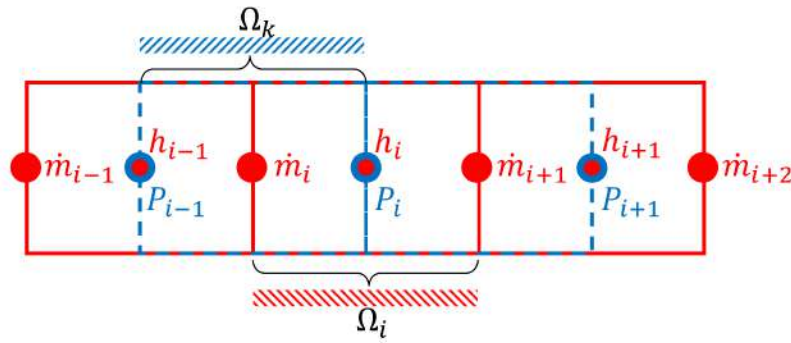


Figure 5.10: Staggered grid

Mass nodes, belonging to Ω_i (red volume in fig. 5.10), are positioned on the bounds of the cell, while enthalpy nodes, belonging to the same volume, Ω_i , are positioned in the centre of red grid. This last position also corresponds to pressure nodes, positioned on the bounds of Ω_k (blue volume in fig. 5.10), shifted by one-half control volume than mass nodes. This configuration allows the minimisation of errors related to the calculation of the fluid thermophysical properties (based either on P and h) and reduces instabilities related to the presence of velocity and pressure variables on the same node [25].

The numerical model has been developed to use the thermal-hydraulic/electrical analogy on ESACAP^(C) solver [16]. Mass, momentum and energy equations have been rewritten in order to be consistent with the required network formalism. A finite volume method was used to discretise the Navier-Stokes equations in their 1D form [25]³.

5.4.1 Navier-Stokes equations

Except the higher part of the reservoir, all over the domain the fluid is supposed homogeneous and the control volumes fixed and constant. The general form of Navier-Stokes

³For more details about this model, the interested reader is invited to read ref. [25].

equations integrated on such control volume Ω delimited by the surface Σ , are directly used for single and two-phase fluid state. The integral form of mass conservation equation is:

$$\frac{D}{Dt} \int_{\Omega} \rho d\omega = 0 \quad (5.4)$$

The momentum equation in its integral form is:

$$\frac{D}{Dt} \int_{\Omega} \rho \vec{v} d\omega = \oint_{\Sigma} P \vec{n}_i d\sigma + \int_{\Omega} \rho \vec{g} d\omega + \oint_{\Sigma} \bar{\vec{\tau}} \cdot \vec{n}_i d\sigma \quad (5.5)$$

Finally the integral form of the energy equation on the previously defined control volume is:

$$\frac{D}{Dt} \int_{\Omega} \rho h d\omega = \dot{Q}_{ext} + \frac{D}{Dt} \int_{\Omega} P d\omega - \int_{\Omega} P \operatorname{div}(\vec{v}) d\omega + \int_{\Omega} \bar{\vec{\tau}} : \bar{\vec{D}} d\omega \quad (5.6)$$

With reference to the grid structure reported in Fig. 5.10, the discretised form of conservation equations (continuity, momentum and energy) related to the transport lines and the condenser is reported in the following.

5.4.1.1 General case (vapour and liquid lines, condenser)

Continuity equation Considering a fixed and constant control volume Ω_i , the mass conservation equation can be written in its one-dimensional form, according to the discretisation reported in fig. 5.10 as:

$$\Omega_i \frac{d\rho_i}{dt} = \dot{m}_i - \dot{m}_{i+1} \quad (5.7)$$

Momentum equation Referring to the discretisation reported in Fig. 5.10, eq. (5.5) can be rewritten to agree with the used formalism [25].

As said before, one of the most important characteristics of the Blet's model is the ability to take into account reversed flows into the loop. Momentum equation can be so written in two different forms following the flow direction. Considering, as an example, the control volume Ω_{k+1} , for $\dot{m}_{i+1} \geq 0$ it is [25]:

$$\begin{aligned} \frac{L_i + L_{i+1}}{2} \frac{d\dot{m}_{i+1}}{dt} + \dot{m}_{i+1} \frac{\frac{1}{2}(\dot{m}_{i+1} + \dot{m}_{i+2})}{\frac{\rho_i \Omega_i + \rho_{i+1} \Omega_{i+1}}{\Omega_i + \Omega_{i+1}} S_{i+1}} - \dot{m}_i \frac{\frac{1}{2}(\dot{m}_i + \dot{m}_{i+1})}{\frac{\rho_{i-1} \Omega_{i-1} + \rho_i \Omega_i}{\Omega_{i-1} + \Omega_i} S_i} \\ + (P_{i+1} - P_i) S_{eq,i/i+1} \pm \frac{\rho_i H_i S_i + \rho_{i+1} H_{i+1} S_{i+1}}{2} g \\ + \frac{1}{2} (|\Delta P_{vis,i}| S_i + |\Delta P_{vis,i+1}| S_{i+1}) = 0 \end{aligned} \quad (5.8)$$

and for $\dot{m}_{i+1} < 0$ it is [25]:

$$\begin{aligned} \frac{L_i + L_{i+1}}{2} \frac{d\dot{m}_{i+1}}{dt} + \dot{m}_{i+2} \frac{\frac{1}{2}(\dot{m}_{i+1} + \dot{m}_{i+2})}{\frac{\rho_{i+1}\Omega_{i+1} + \rho_{i+2}\Omega_{i+2}}{\Omega_{i+1} + \Omega_{i+2}}} S_{i+1} - \dot{m}_{i+1} \frac{\frac{1}{2}(\dot{m}_i + \dot{m}_{i+1})}{\frac{\rho_i\Omega_i + \rho_{i+1}\Omega_{i+1}}{\Omega_i + \Omega_{i+1}}} S_i \\ + (P_{i+1} - P_i) S_{eq,i/i+1} \pm \frac{\rho_i H_i S_i + \rho_{i+1} H_{i+1} S_{i+1}}{2} g \\ - \frac{1}{2} (|\Delta P_{vis,i}| S_i + |\Delta P_{vis,i+1}| S_{i+1}) = 0 \quad (5.9) \end{aligned}$$

Where S is the transversal section, normal to the flow, and H the height. Either in eq. (5.8) and (5.9) the sign used for the hydrostatic losses (second-to-last term on the left side) depends on the position of the control volume with respect of the \vec{g} direction.

Energy balance Referring to the control volume Ω_i , in the mesh example reported in Fig. 5.10, the discretised form of the energy equation, if $\dot{m}_i \geq 0$, is [25]:

$$\rho_i \Omega_i \frac{dh_i}{dt} = \dot{m}_i (h_{i-1} - h_i) + \dot{Q}_{ext,i} + \dot{W}_{comp,i} \quad (5.10)$$

and in the reversed flow case ($\dot{m}_i < 0$):

$$\rho_i \Omega_i \frac{dh_i}{dt} = \dot{m}_{i+1} (h_i - h_{i+1}) + \dot{Q}_{ext,i} + \dot{W}_{comp,i} \quad (5.11)$$

In eq. (5.10) and (5.11), $\dot{W}_{comp,i}$ is the term related to the work compression. Blet demonstrated that the latter is about 3% of $\dot{Q}_{ext,i}$, so to simplify the model it has been neglected [25]. $\dot{Q}_{ext,i}$ is heat flux density received by node i from adjacent nodes, considering conduction, convection and radiative exchanges. To calculate such term it is necessary to introduce a thermal network (see also Fig. 5.15d) relating the fluid with the solid walls and the external environment. For its resolution, the thermal network model uses the temperature field obtained by the enthalpy-mass and pressure networks as boundary conditions.

5.4.1.2 Reservoir

Due to its separation in two sections, different formulations have to be used to model this component. In the lower part of the reservoir, the fluid is considered homogeneous. The same formulation as the rest of the loop is used. The higher part requires the use of a non-homogeneous model because of the co-existence of the two fluid phases at every moment.

5.4.1.2.1 Reservoir lower part A schematic of the reservoir, on which the discretisation of Fig. 5.12 is based, is reported in Fig. 5.11. The lower part of the reservoir is discretised using just one node, defined as res, low in Fig. 5.12 and positioned between the last node of the liquid line (l, NI) and the node of the reservoir-evaporator tube (RE).

Mass balance For the mass balance equation, mass exchanges occurring between the lower and the higher part of the reservoir have to be considered. So, the mass flow rate flowing through the orifice, \dot{m}_{res} , is defined as:

$$\dot{m}_{res} = \dot{m}_{res,I} - \dot{m}_{res,O} \quad (5.12)$$

Where the inlet and outlet fluid mass flow rates, $\dot{m}_{res,I}$ and $\dot{m}_{res,O}$, respectively, are evaluated from the overall mass flow network related to the whole loop.

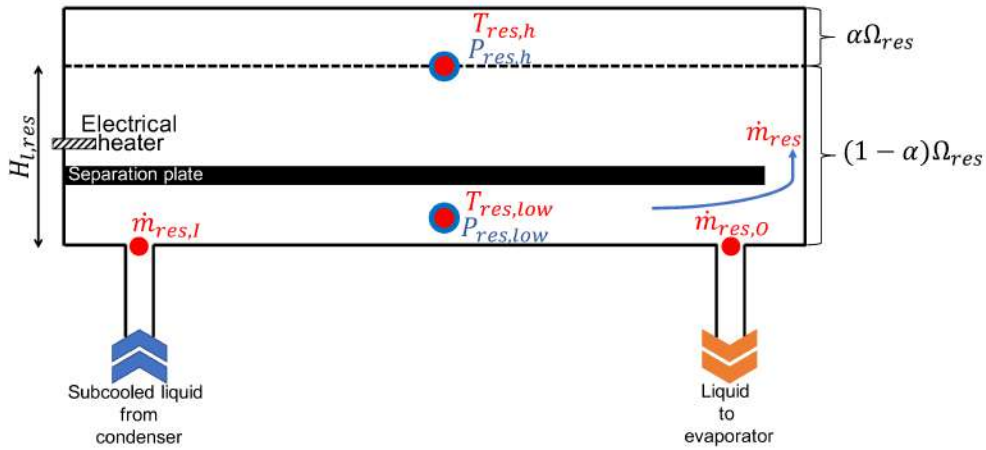


Figure 5.11: Reservoir schematic

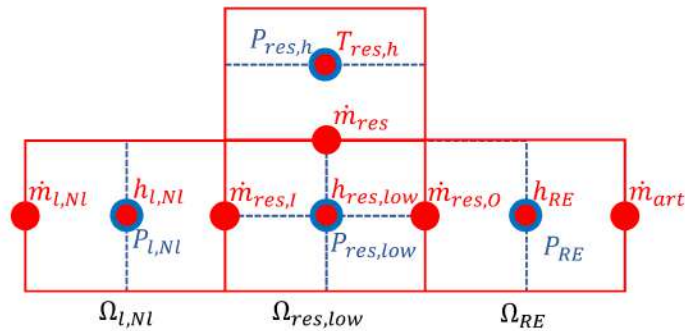


Figure 5.12: Reservoir lower part discretisation

Momentum balance Like transport lines and condenser, in the reservoir's lower part, momentum balance is dependent on the flow direction. Because of the presence of the mass flow rate exchanged between the lower and the higher part, \dot{m}_{res} , the momentum equation has to be written either for inlet and outlet nodes to consider such difference (also defined by eq. (5.12)). Three different cases can be so realised following the direction of the mass flow rate at the inlet, $\dot{m}_{res,I}$, the outlet, $\dot{m}_{res,O}$, and through the orifice, \dot{m}_{res} . In the first case, a positive mass flow rate flows within the inlet and the outlet of the reservoir and, at the same time, a liquid mass flow rate flows from the lower to the higher part. The second case is realised when a positive mass flow rate flows either through the reservoir inlet and outlet, but a negative mass flow rate flows through the orifice (the liquid contained in the higher part flows to the evaporator). These first two cases are realised during normal operations of the loop when a change in its operating conditions occurs: in the first case the required thermal load has been increased and in the second case decreased, for example. The third case, critical, is realised when the liquid contained in the higher part is reversed to the lower section, but exiting from the reservoir either through the outlet and the inlet nodes. The reservoir inlet becomes a "second exit" and the loop does not operate in a "conventional" way. This case, as it will be shown in chap. 9, is realised, for example, during harsh transient accelerations stages or, as explained by Blet, during severe thermal unloads [25]. To consider the described phenomena, discretised momentum equations are reported for the inlet and the outlet nodes of the reservoir [25]. The reservoir inlet considers the semi-volume including the node l, Nl and the reservoir outlet includes the node RE .

At the inlet of the reservoir, between the nodes $P_{l,Nl}$ and $P_{res,low}$, the momentum equation, for $\dot{m}_{res,I} \geq 0$, is:

$$\begin{aligned} \frac{L_{l,Nl}}{2} \frac{d\dot{m}_{res,I}}{dt} + \frac{\dot{m}_{res,I}^2}{\frac{\rho_{l,Nl}\Omega_{l,Nl} + \rho_{res,low}\Omega_{res,low}}{\Omega_{l,Nl} + \Omega_{res,low}} S_L} \\ - \dot{m}_{l,Nl} \frac{\frac{1}{2}(\dot{m}_{l,Nl} + \dot{m}_{res,I})}{\frac{\rho_{l,Nl-1}\Omega_{l,Nl-1} + \rho_{l,Nl}\Omega_{l,Nl}}{\Omega_{l,Nl-1} + \Omega_{l,Nl}} S_L} + (P_{res,low} - P_{l,Nl})S_L \\ + \frac{\rho_{l,Nl}H_{l,Nl}S_L}{2}g + \frac{1}{2}|\Delta P_{vis,l,Nl}|S_L = 0 \quad (5.13) \end{aligned}$$

and for $\dot{m}_{res,I} < 0$ it is:

$$\frac{L_{l,Nl}}{2} \frac{d\dot{m}_{res,I}}{dt} + \frac{\dot{m}_{res,I}^2}{\frac{\rho_{res,low}\Omega_{res,low} + \rho_{res,h}\Omega_{res,h}}{\Omega_{l,Nl} + \Omega_{res,low}} S_L}$$

$$\begin{aligned}
& - \dot{m}_{res,I} \frac{\frac{1}{2}(\dot{m}_{l,Nl} + \dot{m}_{res,I})}{\frac{\rho_{l,Nl}\Omega_{l,Nl} + \rho_{res,low}\Omega_{res,low}}{\Omega_{l,Nl} + \Omega_{res,low}}} S_L + (P_{res,low} - P_{l,Nl})S_L \\
& + \frac{\rho_{l,Nl}H_{l,Nl}S_L}{2}g - \frac{1}{2}|\Delta P_{vis,l,Nl}|S_L = 0
\end{aligned}$$

For the outlet node, between the nodes $P_{res,low}$ and P_{RE} , considering $\dot{m}_{res,I} \geq 0$ and $\dot{m}_{res} \geq 0$, the momentum equation is in the form:

$$\begin{aligned}
& \frac{L_{RE}}{2} \frac{d\dot{m}_{res,O}}{dt} + \dot{m}_{res,O} \frac{\frac{1}{2}(\dot{m}_{res,O} + \dot{m}_{art})}{\frac{\rho_{RE}\Omega_{RE} + \rho_{res,low}\Omega_{res,low}}{\Omega_{RE} + \Omega_{res,low}}} S_{RE} \\
& - \frac{\dot{m}_{res,O}^2}{\frac{\rho_{l,Nl}\Omega_{l,Nl} + \rho_{res,low}\Omega_{res,low}}{\Omega_{l,Nl} + \Omega_{res,low}}} S_{RE} + (P_{RE} - P_{res,low})S_{RE} \\
& - \frac{\rho_{RE}H_{RE}S_{RE}}{2}g + \frac{1}{2}|\Delta P_{vis,RE}|S_{RE} = 0 \quad (5.14)
\end{aligned}$$

while, for the same mass flow direction, but $\dot{m}_{res} < 0$, it becomes:

$$\begin{aligned}
& \frac{L_{RE}}{2} \frac{d\dot{m}_{res,O}}{dt} + \dot{m}_{res,O} \frac{\frac{1}{2}(\dot{m}_{res,O} + \dot{m}_{art})}{\frac{\rho_{RE}\Omega_{RE} + \rho_{res,low}\Omega_{res,low}}{\Omega_{RE} + \Omega_{res,low}}} S_{RE} \\
& - \frac{\dot{m}_{res,O}^2}{\frac{\rho_{l,Nl}\Omega_{l,Nl} + \rho_{res,low}\Omega_{res,low} + \rho_{res,h}\Omega_{res,h}}{\Omega_{l,Nl} + \Omega_{res,low} + \Omega_{res,h}}} S_{RE} + (P_{RE} - P_{res,low})S_{RE} \\
& + \frac{\rho_{RE}H_{RE}S_{RE}}{2}g + \frac{1}{2}|\Delta P_{vis,RE}|S_{RE} = 0 \quad (5.15)
\end{aligned}$$

Finally, if an inversion of the flow occurs ($\dot{m}_{res,I} < 0$) and $\dot{m}_{res} < 0$, it is:

$$\begin{aligned}
& \frac{L_{RE}}{2} \frac{d\dot{m}_{res,O}}{dt} + \dot{m}_{res,O} \frac{\frac{1}{2}(\dot{m}_{res,O} + \dot{m}_{art})}{\frac{\rho_{RE}\Omega_{RE} + \rho_{res,low}\Omega_{res,low}}{\Omega_{RE} + \Omega_{res,low}}} S_{RE} \\
& - \frac{\dot{m}_{res,O}^2}{\frac{\rho_{res,low}\Omega_{res,low} + \rho_{res,h}\Omega_{res,h}}{\Omega_{res,low} + \Omega_{res,h}}} S_{RE} + (P_{RE} - P_{res,low})S_{RE} \\
& - \frac{\rho_{RE}H_{RE}S_{RE}}{2}g + \frac{1}{2}|\Delta P_{vis,RE}|S_{RE} = 0 \quad (5.16)
\end{aligned}$$

Energy balance Considering the flow direction, even for energy balance, two different equations have to be written for this case. When $\dot{m}_{res,I} \geq 0$, the energy equation has the form:

$$\rho_{res,low}\Omega_{res,low} \frac{dh_{res,low}}{dt} = \dot{m}_{res,I}(h_{l,Nl} - h_{res,low}) + \dot{Q}_{ext,res,low} + \dot{W}_{compres,low} \quad (5.17)$$

Due to the absence of the hypothesis of fluid homogeneity in the higher part of the reservoir, if $\dot{m}_{res,I} < 0$ the energy equation is written using the temperature instead of the enthalpy formulation. In this case, eq. (5.17) becomes:

$$\rho_{res,low} \Omega_{res,low} \frac{dh_{res,low}}{dt} = \dot{m}_{res,I} c_{pl} (T_{res,low} - T_{res,h}) + \dot{Q}_{ext_{res,low}} + \dot{W}_{comp_{res,low}} \quad (5.18)$$

where the compression work is $\dot{W}_{comp_{res,low}} = \Omega_{res,low} \frac{dP_{res,low}}{dt}$, and

$$dh = c_p dT + \frac{1}{\rho} (1 - \beta T) dP$$

with β the compressibility factor of the fluid.

5.4.1.2.2 Reservoir higher part In this section of the reservoir, liquid and vapour phases, separated by a well defined interface, co-exist. Because of the just cited reason, the hypothesis of homogeneous fluid cannot be applied anymore and a different approach has to be used to model this part of the loop. In this case, Blet chose to use a “macroscopic” approach.

The reservoir is an expansion tank in which the height of the liquid/vapour interface changes as a function of the working point in order to absorb any volume variation of the fluid in the loop. To consider such volume variation, the volume fraction of vapour in the reservoir, α , is introduced. The latter is defined as the ratio between the volume occupied by the vapour, $\Omega_{v,res}$, and the total reservoir volume, Ω_{res} :

$$\alpha = \frac{\Omega_{v,res}}{\Omega_{res}} \quad (5.19)$$

The mass balance equation assumes the form of a differential equation solved in α . Either liquid and vapour densities are so considered. The mass flow rate exchanged between the lower and the higher part of the reservoir is defined by eq. (5.20):

$$(\rho_{l,res} - \rho_{v,res}) \Omega_{res} \frac{d\alpha}{dt} + \Omega_{res} \frac{d\rho_{v,res}}{dt} \alpha = \dot{m}_{res} \quad (5.20)$$

As the reservoir lower part is modelled using a single node, the pressure in this part of the expansion tank is constant all along the lower part. Moreover, under the hypothesis of saturating vapour in the higher part, the pressure corresponds to the saturation one: $P_{res,h} = P_{sat}(T_{res,h})$. Considering the height of the liquid/vapour interface, $H_{l,res}$, the pressure in the reservoir lower part, $P_{res,low}$ is calculated considering the hydrostatic

pressure:

$$P_{res,low} = P_{res,h} + \rho_{l,res} g H_{l,res} \quad (5.21)$$

The complexity related to the modelling of this component requires the use of some empiric conductances. In Fig. 5.13, the complex thermo-hydraulic model developed by Blet [25], to obtain the thermal and hydraulic couplings in the reservoir higher part, is reported.

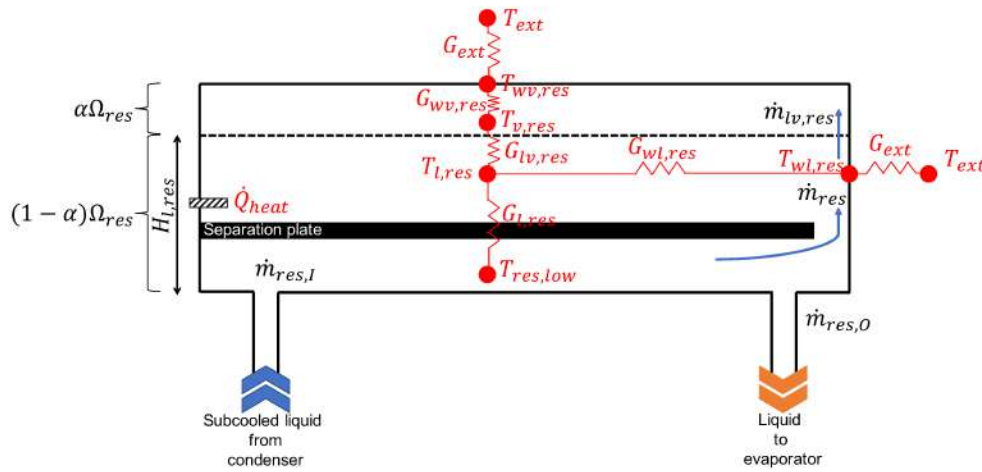


Figure 5.13: Reservoir higher part thermo-hydraulic model

The empiric thermal conductance $G_{l,res}$, coupling the liquid temperature in the higher and the lower part of the reservoir, $T_{l,res}$ and $T_{res,low}$, respectively, considers: the convective heat exchanges between the liquid in the low reservoir and the separation plate; the convective heat exchanges in the higher part of the reservoir, considering the stratification and the heating cartridge, and, finally, the conductive heat transfer through the separation plate and the reservoir walls [25]. The thermal conductance $G_{lv,res}$, considers the conductive heat exchanges within the liquid and the stratification system. The empiric thermal conductances between the wall and the liquid phase and between the wall and the vapour phase, $G_{wl,res}$ and $G_{wv,res}$, respectively, are assumed constant and dependent on the saturation temperature [25].

Considering the model reported in Fig. 5.13, the saturated vapour temperature in the reservoir higher part can be calculated as:

$$\rho_{v,res} c_{p_{v,res}} \alpha \Omega_{res} \frac{dT_{v,res}}{dt} = G_{lv,res} (T_{l,res} - T_{v,res}) + G_{wv,res} (T_{wv,res} - T_{v,res})$$

$$+ \Omega_{res} \frac{d(P_{v,res} \alpha)}{dt} - \dot{m}_{lv,res} h_{lv} \quad (5.22)$$

The evaporation heat flow rate term, $\dot{m}_{lv,res} h_{lv}$, is considered if and only if $\dot{m}_{lv,res} \geq 0$. $\dot{m}_{lv,res}$ is defined as the sum between the mass flow rate flowing within the orifice, \dot{m}_{res} , and the time dependent variation of the vapour volume fraction:

$$\dot{m}_{lv,res} = \dot{m}_{res} + \rho_{l,res} \Omega_{res} \frac{d\alpha}{dt}$$

The liquid temperature in the higher part of the reservoir, $T_{l,res}$, like $T_{v,res}$, is calculated considering the compression work, $\dot{W}_{comp,l}$ and the heating power \dot{Q}_{ext} as well as the thermal network:

$$\begin{aligned} \rho_{l,res} c_{pl,res} (1 - \alpha) \Omega_{res} \frac{dT_{l,res}}{dt} = \\ G_{l,res} (T_{res,low} - T_{l,res}) + G_{lv,res} (T_{v,res} - T_{l,res}) + G_{wl,res} (T_{wl,res} - T_{w,res}) \\ + \dot{Q}_{heat} + \dot{W}_{comp,l} + \dot{m}_{res}^* c_{pl,res} (T_{res,low} - T_{l,res}) - \dot{m}_{lv,res} h_{lv} \end{aligned} \quad (5.23)$$

Where, in eq. (5.23), the term $\dot{m}_{res}^* = \dot{m}_{res}$ if $\dot{m}_{res} \geq 0$, and $\dot{m}_{res}^* = 0$ else. So, the evaporation heat flow rate term, $\dot{m}_{lv,res} h_{lv}$, in eq. (5.23) is only considered when $\dot{m}_{lv,res} < 0$. The energy balance due to the mass flow rate flowing within the orifice from the lower to the higher part of the reservoir is considered for positive or null values of \dot{m}_{res} .

To have a better modelling related to the momentum balance, the pressure in the higher part has to be considered by taking into account the pressure of the liquid and the pressure of the vapour at the interface, $P_{l,res}$ and $P_{v,res}$, respectively. So, following the hypothesis of saturated vapour⁴, it is:

$$P_{v,res} = P_{sat}(T_{v,res})$$

The momentum balance in the higher liquid part is defined as a function of the variation of the height of the liquid/vapour interface, $H_{l,res}$, related to the mass flow rate flowing within the orifice, \dot{m}_{res} :

$$\frac{d(\dot{m}_{res} H_{l,res})}{dt} + \frac{\dot{m}_{res,O}^2}{\rho_{l,res} S_{RE}} - \frac{\dot{m}_{res,I}^2}{\rho_{l,res} S_L} +$$

⁴In ref. [71], it has been observed that the time constant of evaporation/condensation in the higher part of the reservoir is negligible if compared to those of eq. (5.20), (5.22) and (5.23). So, the return to saturated equilibrium is considered instantaneous in the vapour volume of the reservoir.

$$\left(\frac{\dot{m}_{lv,res}}{\rho_{l,res} S_{lv,res}} + \frac{dH_{l,res}}{dt} \right) \dot{m}_{lv,res} + |\Delta P_{vis,res}| S_{eq,res} + \rho_{l,res} g H_{l,res} S_{eq,res} + (P_{l,res} - P_{res,low}) = 0 \quad (5.24)$$

The momentum balance equation in correspondence of the liquid/vapour interface is:

$$P_{l,res} - P_{v,res} = \frac{\dot{m}_{lv,res}^2}{S_{lv,res}^2} \left(\rho_{v,res}^{-1} - \rho_{l,res}^{-1} \right) \quad (5.25)$$

5.4.1.3 Evaporator

Due to complex thermo-hydraulic phenomena occurring there, a “microscopic” approach to model the evaporator behaviour, at pore level of the porous wick, leads to high computation time. Moreover, pretty high difficulties are related to the coupling of such model to the rest of the loop. To solve the problem, Delalandre [26], before, and Blet [71], after, decided to use some empiric parameters for its modelling.

The thermal load, \dot{Q}_{evap} , applied to the evaporator is used to heat the casing and the porous wick, to warm the liquid arriving from the reservoir (until saturation condition in correspondence of the liquid/vapour interface —sensible heat exchange—), for liquid-vapour phase change (latent heat exchange) and for vapour superheating. Introducing the empiric thermal conductance, G_V , and the conductances G_{ch} and G_{chlat} , relying the temperature of the casing, T_C , respectively with the saturation temperature in the porous wick T_V , the fluid temperature in the grooves T_{ch} (Fig. 5.4b) and the fluid temperature in the lateral grooves T_{chlat} (vapour channels), in steady-state conditions eq. (5.26) has to be verified.

$$\dot{Q}_{evap} - \dot{Q}_{loss} = \dot{Q}(G_V) + \dot{Q}(G_{ch}) + \dot{Q}(G_{chlat}) \quad (5.26)$$

Four control volumes are considered for evaporator modelling (see Fig. 5.14). In particular, the volumes are related to the (three) liquid arteries, Ω_{art} , to the whole porous wick, Ω_{por} , to the grooves, Ω_{ch} and to the lateral vapour channels, Ω_{chlat} (see also Fig. 5.4).

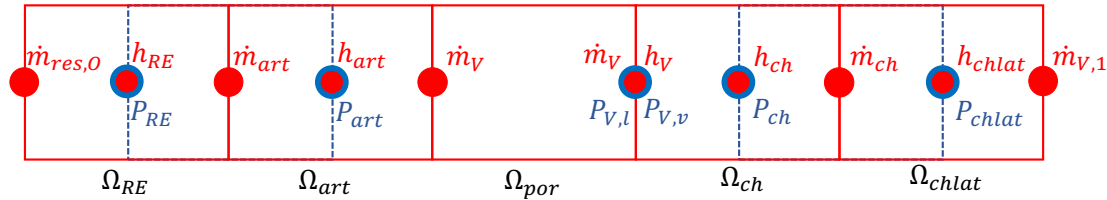


Figure 5.14: Evaporator discretisation

Due to the hypothesis of fully developed 1-D fluid flow in the direction of the thickness of the wick, and complete filling of the latter, the mass flow rate entering and exiting the porous wick is always equal to the evaporating mass flow rate \dot{m}_V . Moreover, the enthalpy is always dependent on the saturation pressure: $h_V = h_{v,sat}(P_{ch})$.

The mass conservation equation, due to the strong hypothesis of complete filling of the wick, assumes the same form of eq. (5.7). The mass flow rate \dot{m}_V is so imposed following the energy balance on the node related to the wick (*por*):

$$\dot{m}_V = \frac{\dot{Q}(G_V)}{\left(h_{lv}\big|_{T_V} + c_{p,l}(T_V - T_{art})\right)} \quad (5.27)$$

The equation related to the momentum balance assumes the same form of eq. (5.13). In correspondence of the volume related to the wick where the liquid is pumped, following the hypothesis of fully developed flow as well as the hypothesis whereby the liquid/vapour interface is considered to be always positioned on the surface of the wick, the pressure difference is given by the Darcy law:

$$P_{art} - P_{V,l} = \frac{\mu_l e_{por}}{\kappa \rho_l S_{por}} \dot{m}_V \quad (5.28)$$

where κ is the permeability of the porous wick and provided by the evaporator manufacturer [50].

The energy balance equation related to the fluid is similar to eq. (5.10) and (5.11), while for the solid part it is:

$$\begin{aligned} \rho_C \Omega_C c_{pC} \frac{dT_C}{dt} = & \dot{Q}_{eva} - \dot{Q}_{loss} + G_V (T_V - T_C) + G_{ch} (T_{ch} - T_C) \\ & + G_{chlat} (T_{chlat} - T_C) \end{aligned} \quad (5.29)$$

where the thermal conductances G_{ch} and G_{chlat} are calculated as a function of the heat transfer coefficients h_{ch} and h_{chlat} , and in turn calculated using standard correlation for a uniformly heated flat plate.

5.4.2 Thermal/electrical analogy

Mass, momentum and energy equations are solved using the electric analogy. The model has been adapted to agree with the formalism used by ESACAP^(TM) [25] that allows a robust resolution of strongly coupled differential equation systems by using the

thermal/electrical analogy. On its basis, temperature and pressure difference in thermal and hydraulic domains can be compared with the voltage difference of an electrical system, while thermal heat flux and mass flow rate can be compared with current variable.

According to the nodal method, each elemental control volume Ω_i , is supposed isothermal and characterised, in the centre, by a thermal capacity $C_i = \rho_i c_{p,i} \Omega_i$. If the thermal conductance $G_{i,j}$ between two adjacent nodes, i and j , is considered, the thermal heat flux exchanged can be in generally written, if the thermal heat flux is directed from the node j to the node i , in the form:

$$\dot{Q}_{i,j} = G_{i,j}(T_j - T_i) \quad (5.30)$$

Vice-versa, $\dot{Q}_{i,j} = G_{i,j}(T_i - T_j)$ if the heat flux is lost by the node i towards the node j . The energy balance equation, considering conductive, convective and radiative heat transfer as well as the k -th heat source heat generation, \dot{q}_k , in the node i , can be so written as:

$$C_i \frac{dT_i}{dt} = \sum_j \dot{Q}_{i,j}^{cond} + \sum_j \dot{Q}_{i,j}^{conv} + \sum_j \dot{Q}_{i,j}^{rad} + \sum_k \dot{q}_k \quad (5.31)$$

When a fluid flow occurs in the system, as well as $\dot{Q}_{i,j}^{cond}$, $\dot{Q}_{i,j}^{conv}$, $\dot{Q}_{i,j}^{rad}$, it is necessary to add to the right term of eq. (5.31) the heat flux related to mass exchange between the node $i - 1$ and the node i . So that, according to the enthalpy formulation used in this model, the heat transported by the fluid is defined as:

$$\dot{Q}_{i-1,i} = \dot{m}_i (h_{i-1} - h_i) \quad (5.32)$$

and eq. (5.31) assumes the form:

$$\rho_i \Omega_i \frac{dh_i}{dt} = \dot{m}_i (h_{i-1} - h_i) + \dot{Q}_{i,j}^{rec} \quad (5.33)$$

where $\dot{Q}_{i,j}^{rec}$ is the “cumulated” thermal flux received by the volume Ω_i due to internal heat generation, \dot{q}_k , and conduction, convection and radiation heat transfer ($\dot{Q}_{i,j}^{cond}$, $\dot{Q}_{i,j}^{conv}$, $\dot{Q}_{i,j}^{rad}$). The particular property of reciprocity related to the heat flux direction in eq. (5.30) is no more valid in eq. (5.32). According to fluid direction, the heat may only be transferred in one direction: from the node $i - 1$ to the node i . The fluidic conductance GF_i , related to the mass flow rate \dot{m}_i , is thus strictly dependent on the flow direction, and for mono-directional flows it is $GF_i = \dot{m}_i$.

The formulation related to eq. (5.33) needs to be modified to consider any change in

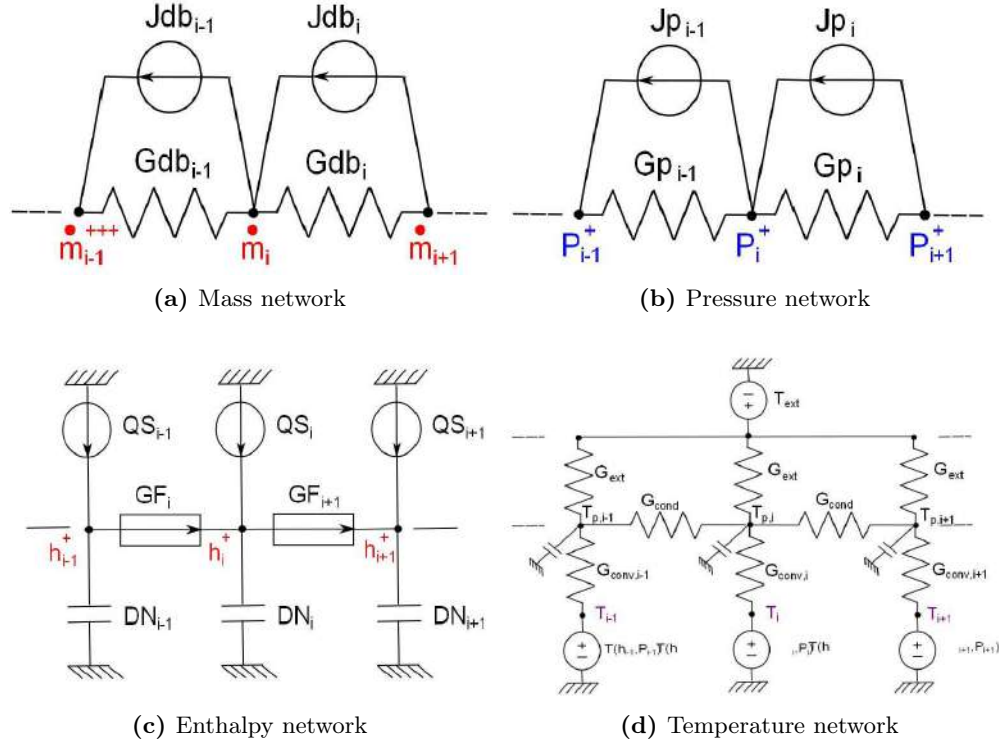


Figure 5.15: Thermal/hydraulic-electrical analogy networks [16]

the mass flow direction. In such case, in fact, $GF_i^{\leftrightarrow} = (\dot{m}_i; \dot{m}_{i+1})$ and eq. (5.33) becomes:

$$\dot{Q}(GF_i^{\leftrightarrow}) = \dot{m}_i^* (h_{i-1} - h_i) + \dot{m}_{i+1}^* (h_i - h_{i+1}) \quad (5.34)$$

Where, $\dot{m}_i^* = \dot{m}_i$ if $\dot{m}_i \geq 0$ and $\dot{m}_{i+1}^* = \dot{m}_{i+1}$ if $\dot{m}_{i+1} < 0$, otherwise they are null: the first term on the right side of eq. (5.34) is related to a positive MFR (from node $i - 1$ to i) and the second term is related to a negative mass flow rate (from node $i + 1$ to i).

Examples of networks used in Blet's model are reported in Fig. 5.15. There, the mass network (fig. 5.15a), related to the continuity equation solution; the pressure network (see fig. 5.15b), related to momentum equation; the mass enthalpy network (see fig. 5.15c), related to the energy balance equation, are shown. Finally, the temperature network (fig. 5.15d) used to relate the fluid model to external (thermal) conditions such as tube wall temperature, ambient temperature, heat power and cold source temperature.

5.5 Conclusion

In this chapter, the main characteristics of the CPILP were described focusing the attention on the physical phenomena governing its operations. CPLIP working principle was explained on the base of the thermodynamic transformation shown on (P, T) diagram and an explanation of the governing physics of each component of the loop has been given to understand its potentials and limitations. After a brief history about the Capillary Pumped Loop for Integrated Power, the experimental facility, used in the context of this work, has been introduced to explain its mechanical, hydraulic and thermal characteristics. A deep description of the measure sensors equipping the experimental loop has been also done to give an idea of the accuracy of measurements that will be presented during the entire description and analysis of this work. It has to be underlined that to increase the quantity of the measurement, more sensors would be required, but such experimental facility is also used for educational purposes. Any kind of modification to the CPLIP 1.1 could not be actually considered. Moreover, although the loop is used by students, after several years, it keeps its characteristics and potentialities. This is, as it will be observed later, one of the main characteristics of these systems: high reliability and robustness. Finally, the numerical model used in this work was described. Obviously, in the model, not all physical phenomena, such as mass and energy exchanges in the evaporator, are considered because of their complexity. It is, after all, a model that describes the loop behaviour using a “system approach”, and it is used to have a quantitative evaluation of the thermal and hydraulic magnitude. Initially, this model was developed to study the behaviour of a three parallel evaporators CPLIP and a validation has been done in this particular configuration. A good agreement between the numerical and the experimental results was observed in this particular case [25]. However, after an adaptation of the described model to the experimental facility here introduced, numerical and experimental results will be compared to show the agreement with new experimental results presented in this study, by adapting the conductances G_V , G_{res} and vapour, condenser, and liquid line geometry, as well as the reservoir one to the experimental facility used in the course of this study.

In the following, the CPLIP behaviour, either in steady and in transient conditions will be numerically and experimentally analysed. In particular, in the next chapter, it will be shown how this kind of cooling system is able to ensure the temperature requirements for power electronics modules. The evaporator thermal conductance will be experimentally obtained and coupled with a finite volume model to obtain the temperature field on electronics components.

CPLIP answer to HASTECS requirements: thermal characterisation

The analysis reported in this chapter is related to steady-state behaviour of the CPLIP. It will be experimentally analysed to understand how the different parameters, such as reservoir and cold source temperature, applied thermal load and vapour line pressure drop, influence the stationary behaviour of the loop. The results related to the use of two different working fluids, ethanol and methanol, are also presented.

A theoretical post-processing tool is used with the purpose to study the influence of the thermal load and the impact of the cold source temperature variation on the thermal conductance. Thermodynamic cycles are built on the base of the real evaporation temperature in the porous wick.

Starting from experimentally obtained thermal conductance curves of evaporator base plate, numerical 3D results of a finite volume model will be introduced to obtain the 3D temperature map and the effective temperature distribution of a real power electronics module.

Finally, the loop transient behaviour will be experimentally studied during an entire mission profile to show how this technology is also able to ensure temperature requirements and to successfully cool the power electronics modules.

6.1 CPLIP experimental steady-state test campaigns

6.1.1 Operating conditions

Using methanol as working fluid, comparing the results obtained by Ayel *et al.* [7, 14] for ethanol and in presence of non condensable gases (NCG) in the case of methanol, a detailed overview of the loop behaviour in different cases is presented. On the basis of the triplet: reservoir temperature, T_{res} ; cold source temperature, T_{sec} and applied thermal power to the evaporator, Q_{th} , a parametric study is introduced by changing the just cited parameters. Furthermore, in order to analyse how thermal response of the loop,

and in particular the evaporator behaviour, is impacted by vapour line pressure losses, the latter will be increased until loop failure, by gradually closing the valve from open to closed condition. Results will be analysed, even in this case, by using an appropriate post-processing tool by which the thermodynamic cycles are constructed.

A synthesis of the tests performed during the two different campaigns is reported in table 6.1.

	T_{res} [°C]	T_{sec} [°C]	\dot{Q} [kW]	N/N_{max}
Influence of thermal load	50	20	0.5 to 5	1
	60	20	0.5 to 5	1
	70	20	0.5 to 5	1
	80	20	0.5 to 5	1
	70	5	0.5 to 5	1
	70	40	0.5 to 5	1
Influence of pressure drop	60	20	1 to 2	1 to 0.25
	70	20	1 to 2	1 to 0.25
	80	20	1 to 2	1 to 0.25

Table 6.1: Summary of experimental tests [12]

During the first test campaign (to study the influence of thermal load), the reservoir temperature, T_{res} , was changed from 50 to 80 °C at constant cold source temperature, $T_{sec} = 20$ °C. For each value of T_{res} , the thermal power has been changed from the minimum to the maximum admissible value (from 0.5 to 5 kW stepping by 0.5 kW). Also, for a reservoir temperature, T_{res} , of 70 °C, two more different cold source temperatures were exploited, 5 and 40 °C, to observe their impact on the thermodynamic cycle.

During the second test campaign (to study the influence of vapour line pressure drop), three different reservoir temperatures were exploited: 60, 70 and 80 °C, at constant cold source temperature ($T_{sec} = 20$ °C) and, for each of them, the number of valve turns was changed from the maximal value ($N/N_{max} = 1$, corresponding to fully opened valve condition —no pressure drop—) to the minimal one ($N/N_{max} = 0.25$, corresponding to the maximum pressure drop possible avoiding the complete occlusion of the line¹). A thermal power applied to the evaporator from 1 to 2 kW was exploited at constant reservoir temperature and for each vapour line pressure drop group.

Non condensable gases (NCG) For each test, the absence of NCG was verified by comparing the actual saturation conditions in the reservoir with the theoretical ones on

¹The value $N/N_{max} = 0$ corresponds to the total closure of the valve.

the saturation curve. The Clausius-Clapeyron relation was used to compare theoretical and experimental points (see Fig. 6.1).

In Fig. 6.1, an example of verification of absence of NCG is reported. The error bars on the tested points indicate a maximal error of $\pm 0.6\%$ due to the accuracy of the platinum sensor. In particular, other than a base accuracy of $\pm 0.1\%$, an accuracy loss of $\pm 0.05\%/year$ is considered.

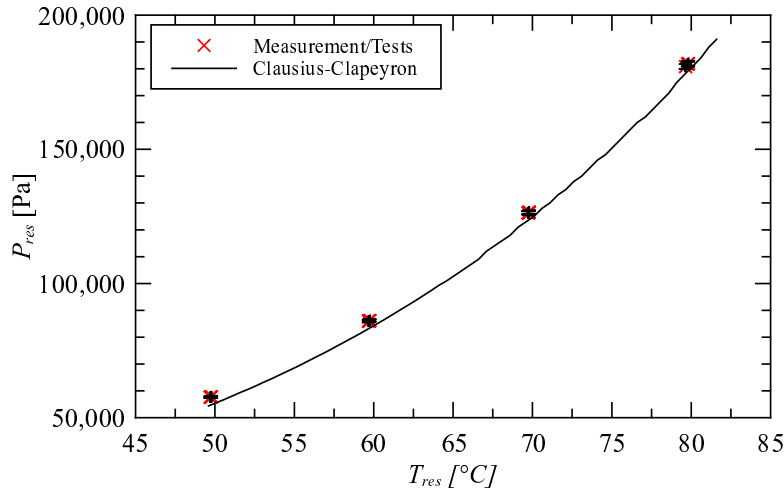


Figure 6.1: Example of NCG absence verification (methanol)

6.1.2 CPLIP thermal response to different heat power levels

In Fig. 6.2, a typical test with methanol as working fluid is reported. The analysis here introduced is based on the assumption of steady-state operating condition for each heat power step² (+0.5 kW).

From the diagram reported in Fig. 6.2, one can trivially notice that, for any heat power load step, the reservoir saturation temperature, T_{res} (black line), remains almost constant as a function of time. A slight temperature lowering occurs during the start-up stage, due to the inlet of cold liquid mass coming from the condenser through the liquid line³.

Red, grey and green lines on the diagram are related to temperature measurement in different positions of the evaporator wall ($T_{diff,max}$ and $T_{diff,min}$, in Fig. 6.2), where a

²For each heat power load variation to the evaporator, the complete stabilisation of the loop was attained before the successive heat power step.

³The behaviour of the Capillary Pumped Loop for Integrated Power during the start-up stage is widely discussed in chapter 8.

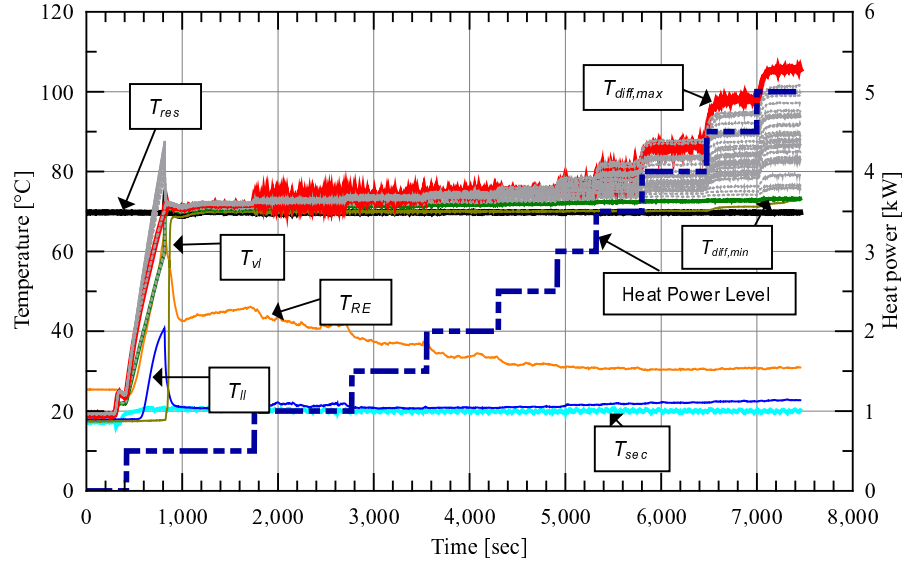


Figure 6.2: CPLIP temperature evolution as a function of the time, for different heat power applied to the evaporator (methanol, $T_{res} = 70^\circ\text{C}$ and $T_{sec} = 20^\circ\text{C}$) [12].

temperature gradient is evident. Temperature distribution decreases progressively from higher temperatures at the top to lower temperatures at the bottom. Accorinti *et al.* [111] associated such temperature gradient to gravity pressure drop that leads to a progressive recession of the evaporation front in the porous wick as soon as the thermal load is increased. That's why $T_{diff,max}$ to $T_{diff,min}$ temperature difference increases with thermal load. For thermal loads over than 2.5 kW, the slight temperature increase of the liquid line, T_{II} , could be due to a pretty slight condenser undersizing.

6.2 Post-processing tool and CPLIP real thermodynamic cycle

In order to obtain the thermal conductance value, based on the evaporator-wall to saturation temperature difference, $G_{ev,V}$, the post-processing tool, described in ref. [14], was used to estimate the real values of evaporation temperature in the porous wick, T_V , by reconstructing the thermodynamic diagram of the CPLIP for a given working point. The tool is based on the reconstruction of a quite simplified version of CPLIP thermodynamic cycle (like that reported in Fig. 6.3) using experimental temperature values as entry. The missing parameters are calculated using the relationship between pressure and temperature on the saturation curve. In steady-state condition, on the basis of the

qualitative thermodynamic cycle reported in Fig. 5.2, the pressure difference between P_V and P_{E_0} represents the capillary pressure head. The latter should be equal to the cumulated viscous pressure losses in the vapour line ΔP_v ⁴, in the liquid line ΔP_l and those due to gravity ΔP_g :

$$P_V - P_{E_0} = \sum \Delta P_v + \sum \Delta P_l + \sum \Delta P_g \quad (6.1)$$

From the knowledge of: experimental values of temperature and pressure in the reservoir (respectively T_{res} and P_{res}), vapour and liquid line inlet and outlet temperatures (T_{vi} , T_{vo} and T_{li} , T_{lo} respectively) and reservoir-evaporator tube temperature T_{RE} , according to Ayel *et al.* [14], the missing parameters can be identified by using the following assumptions:

- The vapour pressure losses in the porous wick may be neglected, because of the equivalent length to the exit (as also shown by Mottet *et al.* [113]);
- Single phase distributed and local pressure drops are calculated using standard correlations;
- In the condenser, two-phase pressure drops were estimated by only considering vapour phase on the condensation length;
- The condenser internal side HTC is calculated on the base of the Chato's correlation (see eq. (B.14) to (B.16));
- The liquid height in the reservoir is considered constant. As also shown in [14], variations of liquid/vapour interface corresponding to thermal power variation are pretty small.

For a given thermal load applied to the evaporator, the mass flow rate flowing within the loop can be computed as:

$$\dot{m} = \frac{Q_{el} - Q_{loss}}{h_{l,v} + c_{p,l}(T_V - T_{RE})} \quad (6.2)$$

where the evaporator to ambient thermal losses term, Q_{loss} , is evaluated by using an empty test as described by Ayel *et al.* [14], and the evaporation temperature in the evaporator (T_V) is iteratively calculated until convergence: mass, pressure and temperature balances on the saturation curve.

⁴Condenser pressure drops are supposed to be only related to vapour flow until condensation length and included into vapour line pressure drops.

Thermodynamic cycles and main thermal characteristics In Fig. 6.3, thermodynamic cycles are reported for two different CPLIP operating conditions and using methanol as working fluid, with constant reservoir and cold source temperatures, $T_{res} = 70^\circ\text{C}$ and $T_{sec} = 20^\circ\text{C}$ respectively, at 0.5 and 5 kW.

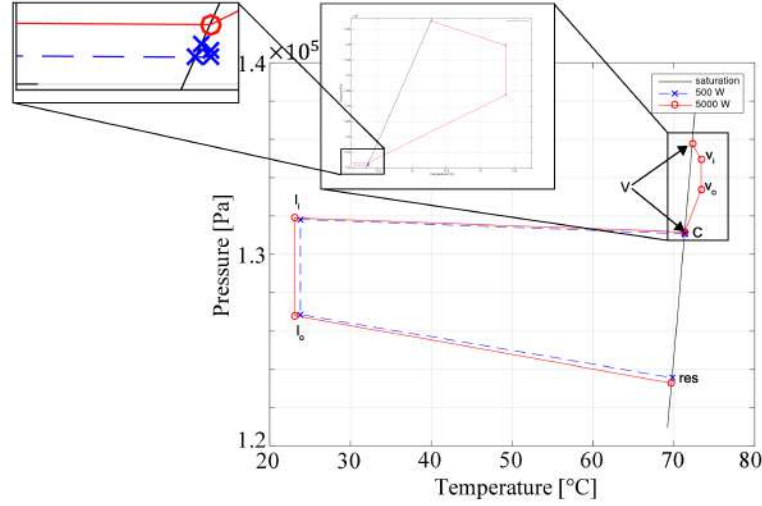


Figure 6.3: CPLIP thermodynamic cycle: comparison at $Q = 0.5\text{ kW}$ and $Q = 5\text{ kW}$ (methanol, $T_{res} = 70^\circ\text{C}$ and $T_{sec} = 20^\circ\text{C}$) [12].

At 0.5 kW, pressure variations in the evaporator grooves, in the vapour line and the condensation front are pretty small when compared to those at 5 kW. In fact, for the lowest thermal load, the pressure variation between the evaporation point (V in the diagram) and the vapour line outlet, v_o , are one order of magnitude lower than those related to the highest thermal power test. At 5 kW, the pressure difference from the evaporator to the condensation front (points V and C on the diagram) is almost the same than gravity pressure losses in the liquid line ($P_{li} - P_{lo}$): the latter is mainly due to a height difference, $H_l = 0.7\text{ m}$, affecting the gravity term ($\Delta P_{g,l} = \rho_l g H_l$).

As soon as reservoir temperature changes, and consequently saturation pressure in the reservoir changes as well, for a fixed thermal power applied to the evaporator, a translation of the thermodynamic cycle on the saturation curve occurs, as shown in Fig. 6.4. Here, the divergence of thermodynamic cycles for the exploited three different reservoir temperatures ($T_{res} = 50, 60, 70^\circ\text{C}$), at constant thermal power and cold source temperature, is shown. For any variation of T_{res} , a translation of operating points occurs while the overall pressure difference remains almost the same for all the three analysed cases.

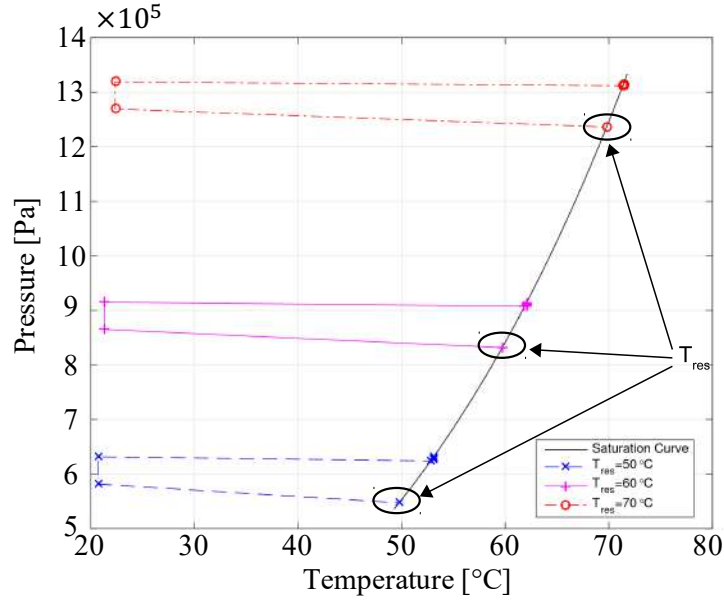


Figure 6.4: CPLIP thermodynamic cycle: comparison at $T_{res} = 50; 60$ and 70 °C (methanol, $Q = 1.5$ kW and $T_{sec} = 20$ °C) [12].

One of the key characteristics of this kind of cooling system is evident when the diagram reported in Fig. 6.4 is observed: at constant heat power supplied to the evaporator, its temperature can be controlled by choosing the operating point, fixed as saturation condition in the reservoir. The slight cold source temperature divergence between the three analysed cases, may be attributed to the slight, previously cited, undersizing of condenser (not sufficient subcooling). Even if too small to be appreciated, the difference between the saturation pressure in the evaporator and the condenser inlet is similar for the three analysed cases.

Worth of attention is the response of the loop related to a variation of the cold source temperature. In fact, the latter is relevant when a temperature change occurs during the different stages of the aircraft mission. When the cold source temperature variation, T_{sec} , is observed at constant thermal load and reservoir temperature, T_{res} , no significative changes in evaporation one, T_V , are noticeable, as it can be easily observed from the diagram reported in Fig. 6.5. Here, three different cold source temperatures are compared at constant thermal load ($Q = 1.5$ kW) and reservoir temperature, $T_{res} = 70$ °C. Except quite small variations, no significative alterations of evaporator saturation temperature are evident. Such variations could be due to pretty small changes of liquid line pressure losses consequent to a change of liquid thermophysical properties (ρ_l , μ_l) with temperature. The nearly independence between evaporator and cold source temperature is due

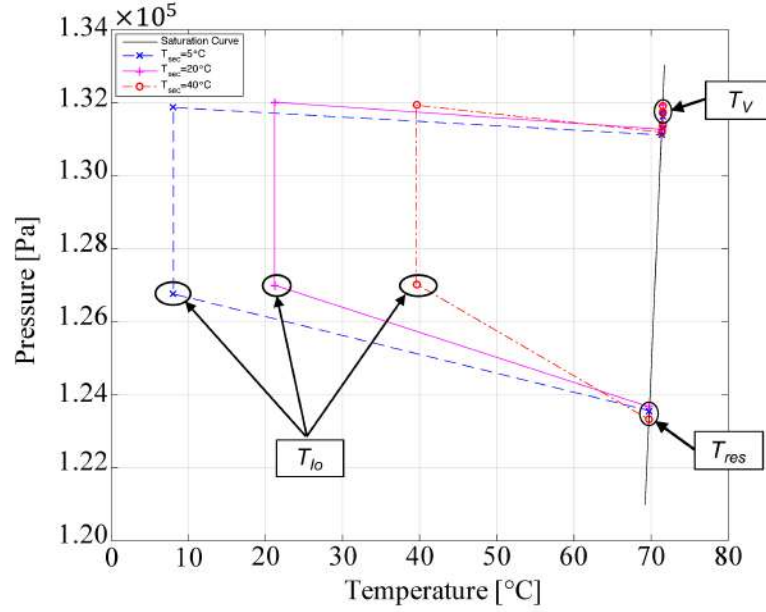


Figure 6.5: CPLIP thermodynamic cycle: comparison at $T_{sec} = 5; 20$ and 40°C (methanol, $Q = 1.5\text{ kW}$ and $T_{res} = 70^\circ\text{C}$).

to a re-adaptation of the condensation length related to the cold source temperature variation. The change in sensible heat (heating of liquid from T_{lo} to T_V) is damped by heat exchanges in the lower part of the reservoir and in the evaporator. Such difference is not apparent at the scale of the position of T_V on the thermodynamic diagram. The independence between the cold source and the saturation temperature in the evaporator makes this kind of technology particularly suitable for all applications where the secondary side temperature changes continuously. Obviously, as underlined by Accorinti *et al.* [12], this is an intrinsic characteristics of two-phase heat exchange, where saturation conditions are imposed.

6.3 CPLIP thermal characterisation for HASTECS specifications

6.3.1 Steady-state experimental results and thermal conductance analysis

Based on the reservoir to evaporator-wall temperature difference, $(\bar{T}_{diff} - T_{res})$, the “rough” evaporator conductance, $G_{ev,res}$, can be obtained from experimental data. Due to the impossibility to directly measure the saturation temperature in the porous wick, T_V , and so to calculate the real thermal conductance, from a purely engineering standpoint

it may be assumed that the reservoir temperature is not so far from the evaporator saturation one. This is the most practical and easy method to obtain the evaporator thermal conductance and to use it for applicative purposes. The latter, measured in $[\text{W} \cdot \text{K}^{-1}]$ can be so calculated as:

$$G_{ev,res} = \frac{Q_{th} - Q_{loss}}{\bar{T}_{diff} - T_{res}} \quad (6.3)$$

Other than the already known symbols, in eq. (6.3), \bar{T}_{diff} is the mean evaporator wall temperature, calculated as the average value of the thirty-two temperature sensors installed on the evaporator wall ($\bar{T}_{diff} = \frac{1}{32} \sum_{i=1}^{32} T_{diff,i}$, see sec. 5.2.1).

By applying eq. (6.3), it is possible to obtain the evolution of evaporator thermal conductance, $G_{ev,res}$, as a function of the thermal load and for different reservoir temperatures and working fluids, as reported in Fig. 6.6. Here, thermal conductance values related to ethanol [14] and methanol [12] are reported, and for the latter the case of presence of NCG [15] is considered as well.

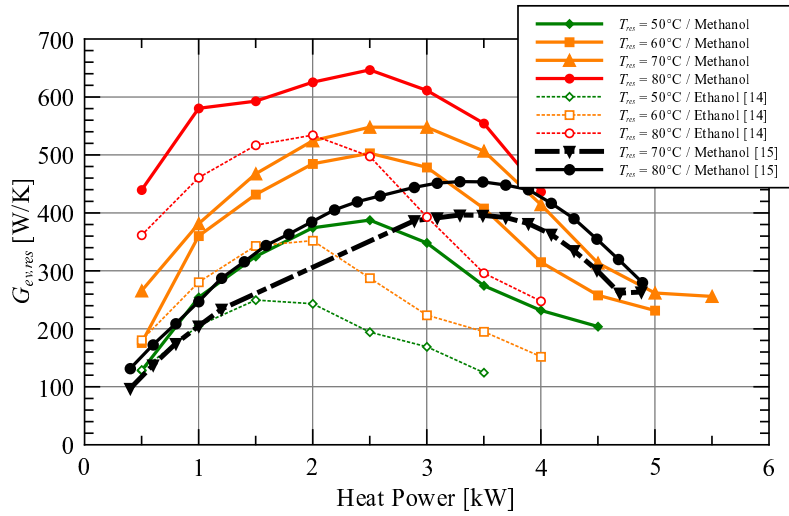


Figure 6.6: Evaporator thermal conductance, $G_{ev,res}$, based on the reservoir saturation temperature as a function of the thermal load (ethanol and methanol, $T_{res} = 50; 60; 70$ and 80°C , $T_{sec} = 20^\circ\text{C}$).

Observing Fig. 6.6, the classical bell-shape can be identified for all curves, independently from the reservoir temperature, working fluid and even in presence of NCG. At constant T_{res} and thermal power, methanol is characterised by higher conductance values than ethanol. Obviously, this difference impacts the evaporator HTC that is related to the thermal conductance through the heat transfer surface area of thermal diffusers.

Evaporator performance are strongly impacted by the presence of NCG, as one can notice considering the curves related to methanol (black curves), also reported by Ayel *et al.* [14]. Their presence in the reservoir, in fact, tends to lower the evaporator thermal conductance and entails a shift of the maximum point of thermal conductance curve to higher power values. At constant thermal load, Q_{th} , the increase of reservoir saturation temperature consequent to higher saturation pressure, related to the presence of NCG, makes the difference $T_{diff} - T_{res}$ rise, leading to lower $G_{ev,res}$ values. Thermal conductance and mean wall temperature strongly depend on the saturation temperature imposed in the reservoir. This is due to the link between T_{res} and T_V on the saturation curve, coupled by the overall pressure drops between the same points, and the vapour mass transfer through the dried part of the porous wick [12].

To calculate the evaporator thermal conductance, but based on the real evaporator saturation temperature, T_V , it is necessary to consider: the thermal load applied to the evaporator, Q_{th} , the losses to the ambient, Q_{loss} , as well as the sensible heat rate, Q_{sns} . In this case, the thermal conductance is calculated as:

$$G_{ev,V} = \frac{Q_{th} - Q_{loss} - Q_{sns}}{\bar{T}_{diff} - T_V} \quad (6.4)$$

and the sensible heat is defined by the difference between the saturation temperature in the evaporator, T_V , and the liquid in the reservoir-evaporator tube, T_{RE} :

$$Q_{sns} = \dot{m} c_{p,l} (T_V - T_{RE}) \quad (6.5)$$

To observe the differences between reservoir-temperature-based and evaporator temperature based thermal conductances, $G_{ev,res}$ and $G_{ev,V}$ respectively, the divergence between T_V and T_{res} must be weighed-up in addition to thermal losses and sensible heat considered in eq. (6.4). In Fig. 6.7, reservoir and evaporator saturation temperatures divergence are reported as a function of thermal load.

T_V remains higher than T_{res} and almost constant for any Q_{th} lower than 3.5 kW. Then, it starts to slightly deviate. In fact, as mentioned above, for an increasing thermal power, the reservoir temperature does not obviously change, while a slight increase in the evaporator saturation temperature, T_V , is noticeable. Despite significative variation of viscous pressure drop corresponding to an increase of power load (see Fig. 6.3), the corresponding temperature change is pretty small. This is due to the link between temperature and pressure on the saturation curve: to a high pressure variation corresponds a small temperature change. This explains why T_V to T_{res} temperature difference is in the order of 1 K at 0.5 kW and about 2.3 K at 5 kW despite the corresponding pressure

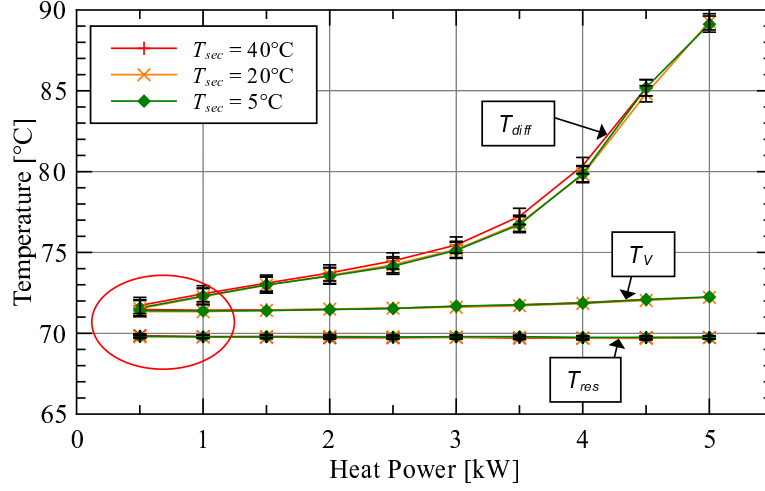


Figure 6.7: Mean diffuser wall temperature, \bar{T}_{diff} ; evaporator saturation temperature, T_V , as a function of the thermal load (methanol, $T_{sec} = 5; 20; \text{ and } 40^{\circ}\text{C}$, $T_{res} = 70^{\circ}\text{C}$) [12].

difference is one order of magnitude higher (or more) for the same power ranges.

The error bars showed in Fig. 6.7 and related to evaporator wall diffuser temperature. They are based on an accuracy of $\pm 0.5\%$ of the measured temperature values. Observing the mean evaporator wall temperature related to the lowest heat power (red circle), the wall to saturation temperature difference in the evaporator is in the same order than the accuracy value. For such low thermal loads, great differences are noticeable in $G_{ev,V}$ calculation, which value is only reliable when upper-bounds of error bars are considered. In fact, if \bar{T}_{diff} tends to T_V , the evaporation-temperature based thermal conductance, $G_{ev,V}$, tends to infinite and the calculation is no more reliable! This is the main reason why, in Fig. 6.8, the $G_{ev,V}$ values are blackened for such low thermal loads. Observing thermal conductance curves (Fig. 6.8), either the ones based on T_{res} and those based on T_V , neglecting the lowest thermal load for which temperature measurements are not reliable, either curve groups have the same trend. When the difference $(\bar{T}_{diff} - T_V)$ is high enough to make the temperature difference $(T_V - T_{res})$ no more significative, the difference $(G_{ev,V} - G_{ev,res})$ tends to zero. Also, worth of attention is the independence between the thermal conductance and the cold source temperature, as already explained in section 6.2. In fact, either for $G_{ev,res}$ and $G_{ev,V}$ curves, no significative differences are noticeable as a function of the cold source temperature.

Dividing the thermal conductance values, G_{ev} , by the evaporator heat transfer surface area, S_{ev} , it is possible to determine the evaporator equivalent heat transfer coefficient ($HTC_{ev} = G_{ev}/S_{ev}$) — particularly useful in the case of modelling heat exchanges

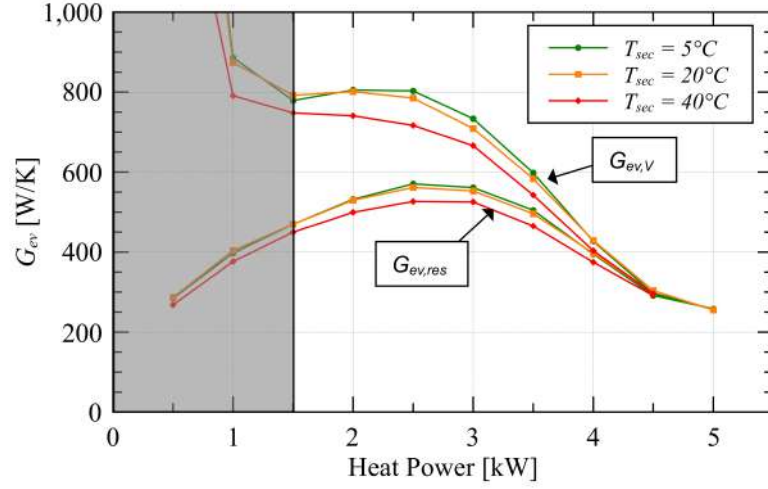


Figure 6.8: $G_{ev,res}$ and $G_{ev,V}$ comparison as a function of the thermal power (methanol, $T_{sec} = 5; 20; \text{ and } 40^\circ\text{C}$, $T_{res} = 70^\circ\text{C}$)

between the evaporator and the power electronics modules, for example —. If HTC_{ev} is plotted as a function of thermal heat flux density, as reported in Fig. 6.9, it is possible to observe, even in this case, the characteristic “bell-shape”, as also shown by Mottet *et al.* [113] at the scale of the porous medium. Error bars indicate an error based on the uncertainty due to thermocouples and electrical power supply used during the tests. Even in this case the lowest $HTC_{ev,V}$ values are blackened for the same reason explained above.

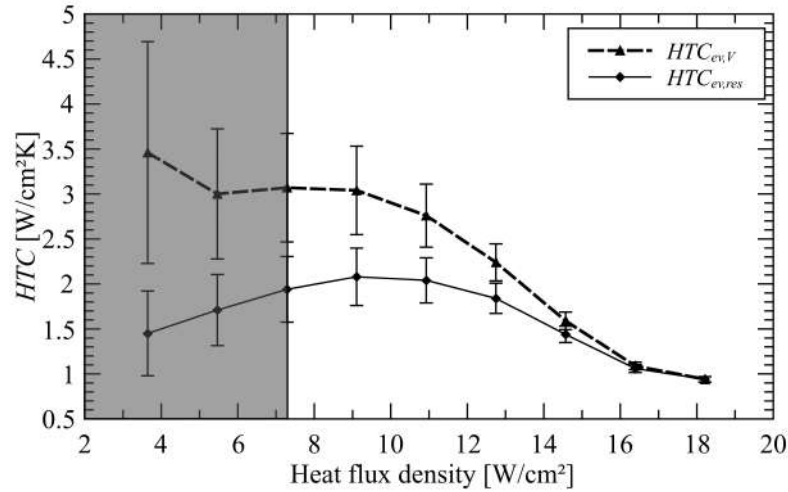


Figure 6.9: $HTC_{ev,V}$ and $HTC_{ev,res}$ comparison as a function of the thermal power (methanol, $T_{sec} = 20^\circ\text{C}$, $T_{res} = 70^\circ\text{C}$).

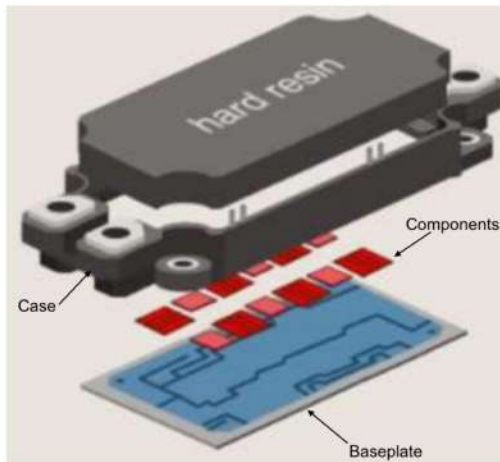
6.3.2 Evaporator-power module numerical analysis

As previously shown, it exists an independence between the cold source temperature (condenser operating conditions and its configuration) and the evaporator. It is thus possible to analyse the evaporator behaviour independently from the rest of the cooling system. In this section, the attention is focused on the evaporator and in particular on the temperature distribution on the junction of electronic components.

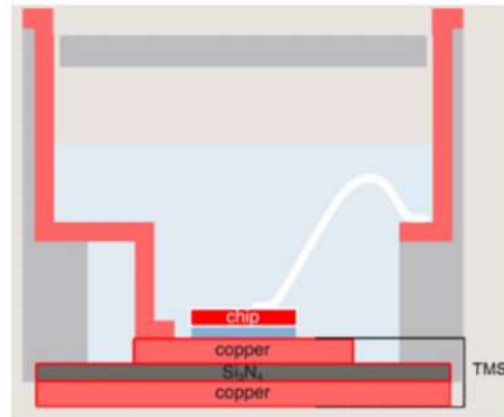
Using a commercial software (Star-CMM+), a finite volume analysis has been performed to obtain the temperature distribution on an exact numerical reproduction of power modules base. In particular, on the basis of experimentally obtained thermal conductance (see Fig. 6.6) as well as the evaporator geometry, dependent on the power modules dimensions, evaporator HTC has been calculated and used as boundary condition. Temperature map on the junction of electronic components was then obtained when they operate in the most critical electrical condition (highest electrical conversion power, lowest electrical efficiency).

6.3.2.1 Power electronics modules characteristics

Following the power electronics modules chosen by WP2 team [21], the *Mitsubishi 7th generation IGBT modules NC-type*, shown in exploded view in Fig. 6.10a, are considered. The proposed power module has baseplate dimensions of $6.2 \times 12.2 \text{ cm}^2$, and is characterised by only three layers between the chips and the baseplate (see Fig. 6.10b). This allows a reduction of the thermal resistance, declared to be 30% lower than previous



(a) Mitsubishi 7th generation IGBT module exploded view [118].



(b) Mitsubishi 7th generation IGBT module section view [118].

Figure 6.10: 7th Generation Mitsubishi module

generation one [118]. Only one layer of Si_3N_4 is inserted between the two copper layers, as it is possible to observe from Fig. 6.10b.

The thermal resistances and the different layer thicknesses, diodes and IGBTs distribution and their number, are reported in the data sheet in ref. [118, 119].

6.3.2.2 Evaporator configuration

In Fig. 6.11, a schematic of the evaporator and its adjoined electronics power modules is reported. The power modules, installed face to face, are mounted in block of two or three (depending on the electronic configuration) on each side of the evaporator, which dimensions are consequent to the power modules ones.

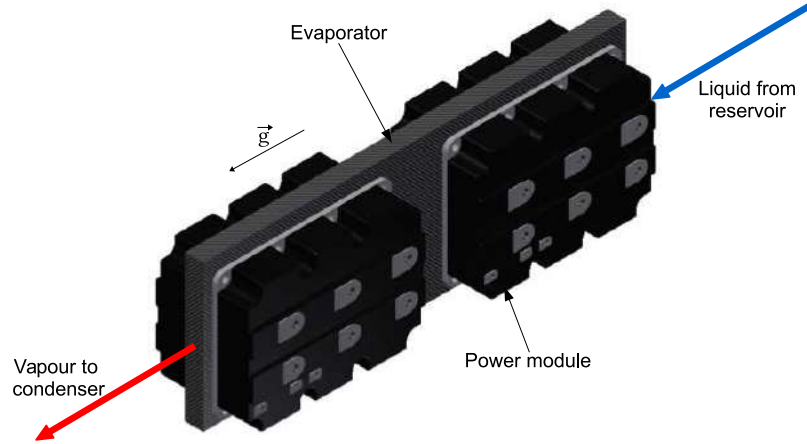


Figure 6.11: Evaporator configuration example [1].

The evaporator is vertically mounted, along \vec{g} direction, and the fluid coming from the reservoir (blue arrow) wets the porous wick contained in it. The nickel evaporator case has a thickness of 1 mm, and the total surface⁵ where power modules are mounted is $18.6 \times 12.2 \text{ cm}^2$. The total evaporator thickness is 1.8 cm. A nickel porous wick with a porosity of 73%, an average pore diameter of $6.3 \mu\text{m}$ and a thickness of 1.4 cm, is contained into the evaporator case, as in [12, 14]. The choice of the same evaporator characteristics is related to the fact that the experimentally obtained thermal conductance values, $G_{ev,res}$, already take into account the evaporator wall thermal resistance.

⁵The discussion reported in this section is referred to the case where three power electronics modules are installed on each side of the evaporator, and three evaporators are used in parallel.

6.3.2.3 Finite volume analysis of power electronics module

On the basis of the data reported on the module specification data-sheet, the module was numerically reproduced⁶. A schematic of power electronic baseplate is reported in Fig. 6.12a.

Finite volume model and boundary conditions Boundary conditions and material layers are schematically reported in Fig. 6.12b.

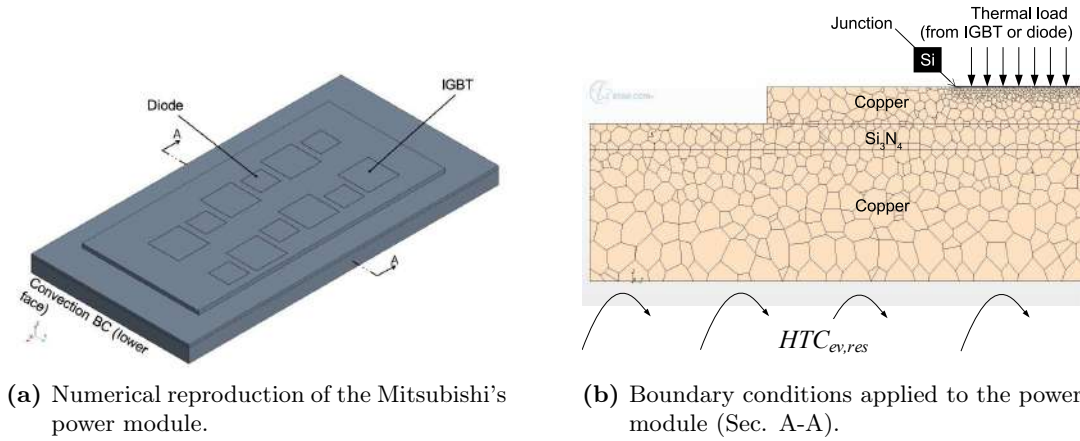


Figure 6.12: Power module scheme and boundary conditions

All the side-walls of the power module are supposed to be adiabatic and the black casing containing the resin layer neglected. A convection boundary condition is applied to the downside wall. Here, the equivalent heat transfer coefficient (HTC) is defined as $HTC_{ev,res} = G_{ev,res}/S_{mod}$, with S_{mod} the module baseplate surface area and $G_{ev,res}$ the reservoir based thermal conductance experimentally obtained (see Fig. 6.6)⁷. The so called “environmental” temperature is equal to the reservoir saturation one: $T_{res} = 70^\circ\text{C}$. A thermal load is applied on the sockets of electronic components and depends on the electronic configuration. NPC (Neutral Point Clamped) is the configuration suggested by WP2 team [21]. The latter allows the power modules to switch differentially: only diodes or only IGBTs work in each power module. In this case, on the basis of the scheme reported in Fig. 6.11, for example, the module positioned in the upper side works using

⁶The plastic case and the hard resin layer (black component in Fig. 6.10a) above IGBTs and diodes have been not considered. No information are given about geometry and thermal characteristics of such layer. It usually is not considered in thermal calculations and no information are reported in data sheet.

⁷The use of $G_{ev,res}$ allows *inter alia* to obtain more conservative junction temperature values because $G_{ev,res} \leq G_{ev,V}$ (see Fig. 6.8)

only IGBTs (largest components in Fig. 6.12a) while the one positioned in the lower side works only using diodes (smallest components in Fig. 6.12a). In this configuration each diode evacuates a thermal power of 155 W and each IGBT a thermal power of 0 W, for the module that uses only diodes. While in power module that only uses IGBT, the thermal power to be evacuated by each diode is just 12 W, but 133 W must be evacuated from each IGBT. The total thermal load to be evacuated is so 16.2 kW (six modules per evaporator), in the configuration here considered.

For simplicity, in the following, $Q_{th,D}$ is the thermal power applied to the diodes and $Q_{th,I}$ is the one applied to IGBTs. We will refer to:

- CASE 1: for the module in which only diodes work ($Q_{th,D} = 155$ W; $Q_{th,I} = 0$ W)
- CASE 2: for the module in which only IGBTs work ($Q_{th,D} = 12$ W; $Q_{th,I} = 133$ W)

A 3D steady-state solver is assumed considering that the high switching frequency (thermal load/unload cycle on the electronic chips), in the order of MHz, is dumped by thermal inertia of the materials constituting power modules and evaporator. Only the energy equation is solved using a multi-domain solver to consider the Conjugated Heat Transfer resolution (CHT) through the different layers of material constituting the power module.

Mesh independence analysis and results A mesh example is reported in Fig. 6.13, where the upside and the downside (interface between the power module and the evaporator wall) views of the power module are respectively reported.

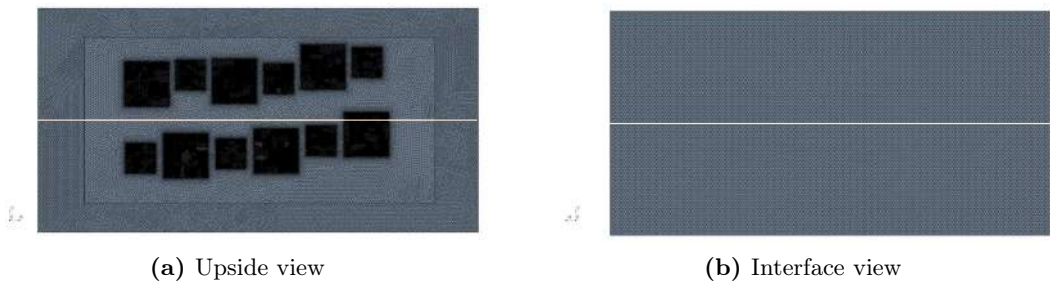


Figure 6.13: Mesh example

A structured polyhedral mesh⁸ was used. It has been refined in correspondence of the electronic component sockets and in correspondence of interfaces between the different material layers. Here, in fact, it is expected to have a heat spreading effect. For each

⁸The polyhedral mesh is a kind of proprietary structured mesh in the used commercial tool (Star-CCM+).

studied case, three different mesh dimensions were used: from the coarser to the finer one, they are defined as $M1...M3$, respectively. For mesh independence calculation, between two successive grids, a maximal temperature difference of 2% has been defined as acceptable⁹. The first grid (M1), characterised by about $2.5 \cdot 10^5$ cells and having the lowest resolution, was compared with the medium dimension grid (about $5 \cdot 10^5$ cells). The difference in the temperature distribution is about 3% in this case. The comparison between the medium and the finer mesh, characterised by about $1.3 \cdot 10^6$ elements, gives a difference lower than 2% in the temperature distribution, which curve is reported in Fig. 6.14. The temperature profiles plotted in Fig. 6.14 are distributed along the light-pink line, shown in Fig. 6.13a and Fig. 6.13b, respectively, on the upside copper surface and at the interface between the evaporator and the power module.

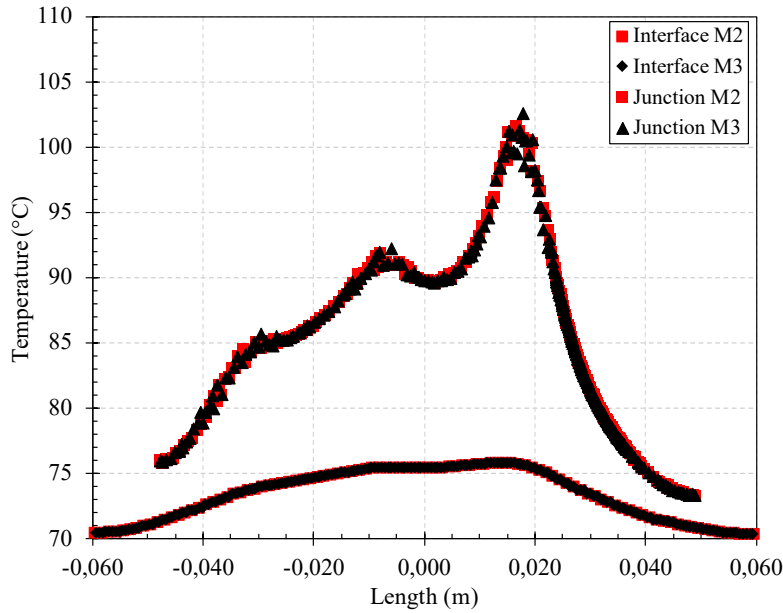


Figure 6.14: Mesh independence temperature distribution (methanol, $T_{res} = 70^\circ\text{C}$)

By using a minimum convergence criterion of 10^{-10} for residuals of energy equation, temperature maps for CASE 1 are reported in Fig. 6.15 and Fig. 6.16. Diodes have side dimension of 0.8 cm, so a thermal heat flux density of about $242 \text{ W} \cdot \text{cm}^{-2}$ is evacuated by each of them. Thanks to the spreading property of copper and Si_3N_4 layers, constituting the power module's base plate, the equivalent heat flux density at the interface between the module and the evaporator is reduced to almost $12.5 \text{ W} \cdot \text{cm}^{-2}$. Despite the presence

⁹Temperature difference is calculated at the same position for two grids, M_n and M_{n-1} , is $\frac{T_{M_{n-1}} - T_{M_n}}{\Delta T_{ref}}$, with $\Delta T_{ref} = T_{M_{n-1}} - T_{ref}$ and $T_{ref} = T_{res}$.

of hot-spots in correspondence of diodes or IGBTs, a flattening of the temperature distribution can be observed in correspondence of the base of the module, from the junction to the interface (see Fig. 6.14).

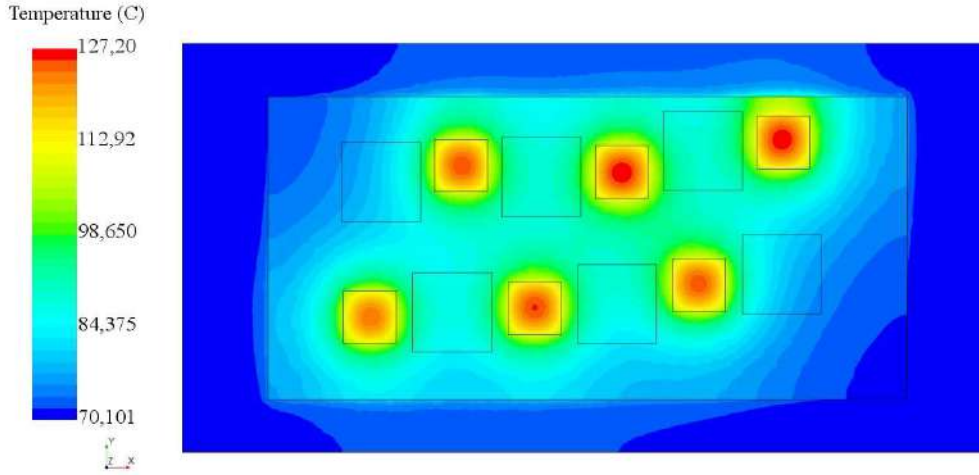


Figure 6.15: Temperature map CASE 1 (junction view): $Q_{th,D} = 155 \text{ W}$; $Q_{th,I} = 0 \text{ W}$ (methanol, $T_{res} = 70^\circ\text{C}$).

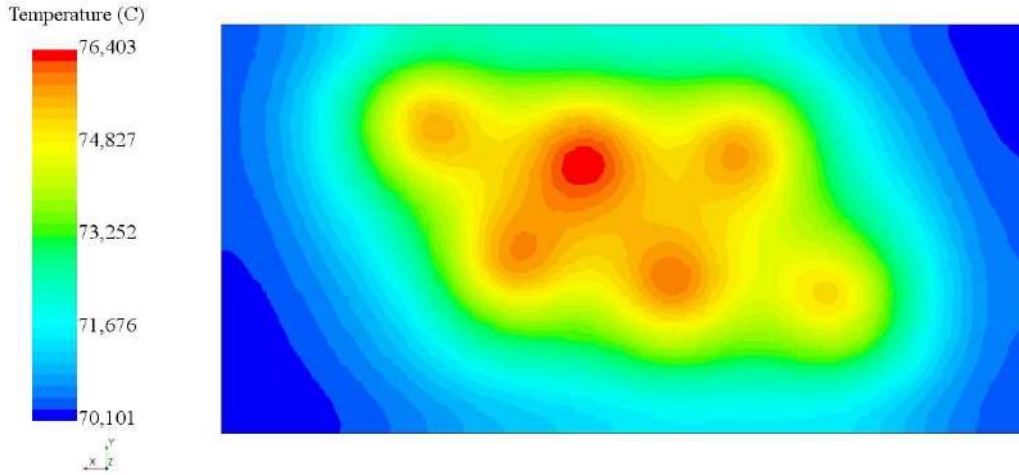


Figure 6.16: Temperature map CASE 1 (evaporator-module interface view, according to Fig. 6.15): $Q_{th,D} = 155 \text{ W}$; $Q_{th,I} = 0 \text{ W}$ (methanol, $T_{res} = 70^\circ\text{C}$).

The same thermal behaviour may be noticed for CASE 2 (see figures 6.17 and 6.18). In this case, for a thermal heat flux density of about $92.5 \text{ W}\cdot\text{cm}^{-2}$ and $18.75 \text{ W}\cdot\text{cm}^{-2}$ applied on each IGBT and diode socket, respectively, the equivalent heat flux density

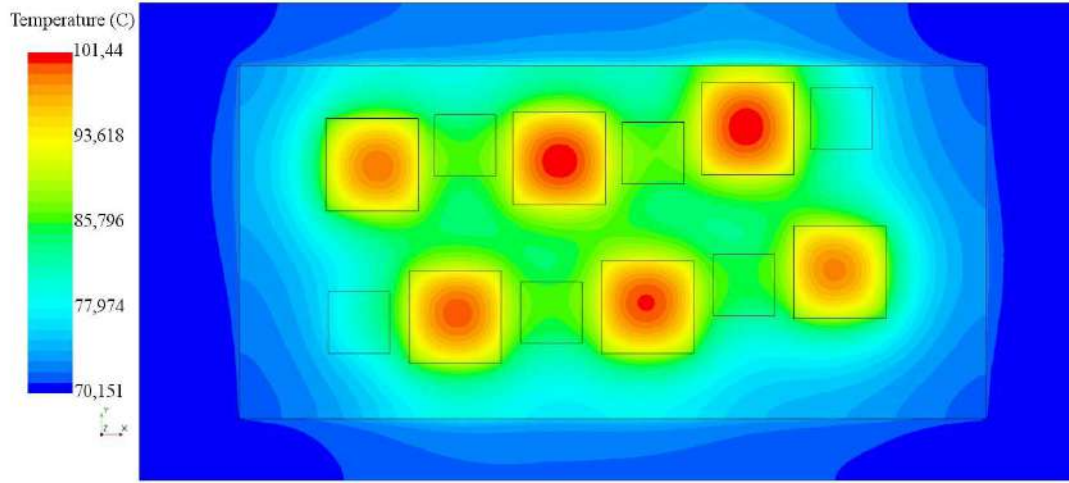


Figure 6.17: Temperature map CASE 2 (junction view): $Q_{th,D} = 12 \text{ W}$; $Q_{th,I} = 133 \text{ W}$ (methanol, $T_{res} = 70^\circ\text{C}$).

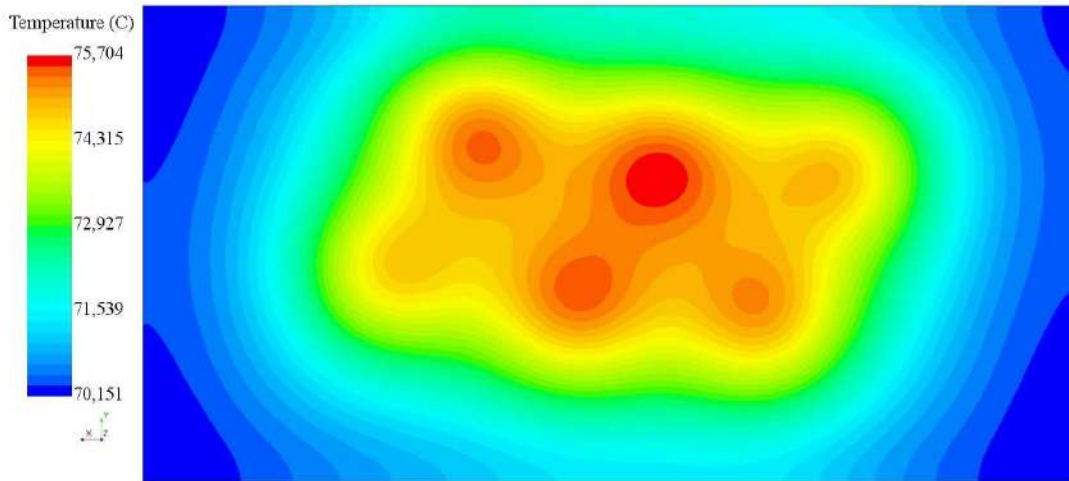


Figure 6.18: Temperature map CASE 2 (evaporator-module interface view, according to Fig. 6.17): $Q_{th,D} = 12 \text{ W}$; $Q_{th,I} = 133 \text{ W}$ (methanol, $T_{res} = 70^\circ\text{C}$).

at the evaporator/power module interface is $11.5 \text{ W}\cdot\text{cm}^{-2}$. The maximum temperature values are 127°C and 101°C for the CASE 1 and the CASE 2 respectively, lower than the maximal allowed junction temperature given by modules constructor (150°C) [118].

6.3.3 Experimental thermal mission profile

To explore the behaviour of the CPLIP in more realistic operating conditions, the mission profile was experimentally tested using the experimental facility described in sec. 5.8. The purpose is to test the CPLIP during severe transient stages of the mission profile,

such as the sudden power increase that occurs between stage I and stage II, for example (see Fig. 6.19).

Considering the electrical configuration NPC-DPWMMAX¹⁰, the maximal total thermal load to be evacuated is $Q_{th} = 16.2 \text{ kW}$ in three-phase: 5.4 kW/phase .

Fig. 6.19 depicts the experimental results for one-electrical phase thermal losses mission profile using the same experimental facility used in [1, 12, 14] and [111] .

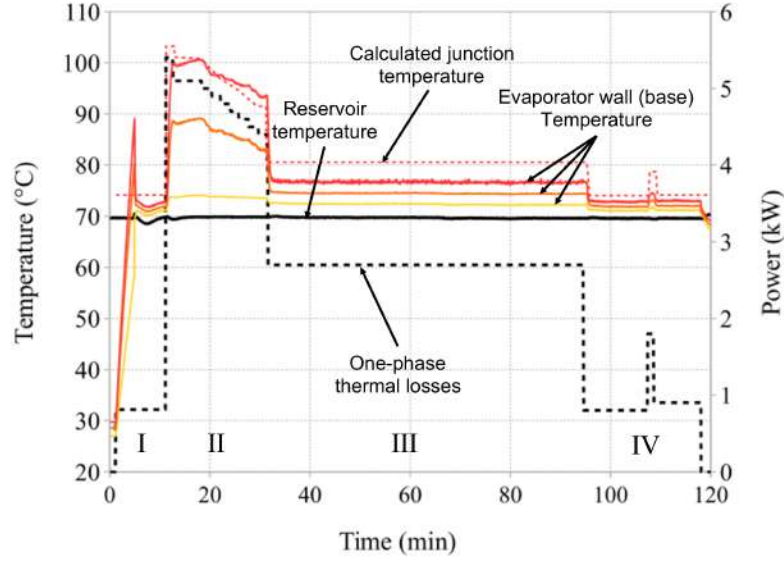


Figure 6.19: Experimental thermal mission profile (methanol, $T_{sec} = 20^\circ\text{C}$, $T_{res} = 70^\circ\text{C}$).

From the stand-by position¹¹ (before stage I), as the power load is applied to the evaporator, 0.8 kW , at the time $t = 0$, a sudden temperature overshoot occurs in correspondence of the evaporator walls (the behaviour of the CPLIP during start-up is widely treated in chap. 8 and in ref. [111]) until start-up of loop operations, triggered by nucleation bubbles in the evaporator. After this point, the evaporator wall temperature suddenly decreases reaching an almost uniform value along the evaporator wall. During the taxi-out stage (I) the thermal load evacuated by the electronic components is constant for about 10 min. At the beginning of the take-off stage (II) the power peak (5.4 kW) is applied to the evaporator. Wall temperature suddenly increases, small perturbations occur in the reservoir: here the temperature slightly decreases before settling to the imposed value. This could be due to a higher liquid mass flow rate that flows from the condenser to the reservoir. The maximal power peak is very limited in time

¹⁰Such electrical configuration is the one retained by WP2 [21] for its efficiency and lightweight.

¹¹No thermal load is applied to the evaporator; the reservoir is maintained at fixed thermodynamic conditions: $T_{res} = 70^\circ\text{C}$; and the cold source temperature is at $T_{sec} = 20^\circ\text{C}$.

and, due to the evaporator thermal inertia, the temperature peak is reached only when the thermal power starts to decrease. Despite the lower thermal load, the evaporator wall temperature continues to increase, but with a lower slope. Once reservoir conditions are stabilised, again, evaporator wall temperature decreases, gradually, following power unload until the end of the climb stage ($t = 30$ min). At beginning of the cruise stage (III), temperature follows a constant power profile and, all along this phase, temperatures are stabilised. CPLIP works in steady state conditions until the end of the cruise at $t = 95$ min, when descent stage begins. Observing temperature distribution on the evaporator walls, a difference can be noticed between the highest and the lowest one (red to yellow line difference). As explained before, this difference could be due to a pressure gradient, between the evaporator inlet and outlet, due to evaporator pressure drop. At the same way, it is expected to observe the same temperature difference on the power electronic module bases. Temperature distribution follows the same shape of thermal load during the remaining stages of the mission profile. Due to the lower power load applied to the evaporator, a lower temperature gradient can be observed on the evaporator walls.

Note that the dashed red curve on the experimental diagram, representing the calculated junction temperature¹², shows the temperature prediction based on the simplified model developed by power electronics team [21, 111] and based on experimental thermal conductance values obtained along this chapter (Fig. 6.9). A slight over-estimation of temperature prediction may be observed during the steady state stages. This could be due to the use of the reservoir-based conductance values, more conservative than evaporator saturation temperature-based ones. However, it is worth of attention that temperature values, in correspondence of power peak, about 103°C , well agree with the predictions based on CFD and is lower than the value suggested by power module constructor (150°C).

6.4 Influence of vapour line pressure drop on the thermal response of the CPLIP

The same methodology and post-processing tool were used to analyse the thermal response of the CPLIP to variations of hydraulic characteristics: vapour line pressure drop.

By following the same methodology and post-processing tool explained above, pressure drop in the vapour line, following the closure of the valve, $\Delta P_{v, valve}$ (see eq. 6.6), must

¹²A simplified mono-dimensional electrical analogy based model has been developed by WP2 [21] according to CPLIP's thermal characteristics explained in this chapter.

be added to the overall pressure drop equation, (6.1):

$$\Delta P_{v,valve} = \left[\frac{\dot{m}}{C_v \rho_v \left(1 - \frac{2 \Delta P_{v,valve}}{3 P_{vi}} \right)} \right]^2 \frac{G_v T_{vi}}{P_{vi}} \times 10^{10} \quad (6.6)$$

where C_v is the flow coefficient relating the pressure drop to the valve number of turns, N , following the relation:

$$C_v = F_c [0.0103 N^4 + 0.0909 N^3 + 0.178 N^2 + 0.3766 N + 0.0016] \quad (6.7)$$

The conversion factor is $F_c = 0.0116$, and the evolving vapour mass flow rate is calculated as:

$$\dot{m}_v = 22.4 C_v \sqrt{\Delta P \cdot P_{sat}} \quad (6.8)$$

For a given and constant thermal load applied to the evaporator, Q_{th} , reservoir and cold source temperature, T_{res} and T_{sec} , respectively, pressure drop in the vapour line has been gradually increased by closing the setting valve (see Fig. 5.8) and attempting steady-state conditions in each case. To give the reader an idea of the global behaviour of the CPLIP corresponding to pressure drops increase, the time dependent diagram of temperature evolution, during a test, is reported in Fig. 6.20 (methanol and constant heat power, $Q_{th} = 1 \text{ kW}$). There, valve overture, indicated on the right side axis, are shown as the ratio N/N_{max} . N is the actual number of turns and N_{max} is the number

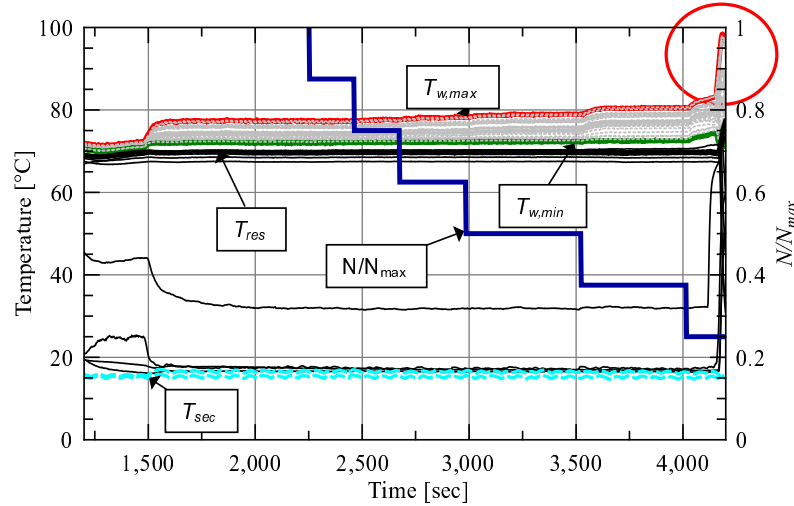


Figure 6.20: Time dependent diagram of temperature evolution of the CPLIP for increasing vapour line pressure drop (methanol, $Q_{th} = 1 \text{ kW}$, $T_{sec} = 20 \text{ °C}$).

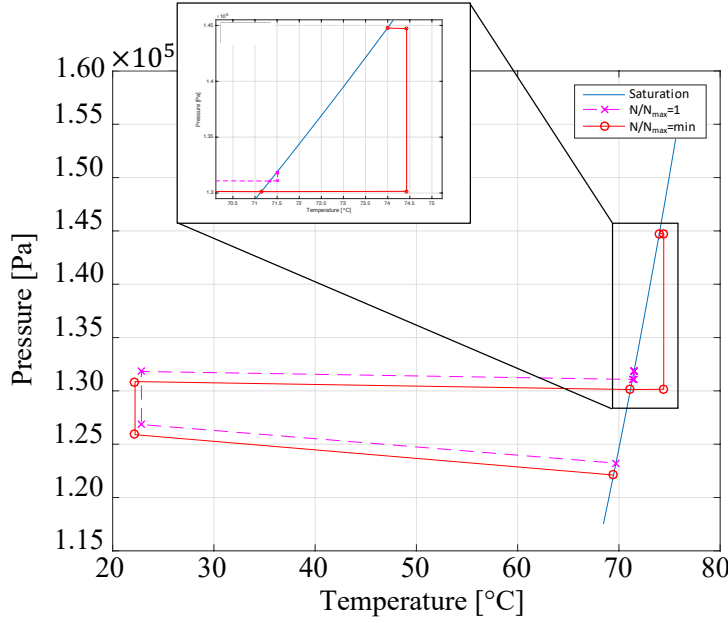


Figure 6.21: Thermodynamic cycle comparison between the highest and the lowest valve over-ture: $N/N_{max} = 0.25$ and $N/N_{max} = 1$ (methanol, $Q_{th} = 1 \text{ kW}$, $T_{res} = 70^\circ\text{C}$ and $T_{sec} = 20^\circ\text{C}$).

of turns corresponding to the fully open condition. The first impression one has, observing the diagram in Fig. 6.20, is that the impact of increasing pressure drop is almost comparable with that of increasing thermal load to the evaporator: the evaporator temperature increases. This behaviour can also be noticed from the thermodynamic diagram comparison reported in Fig. 6.21 where the lowest pressure drop possible ($N/N_{max} = 1$) and the highest one ($N/N_{max} = \min = 0.25$, corresponding to the lowest value of N before loop failure) are compared. The loop failure due to valve closing is highlighted by a red circle in Fig. 6.20. In this case, the overall pressure drop in the loop exceeds the capillary limit of the porous wick [7, 12], see eq. (6.1). The latter is thus no more able to supply the adequate pressure head, no more fluid flows in the loop and dry out occurs in the wick. Evaporator temperature goes out of control.

Temperatures are not only dependent on the applied thermal load, but also on the pressure drops. Vapour line length, loop configuration, condenser typology and configuration and working fluid affect overall pressure drops and consequently the loop response.

By comparing ethanol and methanol as working fluids, considering the mean evaporator wall temperature, \bar{T}_{diff} , from Fig. 6.22, the lowest wall temperatures and lowest sensitivity to vapour line pressure drop are recorded for methanol. Increasing the thermal load, Q_{th} , curve depletion quickens proportionally to valve closure, so CPLIP demonstrates a

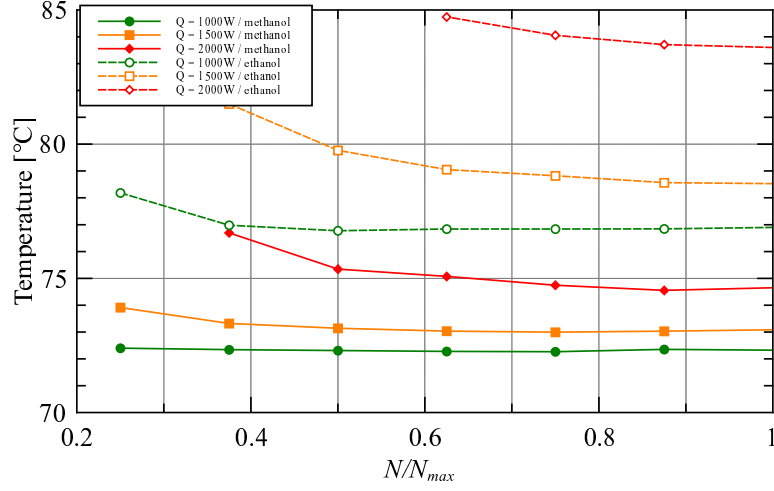


Figure 6.22: \bar{T}_{diff} as a function of N/N_{max} and for different thermal loads (methanol, $T_{res} = 70^\circ\text{C}$; $T_{sec} = 20^\circ\text{C}$).

higher sensitivity to pressure drops: curve slopes increase.

The mean diffuser to reservoir temperature difference, $(\bar{T}_{diff} - T_{res})$, and the mean diffuser to evaporator temperature difference, $(\bar{T}_{diff} - T_V)$, are considered, for comparison purposes, as a function of N/N_{max} , for different thermal loads and for methanol and ethanol (see Fig. 6.23). Basically, at constant thermal load, \bar{T}_{diff} decreases as N/N_{max} increases (see Fig. 6.22). Being the reservoir temperature constant, whatever the position of the valve, the difference $(\bar{T}_{diff} - T_{res})$ decreases as well, either for ethanol and methanol (see Fig. 6.23a). At the same manner, as reported in Fig. 6.23b, because of

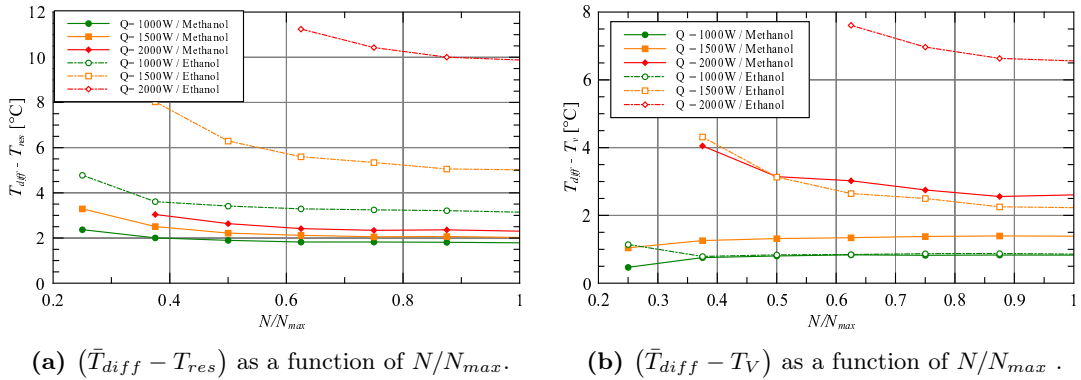


Figure 6.23: Temperature differences as a function of the valve overture (ethanol and methanol, $T_{res} = 70^\circ\text{C}$; $T_{sec} = 20^\circ\text{C}$).

the lowering of the evaporator temperature, T_V , as a function of N/N_{max} , $(\bar{T}_{diff} - T_V)$ decreases too. This behaviour may be justified by a recession of menisci in the porous wick between the interface and the diffuser. In fact, the higher the thermal load, the higher the temperature difference and the slope of the curve because of the presence of an increasing dried portion of the porous wick. The pressure difference around the menisci increases and the evaporation front recesses. As reported by Accorinti *et al.* [12], this could be the reason of the final failure of the loop for high pressure drop at high thermal loads.

As expected, both temperature differences are characterised by the same trend for each working fluid and almost all thermal loads. However, as observed in Fig. 6.7, for low thermal loads, at low N/N_{max} (highest pressure drops), $(T_{diff} - T_V)$ is in the same order of the temperature sensor accuracy. Measurements are no more reliable in this range (see methanol at 1 and 1.5 kW for example). This justifies the change in the slope observed for such curves.

Finally, if the thermal conductance values, based on the real evaporator temperature, are calculated as a function of the pressure drops in the vapour line, the highest conductance value is obtained, as expected, for the lowest thermal load and the highest pressure drop, as reported in Fig. 6.24 (being the curve at 1000 W in the range of high uncertainty given by the blackened area of Fig. 6.8).

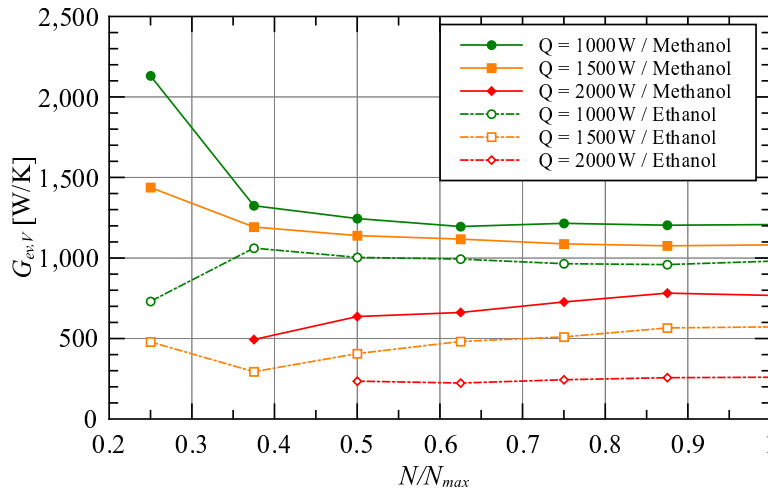


Figure 6.24: Thermal conductance as a function of the pressure drop (ethanol and methanol, $T_{res} = 70^\circ\text{C}$; $T_{sec} = 20^\circ\text{C}$).

Considering the overall pressure drop ΔP as a function of the valve overture and for different power levels (see Fig. 6.25), obviously the lower the thermal power, the higher

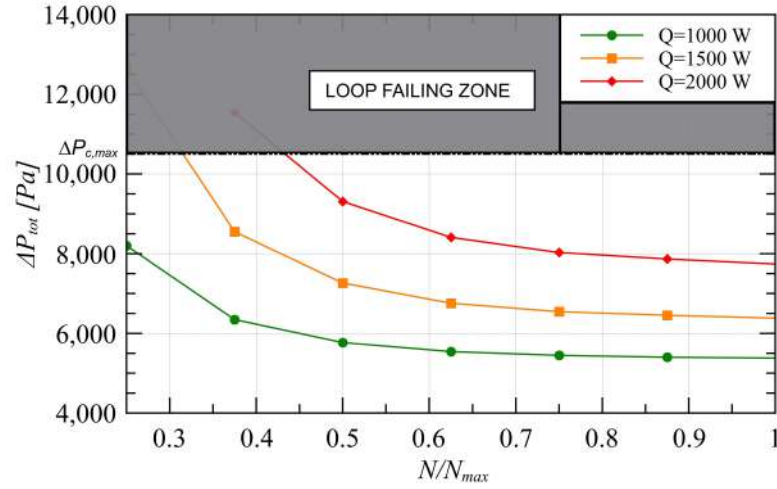


Figure 6.25: Overall pressure drop as a function of valve opening (N/N_{max}) and for different thermal loads (ethanol and methanol, $T_{res} = 70^\circ\text{C}$; $T_{sec} = 20^\circ\text{C}$).

the pressure drop at which the loop can operate without failing. But the higher the thermal power, the higher the pressure gradient. It means that, for the highest thermal loads, the loop failure occurs before low ones, as the prediction of pressure drops above the $\Delta P_{c,max}$ line shows!

6.5 Conclusion

In this chapter, the behaviour of the CPLIP in many experimental operating conditions was introduced. In particular, acting on its thermal and hydraulic characteristics, a detailed explanation of different behaviour of the CPLIP was presented. This chapter was, fundamentally, divided in four parts. In the first part, a thermal characterisation of the CPLIP, using methanol and ethanol as working fluids, has been carried on to understand CPLIP limits and potentialities. A widely extended experimental parametric study was presented to understand the influence of such parameter on the CPLIP working conditions. Due to the inability to directly measure the evaporation temperature in the porous wick, an adapted post-processing tool was used to obtain all the missing parameters on the thermodynamic cycle. In particular, a first study on the influence of different parameters on the thermodynamic cycle was presented to explain, in a more clear way, the main CPLIP working characteristics. It was observed that, due to the intrinsic characteristics of such two-phase cooling system, where saturation conditions are imposed and controlled, an independency between cold source temperature and the

evaporator operating one exists. So, evaporator conductance values are also independent from the secondary side temperature. This behaviour renders this system particularly adapted for the application studied in the context of HASTECS project. Evaporator conductances were experimentally obtained, based either on the reservoir and evaporator temperatures. On the basis of experimentally obtained thermal conductances, it was possible to numerically study the temperature field on a real power module. Based on the finite volume method (on StarCCM+), the energy equation was solved to obtain steady-state temperature distribution in the worst efficiency case and operating condition for the power modules. Despite the very high heat flux density evacuated by electronic chips, the CPLIP, characterised by a very high evaporator HTC, is able to maintain temperature controlled and lower than the maximum value allowed by power-electronics-module constructor. Thanks to spreading behaviour of used power electronics modules, one assists to flattening of the temperature field in correspondence of the base plate (interface between the evaporator and the power module).

To explore the CPLIP behaviour during an entire mission profile cycle, the latter has been successfully tested. The CPLIP is able to evacuate the supplied thermal load, and temperatures on the evaporator walls remain controlled even during the most critical phases (transition between taxi-out and take-off stages, for example). The experimentally obtained temperatures were compared with those obtained by WP2 team from a mono-dimensional electrical analogy based model. It allows to verify, *inter alia*, the temperature prediction. A slight overestimation was found. This allows, however, to be more conservative during design stage of electrical components and its adjoined cooling system.

Finally, to know which is the influence of the vapour line pressure drops and to relate them to the transport distance, a parametric study was conducted, acting on the hydraulic characteristics of the CPLIP. It was found that increasing pressure drops in the vapour line has some similarities with thermal load variation to the evaporator. Methanol and ethanol have the same qualitative behaviour, but, due to the differences in thermophysical properties, they are quantitatively different. Ethanol, in particular, is more sensitive to heat power increase or vapour line pressure drops.

Some differences could exist between CPLIP's behaviour tested in laboratory and real operating conditions. They could be mainly due to a difference in transport lines length and/or a different nature of the condenser. Moreover, in this experimental study, the evaporator was uniformly, and quasi ideally heated by heating resistances, so, some differences could be also due to the use of real switching power modules, having a lower thermal inertia than copper diffuser used in the experimental facility.

CPLIP optimisation for 2025 and 2035 requirements

Capillary Pumped Loop for Integrated Power (CPLIP), seems to be the best solution for power electronics cooling in the context of HASTECS project. From first approximation design (see chapter 4), the power coefficient of three parallel evaporators CPLIP was quite close to target 2025! With the purpose to reduce its mass, in this chapter, its optimisation is proposed either for 2025 and 2035.

7.1 Design point

When talking about system design, the first issue to solve is related to the choice of design point. The latter not only impacts the mass of the system, but also its thermohydraulic behaviour. If the cooling system is oversized, its mass will be higher than the one actually required. As a result, it will be under-exploited. On the contrary, in the case of undersizing, the system is not able to ensure the required cooling and consequences may be catastrophic.

Due to the high variability of thermal losses as a function of time, the choice of design point is impacted by the shape of the mission profile. An energy approach is necessary to choose the best one. The mission profile is divided in five stages, as usual (see Fig. 7.1), and the amount of thermal energy evacuated during each stage is calculated. Taxi out-and-in and landing phases (I, IV and V) are characterised by a quite small amount of thermal losses and their duration in time is relatively short: they will be not considered for the purpose. During the remaining flight stages (II and III), whichever the design point, thermal losses will be surely higher than previous ones. The harsh transient take-off stage (II) is critical. At the very beginning of this phase, power converters work at their maximum power for a quite limited time, almost three minutes (red circle), but a pretty high amount of thermal energy has to be evacuated from electronics components. After that, thermal losses slightly decrease until point D (Fig. 7.1). Thermal losses during cruise stage (III), stationary, are not particularly high, but it lasts longtime.

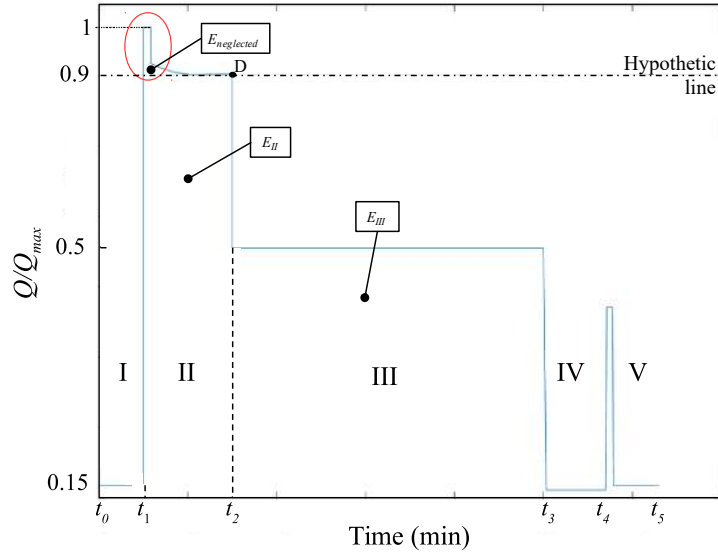


Figure 7.1: Design point choice

Referring to Fig. 7.1, considering only take-off (II) and cruise (III) stages and the hypothetic line¹, three different critical areas can be distinguished on the diagram. The area related to take-off and climb stage, below the line (E_{II}); the area belonging to take-off and climb stage, above that line ($E_{neglected}$); the whole area related to the cruise stage (E_{III}). Considering the four electronic architectures proposed by WP2 [21] for the solution 2025 (FC-DPWMMAX and FC-PWM —Flying Cap Discontinuous Pulse Width Modulation MAX and Flying Cap Discontinuous Pulse Width Modulation respectively—, and NPC-DPWMMAX and NPC-PWM —Neutral Point Clamped—), due to the different efficiency of each electronic configuration², a different amount of heat must be evacuated. In table 7.1, thermal energy calculations are reported for the four electronic topologies in the previously mentioned areas of the mission profile. Thermal energy to be evacuated during take-off stage, E_{II} , is almost 50% than that related to cruise stage, E_{III} . As expected, the design point should consider stage II. Despite the amount of neglected energy, $E_{neglected}$, is between 1.6 and 2% of E_{II} , its absolute value is not negligible and, if point D is chosen as design point, it has to be verified that cooling system thermal inertia is able to damp such amount of not “treated” energy.

¹The line corresponding to the thermal load to be evacuated at the end of stage II (take-off and climb).

²For confidentiality issues is not possible to give any information related to the exact amount of thermal losses to be evacuated for each electronic configuration.

Power electronic topology	E_{II} [MJ]	E_{III} [MJ]	$E_{neglected}$ [kJ]	E_{II}/E_{III}	E_{neg}/E_{II}
FC-DPWMMAX	16.2	36.1	369.5	44.9%	2.2%
FC-PWM	19.4	44.1	395.2	44.0%	2.0%
NPC-DPWMMAX	16.9	38.2	267.3	44.1%	1.6%
NPC-PWM	18.8	42.0	356.5	44.6%	1.9%

Table 7.1: Thermal energy ratios during take-off and cruise stage

After cooling system optimisation, on the basis of precise mass calculation, temperature increase due to amount of neglected energy will be evaluated.

7.2 CPLIP optimisation

To remind, the mass distribution of a three parallel evaporators CPLIP resulting from first approximation design is reported in Fig. 7.2 (see sec. 4.2.3). The resulting first attempt value of thermal power coefficient was $C_{c,th} = 0.33 \text{ kW} \cdot \text{kg}^{-1}$.

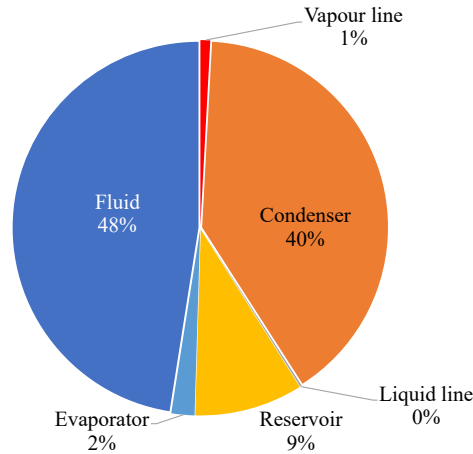


Figure 7.2: Passive two-phase mass distribution (three parallel evaporators CPLIP: — CERBERE—)

As one can notice, condenser, fluid and reservoir are the heaviest components in the loop. Due to the impact of condenser on the fluid and reservoir mass, optimisation process is particularly focused on it to reduce its overall dimensions: the smaller the condenser internal volume, the lower the fluid and reservoir volumes. Moreover, a significant mass reduction can be achieved by using a lightest material than the one used during first approximation design. For compatibility issues between fluid (methanol) and solid material, aluminium cannot be considered. Titanium, already used in aeronautics applications for

similar purposes, has been chosen as constituting material of loop components.

Transport lines geometrical dimensions, which mass is negligible if compared with all other components, cannot be modified furthermore (for mechanical resistance issues, their thickness cannot be reduced below 0.6 mm).

The evaporator dimensions are proportional to power module ones, so this component cannot be modified unless different power modules are used.

7.2.1 Condenser optimisation

The problem of heat exchanger design is not ease-to-solve and involves a multidisciplinary approach. Qualitative and quantitative design considerations and experience-based judgements are necessary to define the optimal heat exchanger (HXG) geometry. During design and optimisation process, thermo/hydraulic approach is only “one side of the coin”. Most decisions are related to manufacturing and economic considerations as well as mechanic and dynamic (vibration) analysis. A trade-off is necessary to reach the optimal heat exchanger final geometry. For given thermo/hydraulic requirements, the solution is not unique, and different optimum solutions exist.

Two different approaches are related to heat exchanger problem. The first one, related to design, is usually called *sizing problem*. It faces with the research of optimal geometric characteristics of a HXG for given industrial process. Materials, heat exchanger configuration, flow arrangement, thermal calculations (HTC, heat transfer surface area), pressure drop *etc.* are related to such process as well. The second approach, usually called *rating problem*, instead, is different in nature. It faces with thermo/hydraulic verification of an already existing heat exchanger or an already designed one to verify if it “answers” to process requirements.

Neglecting mechanical and economic parameters, a scheme of design process is reported in Fig. 7.3 to show how complex this task is. Strong interactions between the different stages of design process make it arduous. The task is based on the assignation of a first attempt geometry, trial, calculation, verification, change of different parameters, and re-trials until a satisfying geometry is reached. The latter is verified by using *trade-off factor(s)*, based on the requirements of the problem, and eventually re-iteration until the satisfaction of all requirements.

Diagram 7.3 can be fundamentally divided in three sections and each of them is representative of a single part of the design task. Process section is related to “problem entries”. It defines heat transfer rate; fluid mass flow rate and temperatures; maximal allowable pressure drops (both for internal and external sides). Operating conditions, HXG architecture, configuration and solid materials are defined here as well. Key char-

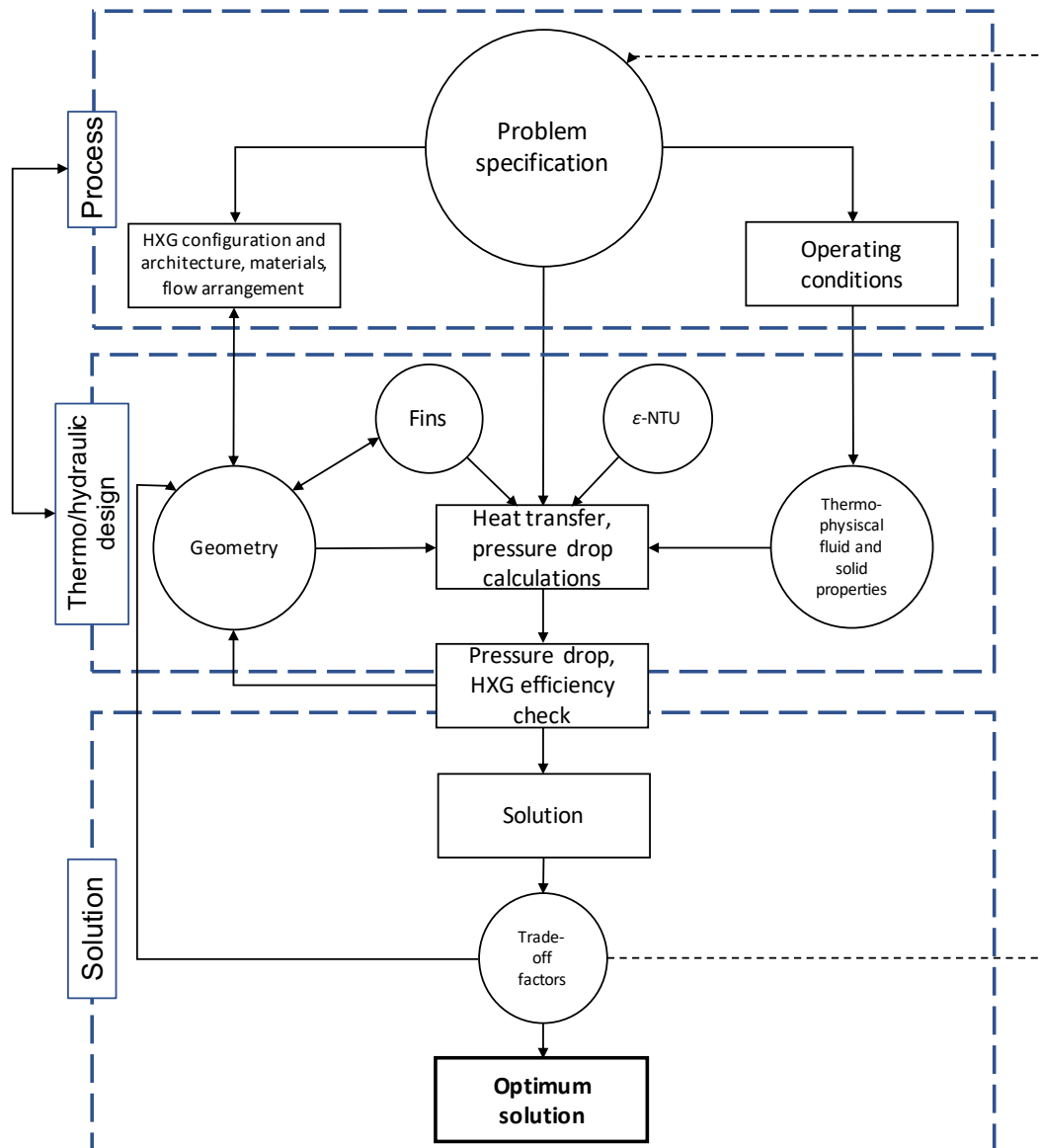


Figure 7.3: Optimisation process of a heat exchanger.

acteristics of heat exchanger, such as flow arrangement, are assigned in this section *a priori* and verified *a posteriori*.

Thermo-hydraulic design section is related to geometry, such as number, geometry and distribution of tubes and fins. Fluid thermophysical properties and resolution method are defined in this section to obtain, on the base of the previously defined parameters, the thermal and hydraulic characteristics of the heat exchanger. Once thermal and hydraulic calculations are executed, the solution is rejected or accepted based on hydraulic and

thermal requirements such as actual-to-allowed pressure-drop ratio and heat exchanger overall efficiency, for example. In the case of rejection of the solution, the process is repeated until global efficiency and pressure drops factors are verified. During this stage, it is sometimes necessary to change some process parameters, such as fluid arrangement to obtain an acceptable solution. Once a possible solution has been obtained, trade-off factors are used to verify if it is the optimum one. If not, once again, geometric characteristics, fluid arrangement, and sometimes operating conditions are re-defined until satisfaction of trade-off factors.

Process is repetitive and based on trials. Solutions must be analysed, at each step, and compared with previous ones. Geometric parameters and configuration have to be changed one by one. Moreover, due to non-linearity between thermo-hydraulic characteristics of the heat exchanger and its geometrical parameters, the process is hard to automate. Designer has to take decisions at each step of the design process until the optimum solution is reached.

Condensers design process is similar to heat exchangers one, but due to difficulties in prediction of two-phase flow pattern (see sec. 5.1.2), it is much more complicated. Different heat transfer mechanisms (desuperheating if any, condensation, subcooling) have to be considered as well as the complex geometries (external and sometimes internal) and the eventual presence of non-condensable-gases.

The continuous variation of the flow pattern inevitably affects the internal heat transfer coefficient and so the overall one. This is the reason why condenser design usually considers an approximate form of the heat transfer rate equation:

$$Q = \check{U} A \Delta T_{lm} \quad (7.1)$$

where the overall heat transfer coefficient \check{U} and the logarithmic mean temperature difference ΔT_{lm} are calculated as:

$$\check{U} = \frac{1}{A} \int_A U dA \quad (7.2)$$

and

$$\Delta T_{lm} = \frac{Q}{\int_A U dA} \quad (7.3)$$

The two last parameters are calculated by integrating equation (7.4).

$$dQ = U \Delta T dA \quad (7.4)$$

Due to such strong variability of temperature and vapour quality, the total condenser heat load is divided in different sub-heat-duty zones (or incremental zones) and, for each

of them, energy balance is solved using the enthalpy formulation, instead of temperature one. Finally, the total heat transfer area is calculated as the sum of areas related to all sub-heat-duty zones:

$$A = \sum_i \frac{Q_i}{U_i \Delta T_{lm,i}}$$

This method is the one usually implemented in the majority of heat exchangers design softwares [17]. To avoid pretty complex calculations related to condenser optimisation process, a commercial software (GRETh-EchTherm³) has been used to design and optimise this component of the CPLIP.

7.2.2 Condenser general characteristics

Ram air is the solution retained as cold source to evacuate the thermal load. The same external air conditions used for first approximation design will be used for the optimisation of the condenser. To remind, for the external side: $u_{air} = 10 \text{ m}\cdot\text{s}^{-1}$, $T_{air(land)} = 33^\circ\text{C}$ (see sec. 1.3) and for the internal side, $T_{sat} = 70^\circ\text{C}$.

Fins must be obviously used to increase condenser external heat transfer surface area. They are generally used on the external side of tubes. Finned tubes heat exchangers are categorised in *individually finned tubes* and *tube-finned exchangers*. In the first case (see Fig. 7.4a), fins, usually circular or pseudo-circular, are installed on each tube. In the second case (see Fig. 7.4b) fins are continue, flat, unique and rely all tubes in the bank. Fins may be installed on the tube using different mechanical technologies: press

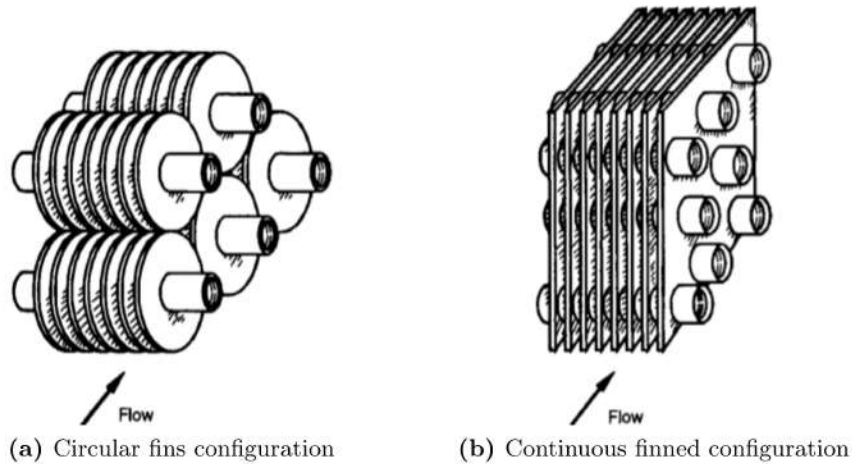


Figure 7.4: Fin configurations used for 2025 solution [17]

³see Appendix C for more information about the used correlations

fit, tension winding, adhesive bonding, soldering, brazing, welding or extrusion [17]. Fin density can vary from 250 to 800 fins/m and their thickness is in general between 0.08 and 0.25 mm. Pressure drop introduced by these devices and their mass should be as low as possible to not negatively influence the drag to lift ratio of the aircraft and the overall power coefficient, C_c [$\text{kW} \cdot \text{kg}^{-1}$]. Fins require the use of a high thermal conductivity material to evacuate as easily as possible the thermal load from the tube to external air. For this reason, a coupling of titanium ($k_{\text{Ti}} \simeq 20 \text{ W} \cdot \text{m}^{-1} \cdot \text{K}^{-1}$), for tubes, and aluminium ($k_{\text{Al}} \simeq 210 \text{ W} \cdot \text{m}^{-1} \cdot \text{K}^{-1}$), for fins, has been chosen⁴. Two different condenser configurations are proposed for 2025 and 2035 solutions.

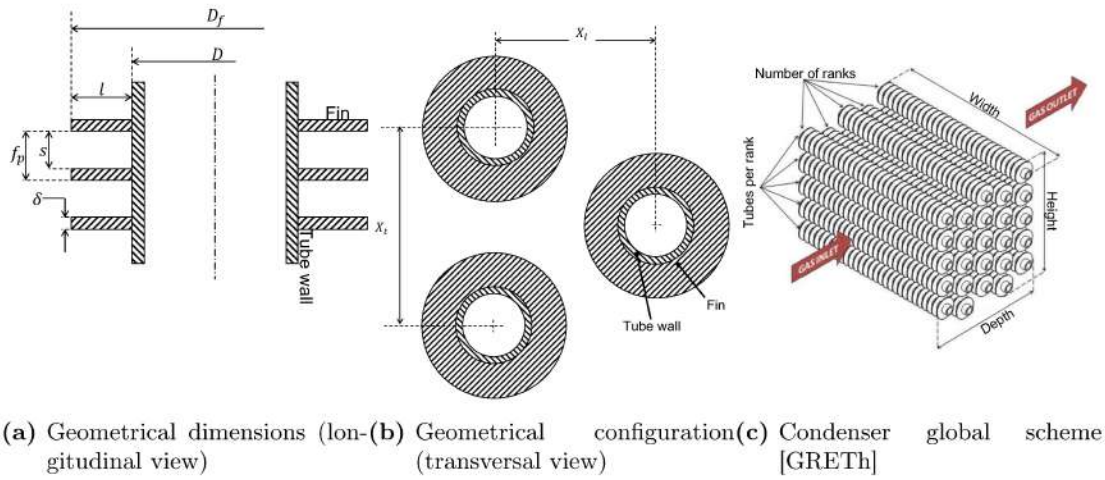
7.2.2.1 A condenser for 2025

At first, for 2025 solution, circular and continuous fins were compared. A parametric study has been made to chose the configuration minimising pressure drop and mass penalty. A different kind of condenser will be introduced for the solution 2035.

Circular fins Geometrical characteristics of circular fins installed in a staggered configuration are reported in Fig. 7.5. All fin geometric characteristics and their configuration have a strong impact on the air-flow characteristics: Reynolds number and heat transfer coefficient [120, 121]. As a consequence, the condenser length is impacted as well. To show the importance of such geometric parameters, fin thickness and fin pitch (δ and f_p) and number of tubes in the bundle (in the transversal and longitudinal directions, X_l and X_t) have been changed, as well as tubes diameter and flow arrangement, to modify the condenser dimensions. Considering a constant thermal power of 15 kW as well as the oversizing to allow subcooling and referring to the geometrical characteristics reported in Fig. 7.5, the results of such parametric study are reported in table 7.2.

Each geometric characteristic of the condenser deeply impacts its behaviour and the change of just one of them leads to a different condenser configuration. External air pressure drop, for example, is impacted by number of ranks, bundle depth and fins geometry. At constant values of δ , l , f_p and longitudinal distance, X_l , the higher the number of ranks, the higher the pressure drop on the air side. This is the reason why the number of ranks should be maintained as low as possible. If fin thickness is increased of $100 \mu\text{m}$, the number of tubes per rank should be increased as well to maintain all other geometric characteristics, including condenser total length, unchanged. Observing, for example, the geometry related to a bundle width of 0.3 m (see table 7.2), increasing the

⁴The contact resistance between tubes and fins is not considered neither for solution 2025 nor for 2035 one.

**Figure 7.5:** Circular fins geometric characteristics

$\delta(\mu\text{m})$	l (mm)	f_p (mm)	Bundle width (m)	Bundle height (m)	Bundle depth (m)	Nbr of ranks	Tubes per rank	Total Length (m)
100	10	1	0.3	0.132	0.67	3	7	17.1
			0.5	0.179	0.35	4	9	18.5
			0.7	0.084	0.47	2	12	17.0
200	10	1	0.3	0.132	0.67	3	17	17.2
			0.4	0.179	0.4	4	10	16.7
			0.7	0.084	0.5	2	12	16.3
300	10	2	0.3	0.132	0.79	3	20	16.5
			0.5	0.084	0.75	2	19	17.2
			0.7	0.084	0.55	2	14	17.5
400	10	2	0.3	0.179	0.56	4	15	16.2
			0.5	0.132	0.51	3	13	16.9
			0.7	0.084	0.55	2	14	17.5
500	15	4	0.4	0.112	1.28	2	24	21.1
600	15	5	0.3	0.112	1.7	2	32	21.9
700	15	6	0.3	0.112	1.8	2	34	23.4
800	15	6	0.3	0.112	1.8	2	34	23.4

Table 7.2: Individually finned condenser geometrical parameters for different fin pitches and thickness

fin thickness, δ , from 100 to 200 μm , the number of tubes per rank increases from 7 to 17! Due to constant bundle height, tubes transversal distance, X_t , decreases: fins are closer and air maldistribution increases. This reduces the overall HXG efficiency and

introduces a pressure drop penalty. Again, comparing results for $\delta = 200$ and $300 \mu\text{m}$, a slight reduction of condenser length is possible by increasing the fin pitch, f_p , of 1 mm. Bundle depth increases as well and a higher number of tubes per rank is required.

All solutions in table 7.2 are equivalent from a thermal point of view (all of them are able to evacuate the same thermal load), but not from a hydraulic standpoint. Fin thicknesses higher than $400 \mu\text{m}$ are not suitable because of pretty high overall condenser volume: one assists to a significative increase of bundle length. In Fig. 7.6 condenser mass and thermal power coefficient are reported as a function of fin thickness, δ , for such solutions of table 7.2 minimising the overall condenser mass. As expected, the increase of fin thickness leads to the increase of the overall condenser mass.

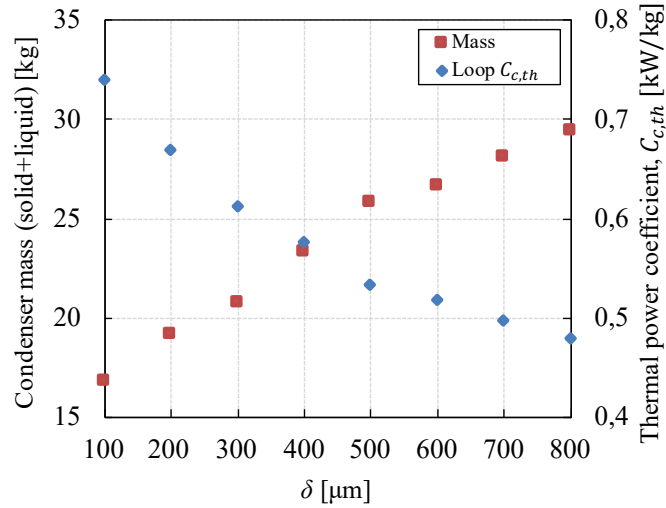


Figure 7.6: Condenser mass and thermal power coefficient as a function of fin thickness, δ .

Continuous finned tubes Mechanical construction of this configuration is quite different than the previous one. Geometric characteristics and tube configuration are reported in Fig. 7.7.

Tubes are inserted in a casing, called *collar*⁵, on which rectangular fins are brazed on. Collar and fins are made of the same material. Tubes are forced to enter into the collar to reduce the contact resistance between them. This configuration is the most used in transport applications such as automobiles radiators. Air is forced to flow among fins and can only interact with tube sections along its path. A thermal interaction between adjacent tubes can occur due to conduction on the fin in X_l and X_t directions. Condenser

⁵Collar internal diameter is the same than tube external one; collar external diameter, D_c , is the tube external diameter + collar thickness (sometimes assumed equal to fin thickness).

design for a thermal load of 15 kW is reported in table 7.3 for different fin thicknesses and pitches (δ and f_p). Condenser behaviour is impacted at the same way than the previous fins typology.

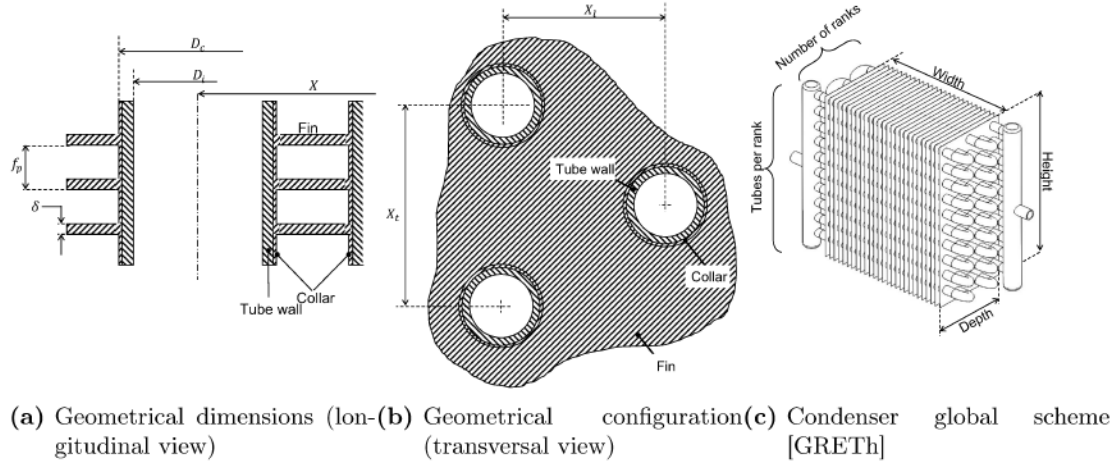


Figure 7.7: Continuous fins geometric characteristics

$\delta(\mu\text{m})$	D_c (mm)	f_p (mm)	Bundle height (m)	Bundle depth (m)	Bundle width (m)	Nbr of ranks	Tubes per rank	Length (m)
1000	1.3	9	0.32	0.155	1.50	2	40	24
100	1.3	2	0.32	0.155	0.95	2	25	15
100	1.3	2	0.32	0.076	1.00	2	28	16.8

Table 7.3: Parametric study of continuous fins condenser.

A comparison of optimised configuration of both typologies, using a fin thickness of $100 \mu\text{m}$, is reported in table 7.4. Continuous fins allow a reduction of the condenser mass as well as a reduction of external side pressure drop and a slightly higher heat exchanger efficiency. This configuration is the one used for 2025.

Configuration	$\delta(\mu\text{m})$	Mass (kg)	Volume (m^3)	Loop C_c ($\text{kW} \cdot \text{kg}^{-1}$)
Individually finned	100	16.6	0.026	0.67
Continuous finned	100	13.3	0.044	0.74

Table 7.4: Condenser configurations comparison.

7.2.2.1.1 Optimised solution for 2025

Condenser Optimised geometric and thermo-hydraulic characteristics are reported in table 7.5 and 7.6, respectively, for a continuous finned condenser⁶.

The same tube thickness of transport lines, 0.6 mm, has been used for all optimised solutions. A fluid arrangement of four fluid passages has been previewed independently from thermal load and number of tubes composing the condenser. Fins and bank geometric characteristics (δ , f_p and X_l , X_t respectively) are unchanged as well, while condenser external dimensions vary as a function of length and number of tubes to adapt condenser thermo-hydraulic characteristic to the thermal load to be evacuated. On the internal side, the resolution method reported in sec. C.1 is used by the software for thermo-hydraulic resolution. Actually, for thermal calculation, Thome's condensation heat transfer model [122, 123] (see C.1.2.2) is used, but no outputs are given about the resulting condensation regime. The reason of constant internal heat transfer coefficient as a function of thermal power are not known.

Considering the mass of the cooling system as trade-off factor, as usual, if just fins geometrical characteristics were modified it could be very difficult to achieve an optimum solution. In fact, to a reduction of fin mass corresponds a proportional increase of tubes mass to damp the lower heat transfer surface area and the HTC reduction. To better understand, let's analyse two condenser solutions. Both are designed to evacuate a nominal thermal load of 16 kW, but using two different fin densities.

The first one, corresponding to the optimum solution (reported in tables 7.5 and 7.6), has a fin density of 833 fins/m (corresponding to a fin pitch $f_p = 1.2$ mm). The second one, with a fin density of 416 fins/m, is identical to the first one, except for the fin pitch which is the double ($f_p = 2.4$ mm). An increase in fin pitch, f_p , leads to condenser undersizing of 27%, if all other geometrical dimensions remain unchanged. Such undersizing is obviously due to a not sufficient heat transfer surface area and to a slight lower HTC. To damp such fin pitch, f_p , variation, the number of tubes per rank should be increased from 22 to 32 and the single tube length from 0.55 to 0.62 m. The condenser is almost 8 m longer! In Fig. 7.8 a comparison of condenser mass distribution is reported for optimised and not optimised solutions (Fig. 7.8a and 7.8b, respectively). A reduction of fin mass leads to an increase of the volume of fluid due to additional tube length and, considering titanium density (used for tubes), almost double than aluminium one (used for fins), the additional mass is significantly higher. The condenser total mass increases of about

⁶With the purpose to provide WP6 (optimisation team, see chap. I) with CPLIP mass trend as a function of power electronics thermal losses, the cooling system has been optimised in the range 5 – 30 kW.

Nominal thermal power (kW)	$\delta(\mu\text{m})$	D_{int} (mm)	D_c (mm)	f_p (mm)	Bundle width (m)	Bundle height (m)	Bundle depth (m)	Nbr of ranks	Tubes per rank	X_t (mm)	X_l (mm)
6	100	3.8	5.2	1.2	0.3	0.265	0.099	8	15	17.7	12.4
8	100	3.8	5.2	1.2	0.37	0.283	0.099	8	16	17.7	12.4
10	100	3.8	5.2	1.2	0.47	0.283	0.099	8	16	17.7	12.4
12	100	3.8	5.2	1.2	0.5	0.319	0.099	8	18	17.7	12.4
14	100	3.8	5.2	1.2	0.61	0.300	0.099	8	17	17.7	12.4
16	100	3.8	5.2	1.2	0.55	0.389	0.099	8	22	17.7	12.4
18	100	3.8	5.2	1.2	0.61	0.389	0.099	8	22	17.7	12.4
20	100	3.8	5.2	1.2	0.69	0.389	0.099	8	22	17.7	12.4
25	100	3.8	5.2	1.2	0.72	0.46	0.0992	8	26	17.7	12.4

Table 7.5: Optimised solution geometry, 2025

Effective thermal power (kW)		Thermal efficiency (%)		HTC_{int} ($\text{W}\cdot\text{m}^{-2}\cdot\text{K}^{-1}$)		HTC_{ext} ($\text{W}\cdot\text{m}^{-2}\cdot\text{K}^{-1}$)	ΔP_{int} (Pa)	ΔP_{ext} (Pa)	Area (m^2)
C	S	G	F	C	S				
6	0.45	87.65	87.04	2383	224.3	92.53	57.54	120.8	11.54
7.97	0.60	87.58	86.97	2383	224.3	93.21	101.9	122.9	15.18
10.05	0.76	87.67	87.06	2383	224.3	92.39	214.9	120.3	19.28
12.02	0.91	87.65	87.04	2383	224.3	92.53	266.8	224.3	23.08
13.99	1.06	87.59	86.98	2383	224.3	93.17	497.8	122.8	26.59
16.06	1.21	87.70	87.09	2383	224.3	92.1	350.4	119.4	31.02
18.03	1.361	87.62	87.01	2383	224.3	92.83	495	121.7	34.41
20.11	1.52	87.71	87.11	2383	224.3	91.92	689.9	118.8	38.92
25.02	1.89	87.64	87.03	2383	224.3	81.17	784.9	1210	48.00

Table 7.6: Optimised solution thermo-hydraulic characteristics, 2025 (C: condensation zone; S: subcooling zone; G: global; F: fin)

23%, from 7.8 to 10.1 kg (fluid included), and the total loop mass increases from 11.8 to 15 kg⁷: it's about 21%! —Once optimal fins geometry has been found it is better to act on the bank configuration to achieve required results—.

Optimisation results Except the evaporator, which dimensions are related to power electronics modules⁸, CPLIP components mass increases as a function of thermal load.

⁷Overall loop mass increase is also due to reservoir volume mass augmentation.

⁸2025's power module dimensions, evaporator characteristics and configuration have been deeply explained in sec. 6.3.2

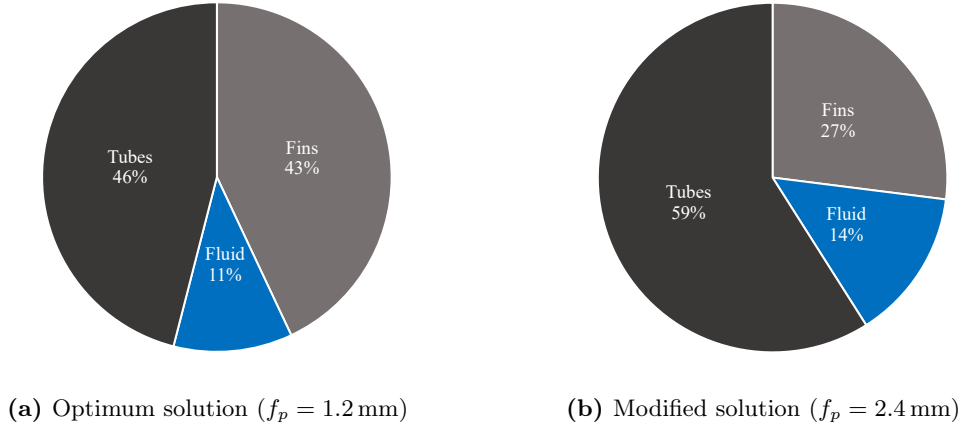


Figure 7.8: Condenser mass distribution for optimised and not optimised solution

Fig. 7.9 depicts the overall loop mass (Fig. 7.9a) and thermal power coefficient (Fig. 7.9b) variation as a function of power electronics thermal losses for solution 2025. As expected, the higher the thermal power to be evacuated, the higher the mass of the cooling system. One may notice that, m_{th} , is linearly related to the thermal load, Q_{th} , as:

$$m_{th} = a Q_{th} + b \quad (7.5)$$

where coefficients a and b are respectively 0.5681 and 2.7323. In particular, the presence of coefficient b is due to a constant evaporator mass whatever the thermal load⁹.

Thermal power coefficient, $C_{c,th}$, has a hyperbolic trend and is characterised by the same coefficients than eq. (7.5):

$$C_{c,th} = \frac{Q_{th}}{m_{th}} = \frac{Q_{th}}{a Q_{th} + b} \quad (7.6)$$

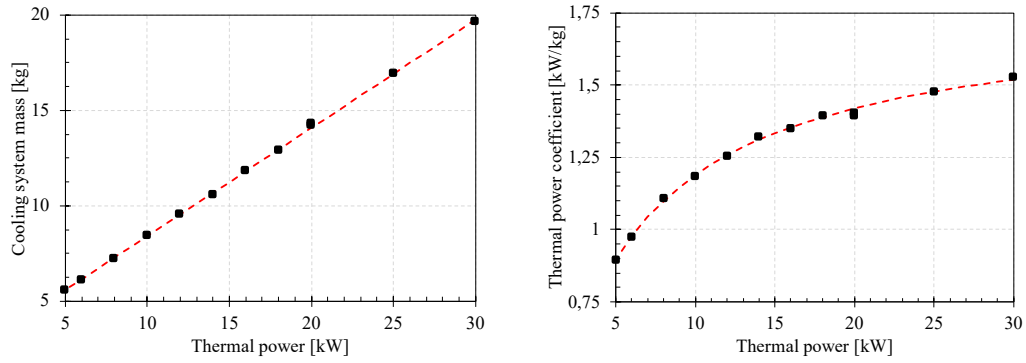
An important mass reduction than first approximation design is evident observing both mass and thermal power coefficient diagrams. Optimisation has led to a significant reduction of the cooling system overall mass, obtaining a thermal power coefficient of $1.33 \text{ kW} \cdot \text{kg}^{-1}$ for the 15-kW-CPLIP¹⁰.

An example of mass distribution for a 16-kW-CPLIP is reported in Fig. 7.10. The smaller condenser leads to a reduction of total fluid and reservoir masses, while the evaporator perceptual-weight has obviously increased due to total weight reduction.

Considering the four electronic topologies proposed by WP2 team [21] for 2025, the

⁹The value of coefficient b agrees with the evaporator total mass.

¹⁰This thermal losses amount has been used of the first approximation design in chap. 4.



(a) CPLIP mass variation as function of the thermal load (2025)

(b) Thermal power coefficient (C_{cth}) trend as function of the heat power (2025)

Figure 7.9: Cooling system overall mass and thermal power coefficient as a function of the thermal load

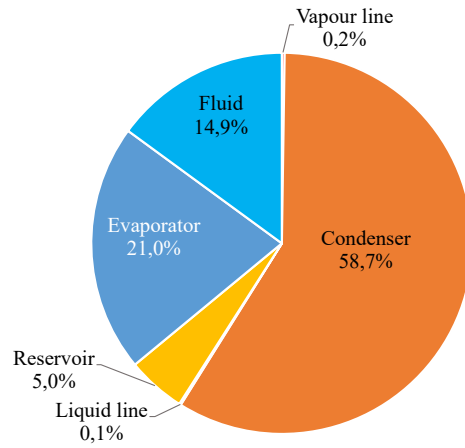


Figure 7.10: Components mass distribution for 16 kW CPLIP

related cooling system optimised results are reported in table 7.7. The highest power coefficient ($> 19 \text{ kW} \cdot \text{kg}^{-1}$, higher than the $15 \text{ kW} \cdot \text{kg}^{-1}$ required for target 2025) was reached for the NPC-DPWMMAX topology [1]. The latter, from an electronic point of view, is characterised by the lowest mass, and the highest electric efficiency: the one that minimise the thermal losses. —Considering the whole system, power electronics and its adjoined cooling *apparatus*, the best solution is not the one composed by two optimised subsystems, but the one characterised by the best trade-off—.

Power electronics topology	Cooling system mass (kg)	Power electronic mass (kg)	$C_{c,th}$ (kW·kg ⁻¹)	C_c (kW·kg ⁻¹)
FC-DPWMMAX	10.5	83	1.29	16.04
FC-PWM	14.0	83	1.16	15.46
NPC-DPWMMAX	11.1	65	1.26	19.71
NPC-PWM	12.3	65	1.27	19.41

Table 7.7: Optimised results for the proposed electronic topologies (2025) [1, 21]

7.2.2.2 A condenser for 2035

2025 solution is characterised by a condenser which has been optimised to minimise as much as possible the whole mass of the loop, but its perceptual weight in CPLIP distribution is still high. With the purpose to further reduce the overall cooling system mass for 2035, another condenser technology must be selected. Such technology has to be characterised by the highest external HTC possible to reduce the solid mass. Moreover, it should contain the lowest amount of fluid with the purpose to reduce the reservoir volume and its fluid content.

Louvered fin heat exchangers (see Fig. 7.11) are characterised, on the external side, by a complex, “interrupted” fin geometry. The “breaking” of the fins allows, of course, to an increase of heat transfer surface area, but it is marginal if compared to the heat transfer coefficient enhancement.

Other than the already known dimensions, in common with “conventional” fins (fin pitch, height and thickness), louvered fins are characterised by the louver angle, louver pitch and louver height, L_α , L_p and L_h , respectively, in Fig. 7.11b.

To enhance the external side heat transfer coefficient, the physics principle beyond louvered fins is based on the rupture of the fluid boundary layer passing through two fins. A portion of air flows through two adjacent fins while another portion deviates flowing through louvers. Among them, boundary layer is broken creating counter-rotating recirculation zones respectively to the leading edge and the detachment bound of the louver itself. Thanks to them, heat transfer coefficient can increase up to three times the one of a not interrupted surface [124]. As one may easily guess, this kind of technology is characterised by higher pressure drops than conventional ones.

With the purpose to reduce the volume of fluid in the condenser and to increase the overall condenser performances, microchannels are used on the internal side. Despite the high pressure drops related to such technology (see. chap. 3.2.2), they are lower than the residual pressure drop calculated considering $\Delta P_{cap,max}$ (see eq. (2.13)) for any exploited

thermal power. Based on the same optimisation criterion used for the solution 2025, and following the same methodology, optimised condenser geometry and thermo-hydraulic characteristics for different thermal loads are reported in table 7.8 and 7.9.

Like the 2025 solution, titanium is the material used for tubes and aluminium is the

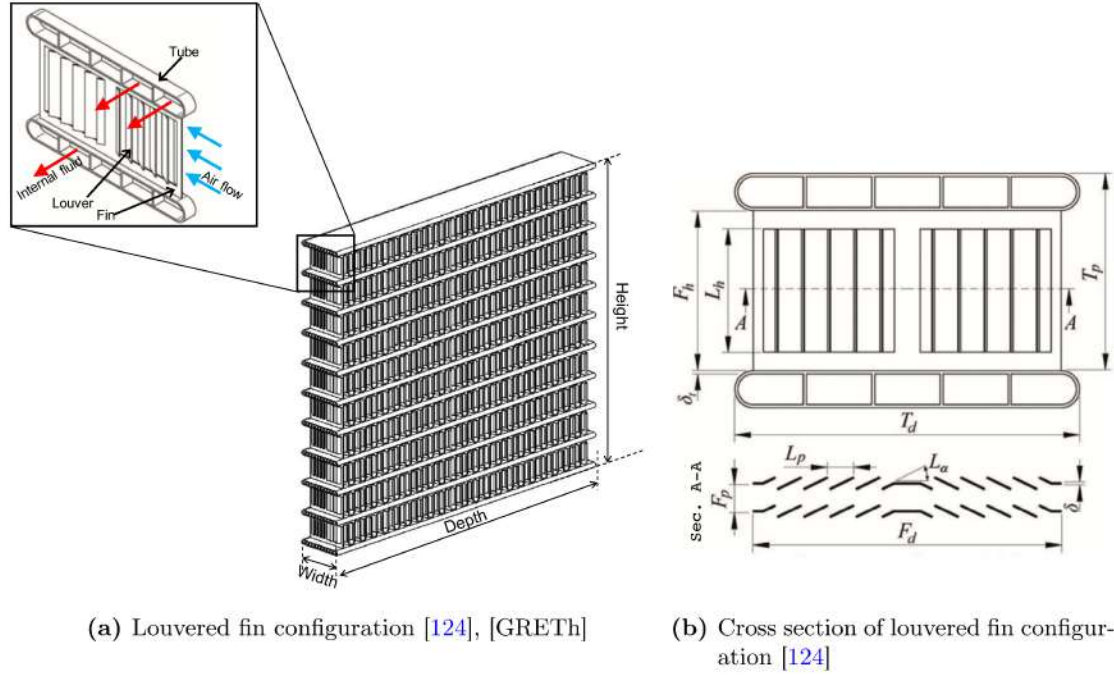


Figure 7.11: Louvered fin condenser

Nominal thermal power (kW)	Fins			Louver			Bank				
	δ (μm)	f_p (mm)	F_h (mm)	L_h (mm)	Height (mm)	L_p (mm)	Width (m)	Height (m)	Depth (m)	N tubes	M. chs/ tube
6	100	1	8	7	0.35	0.5	0.04	0.105	0.175	12	30
8	100	1	8	7	0.35	0.5	0.0364	0.133	0.23	15	30
10	100	1	8	7	0.35	0.5	0.04	0.152	0.24	17	33
12	100	1	8	7	0.35	0.5	0.0364	0.171	0.265	19	30
14	100	1	8	7	0.35	0.5	0.0364	0.180	0.35	20	30
16	100	1	8	7	0.35	0.5	0.0364	0.189	0.37	21	30
18	100	1	8	7	0.35	0.5	0.0376	0.199	0.38	22	31
20	100	1	8	7	0.35	0.5	0.040	0.208	0.31	23	33
25	100	1	8	7	0.35	0.5	0.0424	0.282	0.35	23	35

Table 7.8: Optimised solution geometry, 2035

Effective thermal load (kW)		Thermal efficiency (%)		HTC_{int} ($W \cdot m^{-2} \cdot K^{-1}$)		HTC_{ext} ($W \cdot m^{-2} \cdot K^{-1}$)	ΔP_{int} (Pa)	ΔP_{ext} (Pa)	Area (m ²)
C	S	G	F	C	S				
5.027	0.466	-	-	3707	1238	320.7	228.2	884	1.39
7.977	0.698	-	-	4239	1538	320.3	423.3	749.3	2.11
10.05	0.880	-	-	4254	1238	321.1	584.5	877	2.76
12.02	1.051	-	-	4543	1572	322.4	888.6	758.4	3.12
13.99	1.223	-	-	4728	1592	324.0	1165	768.1	3.61
16.06	1.405	-	-	4900	1630	326.6	1419	784.9	4.06
18.03	1.577	-	-	4972	1672	330.4	1598	854	4.54
20.11	1.759	-	-	4977	1712	341.2	1633	1034	4.90
25.02	2.189	-	-	5308	1851	354.5	2461	1271	5.86

Table 7.9: Optimised solution thermo-hydraulic characteristics, 2035 (C: condensation zone; S: subcooling zone; G: global; F: fin)

one foreseen for fins. Rectangular, 0.2-millimetres-thick tubes are equipped by 1 mm-side-microchannels, spaced of 0.2 mm, which number varies as a function of the thermal load. The internal fluid traverses the condenser in two passages. $N - 1$ tubes are fed-up in parallel, so that the mass flow rate is fairly shared among them (1st passage), while for the second passage, the total amount of fluid is conveyed to flow within the last tube. A manifold is used at the inlet to supply the $N - 1$ tubes and at the outlet to receive the subcooled liquid from the last tube just before the CPLIP's liquid line. Such asymmetry in the mass flow arrangement allows a significative reduction of the overall condenser mass whatever the thermal load. Despite the high pressure drop, either on the internal and on the external side, the condenser is significantly performant if compared to the solution proposed for 2025. In fact, as one can notice from table 7.9, the use of louvered fins allows a significant increase of external HTC, three times higher than the one of 2025 (see tab. 7.6). Such high values of HTC lead to the decrease of the heat transfer surface area, allowing a significative mass saving. Considering the 16 kW solution, for example, the required heat transfer surface area is almost eight times lower for the louvered finned microchannel condenser. Mass distribution of the condenser (see Fig. 7.12) is almost the same than the classical solution, but its total mass is pretty lower.

Optimisation results The same electronic configuration than 2025 has been pre-viewed by WP2 for the solution 2035 (NPC-DPWMMAX) [21]. Power electronics thermal losses are the same, but a different kind of power module is employed with the purpose to make the entire electronic system lighter. Power modules are larger than 2025 ones, they

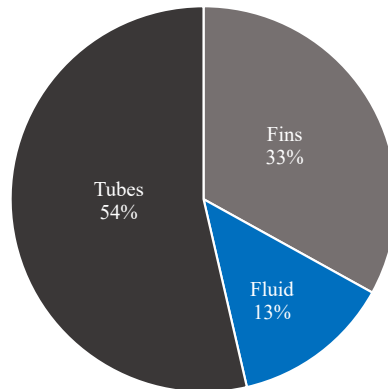


Figure 7.12: Louvered fins and microchannels condenser mass distribution example

are squared ($160 \times 160 \text{ mm}^2$), and only two power modules per electric phase are used. This configuration, under an electronic standpoint, allows mass saving due to reduction of electrical capacities [21]. Even in this case power modules are installed on the evaporator face-to-face resulting in a three parallel evaporators CPLIP. As result, considering the thermal losses related to this electronic configuration, the adjoined cooling system mass, equipped by a louvered fin-microchannels condenser, is just 5.5 kg and, taking into account a power electronics system mass of 22 kg [21], the related global power coefficient¹¹, C_c , overcomes $54 \text{ kW} \cdot \text{kg}^{-1}$! If the main issue of solution 2025 was related to the reduction of condenser mass, in this case, room for improvement are no longer possibles. Condenser is the smallest possible while the evaporator represents the critical component. In fact, observing Fig. 7.13, where a 16-kW-optimised CPLIP components mass distribution is reported, the evaporator is about 72% of total mass, while the cumulated mass of all other components is almost one quarter of total! This solution is the closest to the ideal case: the mass of the entire cooling system is concentrated where power modules are positioned. Cooling system overall mass and thermal power coefficient trends as a function of the thermal load are reported in Fig. 7.14a and 7.14b respectively. The same trends than 2025 has been obviously found, but they are quantitatively different. This solution allows a mass lowering up to six times the 2025's solution with the consequent “boosting” of the thermal power coefficient up to three times.

¹¹2035 target is $25 \text{ kW} \cdot \text{kg}^{-1}$

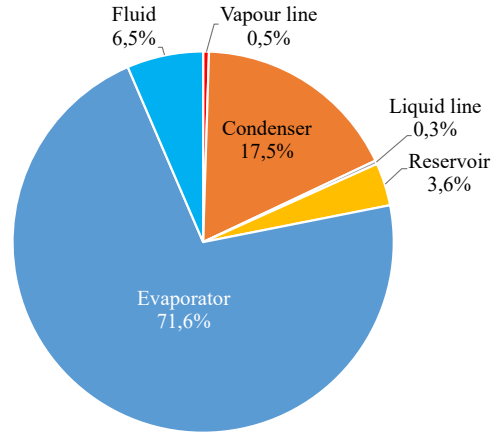


Figure 7.13: Louvered fin-microchannels equipped CPLIP mass distribution

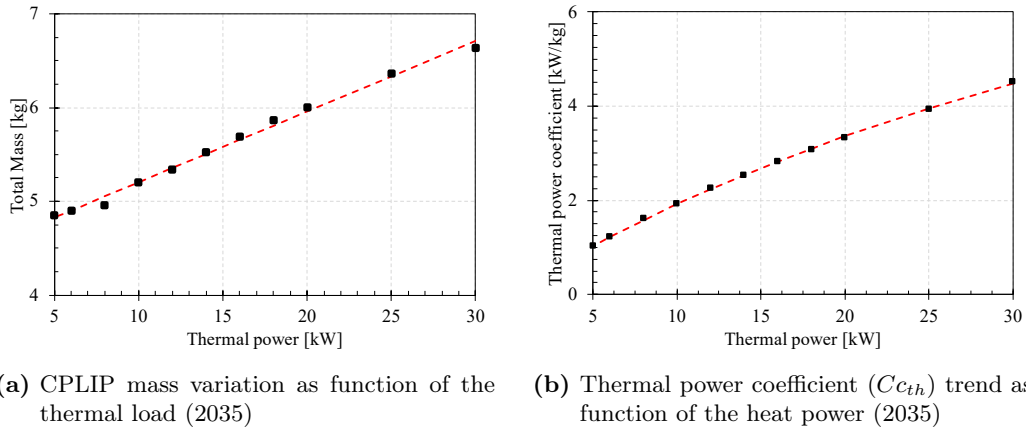


Figure 7.14: Mass and thermal power coefficient as a function of the thermal load (2035)

7.3 Back to design point

To choose the design point, it was necessary to consider the entire mass of the cooling system to check if its thermal inertia could be used to damp the lack of neglected energy, $E_{neglected}$, during the take-off stage (see sec. 7.1 and Fig. 7.1).

In general, if no cooling is foreseen, the thermal energy accumulated in a given interval of time is:

$$E_{neglected} = \int_{t_1}^{t_2} Q_{th}(t) dt \quad (7.7)$$

and also,

$$E_{neglected} = C_{eq} \Delta T \quad (7.8)$$

where the equivalent thermal capacity, C_{eq} , is given by the parallel of thermal capacities of the whole CPLIP (solid and filling liquid)¹²:

$$C_{eq} = m_s c_{p,s} + m_l c_{p,l} \quad (7.9)$$

Combining eq. (7.7) and (7.8), the temperature increase, ΔT , due to the absence of the cooling system to evacuate the thermal load, $Q_{th}(t)$, may be obtained as:

$$\Delta T = \frac{\int_{t_0}^{t_1} Q_{th}(t) dt}{C_{eq}} \quad (7.10)$$

Considering the four electronics topologies proposed by WP2, and considering the design point marked by the letter D in Fig. 7.1, the neglected thermal load shape as a function of time, $Q_{th}(t)$, is reported in Fig. 7.15a. Under the hypothesis that the neglected thermal energy, $E_{neglected}$, is accumulated by the entire mass of the cooling system, the temperature increase due to not evacuated thermal load (calculated according to eq. (7.10)) as a function of time is reported in Fig. 7.15b.

Even if, for the best performing electronic configuration (the one characterised by the best efficiency, NPC-DPWM MAX, grey lines on diagrams 7.15), the quantity of neglected thermal energy is about 2% of the take-off one (see table 7.1), at the end of take-off the system is subject to a temperature rise higher than 30 K.

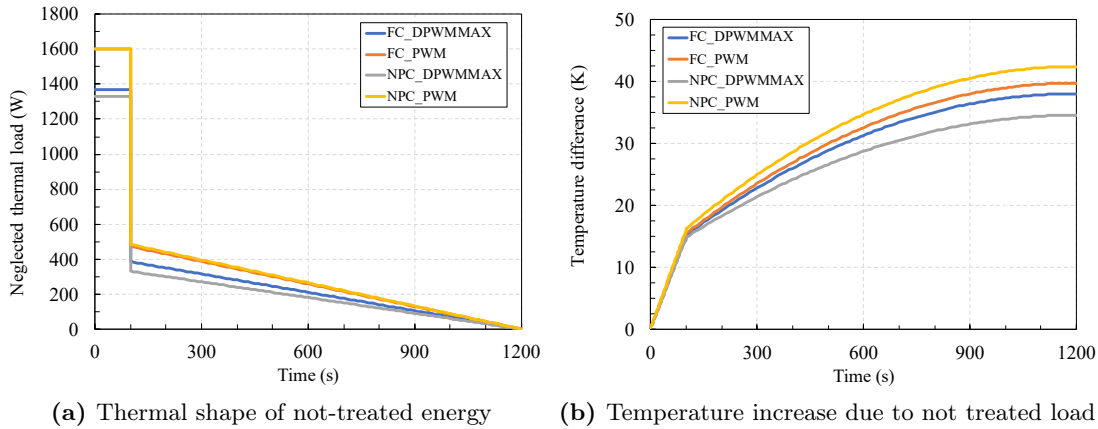


Figure 7.15: Thermal load shape and temperature increase due to not treated thermal energy

CPLIP's thermal inertia cannot damp such amount of neglected energy, $E_{neglected}$, and, to avoid catastrophic consequences, the highest value of thermal losses must be chosen

¹²In reality only evaporator, vapour line and condenser solid and liquid parts should be considered for the purpose. The entire CPLIP mass has been used here to be conservative.

as cooling system design point!

7.4 Overall power coefficient

Targets to be achieved for power electronics and its adjoined cooling system either for 2025 and 2035 are stated here to remind:

- 2025: $15 \text{ kW} \cdot \text{kg}^{-1}$
- 2035: $25 \text{ kW} \cdot \text{kg}^{-1}$

Power coefficient trend as a function of thermal load, for constant power electronics mass, m_{el} , and constant electrical power to be converted, Q_{el} , is here proposed with the purpose to study the variation of total power coefficient, $C_{c,tot}$, as a function of thermal losses, Q_{th} . Considering that cooling system mass, m_{th} , is linearly related to them, see eq. (7.5), the total power coefficient, expressed by the ratio $C_{c,tot} = \frac{Q_{el}}{m_{el}+m_{th}}$, assumes the hyperbolic form described by eq. (7.5). Due to such relation, power coefficient trend is characterised by a decreasing hyperbolic shape.

$$C_{c,tot} = \frac{Q_{el}}{m_{el} + (a Q_{th} + b)} \quad (7.11)$$

Fig. 7.16 shows power coefficient interpolated data for different thermal losses and for 2025 and 2035 solutions. Here, power electronics mass, m_{el} , is considered constant whatever the thermal losses: 65 and 22 kg, for 2025 and 2035 solutions, respectively. Moreover, the total electrical power is also considered constant, $Q_{el} = 1\,500 \text{ kW}$.

As one can easily notice both solutions overcome the target imposed in the context of the HASTECS project!

Solutions for 2025 and 2035 are similar considering the cooling technique. Both solutions share the same components and materials, but not the condenser technology. In 2025 solution, the condenser was the heaviest component allowing room for improvement for 2035 solution, while in the latter the evaporator is the most critical component in the loop. Also, after optimisation, the difference in terms of mass, between 3 independent CPLIPs and three parallel heads CPLIP, is absolutely negligible. Thanks to the use of a cutting-edge technology, allowing to boost condenser external HTC and to increase the compactness of the heat exchanger, requirements of 2035 have been overtaken!

In this work the attention is only focused on thermal and hydraulic issues, and mechanical ones are not addressed. Thus, mass calculations do not consider fixation devices, mechanical construction and other kind of accessories that obviously lead to an increase

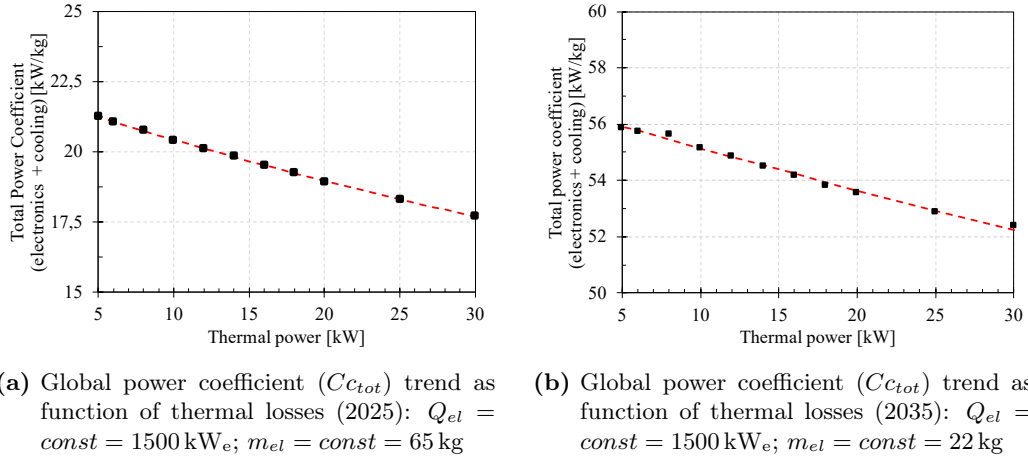


Figure 7.16: Global power coefficient trends for 2025 and 2035 solutions

of the overall mass. It has to be underline that, however, the obtained results allow room for manoeuvre!

7.5 Conclusion

In this chapter CPLIP was designed and optimised following the HASTECS' requirements for 2025 and 2035. After a discussion about the complex optimisation process linked to the condenser, and about the most suitable fin configurations to be used, optimised CPLIP results for 2025 have been presented for the four electronics configurations. Each of them is characterised by a different efficiency. Considering either electronics components and the adjoined cooling system, the configuration allowing the highest mass saving was the NPC-DPWM MAX. In this case, the obtained power coefficient was pretty higher than requirement for 2025 ($> 19 \text{ kW} \cdot \text{kg}^{-1}$).

With the purpose to further reduce the mass of the cooling system, a louvered fins-microchannels condenser was selected for the solution 2035. The latter allows a reduction of the solid mass thanks to enhancement of external side HTC, and a reduction of the fluid amount in the loop thanks to the use of microchannels. The cooling solution proposed for 2035 is "impressive". Despite the electronic configuration is the same than 2025 (the same thermal power must be evacuated), the overall CPLIP mass has been sensibly reduced. Overall power coefficient boosting comes from either electronic and cooling system mass reduction. It is more than twice than the requirement for 2035! However, no accessories and fixation system are considered in calculation at this stage, but the results are encouraging and allows room for manoeuvre.

Part IV

CPLIP behaviour under severe transient conditions

This part is related to the transient behaviour of CPLIP. Its start-up and its response to sudden and violent accelerations are here introduced. The previously introduced numerical model will be used to explain and to understand the phenomena experimentally observed during start-up of the CPLIP in different initial conditions. In the second case, harsh acceleration stages are numerically studied. Weakness and the critical componets of this particular cooling system together with a physical explanation of the different phenomena are introduced in this part.

Severe transient phases: Start-up

CPLIP's start-up is worth of attention, as observed in sec. 6.3.3. To have a deeper knowledge of limitations related to this kind of technology, in this chapter a transient study on start-up phases is proposed. In particular, it is interesting to exploit how environmental conditions, such as vapour line initial temperature, affect thermo/hydraulic CPLIP behaviour during this critical stage.

An analysis based on experimental and numerical results is proposed. The same experimental facility used in previous chapters (5 and 6) and works (see ref. [1, 7, 12, 14, 49, 111, 115]) is used here (see Fig. 8.1)¹. Experimental observations are backed up by precise numerical results, based on 1D model, already described in chap. 5, allowing a better understanding of different phenomena occurring during this critical and delicate stage. The attention is in particular focused on vapour line solid walls, to get quantitative evaluation of the influence of their initial temperature and so of energy exchanges between them and vapour. As it will be shown in the following, thermal load applied to the evaporator is not the only parameter to be considered during CPLIP's start-up.

8.1 Experimental operating conditions

The attention is focused on vapour line initial temperature and how the latter influences energy exchanges between vapour, flowing in it, and solid walls. In other terms, solid walls thermal inertia plays a fundamental role in successful start-up of the CPLIP. To consider thermal inertia influence, from a numerical stand point, it is sufficient to suppress tube thermal capacity, inhibiting the solid specific heat, c_p , but from an experimental point of view it is necessary to act on walls initial temperature to modify the amount of energy exchanged between the fluid and the solid itself.

By keeping fixed and constant reservoir saturation and cold source temperatures, respectively $T_{res} = 70^\circ\text{C}$ and $T_{sec} = 20^\circ\text{C}$, start-up of the loop has been exploited applying different intensities of thermal load steps to the evaporator and using two vapour line

¹The setting valve will be not used in this study, which is why it is not represented in the in the scheme.

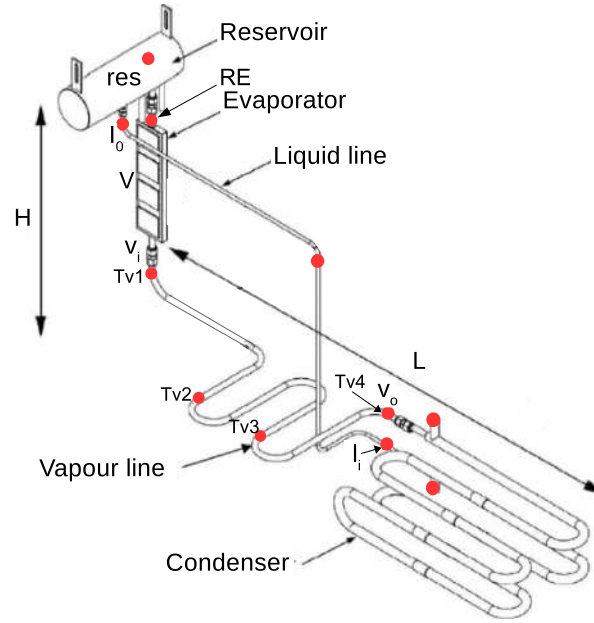


Figure 8.1: CPLIP: experimental facility

solid-wall initial thermal conditions. For simplicity, in the following the definition of cold and hot start-up will be used.

Cold-start-up Start-up condition using vapour line solid walls initial temperature equal to the environmental one (around 20°C);

Hot-start-up Start-up condition using vapour line solid walls initial temperature higher than the environmental one (between 30 and 60°C).

In order to experimentally investigate the influence of vapour tube initial temperature, the latter should be modified to reach the expected value. According to this, the complex heating process of vapour line walls is shown in Fig. 8.2. Such process, for practical purposes, has been divided in four stages: I to III (+hot start-up — IV —).

During stage I the loop is in stand-by position. No thermal load is applied to the evaporator, reservoir is kept to desired saturation conditions and cold source temperature is maintained fixed. In order to heat the vapour line, at the beginning of stage II, power supplied to the evaporator is turned-on and secondary side condenser temperature is set-up to desired vapour line solid wall temperature (50°C for example in this case). The heating process starts here. Condenser cold source temperature increases up to its imposed value and liquid temperature at the outlet of the condenser consequently

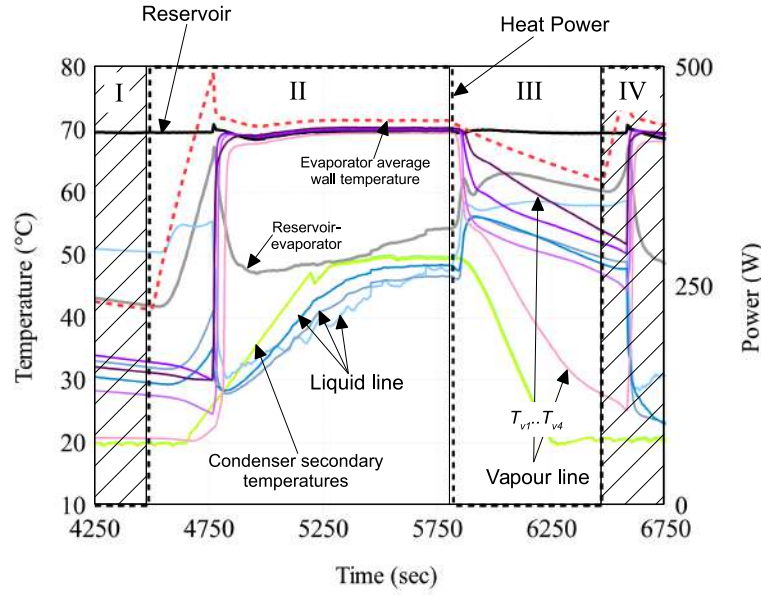


Figure 8.2: Heating process of the vapour line solid walls (methanol, $T_{res} = 70^\circ\text{C}$).

follows such increase. Once steady-state conditions reached, power supply is cut-off and cold source temperature is set-up to the desired value (20°C): stage III begins. Liquid flows back from the reservoir heating the liquid line (blue curves) and subcooled liquid, which temperature is by now close to the cold source one (around 50°C at the end of stage II), flows back and invades condenser and vapour line. At this stage, vapour line solid walls temperature suddenly decreases up to liquid temperature, so they are slightly cooled down. Once the vapour line temperatures have reached the required value, the hot test can begin. Unfortunately, a temperature gradient is present along the vapour line, from the inlet to the outlet. It depends on the proximity of such components like evaporator or condenser. As soon as the cold source temperature has reached the desired value (20°C in this case), power load step is applied to the evaporator: hot start-up test begins (phase IV).

8.2 Start-up behaviour

8.2.1 A severe start-up condition

The response of the CPLIP to a high intensity heat load step, from 0 to 5 kW, during a cold start-up at fixed reservoir and cold source temperature, respectively, $T_{res} = 70^\circ\text{C}$ and $T_{sec} = 20^\circ\text{C}$, is described in this section. The diagram of the response of the

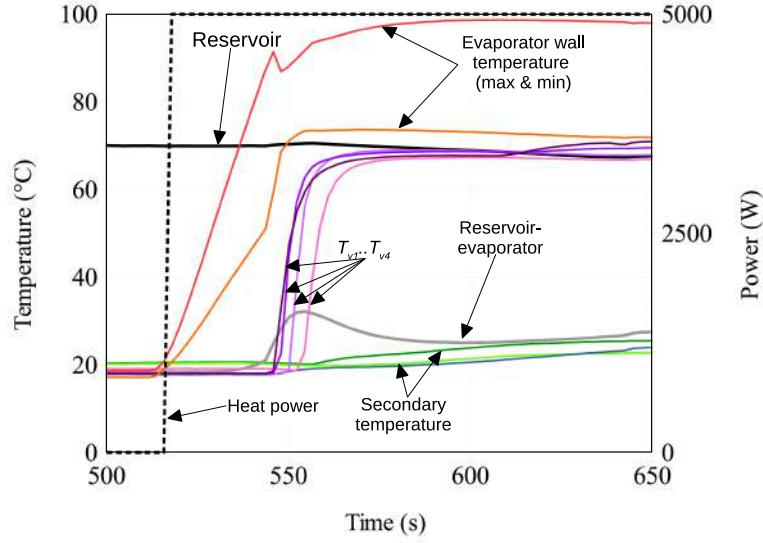


Figure 8.3: 0 – 5 kW cold start-up (methanol, $T_{res} = 70^\circ\text{C}$, $T_{sec} = 20^\circ\text{C}$).

loop is reported in Fig. 8.3². As the power step is applied to the evaporator, the wall temperature increases as quickly as severe the power step is. The evaporator wall temperature continues to rise until vapour is formed in the wick. Evaporator wall is characterised by a temperature difference, red to orange curves' gap (see Fig. 8.3). Following the height of the evaporator, such difference may be attributed to pressure variation between the inlet and the outlet of the evaporator itself: gravity pressure drops lead to progressive recession of evaporation front in the porous wick as a function of temperature levels [111] (see also sec. 6.1.2). When the bottom of the evaporator experiences a temperature peak, due to the onset of nucleation in the wick, its higher part is subject to a fast change in temperature profile. At the same time, temperature increases into reservoir-evaporator tube (grey curve). During start-up, as well as “thermosyphon effect”, from evaporator through the reservoir-evaporator tube, some vapour bubbles percolate the porous wick and flow back to the reservoir. However, no dry-out occurs and liquid, permanently supplied by gravity from reservoir, continues to wet the porous wick. Once saturation conditions stabilised, the temperature difference on evaporator wall stops changing (red to orange curve gap) and vapour, finally, abruptly leaves the evaporator flowing within the vapour line to the condenser. Vapour front transit, through the different sections of the vapour line, may be followed by temperature rise registered by the thermocouples installed on it, one-by-one, from T_{v1} to T_{v4} (dark to light violet

²To simplify the reading, liquid line temperatures were intentionally omitted. They are not relevant for the phenomena here considered.

curves in the diagram). Vapour line is initially filled of liquid at “ambient” conditions ($\simeq 20^\circ\text{C}$), so vapour front passage (pushing-out the liquid) thorough a given section is characterised by a solid wall temperature rise. Sensors register such increase that, as a function of time, has a sigmoid-like shape (as it will be seen in sec. 8.3).

Once vapour front has left the evaporator and liquid has reached the condenser, sub-cooled liquid flows at first in the liquid line and so in the lower part of the reservoir where it is slightly heated. From there, it flows to the evaporator inlet cooling down the reservoir evaporator tube walls until its value is more or less stabilised to the cold source one. The slight increase of inlet and outlet cold source temperatures (light and dark green curves, respectively) is due to slow response of the cryostat. The latter, in fact, is not fast enough to compensate for the occurring high thermal power variation [111].

The loop is able to starts its operations with no particular problems if a high amplitude heat load step ($0 - 5\text{ kW}$) is applied to the evaporator at “low” initial vapour line solid wall temperature. On the contrary, increasing vapour line initial temperature, the loop is not longer able to boot, even in the case of a one-kilowatt-lower load step. In Fig. 8.4, a failing hot start-up of a four-kilowatts-heat power step is reported.

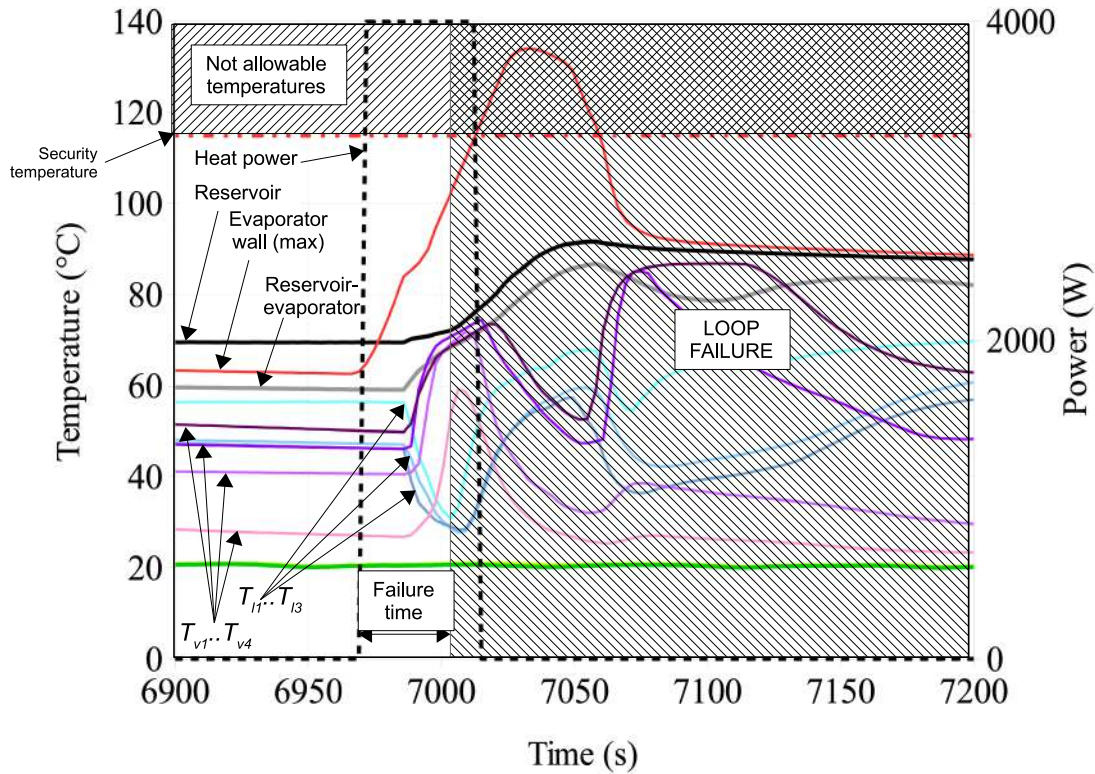


Figure 8.4: 0 – 4 kW hot start-up failure (methanol, $T_{res} = 70^\circ\text{C}$, $T_{sec} = 20^\circ\text{C}$).

Like the first case, after power charge, evaporator wall temperature³ (red line in the diagram) increases, but as the vapour front leaves the evaporator (dark violet curve rise) its shape is slightly modified, but ever growing. At this stage, reservoir saturation temperature (black curve) is modified: vapour bubbles percolate and flow back from the evaporator warming the liquid contained in its lower part. Vapour front flows within the vapour line (all temperature sensors record vapour front passage) and liquid line temperature lowers. At the end of failure time, slope of temperature profiles in the vapour line changes for the first three sections while liquid line temperature rises — no more subcooled liquid is supplied by the condenser —. Continuous percolation from evaporator heavily modifies saturation conditions in the reservoir: reservoir-evaporator line temperature increases (grey line). Once thermal load has been cut-off by security system, evaporator temperature continues to rise due to copper diffusers thermal inertia. The rise of reservoir temperature continues until new saturation conditions are reached. At this moment, in presence of new equilibrium condition the loop seems to re-start! This is testified by the sudden lowering of evaporator walls temperature (red curve), by vapour front passage recorded through the sections of the vapour line (violet curves temperature increase) and by the lowering of liquid line temperature. Cool liquid has reached the lower part of reservoir finally stopping its temperature rising. No thermal load is applied to the evaporator and vapour flow ceases when its saturation conditions reach the reservoir ones. Reservoir and evaporator temperatures slightly decrease, weakly cooled down by natural convection heat exchanges with the external ambient air.

Different tests have been performed to know the start-up limit conditions. In table 8.1, a synthesis of the successful and unsuccessful start-ups is reported.

Power step intensity (kW)	0-0.5	0-2	0-4	0-5
Cold start-up	OK	OK	OK	OK
Hot start-up	OK	OK	X	X

Table 8.1: Successful and unsuccessful start-up synthesis

8.2.2 Low intensity power load step: experimental analysis

Let's now give a look to a working hot start-up and compare it to its cold counterpart. To show how vapour line tubes' thermal discharge influences the overall loop behaviour, a low thermal load power step is used. It has to be considered that all the analyses here introduced are also valid for higher intensity load steps, while the loop is obviously

³For readability issues only the maximal evaporator wall temperature is in this case reported.

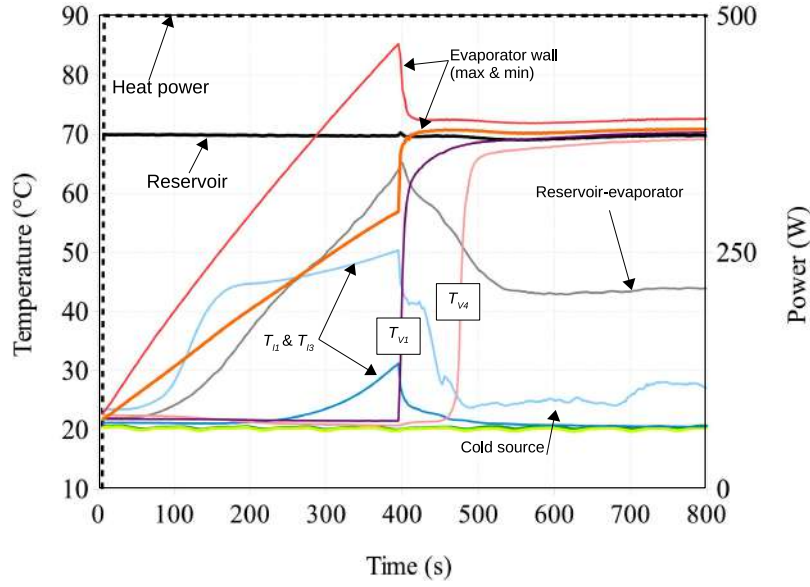


Figure 8.5: Cold start-up (methanol, $T_{res} = 70^\circ\text{C}$, $T_{sec} = 20^\circ\text{C}$)

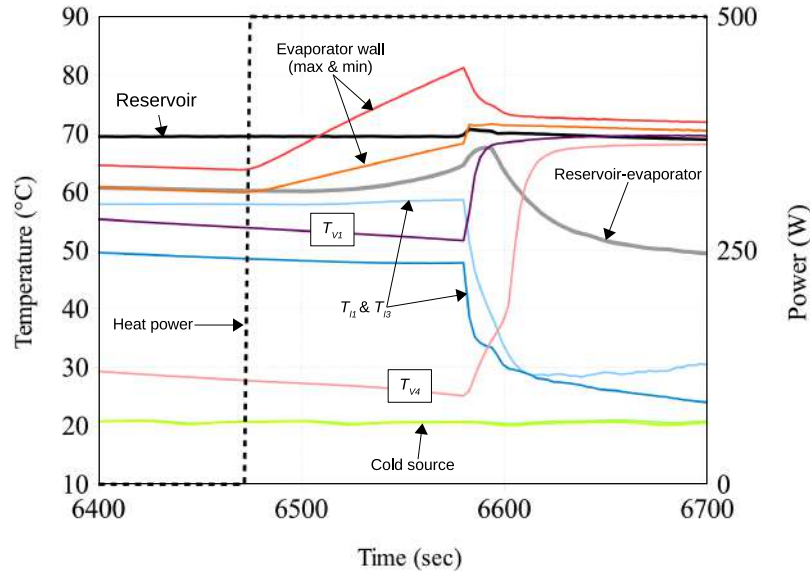


Figure 8.6: Hot start-up (methanol, $T_{res} = 70^\circ\text{C}$, $T_{sec} = 20^\circ\text{C}$)

still operating. Cold and hot start-ups for a heat load step of 0.5 kW, with methanol as working fluid, are reported in Fig. 8.5 and Fig. 8.6, respectively.

As the power step begins, even in this case a temperature gradient is present on evaporator wall, from the bottom to the top (red and orange lines on the diagrams). Temperature on evaporator wall continues to rise until vaporisation of the liquid occurs in the porous wick, after a sufficient superheating highlighted by the temperature peak.

Comparing the start-ups at 5 kW and 0.5 kW, the evaporator wall temperature obviously increases more slowly in the case of low thermal loads (400 s versus 40 s respectively). During this first stage, the reservoir-evaporator temperature (grey curve) rises. Like the previous case, this is mainly due to natural convection effect occurring in the loop before evaporation in the porous wick. The liquid, heated by the evaporator, flows back to the reservoir and, from there, into the liquid line by gravity. This explains the temperature increase recorded in the liquid line from the moment when the power load is applied to the evaporator, to the time when evaporation occurs. Once vapour front has left the evaporator and the liquid is pushed in the good direction, one assists to a lowering of reservoir-evaporator and liquid line temperatures: subcooled liquid flows from the condenser to the reservoir. Temperatures are stabilised and the loop works in steady-state condition.

In Fig. 8.6 the behaviour of the CPLIP is reported in the case of a hot start-up with an initial vapour line temperature between 30 and 60 °C and using the same operating conditions than before. Even in this case, as the thermal load is applied to the evaporator walls, one assists to a slight temperature rise of reservoir-evaporator tube and liquid line due to thermosyphon effect. The slope of the temperature gradient on the evaporator wall is the same than the cold case, but as the vapour quits the evaporator, the progression time of the vapour front through its line is much lower than before⁴. Vapour front takes about 68 s in the cold case (Fig. 8.5) and 18 s in the hot case (Fig. 8.6) to cross the whole vapour line from the inlet to the outlet. A velocity variation has occurred. The vapour front-flow in the hot case is quicker than the cold one. It is interesting to evaluate vapour front velocities, for different thermal loads applied to the evaporator and for different vapour line temperatures to investigate which phenomena are at the basis of the loop failure for pretty high heat load steps.

8.3 Vapour front velocity evaluation

To remind, vapour front evolution in the vapour line can be followed by observing temperature profile in correspondence of a given section. Temperature profiles are characterised by a sigmoid-like shape, whatever the heat load and the section. Such shape is well described by eq. (8.1) and qualitatively reported in Fig. 8.7.

$$T_{v,n} = T_0 + \frac{\Delta T}{b + c e^{-(\Delta \cdot t + f)}} \quad (8.1)$$

⁴One can notice that the time scale (x -axis) in Fig. 8.6 is reduced if compared to Fig. 8.5.

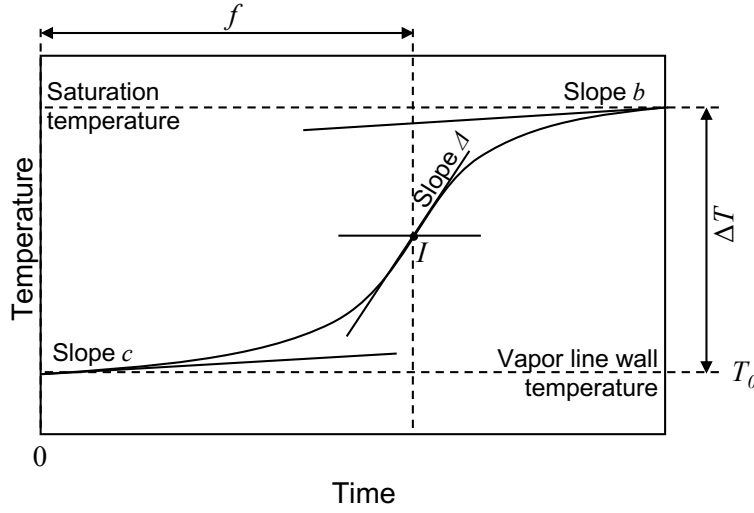


Figure 8.7: Qualitative sigmoid profile as a function of the time

ΔT is the temperature difference between saturation and vapour line initial wall temperature, T_0 , respectively; b and c are tangent values above and below the inflection point I , which slope is Δ . Finally, f is the time that elapses between the power load application and the point corresponding to I .

Experimental vapour front velocity evaluation in different start-up conditions is obtained by fitting temperature measurements in correspondence of the different sections where the thermocouples are installed, and measuring the time difference between the inflection points, I . So, from the knowledge of thermocouple distances, reported in table 8.2, vapour front velocity value is simply obtained as:

$$v = \frac{\Delta x}{\Delta t} \quad (8.2)$$

Range	Distance [cm]
Evaporator outlet- T_{v1}	8
$T_{v1} - T_{v2}$	49
$T_{v2} - T_{v3}$	69
$T_{v3} - T_{v4}$	79

Table 8.2: Thermocouples distances

Curve fitting, on the basis of eq. (8.1), for 2 kW-hot and cold start-up tests are reported in Fig. 8.8.

Resulting velocities for 0.5 and 2 kW-hot and cold tests are reported in table 8.3.

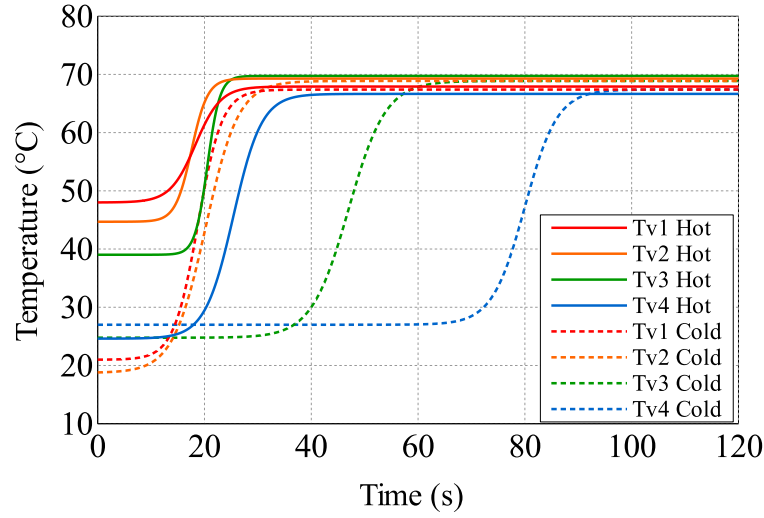


Figure 8.8: Temperature profiles as a function of the time, fitted curves for $Q_{th} = 2$ kW (methanol, $T_{res} = 70$ °C, $T_{sec} = 20$ °C).

Range	Velocity [cm·s ⁻¹]			
	0-0.5 [kW]		0-2 [kW]	
	Cold	Hot	Cold	Hot
$T_{v2} - T_{v3}$	2.3	10.3	2.6	24.6
$T_{v3} - T_{v4}$	2.1	7.0	2.4	14.5

Table 8.3: Velocity evaluation for hot and cold start up at 0.5 kW and a 2 kW power steps

As one can observe from table 8.3, vapour front velocity is more impacted by initial vapour line temperature than applied thermal load. During cold start-up, either 0.5 and 2 kW load steps are characterised by nearly same velocity values. On the contrary, during hot start-up, a one order of magnitude higher velocity value was found. The higher the initial vapour line temperature, the higher the vapour front velocity during the start-up. Vapour front velocity variation from cold to hot start-up could be the reason of unsuccessful start-ups of the loop for quite high heat power steps (4 and 5 kW).

8.4 Discussion

The lower vapour front velocity, during the cold start-up, is due to a higher amount of energy exchanged between the fluid and the solid walls of the vapour line.

During hot start-ups, the increase of vapour front velocity may be due to a reduction of the energy of vapour re-condensation during its flow in a colder tube. In this case,

in fact, vapour temperature decreases below the equilibrium, so it condensates. Vapour pressure decreases as well as vapour front velocity. So, a lower energy of condensation during the loop start-up can be attributed to still high wall temperatures. This leads to a lowering of the hydraulic time constant.

During discharging phase, the amount of energy accumulated by vapour line tube walls can be calculated by eq. (8.3):

$$\begin{aligned} E_t &= (\rho c_p)_{tube} \pi (r_e^2 - r_i^2) \int_{x=0}^{L_v} [T_{fin}(x) - T_0(x)] dx \\ &\simeq (\rho c_p)_{tube} \pi (r_e^2 - r_i^2) L_v \Delta T_v \end{aligned} \quad (8.3)$$

where, r_e and r_i are vapour line external and internal radii respectively, L_v its length and $T_0(x)$ the initial tube temperature at time $t = 0$, and $T_{fin}(x)$ the final tube temperature reached by vapour line in steady state condition. In particular, it can be assumed that, in steady state condition, the latter is almost equal to reservoir saturation temperature, T_{res} , as it may be observed from Fig. 8.8.

If eq. (8.3) is applied to the cold start-up case, which initial tube temperature, T_0 , is 20 °C, and the final one is $T_{fin} \simeq T_{res} = 70$ °C, the energy, E_t , released by vapour to tube walls is:

$$E_t|_{T_0=20^\circ\text{C}} \simeq 8.8 \text{ kJ}$$

Assuming a thermal load, $Q_{th} = 0.5 \text{ kW}$, the latter should be supplied for a delay of 17.5 s to obtain such amount of energy, E_t . At the same way, calculating the equivalent amount of energy for the hot start-up case, the energy, E_t , released by vapour is obviously lower:

$$E_t|_{T_0=40^\circ\text{C}} \simeq 5.3 \text{ kJ}$$

This corresponds to a delay of 10.5 s for a thermal load of 0.5 kW supplied to the evaporator. The highest amount of energy is extracted by the fluid, about 9 kJ during the cold start-up, to heat the tube walls and consequently to condensate the vapour flowing within the vapour line. The lowest amount of energy required during hot-start up, about 5 kJ, leads to a lower amount of condensing vapour within the vapour line.

The lower amount of condensed vapour, during hot start-up, leads to higher vapour front velocities. Pressure drop in the vapour line is proportional to the square of velocity. For pretty high vapour front velocities the pressure in the line could be higher than $\Delta P_{c,max}$ (loop failing zone in Fig. 6.25), leading to loop start-up failure.

It has to be underlined that the presence of the insulating foam installed on the external side of the vapour line tube wall does not impact the solid thermal capacity. In fact,

the thermal capacity of the tube metallic wall is 10^3 times higher than the insulating expanded foam one.

8.5 Experimental and numerical results comparison

8.5.1 Effect of vapour line wall temperature

For the comparison reported in this section, the model presented in section 5.4 is used and results obtained by simulations are compared with experimental ones. The purpose, here, is to explain how thermal inertia of solid tube wall influences vapour distribution in the vapour line. In fact, as observed in sec. 8.3, the behaviour of the vapour front is strictly related to solid walls thermal inertia: the higher or the lower amount of energy used to heat the vapour line tube wall influences the amount of condensing vapour impacting the velocity distribution of the vapour front.

To validate numerical results, the same boundary and initial conditions used during experimental tests were applied. In Fig. 8.9 a comparison between experimental and numerical curves is reported. There, temperature profiles are reported for positions where thermocouples are installed, $T_{v1 \rightarrow v4}$, for experimental (continuous lines) and numerical (dotted lines) curves and using the same operating conditions: $Q_{th} = 0.4 \text{ kW}$, $T_{res} = 70^\circ\text{C}$ and $T_{sec} = 20^\circ\text{C}$.

Experimental and numerical temperature shapes well agree at least for the last two thermocouples, $T_{v3} - T_{v4}$, while a substantial difference is evident observing temperature profiles of the first two thermocouples, $T_{v1} - T_{v2}$ ⁵. It is evident that both temperature sensors record a *quasi*-instantaneous temperature rise, while after a certain time temperature profile of section T_{v2} diverges from T_{v1} . This behaviour could be related either to vapour front shape and vapour line solid wall thermal inertia. In fact, as vapour is formed into the evaporator it enters the vapour line. At this point, a sudden inclusion of vapour into the liquid contained in the vapour line occurs. Because of the violence of this phenomenon, the first two thermocouples are apparently affected, at the same time, by the temperature rise due to the vapour front passage (dotted circle). The latter, flowing within the vapour line becomes flatter and, far from the vapour line inlet, the amount of liquid tends to increase because of the vapour re-condensation. On the other hand, observing temperature profiles resulting from numerical simulations, one can observe a more “relaxed” start-up behaviour. In this case, the vapour front passes through the analysed sections, crossing them one by one, and no particular interesting phenomena may be noticed. Divergence between experimental and numerical results is due to va-

⁵Even if at the end of the process, T_{v2} experimental curve well fits with the numerical one.

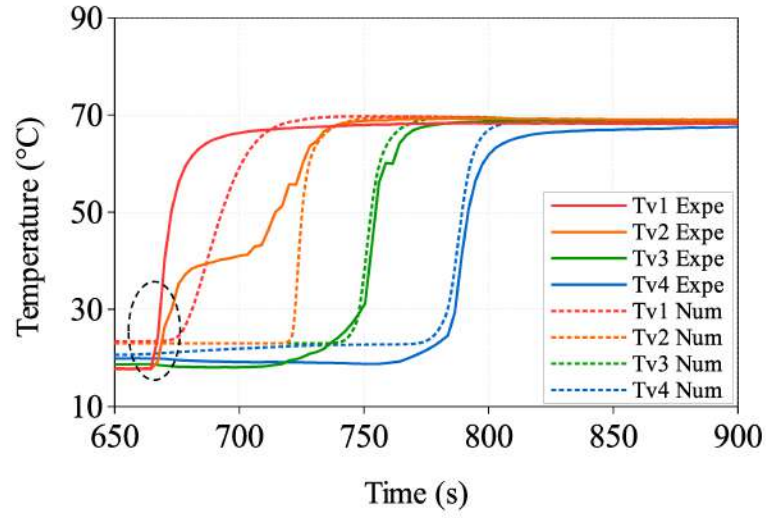


Figure 8.9: Experimental and numerical comparison for a cold start-up (methanol, $Q_{th} = 0.4 \text{ kW}$, $T_{res} = 70^\circ\text{C}$, $T_{sec} = 20^\circ\text{C}$).

pour front shape, modelled as a *piston shape* in the numerical tool, being the model one dimensional and homogeneous. In reality, vapour front shape is much more complicated (see Fig. 8.10) especially at the very beginning of the process. However, today, the causes of the divergence occurring between the measurements of the thermocouples T_{v1} (red line) and T_{v2} (orange line) after a given lapse of time are not well known. This could

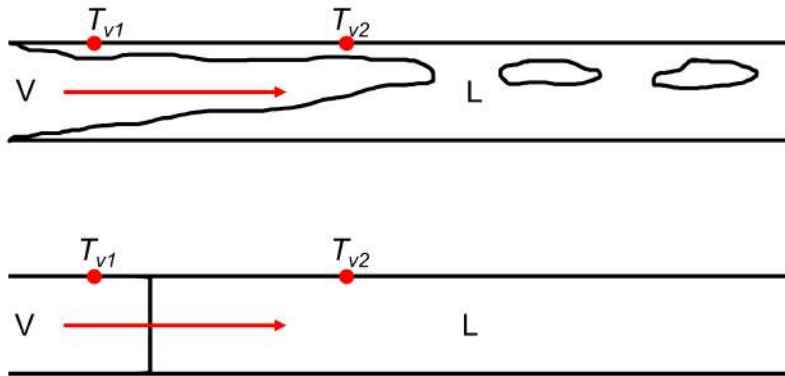


Figure 8.10: Vapour front qualitative shapes: real (up), numerical (piston shape, down)

be due to an expansion, followed by a contraction of the vapour front during the first moments of start-up, but it is just a speculation that may be only confirmed by optical visualisations.

8.5.2 Effect of vapour line wall thermal inertia

As expected, a strict connection between hydraulic and thermal characteristics of the CPLIP exists. A different distribution of fluid phases determines a different pressure field distribution that consequently impacts the velocity field. This is the cause of velocity variations if initial vapour line temperature conditions are modified. For this reason, in order to assess vapour line initial temperature influence on the dynamic response of the loop, a new theoretical study has been performed: numerical calculations have been done taking into account and not walls thermal inertia. From a numerical point of view, this can be easily done by suppressing solid thermal capacities from the thermal network model (see Fig. 5.15d).

In Fig. 8.11, results of simulations with (continuous lines) and without (dashed lines) thermal inertia are reported. Temperature profiles are largely affected by the solid wall thermal capacity, and at the same way than experimental results for hot and cold start-ups (see Fig. 8.8). In fact, as soon as solid walls thermal inertia is not considered, one assists to a reduction of time required by vapour front to cross the vapour line,

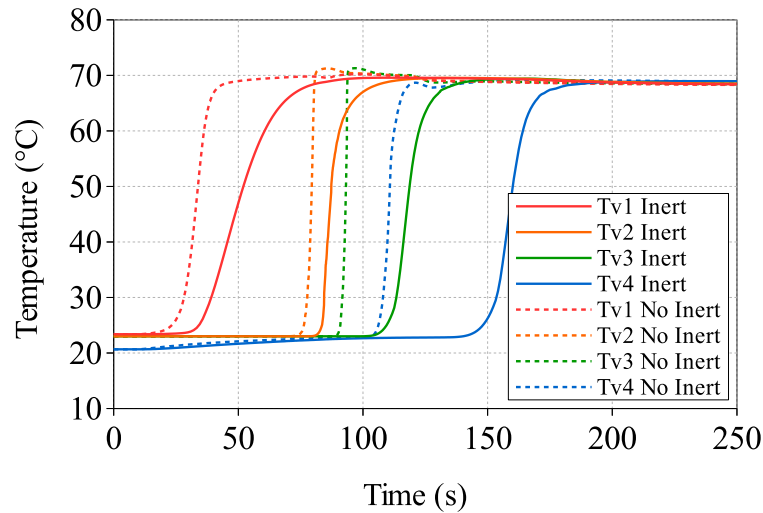


Figure 8.11: Vapour line temperature profiles with (continuous lines) and without (dashed lines) solid wall thermal inertia (methanol, $Q_{th} = 0.4 \text{ kW}$, $T_{res} = 70^\circ\text{C}$, $T_{sec} = 20^\circ\text{C}$)

temperature profiles are stepper and have, at least for the last three thermocouples, a temperature overshoot. Such slight superheating is recorded just before the assessment to the final temperature value. On the contrary, the first thermocouple is impacted by heat conduction from evaporator and its thermal inertia, damping the temperature overshoot that should be present as well.

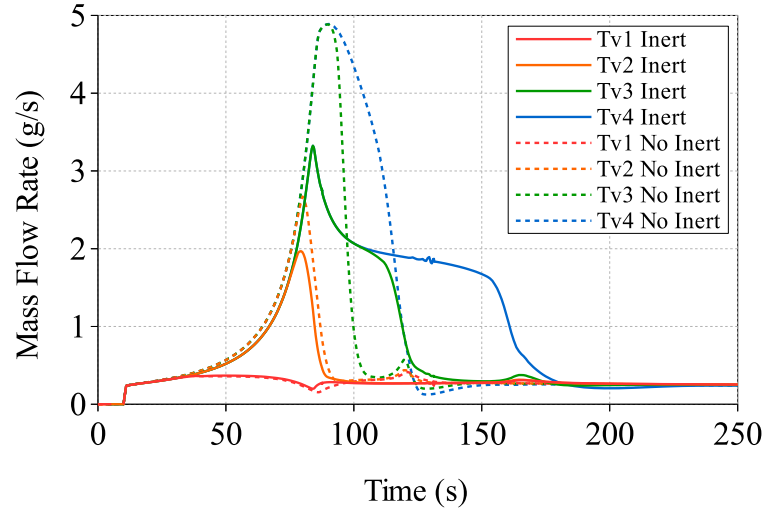


Figure 8.12: Mass flow rate profiles with (continuous lines) and without (dashed lines) solid wall thermal inertia (methanol, $Q_{th} = 0.4 \text{ kW}$, $T_{res} = 70^\circ\text{C}$, $T_{sec} = 20^\circ\text{C}$)

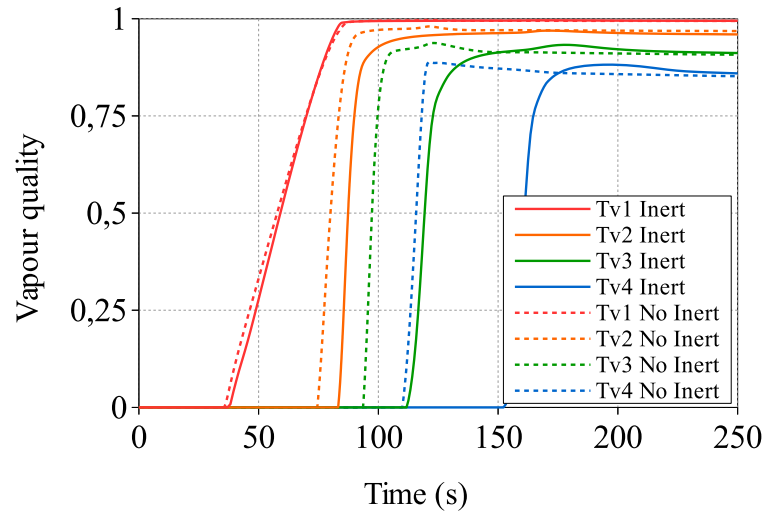


Figure 8.13: Vapour quality profiles with (continuous lines) and without (dashed lines) solid wall thermal inertia (methanol, $Q_{th} = 0.4 \text{ kW}$, $T_{res} = 70^\circ\text{C}$, $T_{sec} = 20^\circ\text{C}$)

The mass flow rate evolving in the loop, at constant thermal power applied to the evaporator, $Q_{th} = 0.4 \text{ kW}$, at $T_{res} = 70^\circ\text{C}$ and $T_{sec} = 20^\circ\text{C}$, with and without thermal inertia is reported in Fig. 8.12. During the very beginning of start-up stage, vapour pushes the liquid within the vapour line to the condenser. Vapour and liquid phases have thus the same velocity. In a given section of the vapour line, due to higher density of the liquid, the mass flow rate value increases up to its maximum value. As soon as liquid fraction decreases, the density decreases as well and mass flow rate experiences a lowering until settling to steady state condition. Both vapour quality and mass flow rate diagrams are influenced by energy exchanges between fluid and solid walls. In particular, observing vapour quality (see Fig. 8.13), thermal inertia decelerates the settling process to the steady vapour quality value for a given section: curves are smoother. This phenomenon is due to vapour re-condensation mechanism described before. By considering no thermal inertia curves in Fig. 8.11 (dashed lines), temperature overshoot, observed in correspondence of section T_{v2} , T_{v3} , and T_{v4} may be attributed to mass flow rate reduction occurring due to lower density of vapour. The minimum mass flow rate occurs when the maximum vapour quality is reached all over the vapour line: CPLIP is stabilised and it operates in steady-state conditions.

8.6 Conclusion

In this chapter, an analysis of the start-up behaviour of a CPLIP is presented in order to have a better understanding of the phenomena occurring during this complex phase. Experimental tests were performed using methanol as working fluid. Results for different vapour line initial conditions were compared to evaluate the influence of thermal inertia on the vapour front behaviour during the loop start-up. Numerical simulations were compared with experimental results during cold start-ups to testify the correctness of interpretation of experimental data. For all experimental tests and numerical simulations, a constant reservoir temperature of 70°C was used. To understand the differences between “relaxed” and extremely severe start-up conditions, CPLIP was pushed up to reach its operating limits during some specific start-ups. The comparison between a severe (5 kW) and a more relaxed (0.5 kW or 2 kW) cold start-up showed that vapour front velocity values are similar for low power step cases, while for high intensity heat power step start-up velocity is one-order-of-magnitude higher. To understand and justify such results for hot and cold cases, an energy based analysis, considering the importance of thermal inertia of vapour line tubes, was performed. It was observed that the variation of vapour front velocity is due to a recondensation of the vapour on the vapour line wall,

more significant during cold start-ups due to a higher difference between fluid and tube initial temperatures. So, as the initial vapour line temperature is low, the vapour front velocity decreases, resulting in higher settling times and quicker vapour quality increases. The vapour line initial temperature determines the quantity of energy that is dissipated by the fluid to the tube walls. This energy, directly related to the recondensation phenomenon on the tube walls, has an impact on the pressure and mass distributions of the vapour phase and, so, on the vapour front velocity and shape. Further studies need to be performed, particularly in terms of experimental visualisations and numerical volume of fluid simulations (of the vapour flow in the vapour line during such transient start-ups) in order to completely validate the assessments given in this chapter from the obtained results.

It has to be underlined that, in the context of HASTECS project, the most critical phases are realised, on the basis of the actually held data, on the ground, where the CPLIP is required to boot at temperatures lower than 40°C . Also, observing Fig. 8.14, where the initial and the final phases of the experimentally exploited mission profile are reported, one may notice that start-up occurs at the beginning of the taxi out stage at low thermal load. In such conditions no particular problems are related to loop start-up.

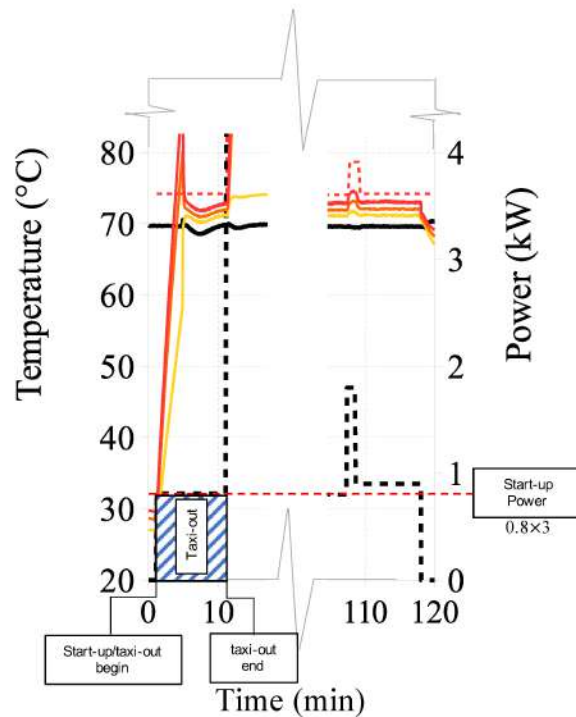


Figure 8.14: Real start-up condition $3 \times 0.8 \text{ kW}$ (methanol, $T_{res} = 70^\circ\text{C}$, $T_{sec} = 20^\circ\text{C}$)

CPLIP behaviour under sudden and violent acceleration stages

Equipment verification in presence of violent acceleration fields is necessary for such systems that will be installed on flying vehicles. During “turbulence” stages, in fact, equipments are strongly stressed for a limited lapse of time. In this brief and last chapter, an introduction to CPLIP behaviour during such sudden and violent acceleration stages is described. Starting from a simple acceleration impulse, hydraulic behaviour of CPLIP will be numerically analysed, using the already described model (see chap. 5), to understand which components of the loop are mostly impacted. An acceleration peak of a given intensity is used for the study to explain hydraulic and thermal effects on the loop. Finally, to have a first overview of the most impacting parameters on CPLIP behaviour, a parametric study is proposed, changing impulse time duration, amplitude and condenser-to-reservoir height difference.

Limitations of the present study *It is expected to have more questions than answers at the end of this chapter!* This study should be seen as an introduction to a pretty higher difficult research subject related to the study of transient and violent acceleration fields perturbing the operations of the CPLIP.

Strong limitations are related to the nature of the model and to the absence of validation of results. The model here used, the Blet’s one [25], is a 1-D finite volume homogeneous model, in which the evaporator is modelled by using a macroscopic approach. So, any effect of acceleration field modification on the wick operating mechanisms, unfortunately, cannot be observed using this model. Any thermo-hydraulic effect, like, for example, bubbles back-flow to the reservoir lower part, potentially leading to loop failure, cannot be assessed. Similarly, the way the acceleration field variation modifies the fluid distribution in the evaporator and how it behaves in such cases, will remain an open question. In fact, the way the liquid phase spreads in the evaporator is surely impacted by acceleration field variation and changes in turn the way the porous wick behaves. The reservoir-evaporator tube is characterised by a gravity driven liquid flow. The discretisa-

tion of such component by using just one volume, results in a strong limiting condition, and does not allow to observe “what really is going on”. In fact, a change in gravity field could lead to a different pressure distribution at the inlet and at the outlet of the tube, and being the latter related to the evaporator, it could often play a role, on its behaviour.

On reservoir side, despite the ability to take into account mass and energy exchanges between reservoir higher and lower parts, and between the lower part and the liquid line, the reservoir lower part is modelled by just one node, and the fluid flow is one-dimensional. To be clear, “the reservoir lower part is modelled as a 0.3-meter-long tube characterised by just one node”. Even in this case, a difference in pressure distribution could not be taken into account neither at the inlet nor at the outlet of this component.

Due to the use of empirical conductances, any change in their value, consequent to a transient acceleration field, may be not considered as well¹.

Two-phase flow homogeneity hypothesis represents a limiting factor as well. Following the definition given by Goncalves and Patella: “[...] *in homogeneous model the phases are assumed to be in kinematic and thermodynamic equilibrium: they share the same pressure, P , temperature, T , and velocity, u [...]*” [125]. During sudden transient stages, homogeneity of two-phase flow is not ensured and such equilibrium is broken!

Actually, either numerical and physical problems have to be assessed during this study and nowadays it is difficult to say if divergence issues encountered during the study come from a “not well posed condition” or by a physical danger for the loop. To avoid any kind of instability, a low thermal load (1 kW) has been used to complete the following study.

However, despite all its limitations — in this application case — the model is able to give “acceptable” results, suggesting basic and qualitative behaviour of the loop during sudden acceleration stages. The attention will be especially focused on hydraulics effects, such as competition between the liquid back-flow into the condenser and the vapour phase compression in the vapour line. In particular, this study allows to identify most delicate components in the loop during such critical stages.

9.1 Accelerations in civil flight applications

Acceleration field maximal intensity depends on the position of the equipment on the aircraft and on its operating requirements. The latter are divided in three categories (A, B and C), defined by data sheet and applicable to equipments:

A which are not required to work during manoeuvre stage.

¹It should be also reminded that the definition itself of thermal conductance requires its measurement in steady state conditions.

B which are required to reliably operate in manoeuvre stage.

C which are required to operate after an emergency landing.

Local acceleration field intensity is strongly influenced by the position of the equipment in the aircraft. Information are so given depending on the position: VTP (Vertical Tail Plane), HTP (Horizontal Tail Plane), fuselage and, finally, wing zone. The latter is divided in up to engine and after the engine. Table 9.1 reports, as an example, the acceleration modules for an equipment installed on the wing up to the engine, as the solution retained in this work has been considered to be placed in the nacelle. Acceleration values are given for forward (FWD), toward (AFT), UP, DOWN and lateral (LAT) directions. Moreover, arbitrary and non-arbitrary mounted equipments should be considered as well.

The cooling system retained during this work is supposed to be installed in the nacelle and acceleration intensity field is considered for an up-to-engine non-arbitrary mounted equipment. Under the hypothesis that the CPLIP is not required to surely work after an emergency landing, but it must, during manoeuvre state, category B has been chosen for acceleration levels.

	Arbitrary Mounted	Non-arbitrary mounted				
		FWD	AFT	UP	DOWN	LAT
Functional test Category A & B	8g	8g	2g	2g	5.5g	3g
Functional test Category C	13g	13g	9g	8.5g	6g	4.5g
Structural test	13g	9g	3g	8.5g	6g	4.5g

Table 9.1: Acceleration modules, wing zone up to O/B engine

However, no information are given about the time lasting of such acceleration stage. In absence of such information, time will be arbitrarily chosen.

9.2 Simulation conditions

For simulations, the previously described Blet's model [25] (see chap. 5) has been modified in order to agree with the requirements of the problem.

According to the qualitative diagram reported in Fig. 9.1, once the CPLIP operates in steady-state conditions, an acceleration impulse is applied to the loop at the time t_{init} . Acceleration field increases from normal gravity state to the maximum acceleration value: $\vec{a} = k \vec{g}$ with $1 \leq k \leq 8.5$. After the peak, at time t_{gp} , acceleration value decreases

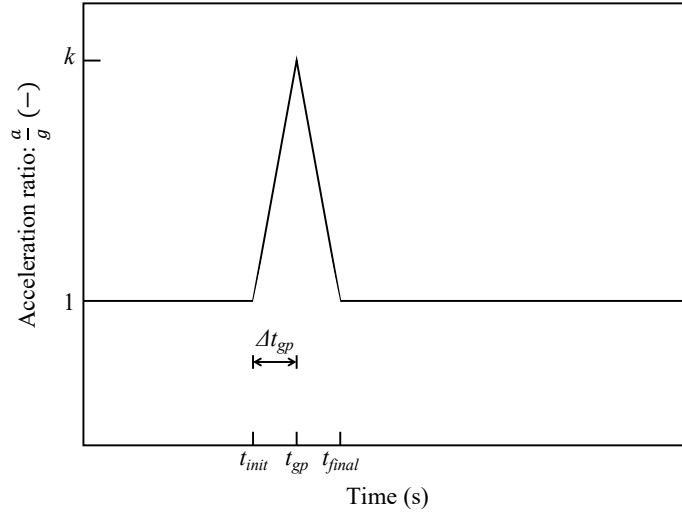


Figure 9.1: Qualitative diagram of acceleration impulse used for study

down to normal gravity at time t_{final} . From this moment, the loop continues — if it can — to operate in normal conditions.

For all the cases presented in this chapter, the thermal load², Q_{th} , applied to the evaporator is constant and equal to 1 kW, while reservoir and cold source temperatures are, respectively, $T_{res} = 70^\circ\text{C}$ and $T_{sec} = 20^\circ\text{C}$.

9.3 CPLIP behaviour under perturbed transient acceleration field

Hydraulics To study the influence of sudden acceleration stages on CPLIP behaviour, an impulsion intensity of $3g$ will be considered for a time duration $\Delta t_{gp} = 0.5\text{ s}$. Perturbed acceleration stage starts³ at 2130 s and lasts 1 s. The gravity term, $\rho g H$, responsible for the highest pressure drop in the loop (see eq. 6.1) for the fluid phase characterised by the highest density, ρ , is obviously impacted by acceleration variation.

In Fig. 9.2, pressure profiles at the inlet and the outlet of vapour and liquid lines are reported for such acceleration value. Vapour line inlet to outlet pressure difference (circled and crossed red lines in the diagram), $\Delta P_{vapour\ line}$, is quite small when compared

²Due to some stability issues of the model, which reason are not today known, the thermal load has been chosen to be the highest possible, allowing to reach a value of 8.5g during the parametric study. However, being this parameter constant during all the present discussion, it will not influence understanding of phenomena and conclusion.

³The beginning time has been arbitrary chosen with the only condition that it should be far enough from start-up and so to allow full steady operations before the acceleration impulse.

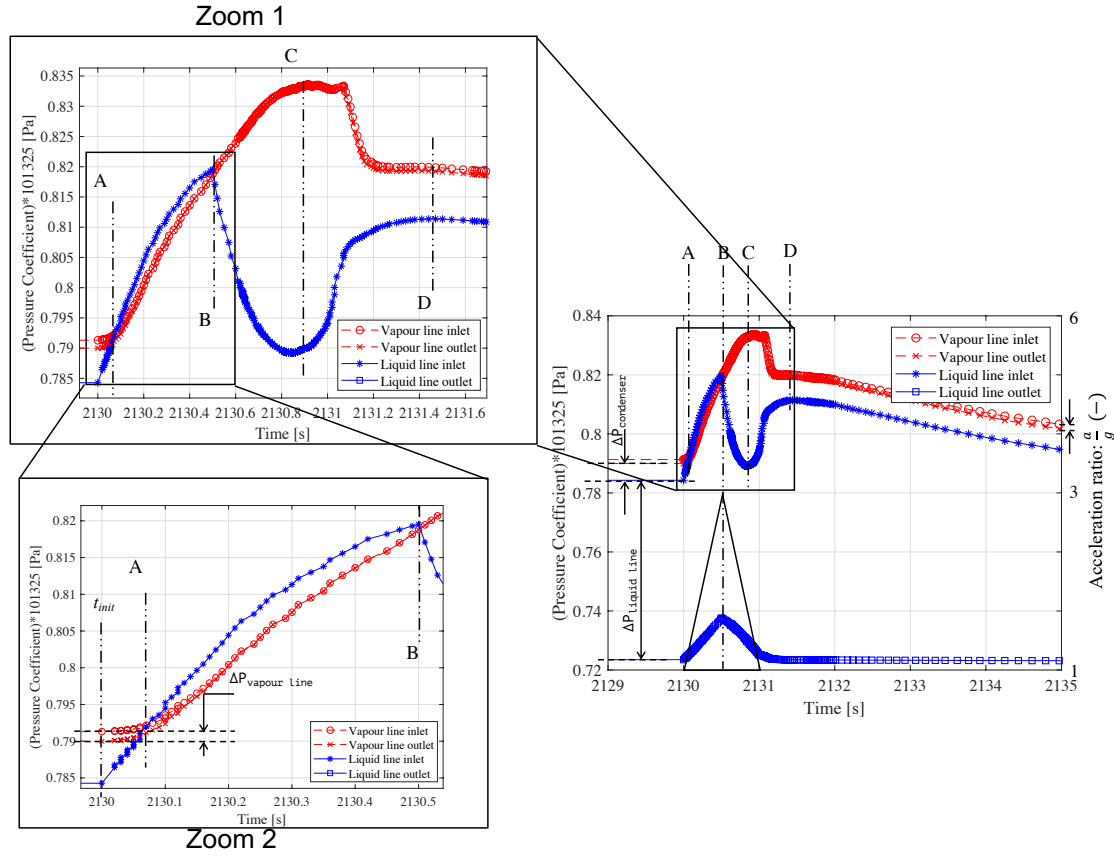


Figure 9.2: Total pressure variation diagram during acceleration impulse (methanol, $Q_{th} = 1 \text{ kW}$, $T_{res} = 70^\circ\text{C}$, $T_{sec} = 20^\circ\text{C}$, $3g$, $H = 90 \text{ cm}$)

to liquid line one (star and squared blue lines), $\Delta P_{liquid \text{ line}}$, where the weight of gravity pressure drop is much higher than viscous one. Pressure drops in the condenser (vapour line outlet to liquid line inlet pressure difference), $\Delta P_{condenser}$, are reported as well.

To understand the phenomena occurring during sudden acceleration stages, the pressure diagram in Fig. 9.2 has been divided in five stages. The first stage, starting at 2130sec (corresponding to the perturbation beginning time, t_{init}) and ending in A, is characterised by a range of pressure values at the inlet of liquid line (blue curve) lower than those at the outlet of vapour line (red line — see also Zoom 2 in Fig. 9.2 —). During this stage, pressure at condenser outlet rises faster than pressure at condenser inlet until intersection in correspondence of point A. The latter has been chosen as the point where the liquid pressure at the outlet of the condenser becomes higher than the pressure at the inlet, demonstrating a transition to a counterflow after the beginning of the acceleration perturbation. Between points A and B, the pressure at the outlet of the condenser

remains higher than the one at the inlet. Once the acceleration peak reached (point B is positioned in correspondence of such peak), the pressure at the outlet of the condenser decreases and re-becomes lower than the one at the inlet. Point B also corresponds to the maximal pressure achieved at condenser outlet. Between B and C, pressure at condenser outlet falls down (blue curve), while at the inlet it continues to rise (red curve). In correspondence of point C, the pressure drop in the condenser is the highest possible (during the transient stage): the pressure at the inlet reaches its maximum, while the one at the outlet reaches its minimum. After point C, acceleration impulse influence is going to run out and pressures at inlet and outlet of the condenser get close until point D. The latter corresponds to the maximum pressure value reached at the outlet of the condenser before the slow return to steady state conditions. Equilibrium is re-established in the condenser, at the inlet and at the outlet. Despite both curves decrease, they run alongside until settling in steady state conditions and their difference is constant. Pressure difference between vapour line inlet and outlet is also re-established, testifying that vapour is still flowing in the line. Observing liquid line outlet shape (squared blue curve), one may notice, instead, that the time variation of pressure simply follows acceleration impulse shape. As the reader has surely noticed, during sudden acceleration stages the condenser is the key component driving the behaviour of the CPLIP.

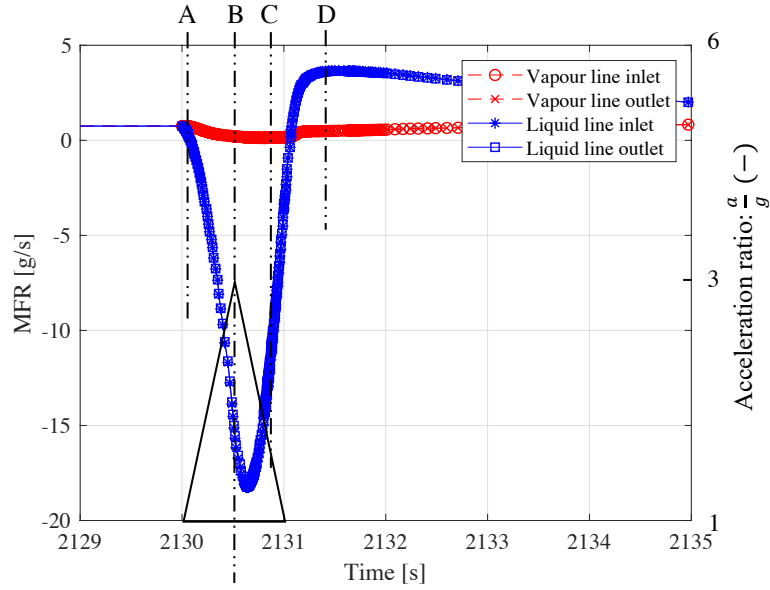


Figure 9.3: Mass flow rate variation diagram during acceleration impulse ($Q_{th} = 1 \text{ kW}$, $T_{res} = 70^\circ\text{C}$, $T_{sec} = 20^\circ\text{C}$, $3g$, $H = 90 \text{ cm}$)

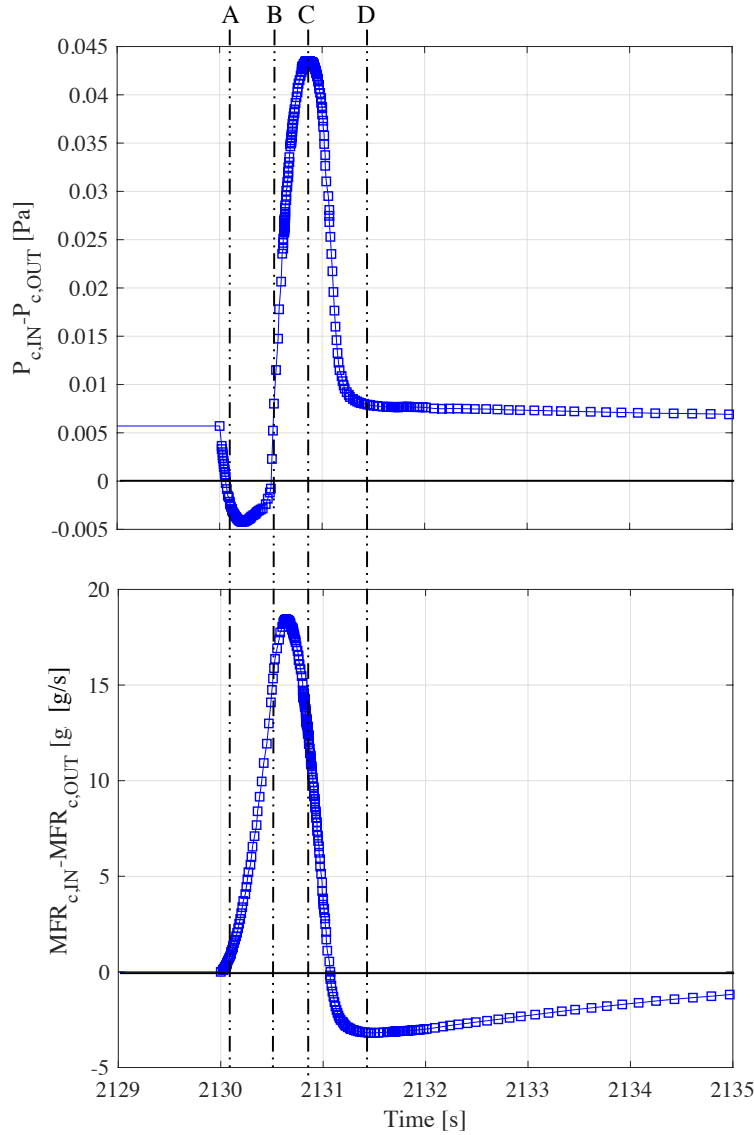


Figure 9.4: Condenser inlet to outlet pressure (top) and mass flow rate (bottom) difference during acceleration impulse (methanol, $Q_{th} = 1 \text{ kW}$, $T_{res} = 70^\circ\text{C}$, $T_{sec} = 20^\circ\text{C}$, $3g$, $H = 90 \text{ cm}$)

Liquid and vapour mass flow rate behaviour are reported in Fig. 9.3 for the same positions than Fig. 9.2. While in Fig. 9.4, condenser inlet to outlet pressure and mass flow rate difference relations are graphically reported. There, the same division has been used as well.

From the beginning of the acceleration impulse (2130sec), the pressure difference, $P_{C,IN} - P_{C,OUT}$, decreases and becomes negative after point A and condenser inlet to

outlet mass flow rate difference, $MFR_{C,IN} - MFR_{C,OUT}$, increases. A mass of liquid flows back from reservoir to the condenser while vapour flows in the positive direction⁴. Masses of fluid enter in the condenser both from the inlet (vapour) and the outlet (liquid), so the condition $|\dot{m}_{C,OUT}| > |\dot{m}_{C,IN}|$ is verified all along the duration of the perturbation. The MFR of liquid, flowing from the reservoir, continues to rise until point B, corresponding to the condition $P_{C,IN} = P_{C,OUT}$. There, the mass flow rate, after a slight delay (time occurring between point B and maximum liquid MFR entering the condenser) reaches its maximum value. Despite the reversed flow of liquid, vapour phase continues to flow from the evaporator to the condenser. Its mass flow rate decreases with time and, according to the vapour line inlet-to-outlet pressure difference, observed in Fig. 9.2, it never becomes negative. It reaches its minimum in C where the pressure drop in the condenser is the highest one. The mass flow rate difference continues to drop until it intersects one more time the zero axis (equivalence between inlet and outlet mass flow rates). It temporarily re-becomes negative: liquid mass flow rate exiting the condenser is higher than the vapour entering one (piston flow). Once point D reached, the mass flow rate difference is the lowest one, and the first “zero-gradient point” in pressure difference diagram is reached. From now the system is going to be settled until normal gravity steady conditions.

The increasing amount of liquid, flowing back from reservoir to condenser, naturally pushes back the vapour, impacting condensation length as well as the vapour mass flow rate (due to its pressure increase). Recession of condensation front in the condenser is shown in Fig. 9.5 (two-phase length). As acceleration peak begins, vapour is pushed back by the mass of liquid flowing from the reservoir. As soon as acceleration peak is reached, liquid phase continues to expand back. Vapour is still compressed by liquid, until the pressure of the latter decreases (from point B to C). Expansion of liquid continues during gravity discharge and, just before the end of the impulse, the pressure in vapour line settles as soon as the negative mass flow rate of liquid diminishes. The increase in vapour pressure continues during the discharging phase as well as the liquid pressure lowering. As soon as the positive liquid mass flow rate is re-established, condensation length slowly increases, driven by the re-established pressure equilibrium between vapour at condenser inlet and subcooled liquid at the outlet. The liquid thrust during the transient stage is responsible of the recession of condensation front in the condenser. During such liquid expansion within the condenser, vapour is compressed, its mass flow rate slightly decreases all along the duration of the acceleration impulse, but it never becomes zero (as it may be seen in Fig. 9.3).

⁴From the evaporator to the condenser.

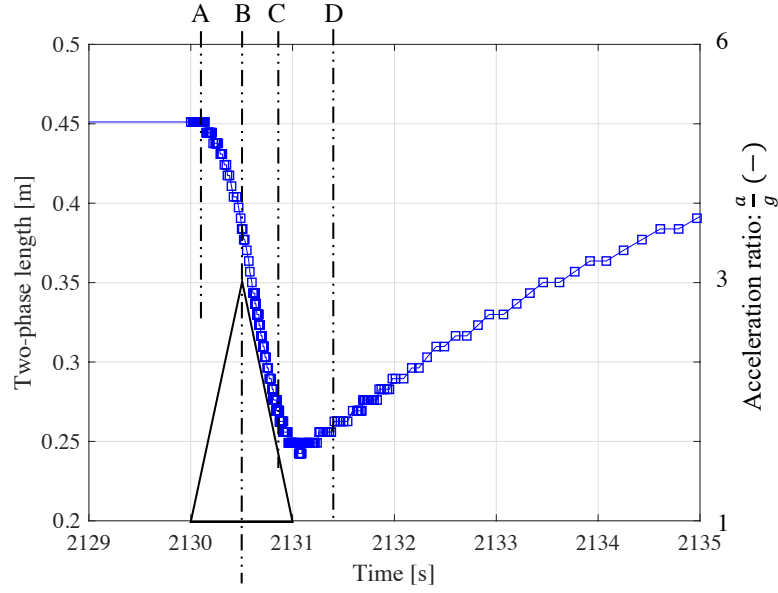


Figure 9.5: Two-phase length variation during acceleration impulse (methanol, $Q_{th} = 1$ kW, $T_{res} = 70^\circ\text{C}$, $T_{sec} = 20^\circ\text{C}$, $3g$, $H = 90$ cm)

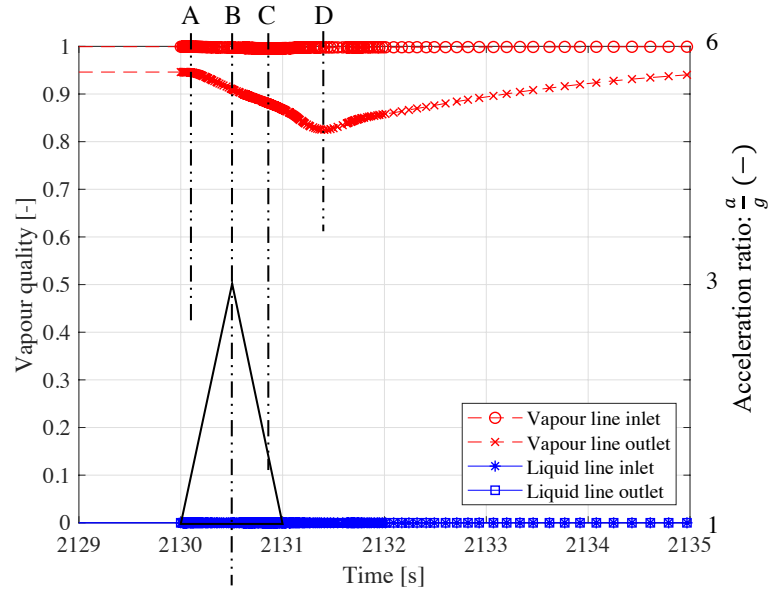


Figure 9.6: Vapour quality variation during acceleration impulse (methanol, $Q_{th} = 1$ kW, $T_{res} = 70^\circ\text{C}$, $T_{sec} = 20^\circ\text{C}$, $3g$, $H = 90$ cm)

Indeed, as vapour is still produced in the wick, it continues to flow in the vapour line. Vapour quality at vapour line inlet is not affected by acceleration stage, but at the outlet, as expected, its value decreases (see Fig. 9.6). This behaviour could be due to

recession of condensation front (see Fig. 9.5) pushed back by liquid. The condensation length reduction could be not only due to liquid thrust, but also to a higher vapour pressure. In fact, after the maximum in acceleration peak, vapour pressure increases due to reversed liquid flow rate, but its temperature slightly increases allowing a higher amount of condensing vapour due to increasing equivalent saturation temperature. The higher pressure makes the vapour to condensate faster, so a new mass of liquid is formed. Once the point D is reached, vapour quality slightly comes back to “normal” values.

Temperatures Fig. 9.7 depicts temperature variations in the evaporator and in the reservoir-evaporator tube as well as in all the previously considered sections and for the same acceleration impulse. As the reader surely notices, the temperature variation as a function of time is no particularly relevant for the evaporator, for the reservoir-evaporator tube and the vapour line inlet, but a small change in temperature shape at inlet and outlet sections of the vapour line is worth of attention. Such small temperature augmentation at vapour line, inlet and outlet (red lines), could be due to the increase in pressure generated by the vapour compression due to liquid back-flow. To a higher vapour pressure corresponds a higher saturation temperature but, due to evaporator thermal inertia, the following augmentation of the evaporator temperature is slower. The saturation temperature temporarily becomes close to the evaporator one and this causes

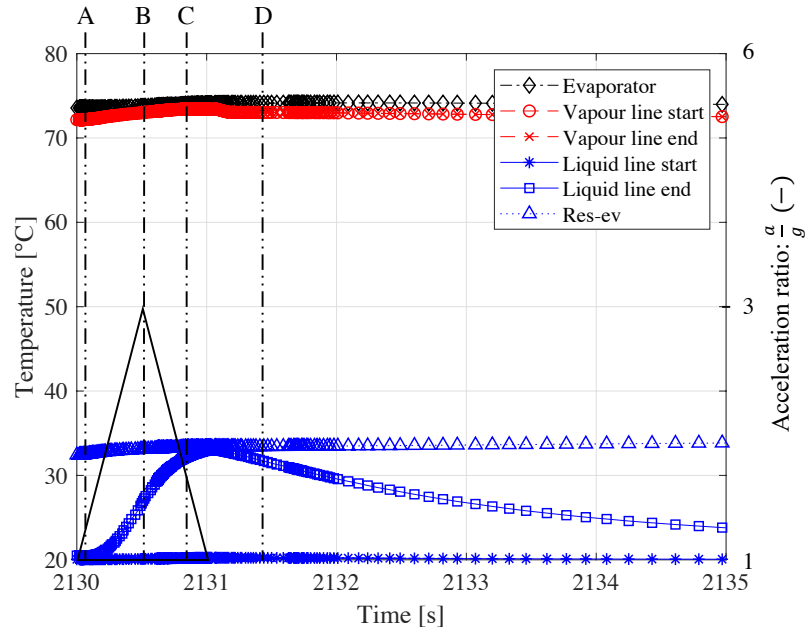


Figure 9.7: Temperature variation during acceleration impulse (methanol, $Q_{th} = 1 \text{ kW}$, $T_{res} = 70^\circ \text{C}$, $T_{sec} = 20^\circ \text{C}$, $3g$, $H = 90 \text{ cm}$)

the vapour mass flow rate diminution observed in Fig. 9.3. Liquid line outlet temperature significantly changes. An amount of liquid flows through the reservoir orifice, from the higher part. A part of hot liquid flows from the reservoir to the evaporator, while another part flows back to the liquid line. The last section of the tube is thus gradually heated. Obviously, due to higher thermal time constants, this phenomenon is slightly slower than the hydraulic one. Once the liquid mass flow rate re-starts to flow from the condenser to the reservoir, subcooled liquid cools down the reservoir inlet section until settling to steady-state equilibrium and its stabilisation to cold source value.

9.4 Parametric study

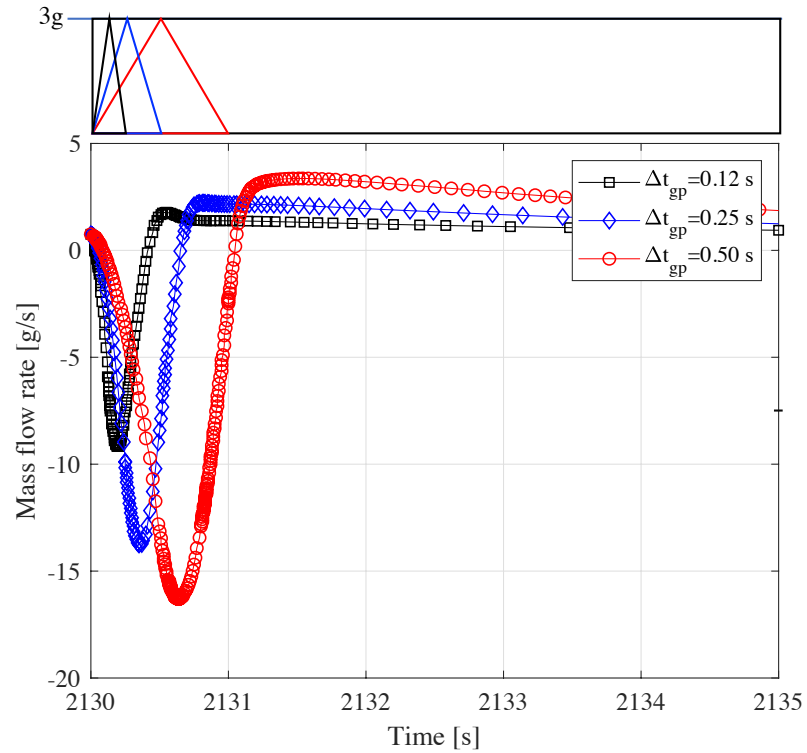
The three parameters, acceleration intensity, k , time duration, Δt_{gp} , and difference of height between condenser and reservoir, H , influence the behaviour of the CPLIP during such transient stage. As explained in chap. 5, in CPLIP, liquid line pressure drop is more impacted by gravity forces than viscous ones. Due to the difference of height between condenser and reservoir, this section of the loop is the mostly influenced by gravity field modification (expressed as $\rho(kg)H$). Likewise the factor k , the response of the loop is impacted by the height between the condenser and the reservoir, H , that is a design parameter⁵. To have an idea on how each parameter affects the loop, three different condenser to reservoir height differences, H , were exploited: 30, 60 and 80 cm; and acceleration values from 2 to 8.5 g were studied at different heights, H . In table 9.2 a synthesis of the performed simulations is reported. For the study, acceleration values up to 8.5g have been considered, stepping by 0.5g. For numerical stability issues⁶, the height H has been gradually reduced for an increasing value of factor k . Finally, to explore the effect of the duration of acceleration perturbation, Δt_{gp} , values of 0.12, 0.25 and 0.5 sec have been explored.

It has been observed that, consequently to acceleration perturbation, the liquid back-flow to the condenser results from the amount of liquid flowing through the orifice from the higher part of the reservoir within the lower part and, finally, to the liquid line. Reservoir inlet becomes an outlet realising the issue described in sec. 5.4.1.2. All the three parameters considered in this chapter influence the amount of liquid flowing back to condenser. First of all, let's analyse the influence of impulse duration, Δt_{gp} .

⁵Obviously, the "tilt" or "inclination", could change the equivalent height between the reservoir and the evaporator, but in this work such parameter is just considered as a design parameter.

⁶Up to date, the reasons of calculation divergence for high acceleration values and high heights are not known. Such divergence could be either due to numerical stability or to physical reasons.

Acceleration $k \cdot g \text{ (m} \cdot \text{s}^{-2})$	Height, H (cm)
2g	30, 60, 80
2.5g	30, 60, 80
3g	30, 60, 80
3.5g	30, 60, 80
4g	30, 60
4.5g	30, 60
5g	30, 60
5.5g	30
6g	30
6.5g	30
7g	30
7.5g	30
8g	30
8.5g	30

Table 9.2: Performed simulations**Figure 9.8:** Acceleration impulsion time duration, Δt_{gp} , effect condenser outlet mass flow rate (methanol, $Q_{th} = 1$ kW, $T_{res} = 70$ °C, $T_{sec} = 20$ °C, $H = 80$ cm, $3g$)

In Fig. 9.8, such parameter variation is reported at constant thermal load, reservoir and cold source temperature, condenser to reservoir height difference, H , and acceleration factor, k . The more the acceleration impulse lasts, the higher the amount of liquid flowing from reservoir to the condenser. Once the acceleration perturbation ends up, the settling time depends on the fluid mass accumulated in a lapse of time: the smaller the amount of fluid flowing back to the condenser (the lower the Δt_{gp}), the shorter the settling time (from the mass flow rate overshoot to the complete stabilisation of the flow). Perturbations lasting more, need a longer time for settling (see 0.12 s — black — to 0.50 s — red — curve difference for example). Thus, the settling time depends on the equivalence between the areas $\Xi = \Gamma$ (see Fig. 9.9), representing the amount of fluid mass accumulated during the perturbation and the mass of fluid that has to return.

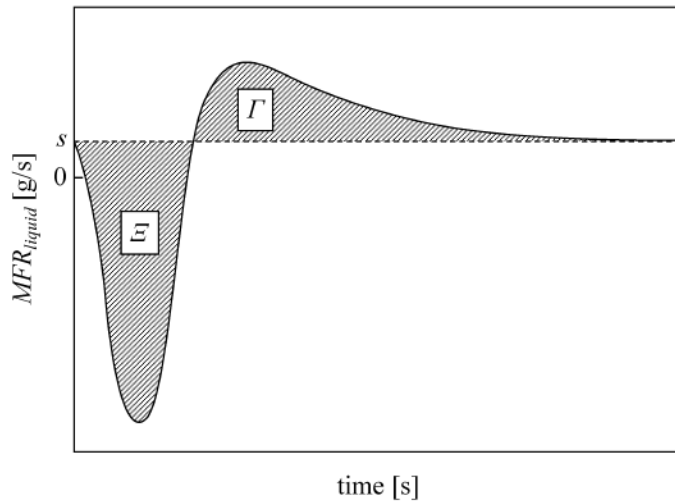


Figure 9.9: Qualitative diagram of accumulated liquid mass during perturbation (area Ξ) and returning mass during settling (area Γ)

The difference of height between condenser and reservoir obviously influences the amplitude of the reversed flow rate during the acceleration impulse (Fig. 9.10). The higher the difference of height between condenser and reservoir, H , the larger the pressure drop and so the amount of mass flow rate flowing back in the liquid line. Actually, the difference of height plays a significant role on acceleration term of pressure drop, $\rho(kg)H$. This impacts back-flowing liquid mass flow rate and condensation length.

Finally, in Fig. 9.11, parametrisation of acceleration intensity factor, k , at constant condenser-to-reservoir height difference and impulse duration, is reported. As expected, according to Fig. 9.11a, the higher the acceleration intensity, the higher the back-flow amplitude and so the settling time necessary for the loop to return to steady state

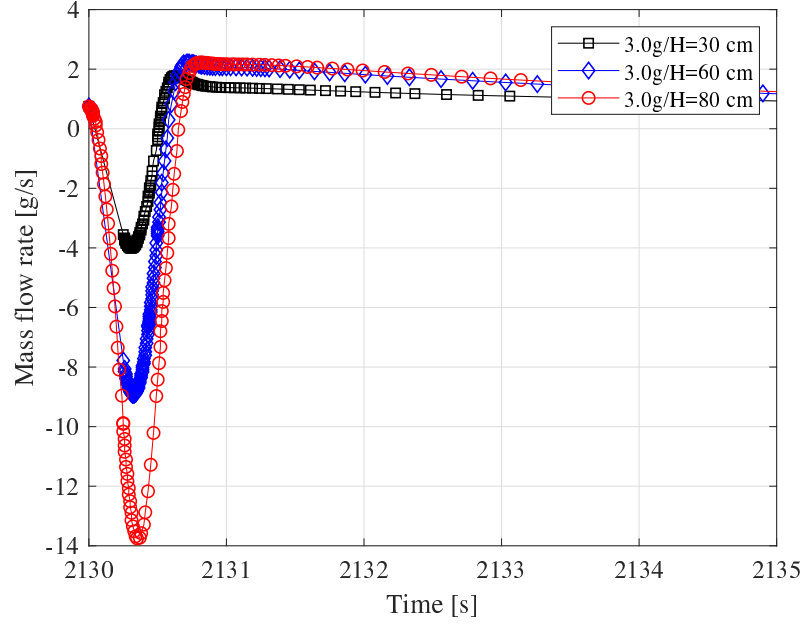


Figure 9.10: Condenser-to-reservoir height difference effect on condenser outlet mass flow rate (methanol, $Q_{th} = 1 \text{ kW}$, $T_{res} = 70^\circ\text{C}$, $T_{sec} = 20^\circ\text{C}$, $\Delta t_{gp} = 0.25 \text{ sec}$, $3g$)

conditions. Also, according to Fig. 9.11b, the higher the acceleration impulse, the higher the condensation length reduction.

Observing pressure variation as a function of acceleration intensity (see Fig. 9.12), pressure shape does not change with acceleration intensity but, obviously, like mass flow rate and condensation length, the higher the acceleration amplitude, the higher the pressure perturbation at the exit of the condenser and the longer the time necessary for settling in steady state conditions. The same pressure shape than Fig. 9.2 may be noticed, but due to a smaller Δt_{gp} and, according to acceleration impulse value, it appears to be more “stretched”.

For the highest value of acceleration impulse, the highest total pressure drop (temporarily introduced by the fast acceleration perturbation) has been compared with the maximum capillary pressure head, resulting in $\Delta P_{8.5g} < \Delta P_{c,max}$ ($\Delta P_{8.5g} = 7500 \text{ Pa}$ for $\Delta P_{c,max} = 10700 \text{ Pa}$). It seems that capillary pumping capacity is not affected by the chosen height, $H = 30 \text{ cm}$, coupled with the maximum acceleration intensity and for a time lasting impulse of 0.25 sec . Moreover no liquid has been attained at the inlet of the condenser during the highest intensity impulse. However, it should be underlined that a transient phenomenon is considered here and more precise studies are needed.

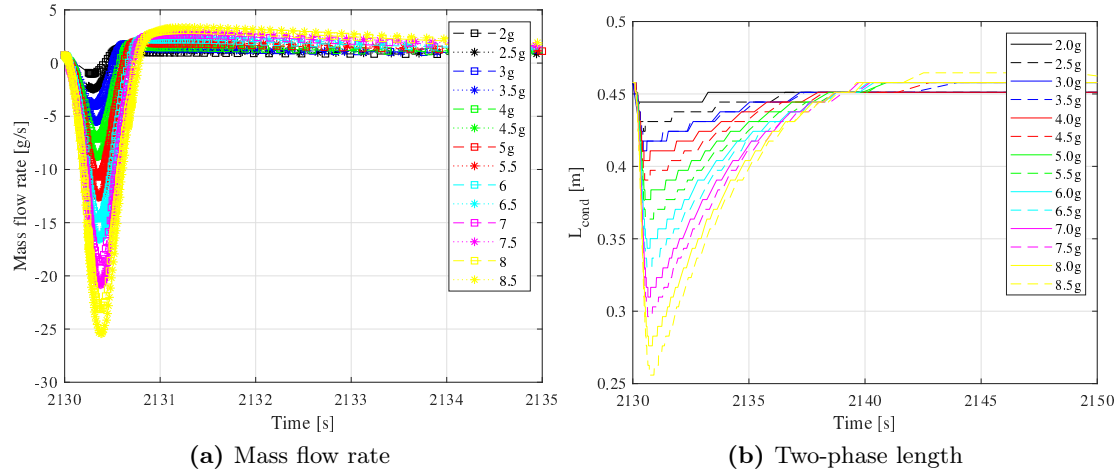


Figure 9.11: Acceleration impulse intensity effect on the reversed mass flow rate and condensation length (methanol, $Q_{th} = 1 \text{ kW}$, $T_{res} = 70^\circ\text{C}$, $T_{sec} = 20^\circ\text{C}$, $\Delta t_{gp} = 0.25 \text{ sec}$, $H = 30 \text{ cm}$)

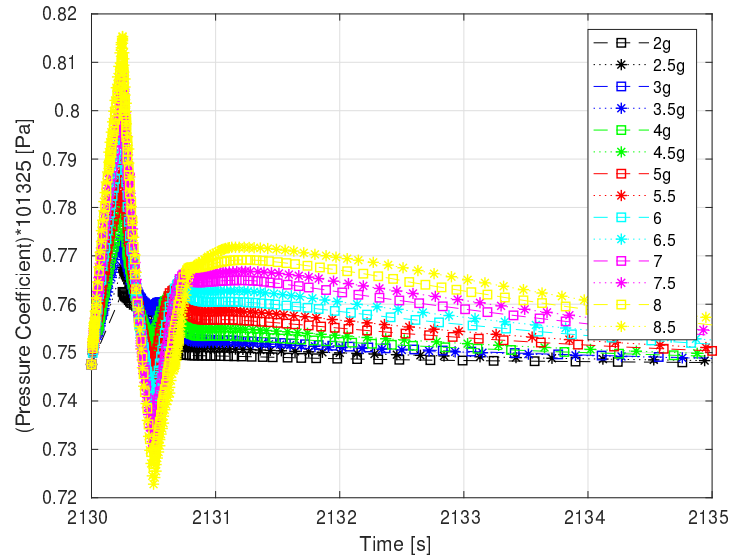


Figure 9.12: Pressure at condenser outlet for different acceleration intensity (methanol, $Q_{th} = 1 \text{ kW}$, $T_{res} = 70^\circ\text{C}$, $T_{sec} = 20^\circ\text{C}$, $\Delta t_{gp} = 0.25 \text{ sec}$, $H = 30 \text{ cm}$)

9.5 Conclusion and perspectives

In this chapter a brief study on transient acceleration stages has been proposed. The purpose was to identify the main components in the CPLIP that are mostly influenced by sudden and violent acceleration stages. Because of the impossibility to experimentally

validate the numerically observed phenomena, this chapter should be seen as introduction and inspiration for future studies.

After an introduction about severe acceleration stages occurring in aeronautics field⁷, to have a better comprehension of phenomena occurring in the loop, a simple case study has been considered. By using an acceleration impulse, hydraulic effects and, to a lesser extent, thermal effects on the loop were studied. Finally, a parametric study has been used to understand the effect of each influencing parameter such as acceleration impulse intensity and time lasting, and difference of height between condenser and reservoir.

From the results obtained, it was observed a strong effect on hydraulics of the loop, but its thermal behaviour seems to be weakly influenced by acceleration impulse. As expected, the first effect of variation of acceleration field has been observed in the liquid line. This component is, in fact, characterised by the higher gravity pressure drop, due to the flow of the highest density fluid. The stronger effect was related to liquid spilling from the reservoir higher part, and within the lower part to the liquid line. The amount of liquid coming from the reservoir participates to condensation length reduction, vapour compression in the vapour line, as well as vapour flow reduction. Vapour seems to be pushed in the vapour line by the capillary forces in the evaporator, but, due to limitations related to evaporator model, actually it is not well known what's going on in the wick. Influencing parameters are, other than acceleration intensity, time duration and condenser to reservoir height difference. An increase of all just expressed parameters negatively influences the loop behaviour. In fact, the higher the acceleration intensity, or its duration or the height difference, the higher the back-flowing mass flow rate. From an engineering stand point the presence of non-return valve at the inlet of the reservoir should be exploited. The latter could help to prevent liquid back-flow effects on the loop during such violent stages.

Further studies are strongly needed on the issue, particularly interesting in the context of HASTECS project. The study presented in this chapter is far to define if the CPLIP is able to resist to turbulence acceleration stages during flight, but it represents a fundamental study to identify the weakest components in the loop. Experimental study is required, as well as a numerical one, using CFD⁸, to analyse the most interesting components to better understand the phenomena that in this chapter we have begun to observe.

⁷The discussion is here only focused on civil aviation. It has to be underlined that Defence and space applications are surely related to higher and different acceleration constraints than those here described.

⁸First CFD calculations has been performed during the last period of this study, but results are not satisfying and are not worthy to be considered in this document.

Part V

Conclusion and Perspectives

This final part of the work is related to general conclusion, perspectives and suggestions for future researches. In particular, in perspectives a newer technology is introduced. The latter is particularly adapted for coupling of power electronics and eMotor coolings.

General conclusion

Issue dealing with heat extraction from high power density electronics components for hybrid propulsion aircraft has been analysed in this work. Despite the high efficiency of such electronics components, the main difficulty is related to the high amount of thermal power losses. The higher the mechanical power required by eMotors, the higher the electrical power to be supplied by power electronics and, even when electric efficiencies are significant, thermal losses are far to be negligible.

Due to the constraints related to low-mass requirements, classical air forced convection cooling systems are not adapted for the purpose! The use of the latter would make the whole system, power electronics and adjoined cooling system, too heavy for its use in a high technological aircraft like the hybrid aircraft might be. Consequently, the use of a cutting-edge technology is necessary to solve the problem.

To find the best cooling system, able to work in critical conditions, like those realised during the mission of an aircraft, a study, focused on different cooling technologies and heat extraction techniques, has been carried out. The high amount of thermal losses to be evacuated and the high required thermal efficiency, made necessary the use of closed loop circuit to transport heat from hot to cold source.

Problem solving can be fundamentally synthesised in three “sub-issues”, each of which is related to a section of the cooling system. In order from the hot to the cold source they are:

1. Research of an adapted technology to extract heat, in the most efficient way (maximising the HTC), and to ensure temperature requirement at level of chips.
2. Research of adapted closed loop circuit: heat transport from hot to cold sources. Such technology should require pretty low amount of energy for its operations and ensure temperature controllability on the hot side whatever the cold source temperature variation. Finally it should be stable, reliable and robust.
3. Research of most performing cold source technology. The latter should be characterised by low thermal resistance between primary side (closed loop circuit side)

and the secondary side (external air circuit). The last condition is necessary to reduce as far as possible heat exchanger dimensions.

Cold plate heatsink is up to now the most used technology in active single and two-phase pumped/vapour-compression technologies. Its working principle is well known, it is ease-to-design and to integrate, but its limitations, related to low heat transfer coefficient and strong dependency of thermal performances on the mass flow rate, do not make of it a suitable technology for HASTECS project. Nowadays different technologies allow to maximise heat exchange rate from chips to coolant to obtain pretty high heat transfer coefficients on the hot side. Jet impingement and spray cooling, microchannels, porous media and metal foams, were compared to have a broad knowledge of current state of the art concerning electronics cooling. Such cooling technologies are successfully used to cool small-dimensions and high performing electronics components. Literature research has demonstrated their effectiveness, but it comes at steep price. The main problems related to the use of these particular cooling techniques is, in fact, related to their pressure drops. Microchannels and metal foams, for example, represent the best solution to be used in active cooling system configuration. They allow high heat transfer coefficients and almost independence of thermal performance on mass flow rate. Otherwise, their related high pressure drops represent a strong limitation. These technologies give their best in active-two-phase configuration, where pressure drop are lower, up to two orders of magnitude compared to single-phase configuration. Actually, sintered porous media are not suitable neither in single nor in two-phase configuration. Pressure drop are higher than those related to microchannels and metal foams. Despite quite high heatsink thermal performances, the required pumping power is extremely high. The higher the pumping power, the higher the pump mass and so the lower the power coefficient, C_c [kW·kg⁻¹] — being the latter the main constraint in aeronautics field —.

Considering the whole cooling system, active and passive closed loop circuits were introduced. The main components of such circuit have been analysed under a thermohydraulic point of view. Pros, drawbacks and potentialities of each solution were introduced. Active single phase cooling systems are not, in general, able to maintain constant temperature level during operation if the secondary side temperature changes as a function of time (how it occurs during the mission of the aircraft), unless a kind of control system is used (regulating valves, variable speed pumps and so on). However, due to high simplicity, well known physical phenomena and design methods, this kind of technology is today widely used. This is the reason why it has been used for comparison purposes. Two-phase active cooling systems are rising technology, and especially vapour compression is quite interesting and begins to be used in aeronautics field. Despite its per-

performances and its ability to maintain the evaporator temperature below the cold source one, this technology is unfortunately at its early stages, and some problems, especially related to compressor hydraulics, and its behaviour during severe acceleration stages, must be solved. Actually, complex regulating systems are required for their operations. The attention was also focused on passive two-phase cooling systems. Working principles of thermosyphons, heat pipes, loop heat pipes and capillary pumped loops (with particular attention to a new kind of gravity CPL) were introduced. Literature results were considered in terms of thermal resistance, transport distance and heat evacuation capability to understand which technology should be the most adapted.

Passive two-phase technologies began to be used for electronics cooling purpose since the thermal heat flux densities became too high. Their performances increase time by time and they are today able to ensure the adequate cooling with relatively high transport distance, as is the case of two-phase passive loops (see LHP/CPL/CPLIP). Loop heat pipes (LHP) and capillary pumped loop (CPL) are worth of attention. Especially, a particular configuration of CPL, the CPLIP (Capillary Pumped Loop for Integrated Power), is able to maintain a constant operating temperature to the evaporator whatever the cold source one and ensuring stability, robustness and reliability.

When talking about aircraft, the choice of the cold source is limited. If heat recovery in the fuel is not considered, only skin heat exchanger and RAM-air are candidates for the cold source. Their coupling with a closed loop cooling system may ensure a better control of cooling rate. Skin heat exchanger is characterised by lower overall performances. It is mainly due to difficulties in use fins to increase the heat exchanger surface area or in general to increase the external side HTC. Higher heat exchanger dimensions characterise this technology if compared with RAM-air one. On the other side, RAM-air is more flexible. It allows the use of a finned, and so more compact, heat exchanger. Moreover, secondary-side duct dimensions can be controlled, during design process, to control and optimise air velocity and maximising the external HTC.

Active single and two-phase cooling systems and passive capillary driven ones, have been compared on the basis of a first approximation design and using the total mass of the cooling system as index, to make the final choice. Actually, neither classic liquid cooling systems nor active two-phase technologies are able to ensure the mass requirement, while not yet optimised CPLIP crosses over the minimal C_c condition.

CPLIP is thus the best solution to be used in the context of this work.

CPLIP main characteristics were described focusing the attention on the physical phenomena governing its operations. An existing experimental facility, used in the context of this work, has been introduced to explain its mechanical, hydraulic and thermal charac-

teristics. An extent description of the measuring sensors equipping the experimental loop has been also done to give an idea of the measurements accuracy presented during the entire description and analysis of this work. — To testify one of the main characteristics of CPLIP: high reliability and robustness, one has to think that, despite the loop is used by students for educational purposes, after several years it keeps its characteristics and potentialities unchanged —.

Numerical model used in this work was also described. Such model, using a “system approach”, has been used to obtain quantitative evaluation of thermal and hydraulic characteristics of the loop and to explain the experimentally observed phenomena. Adaptation of such model to the used experimental facility has been done, modifying evaporator and reservoir thermal conductances G_{ev} , G_{res} ; and vapour, condenser, and liquid line geometries, as well as the reservoir and evaporator ones. Numerical and experimental results have been compared, in transient and steady conditions, to show the agreement [111].

Behaviour of CPLIP in many operating conditions was experimentally studied, and in particular its thermal and hydraulic characteristics were exploited. From widely extended experimental parametric study, thermal characterisation of CPLIP, using methanol and ethanol as working fluids, has been carried out. Because of the inability to directly measure the evaporation temperature in the porous wick, an adapted post-processing tool was used to obtain all missing parameters on simplified thermodynamic cycle. It was observed, that, due to the intrinsic characteristics of two-phase cooling system, where saturation conditions are imposed and controlled, an independence between cold source temperature and evaporator operating temperature exists. Consequently, evaporator thermal conductance values are independent on the secondary side temperature. This behaviour makes this system particularly adapted for the application studied in the context of HASTECS project. Evaporator thermal conductances were experimentally obtained, based either on the reservoir and evaporator temperature. The typical bell shape was got as a function of the heat power. On the base of the experimentally obtained thermal conductances (related to evaporator HTC by the electronics modules base plate surface area) it was possible to numerically study the temperature field on a numerical reproduction of real electronic power module. Based on the finite volume method on StarCCM+, energy equation was solved to obtain temperature distribution in the worst operating condition for power electronics modules and for the less performing electronics configuration (the one characterised by the lowest efficiency). Despite the very high heat flux density evacuated by electronic chips, CPLIP, characterised by quite high evaporator HTC, is able to maintain the temperature value lower than the one allowed by

power-electronics-module constructor! Thanks to spreading behaviour of power-module-layers, one assists to a flattening of temperature field in correspondence of the base plate (interface between the evaporator and the power module) reducing the effect of hot-spots in correspondence of evaporator walls. CPLIP behaviour was experimentally explored during an entire mission profile cycle¹. This technology is able to evacuate the supplied thermal load, and temperatures on the evaporator walls remain controlled even during the most critical phases (transition between the taxi-out and take-off stage for example). The experimentally obtained temperatures were compared with those resulting from WP2's mono-dimensional electrical analogy model, based on the thermal characterisation presented in this work. Such test allowed to verify the good agreement between calculated temperatures and experimentally obtained ones. Results are quite satisfying, even if slight overestimation of junction temperature was found in the model. This, however, allows to be more conservative during the design process of electrical components and their adjoined cooling system.

Some differences could exist between laboratory tested behaviour and real operating conditions. They could be mainly due to a difference in transport lines length and/or a different nature of the condenser. Moreover, in this experimental study, the evaporator was uniformly, and quasi ideally heated by electrical resistances, so, some differences could be due to the use of real switching power modules. In fact, they are surely characterised by pretty different values of thermal inertia than copper, actually used for the thermal diffusers.

To know the influence of the vapour line pressure drops, to relate them to the transport distance, a parametric study was conducted, acting on the hydraulic characteristics of the CPLIP. It was found that the increasing pressure drops in the vapour line have a similar effect than changing the thermal load to the evaporator. Methanol and ethanol have the same qualitative behaviour, but, due to their different thermophysical properties, they bring to quantitatively different results. Ethanol, in particular, is more sensitive to heat power step-up or vapour line pressure drops.

CPLIP was designed and optimised following the HASTECS' requirements for 2025 and 2035. After a discussion about the complex optimisation process linked to the condenser, and about the most suitable fin configurations to be used, optimised CPLIP results for 2025 have been presented for the four electronics configurations proposed by WP2. Each of them is characterised by a different efficiency. Considering either electronics components and the adjoined cooling system, the configuration allowing the highest

¹One third of the maximal thermal load has been here used (5.4 kW, also corresponding to the thermal load of one electrical phase).

mass saving was the NPC-DPWMMAX. In this case, the obtained power coefficient was higher than requirement for 2025 ($> 19 \text{ kW} \cdot \text{kg}^{-1}$, target 2025: $15 \text{ kW} \cdot \text{kg}^{-1}$). With purpose to further reduce the mass of the cooling system, a louvered fins-microchannels condenser was selected for the solution 2035. The latter allows a reduction of the solid mass thanks to enhancement of external side HTC, over three times, and a reduction of the fluid amount in the loop thanks to the use of microchannels. The cooling solution proposed for 2035 is “impressive”! Despite the same electronic configuration than 2025 (NPC-DPWMMAX), the overall CPLIP mass has been sensibly reduced. Cooling system mass related to 2035 solution is one order of magnitude lower than 2025 solution! Overall power coefficient boosting comes, in fact, from either electronic and cooling system mass reduction. It is more than twice the 2035 requirement: over $50 \text{ kW} \cdot \text{kg}^{-1}$, for a target of $25 \text{ kW} \cdot \text{kg}^{-1}$. It has to be underlined that no accessories and fixation system have been considered in calculation at this stage, but the results are encouraging and allow room for manoeuvre.

CPLIP well responds to power electronics cooling requirements either for the targets of 2025 and 2035!

Finally, CPLIP was experimentally and numerically analysed when critical harsh transient conditions occur. The attention was focused on high heat power step start-ups and harsh acceleration stages. Experimental tests using methanol as working fluid were performed changing vapour line initial temperature to evaluate its influence on the vapour front behaviour during start-ups. Numerical simulations were compared to experimental results during cold start-ups to testify the correctness of interpretation of experimental data. To understand the differences between “relaxed” and extremely severe start-up conditions, CPLIP was pushed up to reach its operating limits during some specific start-ups stages. The comparison between a severe (5 kW) and a more relaxed (0.5 kW or 2 kW) cold start-ups showed that vapour front velocity values in the vapour line are similar for the relaxed cases, while in the case of a severe start-up its velocity is one-order-of-magnitude higher. To understand and justify such results for hot and cold cases, an energy based analysis, considering the importance of heat accumulated, due thermal inertia of vapour line tubes, was performed. It was observed that the variation of vapour front velocity is due to recondensation of the vapour on the internal side of vapour line wall. This phenomenon is more significant during cold start-ups due to a higher difference between fluid and tube-initial temperatures. So, as the initial-vapour line-temperature is low, the vapour front velocity decreases, resulting in higher settling times and quicker vapour quality increases. The vapour line initial temperature determines the quantity of energy dissipated by the fluid to the tube walls. Such amount of energy exchanged,

directly related to the recondensation phenomenon on the tube walls, has an impact on pressure and mass distributions of vapour phase and, so, on the vapour front velocity and shape. Further studies need to be performed, particularly in terms of experimental visualisations and numerical volume of fluid (VOF) simulations (of the vapour flow in the vapour line during such transient start-ups) in order to completely validate the assessments given in this work.

It has to be underlined that in the context of HASTECS project, the most critical phases are realised, on the basis of the actually held data, on the ground where the CPLIP is required to boot at temperatures lower than 40 °C and with an applied thermal load of about 2.4 kW (0.8 kW/ePhase). On the basis of results obtained, no particular problems are related to loop start-up in such conditions.

Finally, like all equipments which is required to fly, CPLIP behaviour has been studied during sudden and violent acceleration stage, with the purpose to identify the weakest and the most impacted components in the loop. The study performed in this work should be seen as a beginning for a wider and more complex research on the subject. The study has been fundamentally divided in two parts: a simple case study has been considered to understand the phenomena occurring and to identify how CPLIP is hydraulically and thermally impacted; and a parametric study to understand the effect of each influencing parameter such as acceleration intensity and time lasting, and difference of height between condenser and reservoir.

From results obtained, it was observed a strong effect on hydraulics of the loop, while its thermal behaviour seems to be weakly influenced by acceleration impulse. As expected, the first effect of variation of acceleration field has been observed in the liquid line. This component is, in fact, characterised by the higher gravity pressure drop, due to the flow of the highest density fluid. The stronger effect was related to liquid spilling from the reservoir higher part, and within the lower part to the liquid line. The amount of liquid coming from the reservoir participates to condensation length reduction, vapour compression in the vapour line, and somehow to the vapour mass flow rate reduction into the vapour line. Influencing parameters are, other than acceleration intensity, time duration and condenser to reservoir height difference. An increase of all just expressed parameters negatively influences the loop behaviour. In fact, the higher the acceleration intensity, or its duration or the height difference, the higher the back-flowing mass flow rate. More studies are strongly suggested on the subject, both from experimental and numerical points of view, to continue the assessments of this work.

CPLIP seems to be the best choice for power electronics cooling in the context of HASTECS project, but other studies are required. It could be interesting to experiment-

ally study the behaviour of the CPLIP, in the configuration 2035, to compare the results introduced in this work with experimental ones.

Perspectives

11.1 General perspectives

Capillary Pumped Loop for Integrated Power, CPLIP, is a valuable solution for power electronics cooling in the context of HASTECS project. As observed all along the study, this solution is able to evacuate high power density thermal load from power electronics modules by ensuring temperature requirements and respecting the power to mass ratio constraints, C_c . Actually, this kind of capillary driven loop crosses-over the imposed power coefficient values either for targets 2025 and 2035!

Outstanding questions remain at the end of this study, and they should be retained as input for future researches and development.

The evaporator is the CPLIP's key component. In this study a nickel porous wick has been used, because of its high performances, in terms of HTC, measured on the existing experimental facility. However, it should be interesting to exploit the use of different materials for porous mesh for issues related to the mass of the loop. The use a less dense material could help to further reduce CPLIP overall mass and consequently increase the power coefficient value, C_c . Especially for 2035 solution, that is mostly influenced by evaporator mass.

All experimental tests were performed using heating resistances to simulate the presence of power modules. However, new tests involving the presence of real power electronics converters could be done in order to compare the thermal inertia of actual copper diffusers with real converters one. Moreover, as laboratory conditions are quite different than real operating ones, CPLIP behaviour equipped by an air-liquid condenser should be considered for tests, instead of the coaxial liquid-to-liquid condenser used in the tests. Especially, 2035's condenser configuration should be explored. In this last case, in fact, either external (louver side) and internal side (condensation in microchannels) should be exploited to observe the difference between estimated thermo-hydraulic behaviour and real one. In this case, in fact, the used technology ensures the highest possible internal and external HTC, but pressure drops should be measured to obtain a more precise evaluation.

A joint adventure with a hypothetical aerodynamics team could lead to a better integration of the cooling system into the aircraft, a more accurate knowledge of limitations, related to condenser external side configuration and its impact on lift to drag ratio. Such cooperation could lead to more “appropriate results”. — For a such high technological aircraft, like the hybrid one, it will be necessary to build the aircraft around the subsystem (power electronics cooling in this case), and of course to adapt the latter to be integrated at the best! —

Finally, with the purpose to propose a solution able to merge power electronics and eMotor cooling, a new promising technology should be exploited: Capillary Jet Loop (CJL).

11.2 A newer technology: Capillary Jet Loop (CJL)

Basic principle of CJL is similar to a CPL (Capillary Pumped Loop) in which reservoir has been replaced by a “flow ring”, obviously without, cartridge heater to impose saturation conditions. CJL can be divided in two subsystems, also called rings [18]: two-phase ring, capillary driven, and single phase ring, injector driven. At the end of the vapour line the injector is used to transfer momentum from hot vapour, flowing in the vapour line, to the liquid in the liquid ring. From the liquid ring, where different heat sources may be installed, heat is definitively evacuated through the subcooler. In Fig. 11.1 a schematic of CJL is introduced.

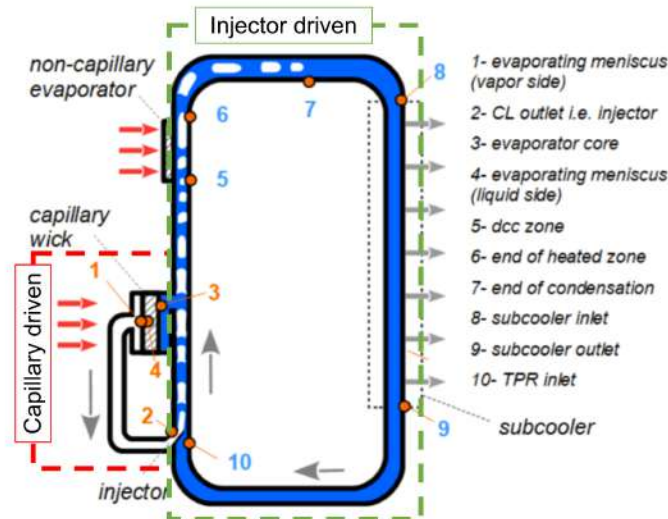


Figure 11.1: Capillary Jet Loop concept [18]

Referring to Fig. 11.1, thermal load is applied to the capillary wicked evaporator

(point 1). There, capillary forces take place allowing vapour flow within the vapour line to the injector (point 2). In the latter, which physical phenomena are quite delicate and complex, vapour kinetic energy is used to transfer momentum to liquid in the external ring (from point 2 to 10). “*Steam injector (SI) is a passive jet pump without moving parts or machineries [...]*” [cit.] [19]. In other words, injector is able to generate an additional pressure head allowing the liquid flow. Injector is in general composed by coaxial liquid and vapour inlet nozzles, mixing section and diffuser (see Fig. 11.2). Following the fluid phase flowing in the inner nozzle as well as the external nozzle inlet

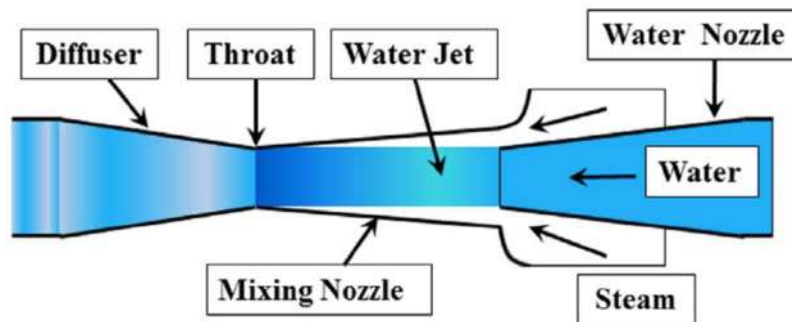


Figure 11.2: Injector principle scheme [19]

direction (coaxial or perpendicular to nozzle axis) different shapes may be used for the inner part. The mixing nozzle, usually converging, allows direct contact condensation of vapour, coming from evaporator, in the liquid phase. In centred liquid jet injectors, interesting for their application in CJL, the vapour nozzle is external and annular. Here, superheated vapour adiabatically expands reaching sonic conditions at the exit of the nozzle: its enthalpy is converted in kinetic energy [126, 19]. At the same time subcooled liquid velocity increases from the inlet to the outlet of liquid nozzle. A high velocity liquid jet is so created. In the mixing nozzle direct contact condensation of vapour occurs due to contact with the high velocity liquid jet. Mass, energy and momentum exchanges occur in correspondence of the interface between the two fluid phases, due to condensation and to quite high temperature and velocity differences between vapour and liquid phases. Complete condensation of vapour should occur in this section of injector. If not, the injector is not working in the appropriate condition [127]. The region where the complete condensation takes place is called *condensation shock* [19]. The latter is violent and, on the contrary of gas-dynamics' shock waves its thickness is significative and comparable with channel diameter [126]. The final section of the injector is the diffuser, allowing to increase fluid pressure from the throat to the exit section — injectors are used in a quite large range of applications. Actually they are particularly interesting to

passively pump coolant in nuclear reactors in emergency cases, for example —. Finally, in the diffuser (divergent section), condensed sub-cooled liquid at the exit of the mixing nozzle decelerates and its pressure further increases from the inlet to the outlet¹. At point 3, a part of liquid wets the porous wick allowing evaporation and capillary pumping to let the vapour cycle to re-start, while another part of the liquid flows to the secondary heat source. In the latter, sensible heat is exchanged increasing the fluid temperature between points 5 and 6. From point 7, liquid flows to the heat exchanger: subcooler. Here, only sensible heat is exchanged with external environment and definitively evacuating the thermal load. From point 9, subcooled liquid flows to point 10, corresponding to the injector inlet. Here, pressure head takes place to let the cycle start again.

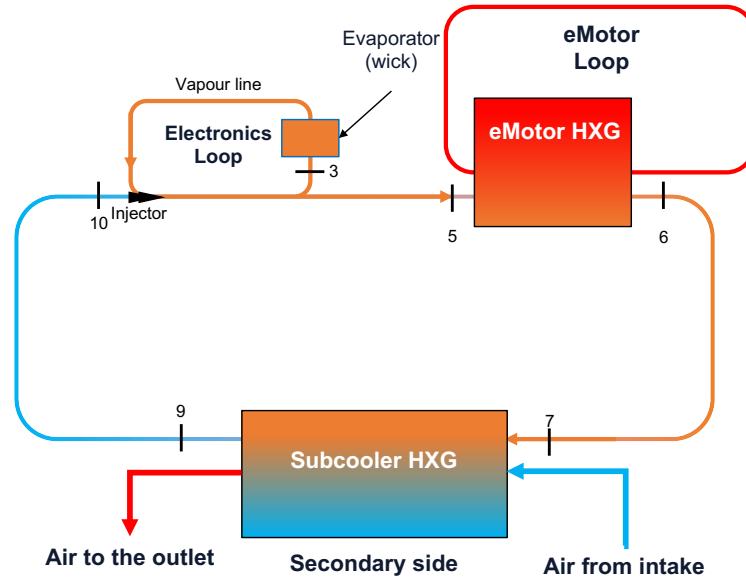


Figure 11.3: Scheme of principle of CJL adapted for HASTEC requirements

¹For the interested reader, references [126, 19, 127] are strongly suggested.

As the reader has surely noticed, this loop does not require any form of external source of energy for its operations: no cartridge heater is used to impose saturation conditions that are so dependent on the subcooler outlet temperature. It follows that any variation of the cold source temperature would impact the internal fluid temperature. The design of this technology is quite complex and should consider some phenomena that up to date still represent an open issue. The injector should be designed and chosen with pretty high attention to maximise its efficiency and to exploit all the potential of this component [126].

A possible scheme of principle of this technology applied to HASTEC project is reported in Fig. 11.3. This technology is worth of attention. Efforts have to be made to design it and to let it work for power electronics and eMotor cooling in the context of Hybrid aircraft. Power coefficients shall be re-thought according to coupling of power electronics modules, eMotor and their adjoined cooling systems. If on one hand louvered fins-microchannels HXG may represent a valuable solution for the subcooler, some efforts have to be done to research the best heat exchanger solution to be used on eMotor side according to performance and mass requirements of aeronautics fields.

Bibliography

- [1] F. Accorinti, N. Erroui, V. Ayel, G. Gateau, Y. Bertin, N. Roux, S. Dutour, M. Miscevic, High-efficiency cooling system for highly integrated power electronics for hybrid propulsion aircraft, in: 28th IEEE International Symposium on Industrial Electronics (ISIE), 2019, pp. 870–877. [doi:10.1109/ISIE.2019.8781086](https://doi.org/10.1109/ISIE.2019.8781086).
- [2] J.-F. Allias, Specification dossier for HASTECS (AIRBUS) (January 2018).
- [3] H. R. W. (McDonnell Douglas Corporation Long Beach Calif.), Skin Heat Exchanger, United States Patent 4819720.
- [4] L.P. Pang, X. Dang, J. Cheng, Study on heat transfer performance of skin heat exchanger, *Experimental Heat Transfer* (28) (2015) 317–327.
- [5] W. Chen, D. W. Fogg, M. Izenzon, C. Kurwitz, A highly stable two-phase thermal management system for aircraft, Tech. rep., SAE Technical Paper (2012).
- [6] D. Ray, P. Kew, *Heat Pipes - Theory, Design and Applications*, fifth edition Edition, BH, 2006.
- [7] V. Ayel, L. Lachassagne, Y. Bertin, C. Romestant, Experimental study on the effect of the vapour pressure losses on a capillary pumped loop for terrestrial application, in: 16th International Heat Pipe Conference, Lyon, France, 2012.
- [8] J. Kim, Spray cooling heat transfer: the state of art, *International Journal of Heat and Fluid Flow* 28 (2007) 753–767.
- [9] A. Sakanova, C. F. Fong Tong, A. Nawawi, R. Simanjorang, K. Tseng, A. K. Gupta, Investigation on weight consideration of liquid coolant system for power electronics converter in future aircraft, *Applied Thermal Engineering* (104) (2016) 603–615.
- [10] K. Boomsma, D. Poulikakos, F. Zwick, [Metal foams as compact high performance heat exchangers](https://doi.org/10.1016/j.mechmat.2003.02.001), *Mechanics of Materials* 35 (12) (2003) 1161 – 1176. [doi:https://doi.org/10.1016/j.mechmat.2003.02.001](https://doi.org/10.1016/j.mechmat.2003.02.001).
URL <http://www.sciencedirect.com/science/article/pii/S0167663603001029>

- [11] Y. Bertin, F. Accorinti, F. Pagnoni, Systèmes diphasiques pour le contrôle thermique de l'électronique de puissance, in: Journée Thématique, SFT (Société Française de Thermique), Toulouse - March 29, 2018.
- [12] F. Accorinti, V. Ayel, Y. Bertin, [Steady-state analysis of a capillary pumped loop for terrestrial application with methanol and ethanol as working fluids](#), International Journal of Thermal Sciences 137 (2019) 571 – 583. doi:<https://doi.org/10.1016/j.ijthermalsci.2018.10.036>. URL <http://www.sciencedirect.com/science/article/pii/S1290072918300681>
- [13] P. J. Marto, Handbook of Heat Transfer (Third Edition), McGraw-Hill, 1998, Ch. 14, pp. 1–54.
- [14] V. Ayel, L. Lachassagne, Y. Bertin, C. Romestant, D. Lossouarn, Experimental analysis of a capillary pumped loop for terrestrial application, Journal of thermophysics and heat transfer 25 (4) (2011) 561–571.
- [15] D. Lossouarn, Etude théorique et expérimentale du refroidissement diphasique à pompage capillaire des convertisseurs de puissance à haute densité de flux de chaleur pour la traction ferroviaire, Ph.D. thesis, ISAE-ENSMA (2008).
- [16] N. Blet, V. Ayel, Y. Bertin, C. Romestant, V. Platel, Transient modeling of cpl for terrestrial applications. part a: Network concept & influence of gravity on the cpl behavior, Vol. India, Kampur, 2013, pp. 263–270.
- [17] R. K. Shah, D. P. Sekulic, Handbook of Heat Transfer (Third Edition), McGraw-Hill, 1998, Ch. 17, pp. 1–65.
- [18] V. Dupont, B. Paran, S. Van Oost, C. Billet, Capillary jet loop, in: Joint 19th IHPC and 13th IHPS, Pisa, Italy, June 10-14, 2018.
- [19] S. Miwa, H. Endo, T. Moribe, H. Sakashita, M. Mori, T. Hibiki, [Investigation of the thermal-hydraulic characteristics of supersonic steam injector](#), Applied Thermal Engineering 109 (2016) 261 – 271. doi:<https://doi.org/10.1016/j.applthermaleng.2016.08.069>. URL <http://www.sciencedirect.com/science/article/pii/S1359431116314235>
- [20] B. Agostini, M. Fabbri, J. E. Park, L. Wojtan, J. Thome, B. Michel, State of art of high heat flux cooling technologies, Heat Transfer Engineering 28 (4) (2007) 258–281.

- [21] N. Erroui, High power conversion chain for hybrid aircraft propulsion, Ph.D. thesis, Laboratoire plasma et conversion d'énergie (ENSEEIHT) (2019).
- [22] Nasa, [Earth atmosphere model](https://www.grc.nasa.gov/WWW/k-12/airplane/atmosmet.html) (2019).
URL <https://www.grc.nasa.gov/WWW/k-12/airplane/atmosmet.html>
- [23] E. G. Colgan, F. Bruce, M. Gaynes, W. S. Graham, N. C. LaBianca, J. H. Magerlein, R. J. Polastre, M. B. Rothwell, R. J. Bezama, R. Choudhary, K. C. Marston, H. Toy, J. Wakil, J. A. Zitz, R. R. Schmidt, A Practical Implementation of Silicon Microchannel Coolers for High Power Chips, *IEEE Transactions on Components and Packaging Technologies* 30 (2).
- [24] P.-X. Jiang, M.-H. Fan, G.-S. Si, Z.-P. Ren, Thermal-hydraulic performance of small scale micro-channel and porous-media heat-exchanger, *International Journal of Heat and mass Transfer* (44) (2001) 1039–1051.
- [25] N. Blet, Analyse expérimentale et par voie de modelisation d'une boucle gravitaire à pompage capillaire multi-évaporateurs, Ph.D. thesis, ISAE-ENSMA (2014).
- [26] N. Delalandre, Analyse par voie de modélisation du comportement thermohydraulique instationnaire des boucles diphasiques à pompage capillaire en environnement gravitaire: application au refroidissement de composants électroniques de puissance soumis à des sollecitations sévères, Ph.D. thesis, ISAE-ENSMA (2011).
- [27] [Power trip: Hastecs energizes the path to hybrid-powered flight](#) [online].
- [28] R. W. Newman, M. Dooley, C. Lui, Efficient propulsion, power, and thermal management integration, in: 49th AIAA/ASME/SAE/ASEE Joint Propulsion Conference, 2013, p. 3681.
- [29] M. Dooley, N. Lui, R. Newman, C. Lui, Aircraft thermal management-heat sink challenge, Tech. rep., SAE Technical Paper (2014).
- [30] R. H. Zimmerman, W. Robinson, Equipment cooling systems for aircraft, part 1, Tech. Rep. 54-359, The Ohio State University Research Foundation (September 1954).
- [31] A. Hashemi, E. Dyson, Performance Characterization of High-Power Electronic Equipment onboard an aircraft, *Heat Transfer Engineering* 21 (2000) 15–24.
- [32] J. F. Andrew, H. L. Quinn, L. Y. Kirk, J. E. Levi, Aircraft thermal management using loop heat pipes: Experimental simulation of high acceleration environments

- using the centrifuge table test bed, Air Force Research Laboratory and SAE International.
- [33] A. Hashemi, E. Dyson, J. Nigen, Aircraft skin-cooling system for thermal management of onboard high-power electronics, *Journal of thermophysics and heat transfer* 13 (14) (1999) 529–536.
 - [34] M. R. Moroney, Ram-air cooling systems for aircraft generators, *Transactions of the American Institute of Electrical Engineers, Part II: Applications and Industry* 76 (4) (1957) 217–221. doi:[10.1109/TAI.1957.6367231](https://doi.org/10.1109/TAI.1957.6367231).
 - [35] [\[link\]](#).
URL https://upload.wikimedia.org/wikipedia/commons/1/1f/Air_intakes_of_RAM_air_for_environmental_control_systems_of_Boeing_747-8I.jpg
 - [36] Design of a ram air driven air cycle cooling system for fighter aircraft pods, AIAA, Thermophysics Conference, American Institute of Aeronautics and Astronautics, Inc., June 17-20, 1996.
 - [37] R. M. Grabow, T. W. Kreter, G. E. Limberg, [A ram air driven air cycle cooling system for avionics pods](#), in: SAE Technical Paper, SAE International, 1986. doi:[10.4271/860912](https://doi.org/10.4271/860912).
URL <https://doi.org/10.4271/860912>
 - [38] Caleffi, [Vasi di espansione](#) (2019).
URL https://www.caleffi.com/sites/default/files/file/01079_it.pdf
 - [39] J. Thome, A. Bruch, Refrigerated cooling of microprocessors with micro-evaporation heat sinks: new development and energy conservation prospects for green datacenters, *Proceedings Institute of refrigeration (IOR)*.
 - [40] J. Homitz, R. Scaringe, G. Cole, Evaluation of a vapor-compression thermal management system for reliability while operating under thermal transients, Tech. rep., SAE Technical Paper (2010).
 - [41] ACT, [Pumped two phase resources](#) (2019) [cited 2019].
URL <https://www.1-act.com/resources/pumped-two-phase-cooling/>
 - [42] J. B. Marcinichen, J. R. Thome, B. Michel, [Cooling of microprocessors with micro-evaporation: A novel two-phase cooling cycle](#), *International Journal of Refrigeration* 33 (7) (2010) 1264 – 1276. doi:<https://doi.org/10.1016/j.ijrefrig>.

2010.06.008.

URL <http://www.sciencedirect.com/science/article/pii/S0140700710001271>

- [43] J. Homitz, R. P. Scaringe, G. S. Cole, A. Fleming, T. Michalak, Comparative analysis of thermal management architectures to address evolving thermal requirements of aircraft systems, Tech. rep., SAE Technical Paper (2008).
- [44] J. R. Barbosa, G. B. Ribeiro, P. A. Oliveira, A state-of-art review of compact vapor compression refrigeration systems and their applications, *Heat Transfer Engineering* 33 (4-5) (2012) 356–374.
- [45] S. Mancin, C. Zilio, G. Righetti, L. Rossetto, Mini vapor cycle system for high density electronic applications, *International Journal of Refrigeration* (36) (2013) 1191–1202.
- [46] S. Trutassanawin, E. A. Groll, S. V. Garimella, L. Cremaschi, Experimental investigation of a miniature-scale refrigeration system for electronics cooling, *IEEE Transactions on Components and Packaging Technologies* 29 (3) (2006) 678–687. [doi:10.1109/TCAPT.2006.881762](https://doi.org/10.1109/TCAPT.2006.881762).
- [47] Mikhal Nikitkin, B. Cullimore, CPL and LHP Technologies: What are the Differences, What are the Similarities, Society of Automotive Engineers.
- [48] V. Dupont, S. V. O. Oost, L. Barremaecker, S. Nicolau, Railwais qualification tests of capillary pumped loop on a train, in: 17th International Heat Pipe Conference, 2013, pp. 311–318.
- [49] L. Lachassagne, Y. Bertin, V. Ayel, C. Romestant, Steady-state modeling of Capillary Pumped Loop in gravity field, *International Journal of Thermal Sciences* 64 (2013) 62–80.
- [50] L. Vasiliev, D. Lossouarn, C. Romestant, A. Alexandre, Y. Bertin, Y. Piatsiushyk, V. Romanenkov, Loop heat pipes for cooling of high-power electronic components, *International Journal of Heat Transfer* 52 (2009) 301–308.
- [51] N. Blet, S. Lips, V. Sartre, Heat pipes for temperature homogenization: a literature review, *Applied Thermal Engineering* 118 (2017) 490–509.
- [52] M. Reyes, D. Alonso, J. R. Arias, A. Velazquez, Experimental and theoretical study of a vapour chamber based heat spreader for avionics applications, *Applied Thermal Engineering* (37) (2012) 51–59.

- [53] K.-S. Ong, C. Lim, Performance of water filled thermosyphons between 30-150oc, *Frontiers in Heat Pipes (FHP)* 6 (1).
- [54] D. Jafari, A. Franco, S. Filippeschi, P. Di Marco, Two-phase closed thermosyphons: a review of studies and solar applications, *Renewable and Sustainable Energy Reviews* 53 (2016) 575–593.
- [55] H. Abou-Ziyan, A. Helali, M. Fatouh, M. A. El-Nasr, Performance of stationary and vibrated thermosyphon working with water and R134a, *Applied Thermal Engineering* (21) (2001) 813–830.
- [56] S. Filippeschi, A. Franco, Experimental analysis of the instabilities effect on the thermal performance of a closed loop two-phase thermosyphon, *Heat Pipe Science and Technology, An International Journal* 5 (1-4).
- [57] [\[link\]](#).
URL <https://samsungrumors.net/samsung-galaxy-s8-will-heatpipe-like-s7/>
- [58] [\[link\]](#).
URL <https://www.apple.com/fr/mac-pro/>
- [59] Sergii Khairnasov, A. Naumova, Heat pipes application in electronics thermal control systems, *Frontiers in Heat Pipes (FHP)* 6 (6).
- [60] J.-S. Chen, J.-H. Chou, The length and bending angle effect on the cooling performance of flate plate heat pipes, *International Communications in Heat and Mass Transfer* 90 (2015) 848–856.
- [61] X. Chen, H. Ye, X. Fan, T. Ren, G. Zhang, A review of small heat pipes for electronics, *Applied Thermal Engineering* 96 (2016) 1–17.
- [62] Stéphane Launay, V. Sartre, J. Bonjour, Parametric analysis of loop heat pipe operation: a literature review, *International Journal of Thermal Sciences* (46) (2007) 621–636.
- [63] J. Gu, M. Kawaji, R. Futamata, Effects of gravity on the performance of pulsating heat pipes, *Journal of Thermophysics and Heat Transfer* 18 (3) (2004) 370–378.
- [64] V. Ayel, Y. Bertin, C. Romestant, G. Burban, Experimental study of pulsating heat pipes tested in horizontal and vertical positions, in: *Proc. 15th International Heat Pipe Conference (Clemson, South Carolina, USA, 25-29 April 2010)*, Vol. 8, 2010, p. 26.

- [65] G. Burban, V. Ayel, A. Alexandre, P. Lagonotte, Y. Bertin, C. Romestant, [Experimental investigation of a pulsating heat pipe for hybrid vehicle applications](#), *Applied Thermal Engineering* 50 (1) (2013) 94 – 103. doi:<https://doi.org/10.1016/j.applthermaleng.2012.05.037>.
URL <http://www.sciencedirect.com/science/article/pii/S1359431112004152>
- [66] V. Ayel, C. Romestant, Y. Bertin, V. Manno, S. Filippeschi, Visualisation of flow patterns in flat plate pulsating heat pipe: influence of hydraulic behaviour on thermal performances, *Heat pipe science and technology, An International Journal* 5 (2016) 377–384.
- [67] H. Han, X. Cui, Y. Zhu, S. Sun, A comparative study of the behavior of working fluids and their properties on the performance of pulsating heat pipes (php), *International Journal of Thermal Sciences* 82 (2014) 138–147.
- [68] V. Ayel, L. Araneo, A. Scalambra, M. Mameli, C. Romestant, A. Piteau, M. Marengo, S. Filippeschi, Y. Bertin, [Experimental study of a closed loop flat plate pulsating heat pipe under a varying gravity force](#), *International Journal of Thermal Sciences* 96 (2015) 23 – 34. doi:<https://doi.org/10.1016/j.ijthermalsci.2015.04.010>.
URL <http://www.sciencedirect.com/science/article/pii/S1290072915001349>
- [69] D. Mangini, M. Mameli, D. Fioriti, S. Filippeschi, L. Araneo, M. Marengo, Hybrid pulsating heat pipe for space applications with non-uniform heating patterns: ground and microgravity experiments, *Applied Thermal Engineering* 126 (2017) 1029–1043.
- [70] S. Lips, A. Bensalem, Y. Bertin, V. Ayel, C. Romestant, J. Bonjour, [Experimental evidences of distinct heat transfer regimes in pulsating heat pipes \(php\)](#), *Applied Thermal Engineering* 30 (8) (2010) 900 – 907. doi:<https://doi.org/10.1016/j.applthermaleng.2009.12.020>.
URL <http://www.sciencedirect.com/science/article/pii/S1359431110000037>
- [71] N. Blet, Y. Bertin, V. Ayel, C. Romestant, V. Platel, Experimental analysis of a capillary pumped loop for terrestrial applications with several evaporators in parallel, *Applied Thermal Engineering* 93 (2016) 1304–1312.
- [72] Y. Maydanik, Loop Heat Pipes, *Applied Thermal Engineering* (25) (2005) 635–657.

- [73] D. Bugby, T. Miller, J. Baker, Multi-Evaporator Two-Phase Loop Cooling System, in: 4th International Energy Conversion Engineering Conference and Exhibit (IECEC), San Diego (California), 2006.
- [74] A. Kaled, S. Dutour, V. Platel, J. Lluc, Experimental study of a Capillary Pumped Loop for cooling power electronics: Response to high amplitude heat load steps, *Applied Thermal Engineering* 89 (2015) 169–179.
- [75] V. Dupont, J.-C. Legros, S. V. Oost, L. Barremaecker, Experimental investigation of CPL pressurized with NCG inside a centrifuge up to 10 G., in: 17th International Heat Pipe Conference, 2013, pp. 303–310.
- [76] P. A. de Oliveira, J. R. Barbosa, Effect of jet length and ambient temperature on the performance a two-phase jet impingement heat sink refrigeration system, *International Journal of Refrigeration* 75 (2017) 331–342.
- [77] K. Oliphant, B. W. Webb, M. Q. McQuay, An experimental comparison of liquid jet array and spray impingement cooling in the non-boiling regime, *Experimental Thermal and Fluid Science* (18) (1998) 1–10.
- [78] H. Bostanci, D. V. Ee, B. A. Saarloos, D. P. Rini, L. C. Chow, Spray cooling of power electronics using high temperature coolant and enhanced surface, ISBN: 978-1-4244-2601-0/09 IEEE.
- [79] Y. Wang, N. Zhou, Z. Yang, Y. Jiang, Experimental investigation of aircraft spray cooling system with different heating surfaces and different additives, *Applied Thermal Engineering* 103 (2016) 510–521.
- [80] L. Lin, R. Ponnappan, Heat transfer characteristics of spray cooling in a closed loop, *International Journal of Heat and Mass Transfer* 46 (2003) 3737–3746.
- [81] M. Molana, S. Banooni, Investigation of heat transfer processes involved liquid impingement jets: A review, *Brazilian Journal of Chemical Engineering* 30 (3) (2013) 413–435.
- [82] B. P. Whelan, A. J. Robinson, Nozzle geometry effects in liquid jet array impingement, *Applied Thermal Engineering* (29) (2009) 2111–2221.
- [83] Q. Guo, Z. Wen, R. Duo, Experimental an numerical study on the transient heat-transfer characteristics of circular air-jet impingement on a flat plate, *International Communications in Heat and Mass Transfer* 104 (2017) 1177–1188.

- [84] B. Horacek, K. T. Kiger, J. Kim, Single nozzle spray cooling heat transfer mechanisms, *International Journal of Heat and Mass Transfer* 48 (2005) 1425–1438.
- [85] C. Wang, L. Wang, BengtSundén, A novel control of jet impingement heat transfer in cross-flow by vortex generator pair, *International Journal of heat and Mass Transfer* 88 (2015) 82–90.
- [86] D. Go, R. A. Maturana, T. Fisher, S. Garimella, Enhancement of external forced convection by ionic wind, *International Journal of heat and Mass Transfer* (51) (2008) 6047–6053.
- [87] F. Douchet, D. Nortershauser, S. L. Masson, P. Gouannec, Experimental study of water cold plate for datacom equipment, in: *ASME-ATI-UIT 2015 Conference on thermal energy systems: Production, storage, utilization and environment*, 2015.
- [88] S. Grohamann, Measurement and modeling of single-phase and flow-boiling heat transfer in microtubes, *International Journal of Heat and Mass Transfer* 48 (2005) 4073–4089.
- [89] A. Avramenko, A. Tyrinov, I. Shevchuk, N. Dmitrenko, A. Kravchuk, V.I. Shevchuk, Mixed convection in a vertical flat microchannel, *International Journal of Heat and Mass Transfer* 106 (2017) 1164–1173.
- [90] B. Alm, U. Imke, R. Knitter, U. Schygulla, S. Zimmermann, Testing and simulation of ceramic micro heat exchangers, *Chemical Engineering Journal* 135S (2008) S179–S184.
- [91] K. Koyama, Y. Asako, Experimental investigation on heat transfer characteristics of a gas-to-gas counterflow microchannel heat exchanger, *Experimental Heat Transfer* 23 (2010) 130–143.
- [92] H. Y. Zhang, D. Pinjala, Y. K. Joshi, T. Wong, K. C. Toh, M. K. Iyer, Fluid Flow and Heat Transfer in Liquid Cooled Foam Heat Sinks for Electronic Packages, *IEEE Transactions on Components and Packaging Technologies* 28 (2).
- [93] L. D. Stevanovic, R. A. Beaupre, A. V. Gowda, A. G. Pautsch, S. A. Solovitz, Integral Micro-channel Liquid Cooling for Power Electronics, in: *Applied Power Electronics Conference and Exposition (APEC), Twenty-Fifth Annual IEEE*, 2010.
- [94] T.-H. Yen, N. Kasagi, Y. Suzuki, Forced convective boiling heat transfer in microtubes at low mass and heat fluxes, *International Journal of Multiphase Flow* 29 (2003) 1771–1792.

- [95] J. Lee, I. Mudawar, Two-phase flow in high-heat-flux micro-channel heat sink for refrigeration cooling applications: Part II-Heat transfer characteristics, *International Journal of Heat and Mass Transfer* (48) (2005) 941–955.
- [96] B. Agostini, A. Bontemps, Vertical flow boiling of refrigerant R134a in small channels, *International Journal of Heat and Fluid Flow* 27 (2005) 296–306.
- [97] G. Hetsroni, M. Gurevich, R. Ronzenblit, Sintered porous medium heat sink for cooling of high-power mini-devices, *International Journal of Heat and Fluid Flow* (27) (2006) 259–266.
- [98] P.-X. Jiang, X.-C. Lu, Numerical simulation of fluid flow and convection heat transfer in sintered porous plate channels, *International Journal of Heat and Mass Transfer* (49) (2006) 1685–1695.
- [99] P.-X. Jiang, M. Li, T.-J. Lu, L. Yu, Z.-P. Ren, Experimental research on convection heat transfer in sintered porous plate channels, *International Journal of Heat and Mass Transfer* (47) (2004) 2085–2096.
- [100] H. Zhang, D. Pinjala, T. Wong, K. Toh, Y. Joshi, Single-phase liquid cooled microchannel heat sink for electronic packages, *Applied Thermal Engineering* 25 (2005) 1472–1487.
- [101] G. P. Peterson, C. S. Chang, Two-phase heat dissipation utilizing porous-channels of high-conductivity material, *Journal of Heat Transfer* 1 (120) (1998) 243–252.
- [102] Z. Chen, P. Cheng, T. Zhao, [An experimental study of two phase flow and boiling heat transfer in bi-dispersed porous channels](#), *International Communications in Heat and Mass Transfer* 27 (3) (2000) 293 – 302. doi:[https://doi.org/10.1016/S0735-1933\(00\)00110-X](https://doi.org/10.1016/S0735-1933(00)00110-X).
URL <http://www.sciencedirect.com/science/article/pii/S073519330000110X>
- [103] T.S. Zhao, Q. Liao, On capillary-driven flow and phase-change heat transfer in a porous structure heated by a finned surface: measurements and modeling, *International Journal of Heat and Mass Transfer* (43) (2000) 1141–1155.
- [104] D. Faulkner, M. Khotan, R. Shekarraz, Practical Design of a 1000 W/cm² Cooling System, in: 19th IEEE SEMI-THERM Symposium, 2003.
- [105] G. Lazarek, S. Black, [Evaporative heat transfer, pressure drop and critical heat flux in a small vertical tube with r-113](#), *International Journal of Heat and Mass Transfer*

- 25 (7) (1982) 945 – 960. doi:[https://doi.org/10.1016/0017-9310\(82\)90070-9](https://doi.org/10.1016/0017-9310(82)90070-9).
URL <http://www.sciencedirect.com/science/article/pii/0017931082900709>
- [106] Z. Zhang, J. Li, P.-X. Jiang, Experimental investigation of spray cooling on flat and enhanced surfaces, *Applied Thermal Engineering* 51 (1-2) (2013) 102–111.
- [107] L. Ortiz, J. E. Gonzalez, Experiments on steady-state high heat fluxes using spray cooling, *Experimental Heat Transfer* 12 (3) (1999) 215–233.
- [108] Y. F. Maydanik, S. Vershinin, Development and investigation of copper-water loop heat pipes with high operating characteristics, *Heat Pipe Science and Technology, An International Journal* 1 (2).
- [109] S. S. Kang, Advanced cooling for power electronics, in: 2012 7th international conference on integrated power electronics systems (cips), IEEE, 2012, pp. 1–8.
- [110] L. Meyer, S. Dasgupta, D. Shaddock, J. Tucker, R. Fillion, P. Bronecke, L. Yorinks, P. Kraft, A silicon-carbide micro-capillary pumped loop for cooling high power devices, in: Nineteenth Annual IEEE Semiconductor Thermal Measurement and Management Symposium, 2003., IEEE, 2003, pp. 364–368.
- [111] F. Accorinti, N. Blet, V. Ayel, S. Dutour, Y. Bertin, [Experimental and Numerical Analysis of Start-Up of a Capillary Pumped Loop for Terrestrial Applications](#), *Journal of Heat Transfer* 141 (9), 091813. doi:[10.1115/1.4044276](https://doi.org/10.1115/1.4044276).
URL <https://doi.org/10.1115/1.4044276>
- [112] M. Kaviany, *Handbook of Heat Transfer* (Third Edition), McGraw-Hill, 1998, Ch. 9, pp. 1–82.
- [113] L. Mottet, T. Coquard, M. Prat, Three dimensional liquid and vapour distribution in the wick of capillary evaporators, *International Journal of Heat and Mass Transfer* 83 636–651.
- [114] C. Figus, Y. Le Bray, S. Bories, M. Prat, Heat and mass transfer with phase change in aporous structure partially heated: continuum model and pore network simulations, *International Journal of Heat and Mass Transfer* 42 (14) (1999) 2557–2569.
- [115] L. Lachassagne, V. Ayel, C. Romestant, Y. Bertin, Experimental study of capillary pumped loop for integrated power in gravity field, *Applied Thermal Engineering* 35 (2012) 166–176.

- [116] S. Beyhaghi, S. Geoffroy, M. Prat, K. M. Pillai, Wicking and evaporation of liquids in porous wicks: a simple analytical approach to optimization of wick design ., *AIChE Journal* 60 (5) 1930–1940.
- [117] N. Blet, V. Ayel, Y. Bertin, C. Romestant, V. Platel, Transient modeling of cpl for terrestrial applications, part b reservoir modeling, Vol. India, Kampur, 2013, pp. 263–270.
- [118] Mitsubishi, 7th Generation IGBT Modules – Standard-Type, Mitsubishi Electric.
- [119] [Mitsubishielectric.com cm600dx-34t/cm600dxdp-34t igbt modules](http://Mitsubishielectric.com/cm600dx-34t/cm600dxdp-34t%20igbt%20modules) [online].
- [120] P. Wais, [Correlation and numerical study of heat transfer for single row cross-flow heat exchangers with different fin thickness](#), *Procedia Engineering* 157 (2016) 177 – 184, selected Papers from IX International Conference on Computational Heat and Mass Transfer (ICCHMT2016). doi:<https://doi.org/10.1016/j.proeng.2016.08.354>.
URL <http://www.sciencedirect.com/science/article/pii/S1877705816325292>
- [121] P. Wais, [Fin-tube heat exchanger optimization](#), in: J. Mitrovic (Ed.), *Heat Exchangers*, IntechOpen, Rijeka, 2012, Ch. 13. doi:[10.5772/33492](https://doi.org/10.5772/33492).
URL <https://doi.org/10.5772/33492>
- [122] J. E. Hajal, J. Thome, A. Cavallini, [Condensation in horizontal tubes, part 1: two-phase flow pattern map](#), *International Journal of Heat and Mass Transfer* 46 (18) (2003) 3349 – 3363. doi:[https://doi.org/10.1016/S0017-9310\(03\)00139-X](https://doi.org/10.1016/S0017-9310(03)00139-X).
URL <http://www.sciencedirect.com/science/article/pii/S001793100300139X>
- [123] J. Thome, J. E. Hajal, A. Cavallini, [Condensation in horizontal tubes, part 2: new heat transfer model based on flow regimes](#), *International Journal of Heat and Mass Transfer* 46 (18) (2003) 3365 – 3387. doi:[https://doi.org/10.1016/S0017-9310\(03\)00140-6](https://doi.org/10.1016/S0017-9310(03)00140-6).
URL <http://www.sciencedirect.com/science/article/pii/S0017931003001406>
- [124] L. B. Erbay, B. Dogan, M. M. Ozturk, [Comprehensive study of heat exchangers with louvered fins](#), in: S. M. S. Murshed, M. M. Lopes (Eds.), *Heat Exchangers*, IntechOpen, Rijeka, 2017, Ch. 4. doi:[10.5772/66472](https://doi.org/10.5772/66472).
URL <https://doi.org/10.5772/66472>

- [125] E. G. da Silva, R. F. Patella, Numerical simulation of cavitating flows with homogeneous models, *Computers and Fluids* 38 (9) (2009) 1682–1696. doi:[10.1016/j.compfluid.2009.03.001](https://doi.org/10.1016/j.compfluid.2009.03.001).
- [126] K. Smierciew, A. Pawluczuk, J. Gagan, D. Butrymowicz, *Thermodynamic analysis of two-phase injector for various working fluids*, *Applied Thermal Engineering* 157 (2019) 113713. doi:<https://doi.org/10.1016/j.applthermaleng.2019.113713>.
URL <http://www.sciencedirect.com/science/article/pii/S135943111930225X>
- [127] K. Smierciew, D. Butrymowicz, T. Przybyliński, A. Pawluczuk, *Investigations of heat and momentum transfer in two-phase injector operating with isobutane*, *Applied Thermal Engineering* 127 (2017) 1495 – 1505. doi:<https://doi.org/10.1016/j.applthermaleng.2017.08.160>.
URL <http://www.sciencedirect.com/science/article/pii/S1359431117326054>
- [128] product-selection.grundfos.com/catalogue [online].
- [129] C.-C. Wang, K.-Y. Chi, C.-J. Chang, *Heat transfer and friction characteristics of plain fin-and-tube heat exchangers, part ii: Correlation*, *International Journal of Heat and Mass Transfer* 43 (15) (2000) 2693 – 2700. doi:[https://doi.org/10.1016/S0017-9310\(99\)00333-6](https://doi.org/10.1016/S0017-9310(99)00333-6).
URL <http://www.sciencedirect.com/science/article/pii/S0017931099003336>
- [130] GRETh, Transfert de chaleur dans les tubes de section circulaire - TM2 (Novembre 1987).
- [131] GRETh, Pertes de pression régulière dans les conduites rectilignes des section uniforme - TM1 (Novembre 1987).
- [132] GRETh, Pertes de pression dans les canaux de section uniforme (June 1999).
- [133] GRETh, Les pertes de pression singulières (1999).
- [134] Y.-J. Chang, C.-C. Wang, *A generalized heat transfer correlation for louver fin geometry*, *International Journal of Heat and Mass Transfer* 40 (3) (1997) 533 – 544. doi:[https://doi.org/10.1016/0017-9310\(96\)00116-0](https://doi.org/10.1016/0017-9310(96)00116-0).
URL <http://www.sciencedirect.com/science/article/pii/0017931096001160>
- [135] Y.-J. Chang, K.-C. Hsu, Y.-T. Lin, C.-C. Wang, *A generalized friction correlation for louver fin geometry*, *International Journal of Heat and Mass Transfer* 43 (12)

- (2000) 2237 – 2243. doi:[https://doi.org/10.1016/S0017-9310\(99\)00289-6](https://doi.org/10.1016/S0017-9310(99)00289-6).
URL <http://www.sciencedirect.com/science/article/pii/S0017931099002896>
- [136] N. Berrada, Transfert de chaleur et perted de pression dans les minis-canaux, Tech. rep., GRETh (2011).
- [137] A. Cavallini, L. Doretti, M. Matkovic, L. Rossetto, [Update on condensation heat transfer and pressure drop inside minichannels](#), Heat Transfer Engineering 27 (4) (2006) 74–87. arXiv:<https://doi.org/10.1080/01457630500523907>, doi:[10.1080/01457630500523907](https://doi.org/10.1080/01457630500523907).
URL <https://doi.org/10.1080/01457630500523907>

Appendix

Working fluid discussion

The choice of the working fluid is one of the most important aspects for efficient cooling systems. It also affects and limits the choice of the material to be used for the cooling system and its components (fluid/solid compatibility issue) as well as global performances. Different working fluids have been studied and compared on the basis of literature data.

Fluids used in single phase cooling systems can be compared using the Mouromtseff number (Mo), defined as:

$$\text{Mo} = \frac{\rho^a k^b c_p^d}{\mu^e}$$

where coefficients a , b , d , e depend on the nature of fluid flow (for internal turbulent flows: $a = 0.908$, $b = 0.13$, $d = 0.092$ and $e = 0.038$). The higher the Mouromtseff number, the higher the fluid performances. In Fig. A.1 the value of Mouromtseff number for different working fluids is reported as a function of temperature.

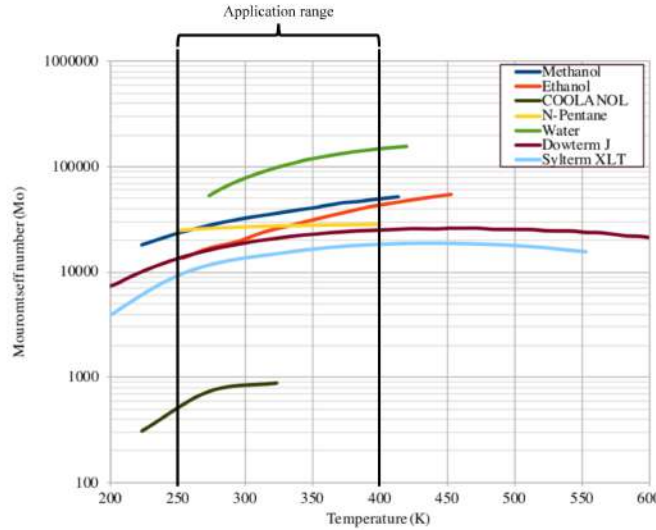


Figure A.1: Comparison between different fluid using Mouromtseff number

As one can notice, water, characterised by the highest value of the Mouromtseff num-

ber, is in absolute the most performing fluid. Despite its performances, water freeze point (0°C at atmospheric pressure) limits its use in aeronautics field. Methanol, ethanol and n-pentane are characterised by quite good performances and low freeze point. This makes these fluids adapted for this application. Especially in the range $250 - 400$ K (Fig. A.1), methanol is the one characterised by better performances than ethanol and n-pentane. In Fig. A.2 a fluid-to-water comparison in terms of thermal conductivity and Mouromtseff number, for each analysed fluid, is reported.

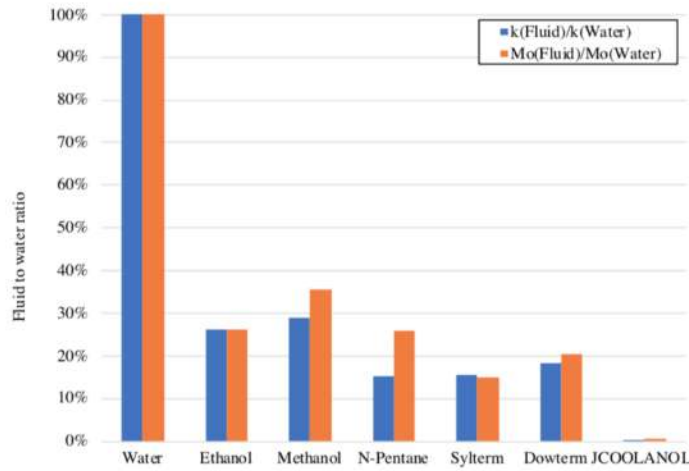


Figure A.2: Fluid to water comparison

Comparison of fluid thermal conductivity could be a good performance indicator. In the example reported in Fig. A.2 Mouromtseff number and fluid thermal conductivity, k , at 60°C are compared for different working fluids and water. The Mouromtseff number could be a good reference to evaluate the performances of a given fluid in single-phase systems. Concerning two-phase systems, active and passive, at our knowledge it does not exist a reference to evaluate fluid performances (except for heat pipes for which the merit number is used). However, the comparison between fluid density and thermal conductivity for liquid and vapour phases are a good index. Experimental studies, based on evaluation of evaporator thermal conductance, such those conducted by Ayel *et al.* [14] and Accorinti *et al.* [12] to evaluate the performances of methanol, ethanol and n-pentane in a CPLIP may give good indications about the fluid choice in two-phase cooling systems.

B.1 Active single phase (liquid cooling) first approximation design

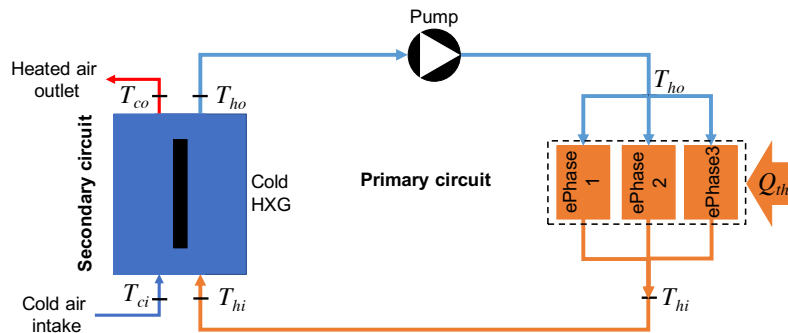


Figure B.1: Single phase cooling system scheme

Three parallel cold plates, one per each electrical phase, are considered.

Cold plate dimensions are related to modules number dimensions. Here, four modules, which dimensions are $12.2 \times 6.2 \text{ cm}^2$ [21], are installed on the cold plate in couple of two and face to face. The thermal load applied on each cold plate is simply given by the total thermal load divided by three. A thermal load of 5 kW is so applied on each cold plate. considering the modules dimensions, the cold plate, reported in Fig. B.2 has dimension $12.4 \times 12.2 \text{ cm}^2$ and thickness of 1.4 cm. Each cold plate is traversed by 1 cm-side-squared section channels. Two different configurations of the cold plate have been considered. The first one, characterised by nine parallel channels, which section is reported in Fig. B.2a and a second configuration, which section is reported in Fig. B.2b, characterised by the presence of the serpentine.

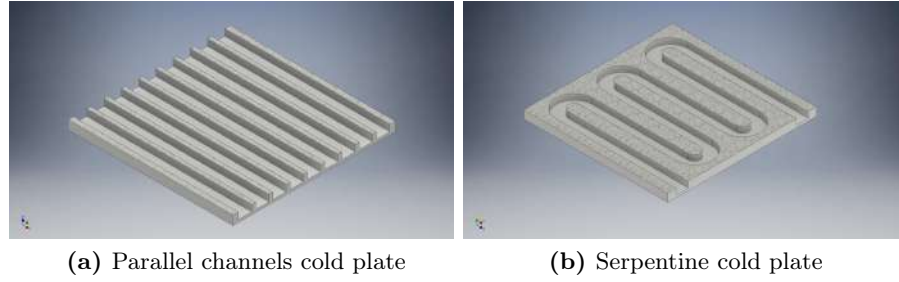


Figure B.2: Two different cold plate configurations

The channels configuration, obviously impacts the temperature distribution on the surface of the cold plate and the pressure drop of the fluid flowing in the cold plate. Lower pressure drop characterises the first configuration and ensures a more uniform temperature distribution from the inlet of the coolant to the outlet. If in the first case, the coolant flow is symmetrical with respect to longitudinal plane, the second configuration is characterised by a non symmetrical flow and an increasing temperature gradient on the surface of the cold plate, from the inlet to the outlet. The mass flow rate, necessary to evacuate the thermal load, is calculated using the eq. (2.3), on the base of a temperature difference of 40°C ($T_{inlet} = 40^{\circ}\text{C}$ and $T_{outlet} = 80^{\circ}\text{C}$). In this stage of the work, the second configuration of the cold plate is assumed, because of the lower pressure drop values.

B.1.2 Pump selection

Pump selection is based on the overall loop pressure drop in the loop and the required mass flow rate.

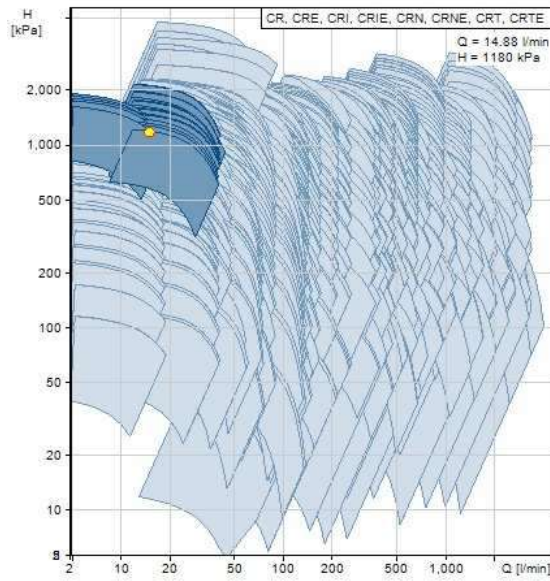
Pump family is chosen on a classical selection diagram like the one showed (see Fig. B.3a), and pump work point verification is done using the pump curve reported in Fig. B.3b.

This procedure is today automated thanks to web applications available on manufacturer web sites¹.

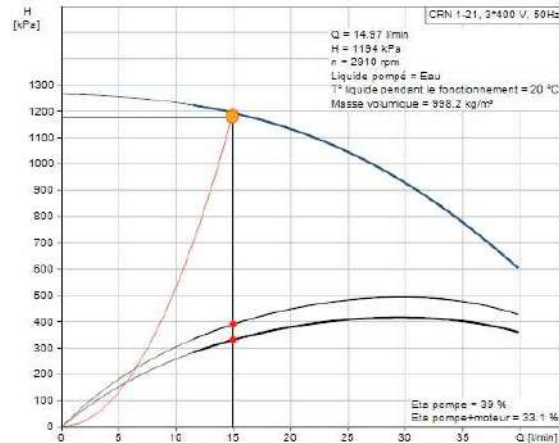
B.1.3 Transport lines

Either hot and liquid line are characterised by the same hydraulic diameter, calculated by eq. (2.1). The fluid velocity is assumed to be constant into the transport lines, at

¹Diagrams reported in this section are an example to show how the choice is made, and they are absolutely not representative of pumps used in this work, chosen by using the already cited web application.



(a) Pump family selection [128]



(b) Working point on pump curve verification [128]

each temperature (the liquid density is assumed constant at the working temperatures), and equal to $2 \text{ m} \cdot \text{s}^{-1}$ to avoid instabilities and eventual corrosion of the tubes due to too high liquid velocities.

B.1.4 Single phase cold heat exchanger

Here, the first approximation design model for the cold HXG of a single-phase cooling system is presented. Two different configurations of cold source will be here introduced. In particular skin heat exchanger, the most adapted solution to evacuate the thermal load in the case where the electronics components are installed in the fuselage (power electronic in the fuselage, PIF), will be designed and compared with RAM-air. The latter is particularly adapted to cases where an intake is needed. In this last case, components to be cooled may be installed in the nacelle (power electronics in the nacelle, PIN) for example. However, it should be considered that RAM-air is the most flexible solution allowing either a configuration in the nacelle or in the fuselage.

B.1.4.1 Skin heat exchanger first approximation design

As already explained in sec. 1.4.1, this technology is characterised by the presence of a tube, in which the hot fluid flows and evacuates the thermal load through the aircraft skin to the external ambient air. A schematic of skin heat exchanger is reported in Fig. B.3a. The sensible heat exchange mechanism is convection from the hot fluid to the tube

walls and from the tube walls to the aircraft skin. So, convection from the skin to the external ambient air. In Fig. B.3b the equivalent electrical network for the skin heat exchanger is reported.

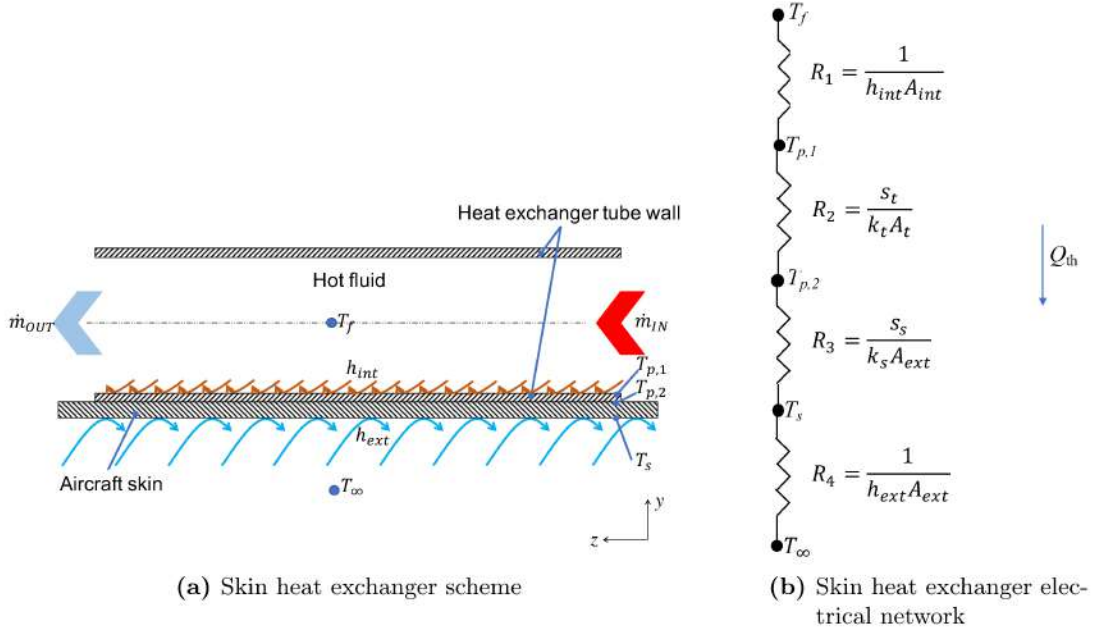


Figure B.3: Skin heat exchanger

To design the skin heat exchanger, a finite volume method, based on the electrical analogy, was used under the following hypothesis and on the base of the schematic reported in Fig. B.4 :

- No heat exchanges between the tube wall and the internal environment of the aircraft (the upside of the tube is adiabatic);
- The heat transfer surface area, for the internal and the external tube side is assumed to be equal ($A_{int} = A_{ext} = \pi D_m dz$): a thermal diffuser is used to spread the heat;
- The conductive resistances are neglected: $(R_1 \wedge R_4) \gg (R_2 \wedge R_3)$;
- Solid thermal capacities are neglected;
- The ambient air temperature does not change as the skin temperature does (the external ambient air is large enough to respect this condition).

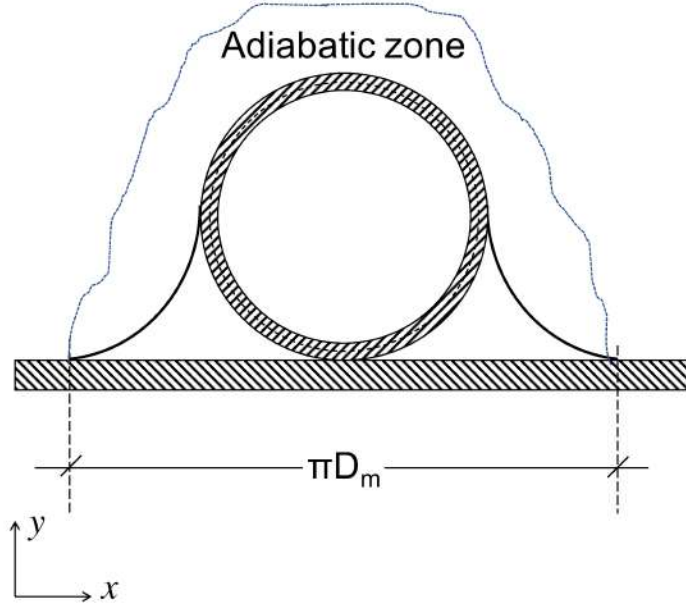


Figure B.4: Hypothesis

- The external heat transfer coefficient is calculated using a modified correlation for the flat plate flow, according to Pang *et al.* [4]:

$$\text{Nu}_{\text{ext}} = 0.2948 \text{Re}_L^{0.5} \quad (\text{B.1})$$

- The internal side heat transfer coefficient is calculated using the following correlation, according to Pang *et al.* [4] that found a good agreement with experimental results:

$$\text{Nu}_{\text{int}} = 0.021 \text{Re}_D^{0.94} \quad (\text{B.2})$$

Under the following hypothesis and discretising using the mesh reported in Fig. B.5, the energy balance equations considered to solve the problem are reported in the system (B.3):

$$\begin{cases} \Delta q_i = \dot{m}_f c_p (T_{f,i} - T_{f,i+1}) \\ \Delta q_i = h_{\text{int}} \pi D_m \Delta z (\bar{T}_{f,i} - T_{s,i}) \\ \Delta q_i = h_{\text{ext}} \pi D_m \Delta z (T_{s,i} - T_\infty) \end{cases} \quad (\text{B.3})$$

Where, in eq. (B.1) and (B.2) the Reynolds number is respectively calculated on the base of flat plate length and the heat exchanger internal diameter. The mean fluid bulk

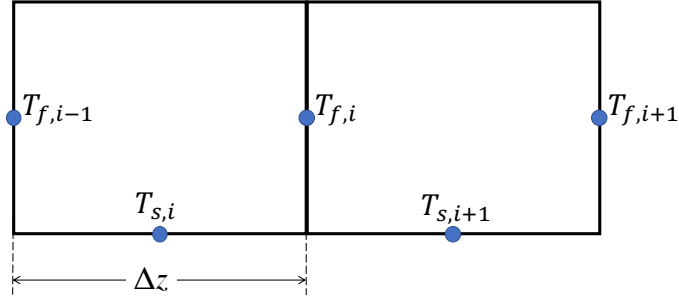


Figure B.5: Mesh configuration

temperature, $\bar{T}_{f,i}$, is the corresponding temperature in the centroid of the cell and calculated as the average between the cell inlet and outlet temperature ($\bar{T}_{f,i} = \frac{T_{f,i} + T_{f,i+1}}{2}$).

The linear system (B.3) may be so easily solved, three equations for three unknown factors: the wall temperature $T_{s,i}$; the cell outlet temperature, $T_{f,i+1}$ and the heat exchanged between the hot and the cold fluid Δq_i .

While the cell outlet temperature is higher or equal to the cold plate inlet temperature, corresponding to 40 °C the system is solved and the parameters found. Obviously, the total skin heat exchange length is given by the sum of all the Δz_i :

$$L_{tot} = \sum_{i=1}^n \Delta z_i \quad (\text{B.4})$$

and the energy balance must be verified :

$$Q_{th} = \sum_{i=1}^n \Delta q_i \quad (\text{B.5})$$

Pressure drops Pressure drops for a single phase flow into a smooth tube, can be calculated by applying the relation:

$$\Delta P = \xi \frac{L_{tot}}{D} \frac{1}{2} \rho u^2 \quad (\text{B.6})$$

where the friction factor, ξ , can be obtained, for a turbulent flow, from the Moody diagram (see Fig. B.6).

B.1.4.2 Cold heat exchanger in a bank configuration

If the skin heat exchanger requires a contact between the heat exchanger tube(s) and the aircraft skin, RAM-air configuration requires the use of a bank of tubes. In this case,

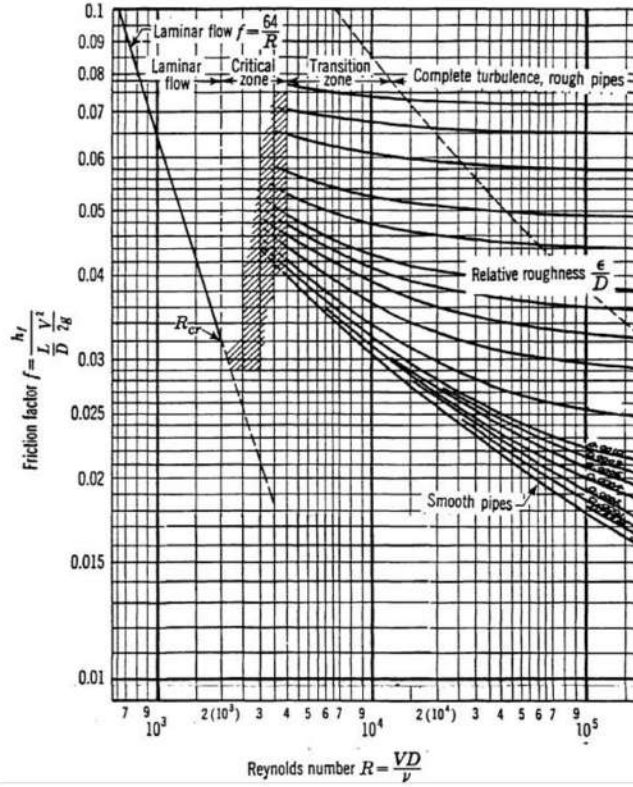


Figure B.6: Moody diagram

the external air velocity can be better controlled, during the design phase, to ensure the adequate heat transfer coefficient.

The configuration used for the first approximation design of the tube bank is reported in Fig. B.7. Here, other than the hypothesis detailed in sec. B, the hypothesis of not externally finned tubes is introduced to simplify the design process.

In this case, the same correlation for the internal side heat transfer coefficient evaluation is used (eq. B.2), while, for the external side, the not finned tube bench correlation is adopted [13]:

$$\text{Nu}_{\text{ext}} = 1.04 \text{Re}_{\text{Dext}}^{0.4} \text{Pr}_{\text{air}}^{0.36} \quad \text{if } 1 < \text{Re}_{\text{Dext}} < 500 \quad (\text{B.7})$$

$$\text{Nu}_{\text{ext}} = 0.71 \text{Re}_{\text{Dext}}^{0.5} \text{Pr}_{\text{air}}^{0.36} \quad \text{if } 500 < \text{Re}_{\text{Dext}} < 10^3 \quad (\text{B.8})$$

$$\text{Nu}_{\text{ext}} = 0.35 \left(\frac{X_t}{X_{ls}} \right)^{0.2} \text{Re}_{\text{Dext}}^{0.6} \text{Pr}_{\text{air}}^{0.36} \quad \text{if } 10^3 < \text{Re}_{\text{Dext}} < 2 \cdot 10^5 \quad (\text{B.9})$$

$$\text{Nu}_{\text{ext}} = 0.031 \left(\frac{X_t}{X_{ls}} \right)^{0.2} \text{Re}_{\text{Dext}}^{0.8} \text{Pr}_{\text{air}}^{0.36} \quad \text{if } 2 \cdot 10^5 < \text{Re}_{\text{Dext}} < 2 \cdot 10^6 \quad (\text{B.10})$$

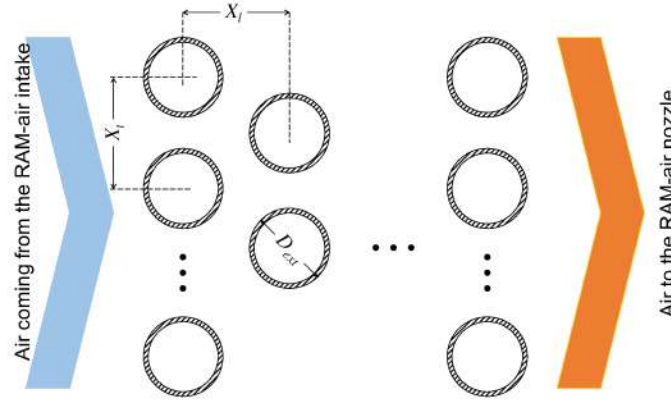


Figure B.7: Tube bank configuration

Where in relations (B.9) and (B.10) $X_{ls} = X_l/D_{ext}$ according to Fig. B.7.

B.2 Two-phase solution first approximation design

B.2.1 The evaporator

As for single phase cold plate, for pumped two phase cooling system, the same simplest evaporator configuration is considered to minimise pressure drops and to not condemn a priori such technology. In fact, even if more performing technologies should be used, such as metal foams or non-sintered porous media, to increase the heat transfer coefficient, here a parallel macro channel evaporator is considered.

B.2.2 Condenser design

B.2.2.1 Skin heat exchanger for a two-phase internal flow: condenser first approximation design

It has been observed that this particular technology is not able to reasonably satisfy the requirements of the problem that is being solved in this work. However, for completeness, a condenser first approximation design, assuming that all the thermal load is used for condensation only and under the hypothesis already detailed in sec. B, is here presented.

Two-phase flows are much complicated than single phase flow. In this case, to solve the problem and to find the appropriate condensing length, it is necessary to find the correct vapour quality change Δx_i for each control volume Δz_i .

The energy balance Δq_i for the control volume Δz_i can in general be expressed as [13]:

$$\Delta q_i = h_{int} A_{int} (T_{sat} - T_{w,k}) = \dot{m} \lambda_{l,v} \Delta x_i \quad (\text{B.11})$$

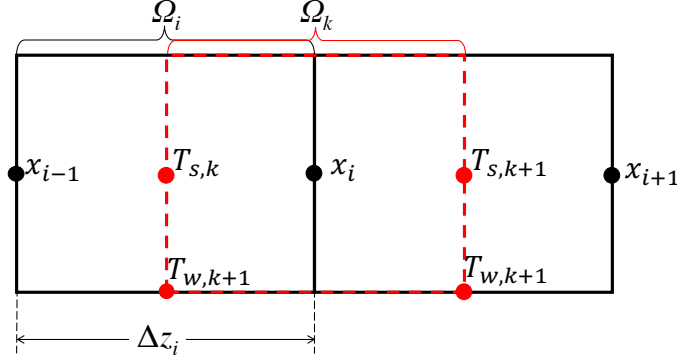


Figure B.8: Mesh configuration for two-phase flow

or

$$\frac{\Delta x}{\Delta z} = \frac{\pi D_c h_{ext} (T_\infty - T_w)}{\dot{m} \lambda_{l,v}} \quad (\text{B.12})$$

Two different shifted grids need to be used in this case: the saturation temperature and the wall temperature are so calculated in correspondence of the grid k , while the inlet and outlet vapour quality in a given control volume are referred to the grid i . Even in this case, the average value in a given control volume Ω_i is given by the mean value between the inlet and the outlet in correspondence of the same control volume.

$$\begin{cases} \Delta q &= h_{ext} A_{ext} (T_w - T_\infty) \\ \Delta q &= h_{int} A_{int} (T_{sat} - T_w) \\ \Delta q &= \dot{m} \lambda_{l,v} \Delta x \end{cases} \quad (\text{B.13})$$

In this case, other than the unknown values of the incremental thermal power exchanged, Δq , the wall temperature, T_w , and the vapour quality change within the control volume, Δx , the internal side heat transfer coefficient is also unknown. The closure equation which may be used is the Chato's correlation:

$$h_{int,m} = \Omega \left[\frac{\rho_l (\rho_l - \rho_v) g \lambda_{l,v} k_l^3}{\mu_l (T_{sat} - T_w) D_{int}} \right]^{\frac{1}{4}} \quad (\text{B.14})$$

where the coefficient Ω , dependent on the fraction of the tube circumference in which vapour is stratified, is related to the void fraction, α_g , following the relation:

$$\Omega = 0.728 \alpha_g^{\frac{3}{4}} \quad (\text{B.15})$$

with:

$$\alpha_g = \frac{1}{1 + \left(\frac{x-1}{x}\right) \left(\frac{\rho_v}{\rho_l}\right)^{\frac{2}{3}}} \quad (\text{B.16})$$

The system composed by eq. (B.13) and eq. (B.14) in this case is non-linear and coupled. To solve the problem, the Newton-Raphson's method will be used.

The wall temperature $T_{w,k}$ can be either calculated from the external side, considering the external HTC, h_{ext} , and from the internal side, considering the internal HTC, h_{int} . In particular, from the external side:

$$T_{w,k}^+ = \left(\frac{\dot{m} \lambda_{l,v}}{\pi D_c h_{ext}} \right) \left(\frac{\Delta x}{\Delta z} \right) + T_\infty \quad (\text{B.17})$$

and from the internal side, considering equations (B.14), (B.15) and (B.16):

$$T_{w,k}^- = T_{sat} - \left(\frac{\dot{m} \lambda_{l,v}}{\pi D_c h_{int}} \right) \left(\frac{\Delta x}{\Delta z} \right) \quad (\text{B.18})$$

where, the h_{int} value is iteratively calculated by changing at each iteration j the vapour quality difference Δx . In particular, imposing a fixed value of the control volume dimension Δz , the initial vapour quality difference Δx is initially related to the spatial dimension by the ratio $\Delta x = 10^{-3} \cdot \Delta z$. Imposing a forbearance value, ε , small enough and in the order of 10^{-8} , the ratio $\frac{\Delta x}{\Delta z}$ is updated at each iteration j as, $\frac{\Delta x}{\Delta z}|_{j+1} = \frac{\Delta x}{\Delta z}|_j + \varepsilon$ while the residual wall temperature difference, $R = T_{w,k}^- - T_{w,k}^+$, is small enough and in the order of 10^{-3} . Only when the convergence is reached for the wall temperature, the control volume counter is updated to the next one until the vapour quality at the exit of the control volume n -th is $x_{i=n} = 0$.

Even in this case, as for single phase HXG, relations (B.4) and (B.5) must be verified.

Pressure drop For two-phase pressure gradient, neglecting gravity, pressure losses may be written in terms of frictional and acceleration components [13]. In particular in differential terms, it can be written as:

$$\frac{dP}{dz} = \left(\frac{dP}{dz} \right)_f + G^2 \frac{d}{dz} \left[\frac{(1-x)^2}{\rho_l (1-\alpha_g)} + \frac{x^2}{\rho_v \alpha_g} \right] \quad (\text{B.19})$$

Where $G [\text{kg} \cdot \text{m}^{-2} \cdot \text{s}^{-1}] = \frac{4\dot{m}}{\pi D_c^2}$ is the mass flow rate per unit area and the frictional pressure gradient term, $\left(\frac{dP}{dz} \right)_f$, can be related to a single phase flow, but using the adapted multiplier ϕ . Being the methanol liquid to vapour viscosity ratio, $\frac{\mu_l}{\mu_g} < 1000$, it is possible to use the Friedel's correlation [13]. In this case, the frictional term is defined

as:

$$\left(\frac{dP}{dz}\right)_f = \phi_{lo}^2 \left(\frac{dP}{dz}\right)_{lo} \quad (\text{B.20})$$

The frictional multiplier is defined as:

$$\phi_{lo}^2 = E + \frac{(3.23 F H)}{\text{Fr}^{0.045} \text{We}^{0.035}} \quad (\text{B.21})$$

and the liquid only pressure gradient is defined as:

$$\left(\frac{dP}{dz}\right)_{lo} = \frac{2 f_{lo} G^2}{\rho_l D_c} \quad (\text{B.22})$$

where the friction factor is $f = 0.079 \text{Re}^{-0.25}$, calculated for vapour phase only and for liquid phase only using respectively the Re number of the given phase.

In eq. (B.21), E is defined as:

$$E = (1 - x)^2 + x^2 \frac{\rho_l f_{go}}{\rho_v f_{lo}} \quad (\text{B.23})$$

F is defined as:

$$F = x^{0.78} (1 - x)^{0.224} \quad (\text{B.24})$$

and H :

$$H = \left(\frac{\rho_l}{\rho_v}\right)^{0.91} \left(\frac{\mu_v}{\mu_l}\right)^{0.19} \left(1 - \frac{\mu_v}{\mu_l}\right)^{0.7} \quad (\text{B.25})$$

The Froude number is calculated as:

$$\text{Fr} = \frac{G^2}{g D_c \rho_h} \quad (\text{B.26})$$

and the Weber number is obtained in the following manner:

$$\text{We} = \frac{G^2 D_c}{\rho_h \sigma} \quad (\text{B.27})$$

The equivalent density ρ_h is defined as:

$$\rho_h = \frac{\rho_v \rho_l}{x \rho_l + (1 - x) \rho_v} \quad (\text{B.28})$$

The evaluation of the frictional term, in each control volume Ω_i is so relatively simple, using the relations from (B.20) to (B.28).

Let's now rewrite the second term of the expression (B.19) to derivate it in a more

simple way:

$$\frac{d}{dz} \left[\frac{(1-x)^2}{\rho_l(1-\alpha_g)} + \frac{x^2}{\rho_v\alpha_g} \right] = \frac{d}{dz} (A+B) \quad (\text{B.29})$$

where obviously

$$A = \frac{(1-x)^2}{\rho_l(1-\alpha_g)} \quad (\text{B.30})$$

and

$$B = \frac{x^2}{\rho_v\alpha_g} \quad (\text{B.31})$$

So, the term:

$$\frac{dA}{dz} = \frac{-\left(\frac{dx}{dz}\right) x - \left(\frac{d\alpha_g}{dz}\right) (x-1) \left(\frac{\rho_v}{\rho_l}\right)^{\frac{2}{3}}}{\left[1 + \left(\frac{x-1}{x}\right) \left(\frac{\rho_v}{\rho_l}\right)^{\frac{2}{3}}\right]^2} \quad (\text{B.32})$$

and

$$\frac{dB}{dz} = \frac{\frac{d}{dz}(x^2) \rho_g \alpha_g - \frac{d}{dz}(\alpha_g) x^2}{(\rho_g \alpha_g)^2} \quad (\text{B.33})$$

Rewriting eq. (B.32) and (B.33) in a discrete form, it is obtained:

$$\frac{d}{dz} (A+B) = A' + B'$$

where

$$A' = \frac{2(1-X)(-\Delta x)\rho_l(1-\mathfrak{A}_g) - [\rho_l(-\Delta\alpha_g)](1-X)^2}{[\rho_l(1-\mathfrak{A}_g)]^2} \quad (\text{B.34})$$

and

$$B' = \frac{2X\rho_v\mathfrak{A}_g - \Delta\alpha_g X^2}{(\rho_v\mathfrak{A}_g)^2} \quad (\text{B.35})$$

In eq. (B.34) and (B.35), the term X represents the vapour quality value in a given control volume and calculated in the centroid of the cell, so like the temperature, the vapour quality is $X = \frac{x_i + x_{i+1}}{2}$. At the same manner, the void fraction of vapour calculated in the centroid of a given cell is $\mathfrak{A}_g = \frac{\alpha_{g,k-1} + \alpha_{g,k}}{2}$.

It is now possible to calculate the two-phase pressure drop in each control volume ΔP_i , calculated from the discretised form of eq. (B.19), and to obtain the total pressure drop as the cumulated pressure drop of the n control volumes. The total pressure drop is so calculated as:

$$\Delta P_{c,tot} = \sum_{i=1}^n \Delta P_i$$

Discussion The external side heat transfer coefficient is strictly related to the aircraft velocity. Even in this case the lowest velocity value, realised during the taxi stages, is considered for the external HTC (h_{ext}). The same external heat transfer coefficient is so applied to this case.

From the thermal calculations, even in the case of condenser design, the use of the skin heat exchanger is not adapted to this study case. In fact, a total length of 920 m was obtained from the calculations and pressure drops too high to let this solution to be retained.

B.2.2.2 Condenser design in tube bank configuration

The same assumptions than those of the single phase heat exchanger are here used. A not finned tube bank configuration is here considered to be inserted in the same RAM-air system, which intake conduits are designed to ensure a minimal air velocity of $10 \text{ m}\cdot\text{s}^{-1}$ during the taxi stages of the aircraft.

In this case, the same correlation from (B.7) to (B.10) are used to evaluate the heat transfer coefficient. In this case, due to the higher tube diameter, and so higher X_t and X_l , see Fig. B.7, the heat transfer coefficient increases up to a value of $110 \text{ W}\cdot\text{m}^{-2}\cdot\text{K}^{-1}$. So a length of 46 m is in this case necessary to completely condense the fluid. The heat transfer surface area corresponding to a condenser tube diameter of 0.021 m is about 3 m^2 to evacuate a total thermal power of 15 kW. If sub-cooling is considered to lower the liquid temperature up to 37°C , about 6.5% of the thermal load is used, requiring an additional condenser length lower than 4 m.

GRETh (EchTherm)

GRETh (Groupment pour la Recherche sur les Echangeurs Thermiques) EchTherm is a calculation software for heat exchanger design and verification. It is based on iterative resolution of appropriate correlations, following the typology of heat exchanger. In this chapter only known characteristics of the software for continuous finned and for louvered fin-microchannels condensers are reported.

C.1 Continuous finned heat exchangers

The external fluid is single phase while condensation and subcooling occur for internal fluid. As better explained in Chap. 7, to have more accurate results, the heat exchanger is divided in different sub-heat duty zones and for each of them all thermo-hydraulic parameters (internal and external HTC, internal and external pressure drops, HXG's efficiency) are calculated.

C.1.1 Limits and hypothesis

As declared by GRETh, the following hypothesis and limitations have to be considered when using such software:

1. In general, fluid thermo-physical properties are evaluated at inlet and outlet temperature and pressure as well as in saturation conditions.
2. Pressure drops at inlet and outlet collectors are not considered
3. For wet air, a constant humidity is considered.

C.1.2 Correlations

C.1.2.1 External side

On the external side (fin side) correlations reported in ref. [129] are used. The Colburn factor, $j = \frac{Nu_T}{Re Pr^{\frac{1}{3}}}$, depends on the number of rows, N , in the heat exchanger. For $N \geq 2$

it is:

$$j = 0.086 \text{Re}_{D_c}^{P3} N^{P4} \left(\frac{F_p}{D_c} \right)^{P5} \left(\frac{F_p}{D_h} \right)^{P6} \left(\frac{F_p}{P_t} \right)^{-0.93} \quad (\text{C.1})$$

where $P3$ is calculated as:

$$P3 = -0.361 - \frac{0.042N}{\ln(\text{Re}_{D_c})} + 0.1581 \ln \left(N \left(\frac{F_p}{D_c} \right)^{0.41} \right) \quad (\text{C.2})$$

$P4$ is a function of $P1 = 1.9 - 0.23 \ln \text{Re}_{D_c}$, and it is calculated as:

$$P4 = -1.224 - \frac{0.076 \left(\frac{P1}{D_h} \right)^{1.42}}{\ln \text{Re}_{D_c}} \quad (\text{C.3})$$

Factor $P5$ in eq. (C.1) is:

$$P5 = -0.083 + \frac{0.058N}{\ln \text{Re}_{D_c}} \quad (\text{C.4})$$

and finally $P6$ is:

$$P6 = -5.735 + 1.21 \ln \frac{\text{Re}_{D_c}}{N} \quad (\text{C.5})$$

Following the same reference, the airside friction factor is calculated as:

$$f = 0.0267 \text{Re}_{D_c}^{F1} \left(\frac{P_t}{P_l} \right)^{F2} \left(\frac{F_p}{D_c} \right)^{F3} \quad (\text{C.6})$$

where P_t and P_l are transversal and longitudinal tube pitch respectively. The factors $F1$, $F2$ and $F3$ are defined as follow:

$$F1 = -0.764 + 0.739 \frac{P_t}{P_k} + 0.177 \frac{F_p}{D_c} - \frac{0.00758}{N} \quad (\text{C.7})$$

$$F2 = -15.689 + \frac{64.021}{\ln \text{Re}_{D_c}} \quad (\text{C.8})$$

$$F3 = 1.696 + \frac{15.695}{\ln \text{Re}_{D_c}} \quad (\text{C.9})$$

As reported by Wang *et al.* [129], eq. (C.1) can correlates almost 89% of experimental Colburn factors within an error of 15%, while eq. (C.6) can describe almost 85% of experimental data within an error of 15%.

C.1.2.2 Internal side

Single phase

Heat transfer Single phase heat transfer coefficient is calculated on the basis of relations reported in ref. [130]. For laminar flows and short pipes, in which $0.1 < \text{Re Pr} \frac{D}{L} < 10^4$, Schlünder's correlation is used:

$$\text{Nu} = \left(3.66 + 1.61^3 \text{Re Pr} \frac{D}{L} \right)^{\frac{1}{3}} \quad (\text{C.10})$$

or, alternatively, Haussen's correlation may be used in the same range:

$$\text{Nu} = 3.66 + \frac{0.19 \left(\text{Re Pr} \frac{D}{L} \right)^{0.18}}{1 + 0.117 \left(\text{Re Pr} \frac{D}{L} \right)^{0.467}} \quad (\text{C.11})$$

If $100 < \text{Re} < 2100$, $L/D < 0.1 \text{Re Pr}$ and $0.6 < \text{Pr} < 100$, Sieder-Tate correlation is applied:

$$\text{Nu} = 1.86 \left(\text{Re Pr} \frac{D}{L} \right)^{0.33} \left(\frac{\mu}{\mu_p} \right)^{0.14} \quad (\text{C.12})$$

For very short pipes, $L/D < 10$, Pohlhausen's equation is used:

$$\text{Nu} = 0.664 \frac{1}{\text{Pr}^{\frac{1}{6}}} \left(\text{Re Pr} \frac{D}{L} \right)^{\frac{1}{2}} \quad (\text{C.13})$$

Between transition and turbulent regimes, the empiric form of Nusselt number is valid:

$$\text{Nu} = a \text{Re}^b \text{Pr}^n \quad (\text{C.14})$$

In this case, classical relations may be applied:

- Dittus-Boelter if $0.7 < \text{Pr} < 120$; $10^4 < \text{Re} < 1.2 \cdot 10^5$ and $L/D > 60$, with $n=0.3$ or 0.4 if the liquid in the tube is respectively cooled or heated.
- Colburn if $0.7 < \text{Pr} < 120$.
- Petukhov and Gnielinski if $0.6 < \text{Pr} < 2000$; $2300 < \text{Re} < 10^6$ and $0 < L/D < 1$:

$$\text{Nu} = \frac{\Lambda/8 (\text{Re} - 1000) \text{Pr}}{1 + 12.7 \left(\text{Pr}^{\frac{2}{3}} - 1 \right) \sqrt{\frac{\Lambda}{8}}} \left[1 + \left(\frac{D}{L} \right)^{\frac{2}{3}} \right] \quad (\text{C.15})$$

where Λ is the Darcy's coefficient.

Pressure drops Here only correlations for smooth and circular-section tubes are reported. As usually, pressure drops are calculated as [131]:

$$\Delta P = \Lambda \left(\frac{L}{D_h} \right) \frac{1}{2} \rho u^2 \quad (\text{C.16})$$

For laminar regimes the Darcy's coefficient is classically [131]:

$$\Lambda = \frac{64}{\text{Re}} \quad (\text{C.17})$$

For turbulent flows, if $2300 < \text{Re} < 100\,000$ it is:

$$\Lambda = \frac{0.3164}{\text{Re}^{\frac{1}{4}}} \quad (\text{C.18})$$

if $2 \cdot 10^4 < \text{Re} < 10^6$, Herman or Filonenko's relation may be used indifferently [131]. According to Herman:

$$\Lambda = 0.00540 + \frac{0.3964}{\text{Re}^{0.3}} \quad (\text{C.19})$$

and according to Filonenko:

$$\Lambda = (1.83 \log \text{Re} - 1.64)^{-2} \quad (\text{C.20})$$

Finally, if $\text{Re} > 10^6$ Karman-Nikuradze's relation is used:

$$\frac{1}{\sqrt{\Lambda}} = -0.8 + 2 \log \left(\text{Re} \sqrt{\Lambda} \right) \quad (\text{C.21})$$

Two-phase

Heat transfer For heat transfer calculations in the case of two-phase heat exchange, Thome's condensation heat transfer model [122, 123] is used. It is based on:

1. Determination of void fraction, ε , using the logarithmic mean void fraction method (LM ε):

$$\varepsilon = \frac{\varepsilon_h - \varepsilon_{ra}}{\ln \frac{\varepsilon_h}{\varepsilon_{ra}}} \quad (\text{C.22})$$

where

$$\varepsilon_h = \left[1 + \left(\frac{1-x}{x} \right) \left(\frac{\rho_v}{\rho_l} \right) \right]^{-1} \quad (\text{C.23})$$

and

$$\varepsilon_{ra} = \frac{x}{\rho_v} \left\{ [1 + 0.12 (1 - x)] \left[\frac{x}{\rho_v} + \frac{1 - x}{\rho_l} \right] + \frac{1.18 (1 - x) [g \sigma (\rho_l - \rho_v)]^{0.25}}{G \rho_l^{0.5}} \right\} \quad (C.24)$$

2. Determination of local flow pattern. Such task is pretty complex and requires the application of a quite wide range of relations and iterative resolution of some equations. It is suggested to consult ref. [122] for more details. Thanks to this task it is possible to identify with a pretty good approximation the flow pattern of each sub-heat-duty zone of the condenser (see sec. 7.2.1).

3. Flow pattern identification. Based on it, different relation must be applied.

a) If flow pattern is annular, condensation HTC has the form:

$$h_c = c \text{Re}_l^n \text{Pr}_l^m \frac{\lambda_l}{\delta} f_i \quad (C.25)$$

where, λ_l is the liquid thermal conductivity and the liquid film Reynolds number is calculated as:

$$\text{Re}_l = \frac{4 G (1 - x) \delta}{(1 - \epsilon) \mu_l} \quad (C.26)$$

The annular liquid film thickness is obtained from:

$$A_l = \frac{2 \pi - \theta}{8} [d^2 - (d - 2 \delta)^2] \quad (C.27)$$

with d internal diameter of the tube, A_l the cross sectional area occupied by liquid phase, and θ the upper-side angle of the tube not wetted by stratified liquid.

Interfacial roughness correction factor, f_i , is calculated as:

$$f_i = 1 + \left(\frac{u_v}{u_l} \right)^{\frac{1}{2}} \left(\frac{(\rho_l - \rho_v) g \delta^2}{\sigma} \right)^{\frac{1}{4}} \quad (C.28)$$

In eq. (C.28), liquid and vapour velocities are $u_l = \frac{G(1-x)}{\rho_l(1-\epsilon)}$ and $u_v = \frac{Gx}{\rho_v \epsilon}$ respectively.

b) If flow pattern is stratified-wavy, convective condensation heat transfer coefficient, h_c ; heat transfer coefficient of condensing film on top perimeter of the tube, h_f , and local perimeter condensing fluid, h_{tp} , have to be considered. h_c

is calculated with eq. (C.25). h_f is:

$$h_f = 0.655 \left[\frac{\rho_l (\rho_l - \rho_v) g h_{lv} \lambda_l^3}{\mu_l dq} \right] \quad (C.29)$$

where dq is the applied heat flux on analysed sub-heat-duty zone. Finally, local perimeter heat transfer coefficient, h_{tp} , is defined as a function of internal radius:

$$h_{tp} = \frac{h_f r \theta + h_c r (2\pi - \theta)}{2\pi r} \quad (C.30)$$

c) If flow pattern is fully stratified, the angle θ_{strat} is calculated from:

$$A_l = \frac{d^2}{8} [(2\pi - \theta_{strat}) - \sin(2\pi - \theta_{strat})] \quad (C.31)$$

or

$$\begin{aligned} \theta_{strat} = 2\pi - 2 \left\{ \pi(1 - \varepsilon) + \left(\frac{3\pi}{2} \right)^{1/3} \left[1 - 2(1 - \varepsilon) + (1 - \varepsilon)^{1/3} - \varepsilon^{1/3} \right] \right. \\ \left. - \frac{1}{200} \varepsilon(1 - \varepsilon) [1 - 2(1 - \varepsilon)] \left[1 + 4 \left((1 - \varepsilon)^2 + \varepsilon^2 \right) \right] \right\} \end{aligned} \quad (C.32)$$

h_c is calculated from eq. (C.25), but considering the roughness correction factor, f_i , calculated as:

$$f_i = 1 + \left(\frac{u_v}{u_l} \right)^{\frac{1}{2}} \left(\frac{(\rho_l - \rho_v) g \delta^2}{\sigma} \right)^{\frac{1}{4}} \left(\frac{G}{G_{strat}} \right) \quad (C.33)$$

h_f and h_{tp} are calculated from eq. (C.29) and (C.30) respectively.

Pressure drops Pressure drops are calculated as reported in ref. [132]. The same method than cf. B.2.2.1 is used to calculate total two-phase pressure drops. Sum of frictional pressure losses, $\left(\frac{dP}{dz}\right)_f$, acceleration pressure losses, $\left(\frac{dP}{dz}\right)_a$ and gravity pressure losses, $\left(\frac{dP}{dz}\right)_g$, are considered for the purpose. Friction pressure losses are calculated as [132]:

$$-\left(\frac{dP}{dz}\right)_f = -0.09 (1 + 2.85X^{0.523})^2 \frac{\mu_v^{0.2} (\dot{m} x)^{1.8}}{\rho_v d^{1.2}} \quad (C.34)$$

where the factor X^2 is defined as:

$$X^2 = \frac{\left(\frac{dP}{dz}\right)_{f,l}}{\left(\frac{dP}{dz}\right)_{f,v}}$$

Acceleration term is calculated as:

$$-\left(\frac{dP}{dz}\right)_f = -\frac{\dot{m}^2}{\rho_v} \frac{dx}{dz} \left[2x + (1-2x) \left(\frac{\rho_v}{\rho_l}\right)^{\frac{1}{3}} + (1-2x) \left(\frac{\rho_v}{\rho_l}\right)^{\frac{2}{3}} - (2-2x) \left(\frac{\rho_v}{\rho_l}\right) \right] \quad (C.35)$$

and gravity term is:

$$-\left(\frac{dP}{dz}\right)_g = g \sin \theta [\varepsilon \rho_v + \rho_l (1 - \varepsilon)] \quad (C.36)$$

Classical relations are used for localised pressure losses, that are calculated as reported in ref. [133].

C.2 Louvered fins & microchannels heat exchanger

C.2.1 Limitations and hypothesis

Even in this case fluid thermo-physical properties are calculated at inlet, outlet and saturation conditions. In this case, pressure drops related to collectors (or manifold) are considered in calculation, only two passages may be considered for calculation.

C.2.1.1 External side

Heat transfer For louvered fins, correlation reported in [134] is used. Such correlation agrees with experimental data at about 89%, within $\pm 15\%$ and gives a mean deviation of 7.6% [134]. The Colburn factor is:

$$j = \text{Re}_{L_p}^{0.49} \left(\frac{\theta}{90}\right)^{0.27} \left(\frac{F_p}{L_p}\right)^{-0.14} \left(\frac{F_l}{L_p}\right)^{-0.29} \left(\frac{T_d}{L_p}\right)^{-0.23} \left(\frac{L_l}{L_p}\right)^{0.68} \left(\frac{T_P}{L_P}\right)^{-0.28} \left(\frac{\delta_f}{L_p}\right)^{-0.05} \quad (C.37)$$

where θ is the louver angle; L_h , L_l , L_p are respectively louver height, length and pitch. δ is the thickness of the tube, while T_p and T_d tube pitch and tube depth respectively.

Pressure drop Correlation presented in ref. [135] is used for air side friction factor calculation. Such correlation agrees with experimental data at 83.1% within $\pm 15\%$ and presents a mean deviation of 9.2%.

The friction factor is calculated as:

$$f = f_1 f_2 f_3 \quad (\text{C.38})$$

where:

$$f_1 = \begin{cases} 14.39 \text{Re}_{Lp}^{(-0.805 \frac{F_p}{F_l})} \left[\ln \left(1 + \frac{F_p}{L_p} \right) \right]^{3.04} & \text{Re}_{Lp} < 150 \\ 4.97 \text{Re}_{Lp}^{(0.6049 - \frac{1}{\theta^{0.2}})} \left[\ln \left(\left(\frac{F_t}{F_p} \right)^{0.5} + 0.9 \right) \right]^{-0.527} & 150 < \text{Re}_{Lp} < 5000 \end{cases} \quad (\text{C.39})$$

$$f_2 = \begin{cases} \left[\ln \left(\left(\frac{F_t}{F_p} \right)^{0.48} + 0.9 \right) \right]^{-1.435} \left(\frac{D_h}{L_p} \right)^{-3.01} \ln^{-3.01}(0.5 \text{Re}_{Lp}) & \text{Re}_{Lp} < 150 \\ \left[\ln(0.5 \text{Re}_{Lp}) \frac{D_h}{L_p} \right]^{-2.966} \left(\frac{F_p}{L_l} \right)^{-0.7931 \frac{T_p}{T_h}} & 150 < \text{Re}_{Lp} < 5000 \end{cases} \quad (\text{C.40})$$

$$f_3 = \begin{cases} \left(\frac{F_p}{L_l} \right)^{-0.308} \left(\frac{F_d}{L_l} \right)^{-0.308} \left(e^{-0.1167 \frac{T_p}{D_m}} \right) \theta^{0.35} & \text{Re}_{Lp} < 150 \\ \left(\frac{T_p}{D_m} \right)^{-0.0446} \ln^{-3.553} \left(\frac{L_p}{F_p} \right)^{\frac{1}{4}} \theta^{-0.477} & 150 < \text{Re}_{Lp} < 5000 \end{cases} \quad (\text{C.41})$$

C.2.1.2 Internal side

Single-phase

Pressure drops

The study [136] reports relations implemented for friction factor, f , evaluation in EchTherm. For laminar regimes:

$$4f = \frac{4C_{f,l}}{\text{Re}^{1.98}}$$

and for turbulent regimes:

$$4f = \frac{4C_{f,l}}{\text{Re}^{1.72}}$$

Two-phase Both used heat transfer and pressure drop relations are taken from ref. [137]. The same method presented in cf. B.2.2.1 has to be applied for pressure drop estimation in mini or microchannels. Cavallini *et al.* [137] presented a method, based on Friedel parameters (cf. B.2.2.1), to calculate frictional pressure gradient in annular flow.

Frictional pressure gradient is:

$$\left(\frac{dP}{dz}\right)_f = \phi_{lo}^2 \left(\frac{dP}{dz}\right)_{f,lo} = \frac{2 \phi_{lo}^2 f_{lo} G}{D_h \rho_l} \quad (C.42)$$

where

$$\phi_{lo}^2 = Z + 3.595 F H W (1 - E)^W = 1.398 P_R \quad (C.43)$$

$$Z = (1 - x)^2 + x^2 \left(\frac{\rho_l}{\rho_v}\right) \left(\frac{\mu_l}{\mu_v}\right)^{0.2} \quad (C.44)$$

$$F = x^{0.9525} (1 - x)^{0.414} \quad (C.45)$$

$$H = \left(\frac{\rho_l}{\rho_v}\right)^{1.132} \left(\frac{\mu_v}{\mu_l}\right)^{0.44} \left(1 - \frac{\mu_v}{\mu_l}\right)^{3.542} \quad (C.46)$$

The coefficient E is calculated as:

$$E = 0.015 + 0.44 \log \left[\left(\frac{\rho_{gc}}{\rho_l}\right) \left(\frac{\mu_l \dot{j}_G}{\sigma}\right)^2 \cdot 10^4 \right] \quad (C.47)$$

if $E < 0.95$, else $E = 0.95$. In eq. (C.42), the factor f_{lo} is:

$$f_{lo} = 0.046 \left(\frac{G D_h}{\mu_l}\right)^{-0.2} \quad (C.48)$$

Once calculated pressure losses from Cavallini's model, the heat transfer coefficient, h_{an} , may be calculated as follows:

$$h_{an} = \frac{\rho_l c_{p,l} \sqrt{\frac{\tau}{\rho_l}}}{T^+} \quad (C.49)$$

where the liquid-vapour interfacial shear stress is calculated as:

$$\tau = \left(\frac{dP}{dz}\right)_f \frac{1}{4} D_h$$

In eq. (C.49), T^+ is defined as follow

$$T^+ = \begin{cases} \delta^+ \text{Pr}_l & \delta^+ \leq 5 \\ 5 \left\{ \text{Pr}_l + \ln \left[1 + \text{Pr}_l \left(\frac{\delta^+}{5} - 1 \right) \right] \right\} & 5 < \delta^+ < 30 \\ 5 \left\{ \text{Pr}_l + \ln [1 + 5 \text{Pr}_l] + 0.495 \ln \left(\frac{\delta^+}{30} \right) \right\} & \delta^+ \geq 30 \end{cases} \quad (C.50)$$

and

$$\delta^+ = \begin{cases} \sqrt{\frac{\text{Re}_l}{2}} & \text{Re}_l \leq 1145 \\ 0.0504 \text{Re}_l^{\frac{7}{8}} & \text{Re}_l > 1145 \end{cases}$$

and

$$\text{Re}_l = \frac{G(1-x)(1-E)D_h}{\mu_l}$$

Heavy duty tests

With the purpose to check CPLIP's resistance and reliability to long duration load, heavy duty tests have been performed. Test campaigns lasted seven days and CPLIP worked at constant thermal load applied to the evaporator up to 9 hours/day. Every day the same thermal load was applied to the evaporator, $Q_{th} = 2 \text{ kW}$, with reservoir and cold source temperatures of $T_{res} = 70^\circ\text{C}$ and $T_{sec} = 20^\circ\text{C}$, respectively. In Fig. D.1 an example of heavy duty test is reported. There, only maximal and minimal evaporator

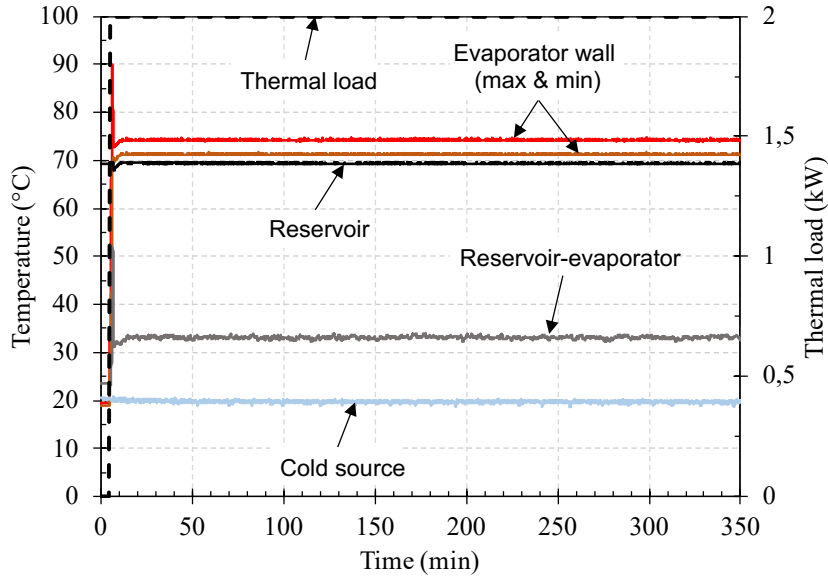


Figure D.1: Heavy duty test (methanol, $T_{res} = 70^\circ\text{C}$, $T_{sec} = 20^\circ\text{C}$, $Q_{th} = 2 \text{ kW}$)

wall, reservoir, reservoir-evaporator line and cold source temperatures are reported for clarity of reading.

During the whole test campaign the loop does not encountered any kind of problem, continuing to work all the time.

Apparently, no chemical reactions occurred in the evaporator, as NCG check demonstrates.

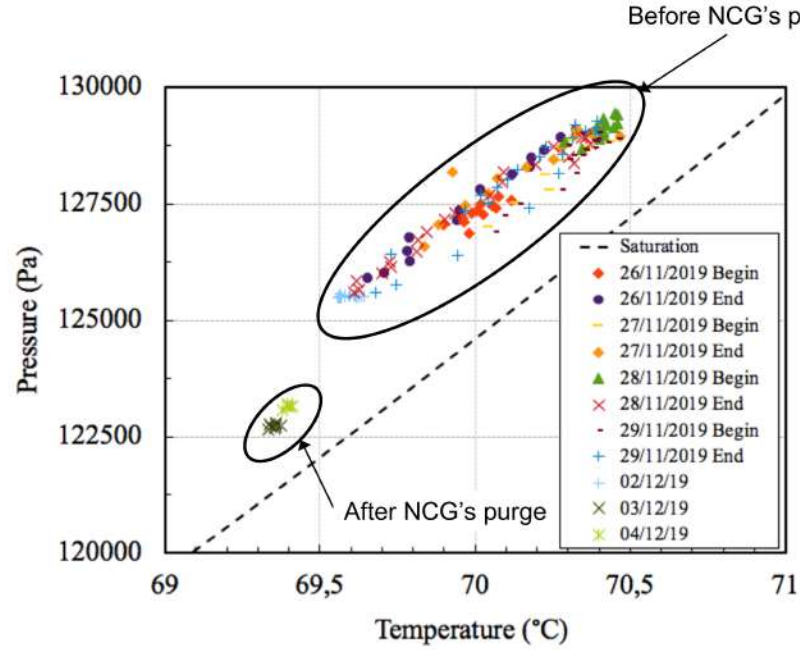


Figure D.2: Saturation conditions in the reservoir before and after the tests (methanol, $T_{res} = 70^\circ\text{C}$)

Presence of non-condensable-gases was checked at the beginning and at the end of each test. No particular phenomena are noticeable as one may observe in Fig. D.2. Pressure and temperature at the beginning and at the end of each test are quite similar. A slight amount of NCG were present in the CPLIP reservoir at the beginning of the test campaign.

CONCEPTION DE SOLUTIONS DE REFROIDISSEMENT PAR VOIE DIPHASIQUE D'ELECTRONIQUE DE PUISSANCE EN CONTEXTE AERIEN REpondant AUX OBJECTIFS DE L'AVION HYBRIDE 2035

Le monde aérien est lui aussi destiné à réduire drastiquement son empreinte environnementale. Cela passe pour partie par l'innovation technologique et la réduction de l'énergie nécessaire à la propulsion. Dans cet objectif, les travaux relatés dans ce mémoire s'inscrivent dans un projet de recherche (Clean Sky 2-HASTECS) visant le développement de propulsion hybride mettant à profit les performances d'une chaîne électrique. Les puissances mises en jeu requièrent de revisiter les solutions de refroidissement pour atteindre les spécifications de puissance massique envisagées à l'horizon 2035. Nous nous intéressons ici à la gestion thermique de l'électronique de puissance qui vise une puissance massique de 25kW/kg à cet horizon. Le travail effectué, essentiellement numérique, est lié à la recherche, au dimensionnement, à l'optimisation, et à l'analyse d'une technologie de refroidissement efficace, caractérisée par une faible masse et capable de contrôler la température des composants électroniques dans les conditions opératoires les plus drastiques. Différentes technologies de refroidissement, actives mono et diphasiques et passives, à pompage capillaire, ont été analysées et comparées sur la base de données disponibles dans la littérature et d'un dimensionnement de première approximation : la solution la plus adaptée a été choisie en utilisant comme critère sa masse spécifique. La solution finalement retenue et présentant le meilleur indice de masse spécifique global est une boucle diphasique CPLIP (Capillary Pumped Loop for Integrated Power), par ailleurs pourvue des caractéristiques thermiques et hydrauliques uniques. Après son dimensionnement, la CPLIP a été optimisée pour répondre aux objectifs à deux horizons successifs, 2025 et 2035 (mentionnons un travail itératif avec les chercheurs responsables du développement de l'électronique permettant une optimisation mutuelle). L'attention a été en particulier concentrée sur le condenseur, le composant le plus lourd de la boucle. La solution 2025 est caractérisée par un condenseur classique air-méthanol, et a démontré sa capacité d'aller au-delà du seuil de 15 kW/kg demandé. La solution 2035, caractérisée par un concept de condenseur innovant : à micro-canaux et à ailettes à persiennes, a permis d'obtenir, après ce travail de co-dimensionnement thermique-électronique, des valeurs de puissance spécifique doubles par rapport à l'objectif 2035. Dans cette thèse, les caractéristiques hydrauliques et thermiques de la boucle CPLIP ont été analysées expérimentalement sur un prototype issu d'études antérieures, et numériquement à l'aide d'un modèle CFD ainsi qu'à l'aide d'un modèle 0D innovant. Les résultats démontrent l'aptitude de la CPLIP à gérer thermiquement l'électronique de puissance pour des cycles de mission d'un avion court ou moyen-courrier, caractérisés par des changements brutaux de puissance thermique, tout en assurant le contrôle de la température des modules électroniques. Enfin, une étude a été conduite portant sur le comportement transitoire de la boucle, en particulier lors des démarrages sévères à très hautes puissances, ainsi que pendant des cycles d'accélération sévères qui caractérisent ce champ d'application. Dans le premier cas, une étude expérimentale et numérique a été menée pour démontrer la capacité de la boucle à démarrer dans les conditions thermiques et environnementales les plus difficiles (haute puissance de démarrage et haute température environnementale). Dans le deuxième cas, une étude numérique a été utilisée pour comprendre quel est le comportement de la boucle quand des champs d'accélération, jusqu'à 10g, perturbent ses conditions opératoires. Ce travail ouvre des perspectives très intéressantes tant du point de vue de l'application que vis-à-vis de la nécessité aujourd'hui d'adopter des approches de recherche couplées pour dimensionner simultanément thermiquement et électriquement l'électronique de puissance.

Mots clés : (Appareils électroniques--Température--Régulation, Électronique de puissance, Simulation par ordinateur, Moteurs hybrides, Avion hybride, Refroidissement, Boucle à pompage capillaire)

TWO-PHASE POWER ELECTRONICS COOLING SOLUTION DESIGN IN AIR CONTEXT ANSWERING TO THE OBJECTIVES OF THE HYBRID AIRCRAFT 2035

Technological innovation and reduction of the energy required for propulsion is necessary to reduce aircrafts environmental impact. The present work is part of the research project Clean Sky 2 – HASTECS, which purpose is the development of a hybrid propulsion aircraft. The high powers involved make classical cooling solutions obsolete, in terms of efficiency, and not suitable for the power to mass ratio required for the target 2035. In particular, the problem related to power electronics cooling is assessed in this work with the purpose to achieve a performance coefficient of 25 kW/kg. This work, essentially numerical, is linked to the research, design, optimisation and analysis of a high efficiency cooling system, able to control power electronics components temperature, operating in pretty severe conditions (high thermal power density, >15kW; cyclic variation of cold source temperature and severe transient phases) and which has to be lightweight to ensure performance coefficient requirements. Different cooling technologies, active single and two-phase and passive capillary driven, have been analysed and compared on the basis of literature data and of a first approximation design: the most adapted solution has been chosen on the base of its specific power [kW/kg]. The solution that has been finally retained is a Capillary Pumped Loop for Integrated Power (CPLIP), which thermal characteristics are quite interesting and unique. After its design, the loop has been optimised to answer to objectives of 2025 and 2035. It is worth of attention the work carried out in collaboration with power electronics team of the same project to achieve a mutual optimisation of the systems. Concerning the thermal side, the attention was focused on the condenser, the heaviest component in the loop. The 2025's solution is characterised by a classical flat plate air-methanol condenser which allowed to cross over the threshold of 15kW/kg for 2025. 2035's solution, on the contrary, is characterised by an innovative condenser typology, using microchannels on methanol side and louvered fins on air side, allowing to obtain more than double of the power coefficient required! In this work, thermal and hydraulic characteristics of the CPLIP have been experimentally analysed, using a prototype deriving from previous studies, and by using CFD and a 0D model. Results show the ability of the CPLIP to control the temperature of power electronics modules during a short and medium-range aircraft mission profile, characterised by sudden changes of thermal load and cyclic variations of the cold source temperature. Finally, a study focused on the transient behaviour of the loop has been carried out. In particular, the start-up of the CPLIP and its behaviour during sudden and violent acceleration stages, characterising this application field, have been exploited. In the first case, an experimental and a numerical study were carried out to demonstrate the ability of the loop to start its operation in the most difficult thermal and environmental conditions (high thermal load and high environmental temperature). In the second case, a numerical study has been performed to understand the behaviour of the loop when an acceleration field up to 10g perturbs its operations. This work opens new interesting perspectives stand points concerning the application itself and the necessity to adopt a multidisciplinary approach to simultaneously thermally and electronically design new generation power electronics.

Keywords: (Electronic apparatus and appliances--Temperature control, Power electronic, Computer simulation, Hybrid aircraft, Cooling, Capillary pumped loop)